University of Southampton

Faculty of Environmental and Life Sciences

School of Ocean and Earth Science

The Hydrologic Cycle and Associated Terrestrial Carbon Cycle Feedbacks during Past Hothouse Climates

by

Emily Hannah Hollingsworth

ORCID ID 0000-0002-7067-6837

Thesis for the degree of Doctor of Philosophy

Dec 2024

University of Southampton

Abstract

Faculty of Environmental and Life Sciences

School of Ocean and Earth Science

Thesis for the degree of Doctor of Philosophy

The Hydrologic Cycle and Associated Terrestrial Carbon Cycle Feedbacks during Past Hothouse Climates

by

Emily Hannah Hollingsworth

Anthropogenic greenhouse gas (GHG) emissions continue to propel Earth towards a 'hothouse' world, with profound ramifications upon global biogeochemical cycles. Yet, the response of complex biogeochemical interactions remain highly uncertain, impeding accurate predictions of future climate change. The development of novel lipid biomarker-based proxies have created the opportunity to characterise the hydrologic cycle and associated terrestrial carbon cycle feedbacks (*e.g.,* rock organic carbon oxidation and methane cycling) in the geologic record. This thesis explores the hothouse worlds (*i.e.* Paleocene and Eocene; ~66–34 Ma) and a hyperthermal event (*i.e.* Paleocene-Eocene Thermal Maximum; PETM; ~56 Ma) of the past, as they provide the closest analogue for a high emission/low mitigation climate scenario. Leaf wax biomarkers indicate that the tropics were characterised by an extremely variable hydrologic cycle during the latest Paleocene (~57–56 Ma). Such conditions may have had far-reaching consequences for rock organic carbon oxidation and methane cycling. To investigate the impact of an intensified hydrologic cycle, new biomarker-based records are established to reconstruct the mobilisation of 'petrogenic' organic carbon (OC_{petro}) and the methane cycle during the PETM. The data reveals widespread delivery of OC_{petro} to the oceans, which is attributed to an increase in extreme precipitation events. Raman spectroscopy is then used to evaluate whether the PETM also coincided with enhanced oxidation of OC_{petro}. Evidence suggests that there was a high OC_{petro} oxidation efficiency in the mid-latitudes, although this appears spatially variable. To reconstruct the methane cycle, a diverse range of bacteriohopanepolyols (BHPs) are identified in a PETM-aged lignite deposit, and specific BHPs show promise as a proxy for methanotrophy in the geologic past. Taken together, there are signs of an increase in both OC_{petro} and methane oxidation during the PETM. Overall, this implicates that these positive feedback mechanisms will likely be sensitive to transient warming in the future, and should thus be incorporated in the newest generation of climate models.

Table of Contents

Table of Figures

Table of Figures

Table of Tables

Research Thesis: Declaration of Authorship

Print name: Emily Hannah Hollingsworth

Title of thesis: The Hydrologic Cycle and Associated Terrestrial Carbon Cycle Feedbacks during Past Hothouse Climates

I declare that this thesis and the work presented in it are my own and has been generated by me as the result of my own original research.

I confirm that:

1. This work was done wholly or mainly while in candidature for a research degree at this University;
2. Where any part of this thesis has previously been submitted for a degree or any other qualification at this University or any other institution, this has been clearly stated;
3. Where I have consulted the published work of others, this is always clearly attributed;
4. Where I have quoted from the work of others, the source is always given. With the exception of such quotations, this thesis is entirely my own work;
5. I have acknowledged all main sources of help;
6. Where the thesis is based on work done by myself jointly with others, I have made clear exactly what was done by others and what I have contributed myself;
7. Parts of this work have been published as:
   - Chapter 1 Section 1.4.4 has been published as Inglis, G.N., Bhattacharya, T., Hemingway, J.D., **Hollingsworth, E.H.,** Feakins, S.J., and Tierney, J.E. 2022. Biomarker Approaches for Reconstructing Terrestrial Environmental Change, *Annual Reviews in Earth and Planetary Science*. 50, pp. 369-394. https://doi.org/10.1146/annurev-earth-032320-095943.
   - Chapter 4 has been published as **Hollingsworth, E.H.**, Elling, F.J., Badger, M.P.S., Pancost, R.D., Dickson, A.J., Rees-Owen, R.L., Papadomanolaki, N.M., Pearson, A., Sluijs, A., Freeman, K.H., Baczynski, A.A., Foster, G.L., Whiteside, J.H., and Inglis, G.N. 2024. Spatial and Temporal Patterns in Petrogenic Organic Carbon Mobilization During the Paleocene-Eocene Thermal Maximum, *Paleoceanography and Paleoclimatology.* 39(2). https://doi.org/10.1029/2023PA004773.
   - Chapter 5 has been published as **Hollingsworth, E.H.**, Sparkes, R.B., Self-Trail, J.M., Foster, G.L., and Inglis, G.N. Enhanced petrogenic organic carbon oxidation during the Paleocene-Eocene thermal maximum, *Geochemical Perspective Letters*. 33. https://doi.org/10.7185/geochemlet.2444.

Signature: Date:

Acknowledgements

I firstly want to thank my supervisor, Gordon. To move countries and start in a new University at the height of the Covid-19 pandemic could have been an isolating experience. But the flexibility, regular meetings, and quick replies meant I never felt alone in the process. Thank you for going through my many drafts (always providing thorough feedback), and for putting up with my many tangential speeches and continued advocacy for my favourite font. Alongside my persisting viewpoints, I have also gained so many new ideas and perspectives for which I have you and many others to thank for.

To Sarge, I will always be grateful to have gone through my PhD in a lab that has a manager like you. You always make time to show and teach others on all that you know (which is a lot!), and with such enthusiasm and in a way that is easy to digest. I am quietly happy for the first couple of years when there were restrictions and less people in the OG group, for I was able to maximise my time learning from you.

A quick thank you to Celina Suarez, a visiting scientist back in 2021, who left me her electric blue folding bike. This bike may be heavier than any normal bike – and slowly falling apart – but it saved me 100s of hours of commuting time, for which I am very happy.

From organising journal clubs with just myself and Gordon, I have enjoyed watching the OG group at the NOC grow. At the beginning there was Marlow – I only wish we got to go on more hikes whilst you were in the UK (though maybe minus the denting of my car!) Then there was Jana, Joe (my PhD 'brother'), Elise, Alex, Mark, Ash – and more recently – Tobias, and Daisy. Although they were few and far between, I have enjoyed every conversation and absorbed a lot from listening to all the talks on research plans and adventures.

Thank you to Amy, Alex and Tereza for welcoming me into office 164/21, and who I got to know during the many pandemic-rule-breaking lunch chats. To Tom, I'm glad we started this PhD journey together! From an all-female office, Tom, Luke, Joe, Fang, Andy, Prem, and baby Florence (or 'proto-geochemist' as labelled by her father) have since joined the 164/21 gang, to make up the loveliest group of people. Thank you for entertaining my annual sunflower growing competition / opportunity to roast each other, and for providing great company over many tea breaks and lunches. Also, a shout-out to those I've enjoyed climbing with!

Thank you to Mr Todd-Jones, my secondary school Geography teacher of 7 years, who sparked my curiosity in Earth Sciences. My choice to pursue academia is ultimately thanks to James Bendle, who introduced me to biomarkers and urged me to apply to a 2-year MSc course at Utrecht University. During this time, I was incredibly fortunate to be taught by many inspiring lecturers. To name a couple, Stefan Schouten provided me with the foundations of everything I needed to know to begin a PhD in organic geochemistry, and furthered my interest and love for biomarkers. Frits Hilgen shaped my perspective and understanding of time, which I needed to transition from the mindset of a geographer to a geologist. Thank you to the many others who have played a mentorship role and helped me grow as a scientist, including Peter Bijl and Appy Sluijs. And to Gavin, the last standing member of my extended supervisory team.

I feel particularly grateful for the collaborators that I have got to work with, so many of whom went above and beyond to support me. Thank you to the technicians (Hayley and Mckenzie), those who sent me samples and data (Felix, Ann, Marcus, Rich, Rhian, Nina, Appy, and Jean), read through manuscripts (Kate, Allison, and Jessica), and listened to my ideas

(Joost). To Rob, I really enjoyed collaborating with you and thank you for showing me everything I needed to know about Raman spectroscopy. Thank you to those at Bristol who were willing to provide me with guidance when I sought it, Rich (my PhD 'grandfather'), David, and Cait. I had the best experience at JAMSTEC (with 高野, 菅, 古賀, 小川, 大河内, 石川, Aymeric, Adam, Calum, and many others) and at NIOZ (with Darci, Ellen, Anchelique, Denise, Nicole, and many others) because I got to meet and work with the friendliest people, whom had a lasting impact on me. And to the many others who influenced me during IsoCamp, conferences, and workshops.

And finally, to my family and friends. My sister, Lisa, who made her home welcome for me to use pre-and post-trips throughout my PhD – very cheap accommodation for London! And thank you for inviting me to the most epic adventure in Peru, what a way to take a much needed break during my writing period. To my Grandma, Grandad, おばあちゃんとおじいちゃん, thank you for always believing in me. I hope to continue to make you all proud.

My best friend of 10 years and counting, Kirsten, who has been there since Day 1 of my academic journey. Thank you for fully taking care of me during a hard time in my undergraduate. You, and then my time in the Netherlands, taught me that stopping and taking care of my health is the most helpful thing I can do when everything starts to feel overwhelming.

Mike, my partner in life and science. Thank you for always being a listening ear, not only to help me work through my emotions but to also bounce and spar ideas with. In truth, you deserve to be acknowledged for a lot of the ideas in this thesis. I could not have made sense of my jumbled thoughts without you. I'll always admire you as a scientist, especially as you're good at the things I struggle with the most. And even though you don't believe it, you are far better at this than I am.

I feel that my efforts have played a minor role towards the completion of this thesis. I am incredibly lucky that I could pursue what I wanted to, and this is all because of my parents. They made sure that they could provide me with the right opportunities and confidence to take this academic path. The irony of rebelling as a teenager and not wanting to go to University, to then end up going and staying for a whole decade! None of this would have been possible without you both (and the numerous motivational speeches). Thank you for giving me all the support and encouragement. 本当にありがとうございました!

List of Abbreviations

ACEX ..... Arctic Coring Expedition

ACL ..... average chain length

ASE ..... Accelerated Solvent Extractor

BDE ..... Bligh Dyer extracts

BF_3 ..... boron trifluoride

BHPs ..... bacteriohopanepolyol

BIT ..... branched and isoprenoid tetraether

BLAST ..... Basic Local Alignment Search Tool

brGDGT ..... branched glycerol dialkyl glycerol tetraethers

BSTFA ..... *N,O*-Bis(trimethylsilyl)trifluoroacetamide

Ca. ..... *Candidatus*

$CaCO_3$ ..... calcium carbonate

CamDor ..... Cambridge-Dorchester Airport

CCD ..... calcite compensation depth

CH_4 ..... methane

CIA ..... chemical index of alteration

CIE ..... carbon isotope excursion

CMIP ..... Coupled Model Intercomparison Project

CO_2 ..... carbon dioxide

CPI ..... carbon preference index

CSIA ..... compound-specific isotope analysis

Da ..... dalton

DCM ..... dichloromethane

DeepMIP ..... Deep-Time Model Intercomparison Project

DGTS ..... deuterated diacylglyceryltrimethylhomoserine

EA-IRMS ..... elemental analyser-isotope ratio mass spectrometer

ECS ..... equilibrium climate sensitivity

EECO ..... Early Eocene Climatic Optimum

ESI ..... electrospray ionisation

EtAc ..... ethyl acetate

EOT..... Eocene-Oligocene Transition

eV ..... electronvolt

FAME ..... fatty acid methyl esters

FID ..... flame ionisation detector

GC ..... gas chromatography

gC ..... grams of carbon

GC-IRMS..... GC-isotope ratio mass spectrometer

GC-MS ..... GC-mass spectrometry

GCM(s) ..... general circulation model(s)

GDGT..... glycerol dialkyl glycerol tetraethers

GHG..... greenhouse gas

GMST..... global mean surface temperature

HCl ..... hydrochloric acid

HESI..... heated electrospray ionisation

Hex..... hexane

$HRMS^2$ ..... high resolution dual stage mass spectrometry

IPA ..... isopropanol

I.S. ..... internal standard

isoGDGT ..... isoprenoid glycerol dialkyl glycerol tetraethers

ITCZ..... Intertropical Convergence Zone

kyrs ..... thousand years

LAT ..... land air temperature

LC ..... liquid chromatography

LC-MS ..... LC-mass spectrometry

$LC\text{-}NH_2$..... aminopropyl silica gel

LSR(s)..... linear sedimentation rate(s)

Ma ..... millions of years ago

MARS..... microwave-assisted extraction system

MAR(s) ..... mass accumulation rate(s)

MAP ..... mean annual precipitation

mcd ..... metres composite depth

MeOH..... methanol

Mg/Ca ..... magnesium-to-calcium ratio

MTM..... multitaper method

myrs ..... million years

m/z ..... mass-to-charge ratio

Na/Al ..... sodium-to-aluminium ratio

NAIP..... North Atlantic Igneous Province

Na_2SO_4..... sodium sulphate

NH_{3aq} ..... aqueous ammonia

NH_4 ..... ammonium

OC_{bio}..... biospheric organic carbon

OC_{petro} ..... petrogenic organic carbon

ODP ..... Ocean Drilling Program

OEP ..... odd-to-even predominance

PCA..... principal component analysis

PETM ..... Paleocene-Eocene Thermal Maximum

PgC ..... petagrams of carbon

PI ..... pre-industrial

POE ..... pre-onset excursion

ppb ..... parts per billion

ppm ..... parts per million

ppmv ..... parts per million volume

rpm..... revolutions per minute

s.d. ..... standard deviation

SDB..... South Dover Bridge

SIM..... selected ion monitoring

SSP ..... Shared Socioeconomic Pathways

SST ..... sea surface temperature

TAR..... terrigenous-aquatic ratio

TCA..... trichloroacetic acid

TDP..... Tanzania Drilling Project

TEX_{86} ..... TetraEther indeX of tetraethers consisting of 86 carbon atoms

Ti/Al..... titanium-to-aluminium ratio

TIC ..... total ion chromatogram

TLE ..... total lipid extract

T_{max} ..... temperature of maximum hydrocarbon yield

TMS ..... trimethylsilyl

TOC ..... total organic carbon

UCM..... unresolved complex mixture

UHPLC..... ultra-high-performance LC

v:v ..... volume per volume

wt. % ..... weight percentage

Δ47..... carbonate clumped isotope

$\delta^{11}B$ ..... boron isotope ratio (^{11}B:^{10}B)

$\delta^{13}C$ ..... carbon isotope ratio (^{13}C:^{12}C)

$\delta^{13}C_{carbonates}$..... $\delta^{13}C$ of carbonates

$\delta^{13}C_{hop}$ ..... $\delta^{13}C$ of hopanes and hopenes

$\delta^{13}C_{org}$..... $\delta^{13}C$ of organic carbon

$\delta^{13}C_{TOC}$ ..... $\delta^{13}C$ of total organic carbon

$\delta^{13}C_{wax}$..... $\delta^{13}C$ of *n*-alkanes

$\delta^{2}H$ ..... hydrogen isotope ratio (^{2}H:^{1}H)

$\delta^{2}H_{wax}$ ..... $\delta^{2}H$ of *n*-alkanes

$\delta^{2}H_{precip}$ ..... $\delta^{2}H$ of meteoric water

$\delta^{15}N$..... nitrogen isotope ratio (^{15}N:^{14}N)

$\delta^{18}O$..... oxygen isotope ratio (^{18}O:^{16}O)

$\varepsilon_{wax/precip}$ ..... apparent isotopic fractionation

μm..... microns

ρ..... dry bulk density (g cm^{-3})

Chapter 1 Introduction

Preface

Over the duration of this research degree, atmospheric carbon dioxide (CO_2) concentrations have risen from 411.12 ppm (Oct 2020) to 425.05 ppm (Dec 2024) as a result of unabated rates of anthropogenic activity (Keeling *et al.*, 2001). Assuming this trend persists, it would only take ~150 years for atmospheric CO_2 concentrations to exceed 800 ppm, levels not seen in the past 33.9 million years (Rae *et al.*, 2021). For this reason, the geologic record beyond the Eocene (~56–34 Ma) and into the Paleocene (~56–66 Ma) provides the best observational source to determine how the Earth will likely operate in a 'high emissions' scenario (SSP5-5.8; Figure 1.1). These insights may further serve as a target against which to evaluate the newest generation of climate models (*e.g.,* Tierney *et al.*, 2020; Lunt *et al.*, 2024). First demonstrated by Eunice Newton Foote in the mid-19th century (Foote, 1856), the relationship between increasing atmospheric CO_2 concentrations and global mean surface temperature has been relatively well-established. Current estimates for SSP5-5.8 predicts 6.6–14.1 °C of warming by the end of the 23rd century, with medium confidence (IPCC, 2021). This will have a major impact on global biogeochemical cycles, however the potential responses are poorly understood. The discoveries and advancements of new 'tools' allow for such processes to be investigated during past high CO_2 states. This thesis aims to reflect the importance of proxy-based data, focusing on a lipid biomarker approach to contribute several new records that reconstruct the hydrologic cycle and associated terrestrial carbon cycle feedbacks during the early Paleogene.

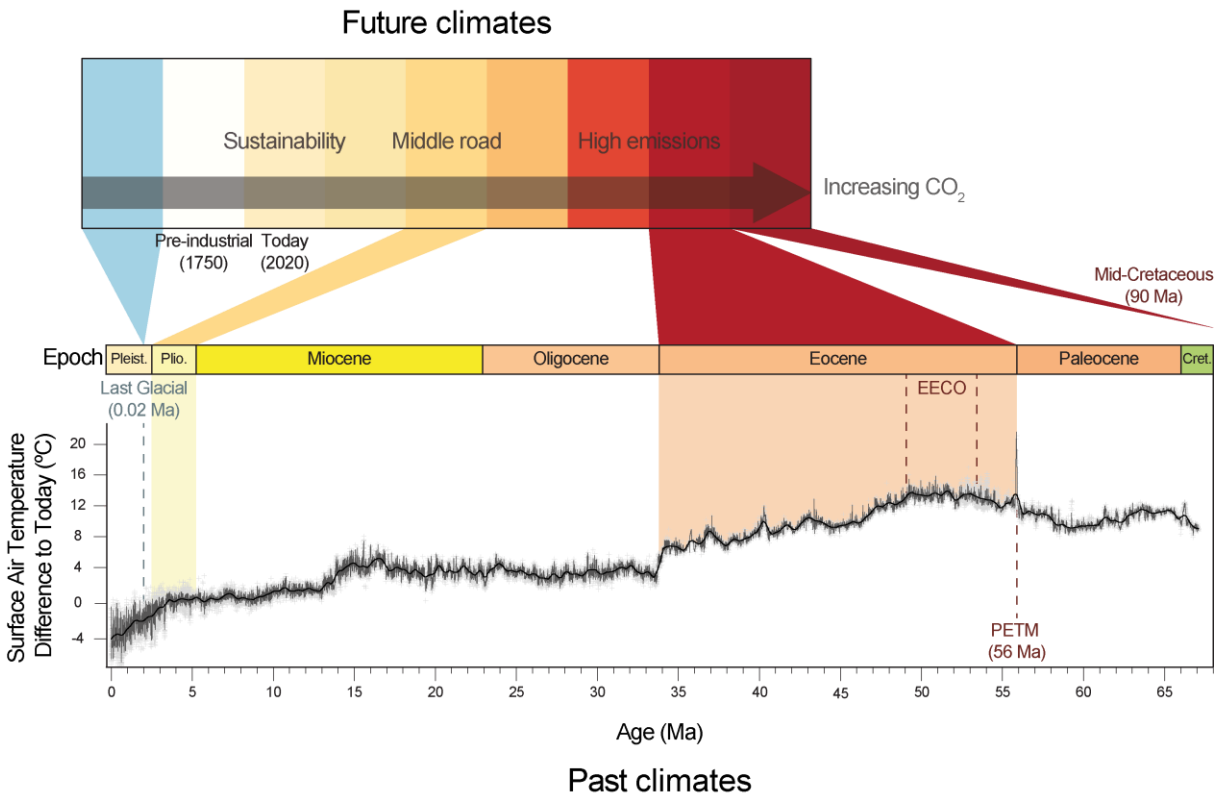

Figure 1.1 **Future climates and their closest past analogues.** Top panel: future climates categorised by global mean annual surface temperature relative to pre-industrial (1750) conditions, ranging from colder (blue) to warmer (red). The three scenarios (*i.e.* 'sustainability', 'middle road', and 'high emissions') correspond to the Shared Socioeconomic Pathways (*i.e.* SSP1-2.6, SSP2-4.5, and SSP5-5.8, respectively) (IPCC, 2013). Both in the past and future, warmer climates are associated with increases in atmospheric CO_2 concentrations (grey arrow). Adapted from Tierney *et al.* (2020). Bottom panel: surface air temperature differences with respect to the Holocene mean temperature of 14.15 °C ('today'), spanning the Cenozoic (66 Ma to present). Reconstructed from a multi-ocean sediment core compilation containing high-resolution records of the stable oxygen isotopic composition ($\delta^{18}O$) of benthic foraminifera. Adapted from Westerhold *et al.* (2020). Pleist.; Pleistocene, Plio.; Pliocene, Cret.; Cretaceous, EECO; Early Eocene Climatic Optimum, PETM; Paleocene-Eocene Thermal Maximum.

Chapter 1 Section 1.4.4 published in *Annual Review of Earth and Planetary Sciences* (Inglis, G.N., Bhattacharya, T., Hemingway, J.D., **Hollingsworth, E.H.,** Feakins, S.J., and Tierney, J.E. 2022. Biomarker Approaches for Reconstructing Terrestrial Environmental Change, *Annual Reviews in Earth and Planetary Science*. 50, pp. 369-394. https://doi.org/10.1146/annurev-earth-032320-095943). GNI wrote the original draft with contributions from all co-authors on writing, reviewing, and editing.

1.1 The Early Paleogene Hothouse

1.1.1 The Background State of the Early Paleogene

The early Paleogene (*i.e.* within the Paleocene to Eocene; ~66–34 Ma) can be considered to be synonymous with the term 'hothouse' (Westerhold *et al.*, 2020). Encompassing the most pronounced global warming trends of the Cenozoic (66 Ma to present; Figure 1.1), a prominent dome-shaped rise and fall in temperature is also interspersed by multiple hyperthermals (see Section 1.1.2). The long-term changes indicate a more gradual increase in temperature from the late Paleocene to the early Eocene, culminating at the Early Eocene Climatic Optimum (EECO; ~53–49 Ma). The EECO was subsequently followed by a cooling towards 'icehouse' conditions, with the establishment of continental-scale Antarctic ice sheets at the Eocene-Oligocene Transition (EOT; ~33.9 Ma). This trend in the background temperatures of the early Paleogene is most clearly depicted in a multi-ocean sediment core compilation of the stable oxygen isotopic composition ($\delta^{18}O$) of benthic foraminifera (Zachos *et al.*, 2001; Zachos, Dickens and Zeebe, 2008; Westerhold *et al.*, 2020). The dataset represents a near continuous record of deep ocean temperature, and ice volume from the Oligocene onwards, at a relatively high temporal resolution of ~100 kyrs.

There are many emerging records of global temperatures during the early Paleogene. Assuming that changes in the deep ocean parallel that of global mean surface temperature (GMST) (Hansen *et al.*, 2013; Valdes, Scotese and Lunt, 2021), and by accounting for the influence of pH on the $\delta^{18}O$ of benthic foraminifera, GMST during the EECO was inferred to be 31.3 ± 1.3 °C (Evans *et al.*, 2024). This estimate is closer to clumped isotope (Δ_{47}) based reconstructions (*e.g.,* Meckler *et al.*, 2022), however is higher than the range of values generated by merging datasets that consist of more direct evidence of surface temperature change (see Inglis, Bragg, *et al.*, 2020 and references therein). The offset is likely driven by the addition of land air temperature (LAT), which may be biased towards lower temperatures (Evans *et al.*, 2024). LAT proxies include the $\delta^{18}O$ of mammal teeth, Δ_{47} of pedogenic carbonate, analyses of fossils and paleosols, and branched glycerol dialkyl glycerol tetraethers (brGDGTs) based indices (see Hollis *et al.*, 2019 and references therein). On the other hand, sea surface temperature (SST) proxies include the $\delta^{18}O$ of surface dwelling carbonaceous and phosphatic fossils (Song *et al.*, 2019), Mg/Ca and Δ_{47} of planktonic foraminifera, and the isoprenoid GDGTs (isoGDGTs) based TEX_{86} index (see Hollis *et al.*, 2019 and references therein). The spatial extent of these records also show that the early Paleogene was characterised by the shallowest pole-to-equator (*i.e.* meridional) temperature gradient of the Cenozoic (*e.g.,* Cramwinckel *et al.*, 2018; Lunt *et al.*, 2021; see Gaskell *et al.*, 2022 and references therein).

Compared to the plethora of literature on temperature trends, changes in the atmospheric CO_2 concentrations during the early Paleogene are of lower temporal resolution and geographically fragmented (*e.g.,* Foster, Royer and Lunt, 2017). Proxies include the boron isotopic composition ($\delta^{11}B$) of foraminifera, stable carbon isotopic composition ($\delta^{13}C$) of C3 land plants (*e.g.,* liverworts) and marine phytoplankton (*e.g.,* alkenones, dinoflagellates, and phytane), and leaf gas exchange and stomatal density based indices (see Hollis *et al.*, 2019 and references therein). However, recent community efforts have progressed the synthesis of available data and contributions of new records (Hönisch *et al.*, 2023). Current best estimates yield atmospheric CO_2 levels in excess of a 1,000 ppm, at 1,470 ppm (+360/-300 ppm), during the EECO (Anagnostou *et al.*, 2020). This dropped to below ~760 ppm by the EOT (*e.g.,* Pearson, Foster and Wade, 2009; Pagani *et al.*, 2011), which agrees with modelling studies that suggest a threshold of ~750 ppm for the observed Antarctic glaciation (*e.g.,* DeConto and Pollard, 2003; DeConto *et al.*, 2008). In conjunction with GMST, this improved CO_2 record provides an opportunity to reassess how climate sensitivity has changed through time. Typically reported as equilibrium climate sensitivity (ECS), this parameter is crucial for forecasting future warming. Inglis *et al.* (2020) demonstrated that the 'bulk' ECS during the EECO was 3.1 °C per doubling of CO_2, with 66 % confidence. This is consistent with the 'very likely' ECS range for the present-day (2–5 °C), stated in the most recent IPCC report (Forster *et al.*, 2021).

1.1.2 Aberrations in the Early Paleogene

The early Paleogene is also punctuated by climate aberrations, occurring over timescales of tens-to-hundreds of thousands of years. These transient trends are most commonly demarcated by a negative shift in the $\delta^{13}C$ values, known as a carbon isotope excursion (CIE). Multiple negative CIEs have been identified in a diverse array of archives (*e.g.,* benthic foraminifera; Figure 1.2). The following discussions focuses on the Paleocene-Eocene Thermal Maximum (PETM; ~56 Ma), as it is the most prominent and well-studied of the CIEs.

1.1.2.1 The PETM

1.1.2.1.1 The Profile of the CIE

Since first discovered over 30 years ago (Kennett and Stott, 1991), the PETM has been found in more than 165 records globally (McInerney and Wing, 2011).The onset of the CIE is defined until the nadir of the $\delta^{13}C$ record, and is on the order-of-millennia (Kirtland Turner, 2018) (Figure 1.2). This is then followed by low and stable $\delta^{13}C$ values for ~94–170 kyrs until the recovery inflection (Zeebe and Lourens, 2019), referred to as the 'body' of the CIE (Bowen *et al.*, 2006). Lastly, the recovery of the PETM took place within ~100 kyrs (Bowen, 2013), and is further divided into Phase I (initial rapid rise in $\delta^{13}C$) and Phase II (final gradual rise in $\delta^{13}C$) (Röhl *et al.*, 2007). Throughout this thesis, references to the 'core' of the PETM

denotes to the combined onset and body of the CIE. Recent publications have also noted a smaller scale excursion preceding the PETM (Sluijs *et al.*, 2007; Self-Trail *et al.*, 2012; Elling *et al.*, 2019; Babila *et al.*, 2022), coined the pre-onset excursion (POE; Bowen *et al.*, 2014). However, it has not been identified in deep-sea sections, perhaps indicating that this was a more localised aberration.

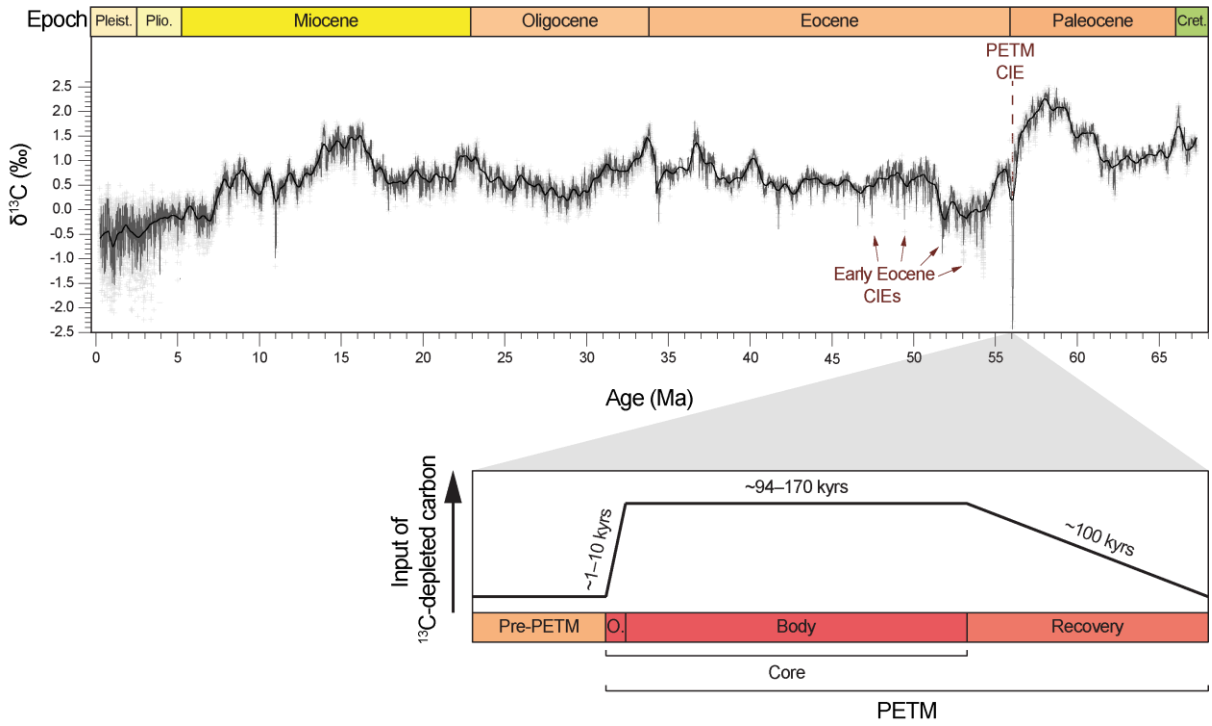

Figure 1.2 **The stable carbon isotopic composition ($\delta^{13}C$) record throughout the Cenozoic (66 Ma to present) and a time-dependent profile of ^{13}C-depleted carbon input during the Paleocene-Eocene Thermal Maximum (PETM).** Top panel: multi-ocean sediment core compilation containing high-resolution records of the $\delta^{13}C$ of benthic foraminifera. The early Eocene and PETM carbon isotope excursions (CIEs) are highlighted. Adapted from Westerhold *et al.* (2020). Pleist., Pleistocene; Plio., Pliocene; Cret.; Cretaceous, EECO; Early Eocene Climatic Optimum, PETM; Paleocene-Eocene Thermal Maximum. Bottom panel: schematic showing the intensity and long duration of ^{13}C-depleted carbon input during the PETM. The core of the PETM includes the onset (O.) and body of the CIE.

1.1.2.1.2 The Cause of the CIE

The CIE of the PETM indicates an injection of ^{13}C-depleted carbon into Earth's active exogenic carbon pool (*i.e.* the ocean, atmosphere, and biosphere). The abrupt onset and sustained CIE suggests that the carbon input was first rapid then slow and continuous throughout the core of the PETM (Figure 1.2). A global carbon cycle perturbation is corroborated by the higher temperatures (see Section 1.1.2.1.3), a decline in surface ocean pH (Penman *et al.*, 2014; see Babila *et al.*, 2018 and references therein), and widespread

deep ocean $CaCO_3$ dissolution (*e.g.,* Zachos *et al.*, 2005). However, the source of this carbon is not yet agreed upon. Several hypotheses have been proposed, triggering the PETM and/or slowly 'leaking' carbon into the ocean-atmosphere system within the body of the CIE.

Found in modern marine sediments, methane (CH_4) hydrates are formed by the trapping of biogenic CH_4 within the crystal structure of water. Though typically stable, the rising deep-ocean temperatures preceding the CIE (*e.g.,* Thomas *et al.*, 2002; Tripati and Elderfield, 2005; Sluijs *et al.*, 2007) have been suggested to have caused the dissociation of gas hydrates (Dickens *et al.*, 1995; Dickens, Castillo and Walker, 1997; Zeebe, 2013). This may have subsequently resulted in seafloor slope failure, exacerbating the liberation of gas (Katz *et al.*, 1999). Although initially widely accepted as the primary source, the prevalence of CH_4 hydrates in a hothouse world (*e.g.,* Buffett and Archer, 2004) and/or the escaping of CH_4 from the seafloor (*e.g.,* Dickens, 2011; Minshull *et al.*, 2016) has yet to be proven theoretically or empirically. Moreover, the relatively small mass of carbon release required, due to the very low $\delta^{13}C$ value of biogenic CH_4 (~-60 ‰; Kvenvolden, 1993), is likely insufficient with the scale of temperature change (Pagani, Caldeira, *et al.*, 2006) and carbonate dissolution (Panchuk, Ridgwell and Kump, 2008). Consequently, other drivers that potentially acted in combination have been invoked, for example the oxidation of organic carbon stored in peats (Kurtz *et al.*, 2003), epicontinental seaways (Higgins and Schrag, 2006), permafrost (Deconto *et al.*, 2012), and/or ancient rocks (Lyons *et al.*, 2019). However, similar to the CH_4 hydrates, scepticism surrounds whether the warm conditions of the PETM would have enabled a large extent of permafrost. There is evidence of organic matter accumulation throughout the Paleocene (*e.g.,* Sloan *et al.*, 1992; Beerling *et al.*, 2009), yet scarce indications of processes that may have induced the destabilisation of these reservoirs (Bowen, 2013), for example the conflagration of peat and biomass deposits (*e.g.,*Collinson *et al.*, 2007; Moore and Kurtz, 2008) or the desiccation of epicontinental seas (*e.g.,* Gavrilov, Shcherbinina and Oberhänsli, 2003). In addition, the relatively large-scale of burning required, due to a higher $\delta^{13}C$ signature (~-22 ‰), seems less feasible in the geologically short time frame of the CIE onset (Higgins and Schrag, 2006).

Furthermore, both theories thus far require prior warming as a trigger. The thawing of permafrost was attributed to orbital forcing (Deconto *et al.*, 2012), although the unprecedented magnitude of the PETM and problems identifying the exact orbital phasing of the PETM (*e.g.,* Piedrahita *et al.*, 2022) has led to volcanism being favoured. In contrast to the other hypotheses, there are multiple signs of volcanic activity related to the North Atlantic Igneous Province (NAIP). This includes the extensive formation of subaerial and submarine flood basalts, seismic scans showing thousands of hydrothermal vents and sills in the Norwegian Sea, tephra layers, and mercury and non-radiogenic osmium isotope anomalies (*e.g.,* Eldholm and Thomas, 1993; Svensen *et al.*, 2004; Storey, Duncan and Swisher, 2007;

Westerhold *et al.*, 2009; Svensen, Planke and Corfu, 2010; Dickson *et al.*, 2015; Jones *et al.*, 2019; Jin *et al.*, 2024). Volcanism was never initially considered, as subaerial carbon emissions are characterised by very high $\delta^{13}C$ values (~-6 ‰). However, Svensen *et al.* (2004) demonstrated that a much more ^{13}C-depleted (~-30 ‰) thermogenic CH_4 could have formed by magma intrusion into carbon-rich sediments in the sills. Frieling *et al.* (2016) then presented data from the first set of samples acquired from these structures. Interestingly, although this confirmed the availability of isotopically light carbon, the dating revealed that the vents formed in the middle of the PETM. However, this is just based on one of the thousands of vents in the Norwegian Sea. A study that was published just a few years' later utilised techniques from the oil industry to further quantify timing (S. M. Jones *et al.*, 2019). Overall, they were able to prove that the carbon emitted from these sills could occur on the timescales of the onset of the CIE. Another recent study argued for the importance of decompression melting of the entrained subcontinental lithospheric mantle in this region (Gernon *et al.*, 2022).

1.1.2.1.3 A New State

The quantity of CO_2 released during the PETM can be estimated for each of the scenarios described above via mass balance calculations. Since the different carbon pools have distinct $\delta^{13}C$ signatures, the mass of carbon required to create the CIE profile from one or more sources can be determined (Table 1.1). The atmospheric CO_2 concentrations can then be calculated for the PETM if the background level of the late Paleocene is known. Although, it is worth noting that most studies have researched the PETM and as a consequence there is a lack of knowledge on the pre-PETM state. Additionally, the magnitude and shape of the CIE varies within and between bulk carbonate and organic carbon samples, as well as other marine (*e.g.,* foraminifera and algal lipids) and terrestrial (*e.g.,* tooth enamel and plant lipids) archives. For example, the CIE exhibited in the $\delta^{13}C$ of benthic foraminifera ranges from -0.6 to -5.1 ‰ (see McInerney and Wing, 2011 and references therein). To date, there has yet to be a consensus on which CIE record is the most reliable.

Table 1.1 Examples of published estimates for mass of carbon input (PgC) during the PETM.

Source	CIE (‰)	$\delta^{13}C$ signature (‰)	Mass of carbon (PgC)	References
Biogenic CH_4	-2 to -3	-60	1,200–2,100	Dickens, Castillo and Walker (1997)
Biogenic CH_4	-4.6	-60	4,300	McInerney and Wing (2011)*
Biogenic CH_4	-3 to -4	-50	Onset: 3,000 Body: 1,480	Zeebe, Zachos and Dickens (2009)
Biogenic CH_4 Thermogenic CH_4	-3 to -4	-50 -30 to -45	Onset: 3,000 Body: 1,500–2,250	Frieling *et al.* (2016)
Biogenic CH_4	POE: -3 CIE: -5.7	-55	Onset: 3,284	Bowen *et al.* (2014)
Biogenic CH_4 Organic matter	-4.2	-60 -22	Onset: 2,500 Onset: 13,000	Cui *et al.* (2011)
Volcanic outgassing	-3.4	-11	10,200–12,200	Gutjahr *et al.* (2017)
Biogenic CH_4 Organic matter	-4.9	-60 -22	Onset/Body, ~3,400/1,600 ~11,300/1,800	Dunkley Jones *et al.* (2018)
Thermogenic CH_4 Volcanic outgassing		-35 -6	Onset: 4,500 Body: 5,160	Kirtland Turner (2018)

Note. *Re-assessed Dickens, Castillo and Walker (1997) with CIE from Diefendorf *et al.* (2010).

Overall, mass balance calculations have yielded atmospheric CO_2 concentrations between ~1,500 to >2,000 ppm during the PETM (Cui *et al.*, 2011; Gutjahr *et al.*, 2017). The reconstructions from CO_2 proxies, such as the $\delta^{11}B$ of foraminifera (1,790 ppm +560/-380 ppm; Anagnostou *et al.*, 2020), fit within this range. The lowest limit inferred via mass balance calculations (*i.e.* ~1,500 ppm) assumes an isotopically light carbon source (*i.e.* biogenic CH_4 from submarine hydrates; Table 1.1). Yet, the rise in temperature could only be modelled with a minimum carbon release of 5,400 to 7,000 PgC (*e.g.,* Pagani, Caldeira, *et al.*, 2006; Meissner *et al.*, 2014). The shoaling of the calcite compensation depth (CCD) also required values greater than 4,480 to 6,800 PgC (*e.g.,* Zachos *et al.*, 2005; Panchuk, Ridgwell and Kump, 2008; Zeebe, Zachos and Dickens, 2009), or 10,200 PgC when the drop in surface ocean pH was simulated (*e.g.,* Gutjahr *et al.*, 2017). Therefore, as alluded to earlier, the relatively small amount of CH_4 needed to produce the CIE does not explain the observed warming and/or ocean acidification. To increase the mass of carbon input whilst adhering to the constraints of the CIE necessitates for more ^{13}C-enriched carbon sources, acting individually or in combination (*i.e.* oxidation of organic matter; Cui *et al.*, 2011; Dunkley Jones *et al.*, 2018, thermogenic CH_4 from volcanic sills; Frieling *et al.*, 2016, and/or mantle-derived carbon; Gutjahr *et al.*, 2017; Kirtland Turner, 2018; Gernon *et al.*, 2022). This is another reason, amongst the new evidence outlined in Section 1.1.2.1.2, for volcanism

becoming more accepted as the primary trigger. However, a singular source is unlikely and the cumulative input of carbon from multiple positive carbon cycle feedback mechanisms should not be overlooked, especially for the body of the CIE. In the context of modern climate change, it is vital to identify the potential drivers (see Section 1.2) and role (see Section 1.3) of these complex carbon cycle processes in past high CO_2 states.

Following the massive input of carbon at the onset of the PETM, there was a transient warming excursion of between 5 °C and 7.1 °C (Frieling *et al*., 2017; Zhu, Poulsen and Tierney, 2019; Inglis, Bragg, *et al*., 2020; Tierney *et al*., 2022; Evans *et al*., 2024). A GMST of 35.2 °C was calculated from the $\delta^{18}O$ of benthic foraminifera (Evans *et al.*, 2024). Much like the EECO, this is higher than the values gained from various averaging of LAT and SST datasets (Inglis, Bragg, *et al.*, 2020). However, a proxy-model data assimilation approach yielded a more comparable value of 34.1 °C (Tierney *et al.*, 2022). With these new estimates, the ECS was found to be much higher than the present-day (6.5 °C, with 95 % confidence; Tierney *et al.*, 2022). This demonstrates that climate sensitivity may be state dependent (*e.g.,* Shaffer *et al.*, 2016; Farnsworth *et al.*, 2019; Zhu, Poulsen and Tierney, 2019; Anagnostou *et al.*, 2020).

1.2 The Hydrologic Cycle during Hyperthermals: Future and Past

The evolution of Earth's climate should not be defined by temperature alone. Fluctuations in the hydrologic cycle are equally fundamental, and concomitant changes in weather patterns will arguably have the most imminent impact on human society (Lee *et al.*, 2021). Despite its importance, little is known in regards to how it may respond to a future hyperthermal.

Following the Clausias-Clapeyron equation, the capacity for the atmosphere to hold water vapour will grow by 7 % with every additional 1 °C of warming. This trend has been substantiated with direct measurements over the last two decades (*e.g.,* Wan *et al*., 2024), supporting the notion that a hothouse world can ultimately result in a wetter world. Yet, this is independent of evaporation and precipitation, the balance of which determines the intensity of the hydrologic cycle (*e.g.,* Trenberth, 1998). Overall, rates of evaporation will also increase with higher temperatures, hence generating more water vapour. The modern atmosphere transports moisture away from divergent zones (*i.e.* the subtropics) and precipitation is induced in convergent zones. The geographical location of these zones may shift, however an amplification of this circulation is anticipated. This is otherwise noted as the 'dry gets drier, wet gets wetter' paradigm (Chou and Neelin, 2004; Held and Soden, 2006). On the whole, state-of-the-art general circulation models (GCMs) agreeably illustrate evaporation dominating in the already arid subtropics and humidity increasing in the net-precipitation areas (Figure 1.3). Increased precipitation is 'very likely' over the high-latitudes and tropical rain belt, and will 'likely' occur in monsoonal regions (Douville *et al.*, 2021). However, the

paradigm does not appear mirrored over land (*e.g.,* Byrne and O'Gorman, 2015). Historical records indicates this to be especially true in the subtropics, and only a total of 10.8 % of the global land area follows this pattern (Greve *et al.*, 2014). Moreover, Figure 1.3 highlights that the lower latitudes exhibit spatial heterogeneity and regions where even the sign of change is conflicting. In addition, although global mean precipitation will increase with warming, it is unlikely that this will distribute uniformly throughout the year. Satellite and in situ data since the 1950s show conflicting results, with some studies identifying reduced seasonality in 62 % of terrestrial ecosystems (*e.g.,* Murray-Tortarolo *et al.*, 2017), whereas others found a strengthened wet period (*e.g.,* Chou *et al.*, 2013). Yet, the majority of land regions have observed more frequent episodic events of heavy precipitation from monsoon and various storm systems and, over some areas, droughts (Douville *et al.*, 2021).

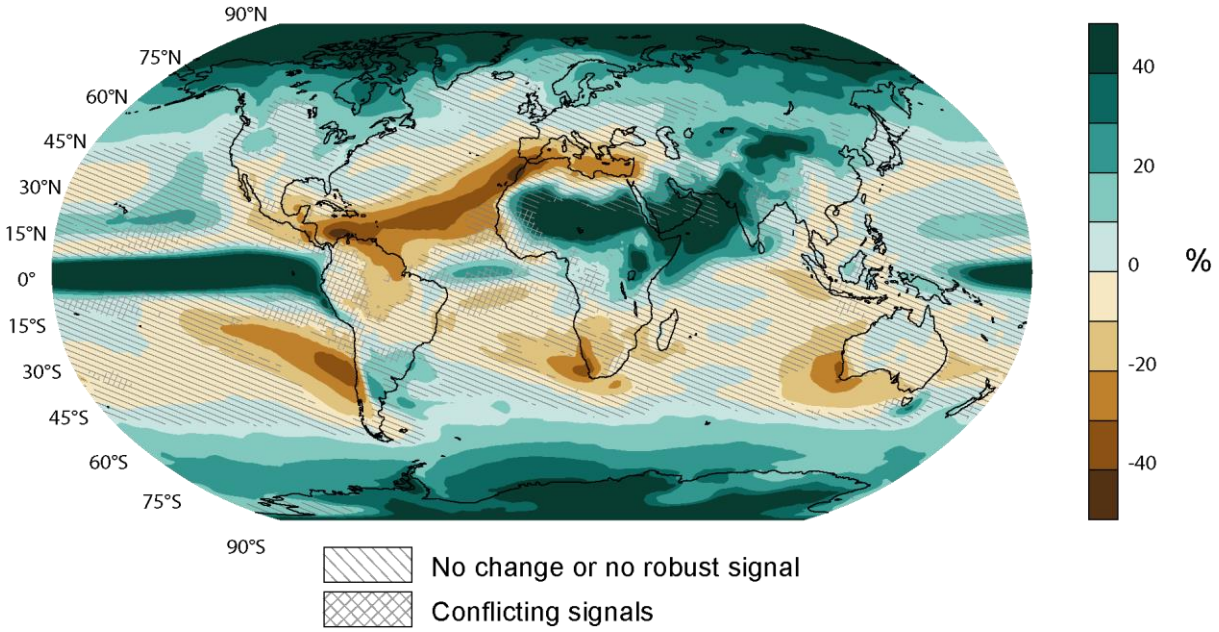

Figure 1.3 **Projected spatial distribution of percentage change in annual average precipitation with 4 °C of global warming relative to the period 1850–1900.** The values were assessed from a 20-year period, based on the Coupled Model Intercomparison Project Phase 6 (CMIP6). Diagonal and crossed lines represent areas with no change or no robust signal and conflicting signals, respectively. Adapted from Lee *et al.*, (2021).

An intensified hydrologic cycle has also been inferred for the PETM, established from a range of sedimentary, geochemical, and biological features. There is consistent evidence of enhanced moisture transport over the northern and southern high-latitudes (*e.g.,* Kaiho *et al.*, 1996; Crouch *et al.*, 2003; Pagani, Pedentchouk, *et al.*, 2006; Waddell and Moore, 2008; Villasante-Marcos *et al.*, 2009; Dypvik *et al.*, 2011; Harding *et al.*, 2011; Kender *et al.*, 2012; Contreras *et al.*, 2014; Willard *et al.*, 2019). There are also signs of greater runoff in the coastal settings of the United States (*e.g.,* Gibson, Bybell and Mason, 2000; John *et al.*, 2008, 2012; Sluijs and Brinkhuis, 2009), whereas both proxies and models indicate higher

rates of evaporation in the continental interior (*e.g.,* Wing *et al.*, 2005; Wing and Currano, 2013). For the latter, multiple evidence support that the drying was transient at the onset of the CIE. This includes lithological measurements (*e.g.,* Foreman, Heller and Clementz, 2012), paleosol characteristics (*e.g.,* Kraus and Riggins, 2007; Kraus *et al.*, 2013), and the $\delta^{18}O$ of mammal teeth (*e.g.,* Secord *et al.*, 2012). A similar change has been suggested for the interior of other large continents, such as Antarctica (*e.g.,* Larrasoaña *et al.*, 2012), and also in the subtropics (*e.g.,* Handley *et al.*, 2008, 2012). Subtropical drying and the strong influence of precipitation in the tropics has been shown by models (*e.g.,* Winguth *et al.*, 2010; Carmichael *et al.*, 2016; Cramwinckel *et al.*, 2023). However, a wetter tropics has yet to be proven with proxy-based data due to a scarcity of sites (Appendix I).

Models additionally exhibit a highly regionalised hydrologic cycle during the PETM. This appears to be expressed in the geologic record, however interpretations and comparisons should be made with caution as each proxy captures different processes at distinct timescales (see Carmichael *et al*., 2017 and references therein). Most notably, several studies have identified that some proxies may reflect variability in sub-annual precipitation rates, rather than mean annual precipitation (MAP). The mid-latitudes in particular revealed heightened seasonality (*e.g.,* Schmitz and Pujalte, 2003, 2007; Egger *et al.*, 2005; Collinson *et al.*, 2007; Kraus and Riggins, 2007; Garel *et al.*, 2013; Kraus *et al.*, 2013; Bornemann *et al.*, 2014). Furthermore, evidence from the high-latitudes (*e.g.,* Sluijs *et al.*, 2011) and subtropics (*e.g.,* Handley *et al.*, 2012) imply the occurrence of episodic and extreme events. This is superimposed on an arid climate in the subtropics and some of the mid-latitude sites (*e.g.,* Schmitz and Pujalte, 2003, 2007; Foreman, Heller and Clementz, 2012), whereas the high-latitude was also characterised by increased MAP. Until recently, sub-annual precipitation rates for the PETM were not well assessed in models. New GCM simulations determine that both seasonality and the frequency of extreme rainfall was greater across multiple regions (Carmichael, Pancost and Lunt, 2018; Kiehl *et al.*, 2018, 2021). These changes will have a profound effect on biogeochemical processes, including driving changes in the terrestrial carbon cycle (see Section 1.3).

1.3 Terrestrial Carbon Cycle Feedbacks

Terrestrial carbon cycle feedbacks are both driven by and regulates the climate on short and long timescales. Therefore, understanding its response and role is critical towards constraining the magnitude of future climate change. Yet, there are considerable uncertainties and even the latest generation of GCMs do not fully incorporate the terrestrial carbon cycle (Canadell *et al*., 2021). The following sections will focus on two under-researched positive feedback mechanisms within the terrestrial carbon cycle: the oxidation of rock-derived ‘petrogenic’ organic carbon (OC_{petro}; see Section 1.3.1); and the methane cycle

(see Section 1.3.2). In particular, discussing observations from the present and past to explore whether they will likely be a source of carbon during a future hyperthermal.

1.3.1 OC_{petro} Oxidation in the Present and Past

The 'textbook' view of the long-term (*i.e.* geological) carbon cycle mostly described the exchange of inorganic carbon between solid Earth degassing and chemical weathering of silicate minerals. However, a growing number of studies have given prominence to the organic carbon cycle, especially the role of OC_{petro} oxidation as a positive feedback mechanism (see Hilton and West, 2020 and references therein). In fact, this process is thought to rival that of the carbon contributed from solid Earth degassing (Zondervan *et al.*, 2023).

The oxidation of OC_{petro} releases carbon back into the ocean-atmosphere system on geological timescales (*e.g.,* Petsch, Berner and Eglinton, 2000; Bouchez *et al.*, 2010). This occurs primarily during the exhumation and lateral transfer of OC_{petro} from land-to-sea. In modern systems, the amount of OC_{petro} mobilised, and thus potentially oxidised, positively correlates to physical erosion rates (*e.g.,* Blair *et al.*, 2003; Komada, Druffel and Trumbore, 2004; Galy, Peucker-Ehrenbrink and Eglinton, 2015; Hilton and West, 2020). However, the consequently higher sedimentation rates also promote the burial and preservation of organic matter in the oceans (*e.g.,* Galy *et al.*, 2007). As such, it is vital to recognise the controls on erosion and other factors that affect the fraction of OC_{petro} that is oxidised (*i.e.* oxidation efficiency). Overall, erosion is largely driven by tectonic (*i.e.* uplift; Hilton and West, 2020) and climatic (*i.e.* precipitation and temperature) processes. The former is challenging to measure, and to some degree less relevant, on human timescales, with the exception of earthquake-induced landslides (*e.g.,* Wang *et al.*, 2020). In terms of the latter, heavy rainfall events have been seen to trigger mass wasting of bedrock that leads to a greater export of OC_{petro} (*e.g.,* Leithold, Blair and Perkey, 2006; Hilton, Galy and Hovius, 2008; Hilton *et al.*, 2011, 2012; Hatten, Goñi and Wheatcroft, 2012; Goñi *et al.*, 2013). Recent warming has exposed OC_{petro}-rich rocks that were previously trapped beneath glaciers (*e.g.,* Horan *et al.*, 2017), showing that temperature can dictate the availability of OC_{petro}, although lithology determines the actual presence and friability. Moreover, climate change can stunt vegetation cover and soil development, creating landscapes prone to erosion. If the geomorphologic conditions remain constant (*e.g.,* Hilton, 2017), climate additionally influences the oxidation efficiency of OC_{petro}. For example, precipitation may change the sediment routing system, extending or reducing the transit time for OC_{petro} oxidation to occur. On the other hand, field-experiments demonstrate a two-fold increase in oxidation rates for every 10 °C rise in temperature (*e.g.,* Soulet *et al.*, 2021).

Overall, these present-day observations hint towards the potential for an enhanced positive organic carbon cycle feedback in a wetter and warmer world. Lyons *et al*. (2019), was the first to indicate that this holds true for the PETM. The study exhibits an order-of-magnitude increase in the delivery of OC_{petro} into the marine realm, ~10–20 kyrs after the onset of the CIE. The oxidation of this OC_{petro} was then quantified to have contributed up to 10,000 PgC during the body of the CIE. Such a large mass of carbon input was proposed to explain the prolonged amplified warming and delayed recovery of the climate system (Lyons *et al.*, 2019). However, this was only based on three sites from the mid-latitudes and subtropics (Figure 1.6), which may not be globally representative.

1.3.2 The Methane Cycle in the Present and Past

CH_4 is second only to CO_2 in its importance as a greenhouse gas (GHG) (Forster *et al*., 2021), although it is 3 orders of magnitude less abundant in the modern atmosphere (Lan, Thoning and Dlugokencky, 2024) and has a shorter lifetime (~10 years; Prather, Holmes and Hsu, 2012). Moreover, CH_4 also oxidises to other GHGs (*i.e.* water vapour and CO_2) and is a precursor of tropospheric ozone (*e.g.,* Crutzen, 1973). Therefore, CH_4 is an essential component of the carbon cycle and influences the chemical composition of the atmosphere.

Wetlands are the single largest natural sources of CH_4 (Canadell *et al*., 2021), as they provide the ideal habitat for CH_4-producing methanogens (see Thauer *et al.*, 2008 and references therein). Methanogens thrive in a multitude of environments that encompass a wide range of thermochemical gradients (Buan, 2018). However, in wetlands, methanogens are vulnerable to changes in the water table as they require saturated soils with low redox potential (*e.g.,* Bubier *et al.*, 2005; Turetsky *et al.*, 2014; Goodrich *et al.*, 2015; Blanc-Betes *et al.*, 2016; Tian *et al.*, 2023). As such, an intensified hydrologic cycle will drastically alter the temporal and spatial distribution of biogenic CH_4 emissions, and will potentially expand wetland areas in the high-latitudes and tropical rain belt. Present-day observations demonstrate that temperature is another key control on the flux of biogenic CH_4 (*e.g.,* Olefeldt *et al.*, 2013; Chu *et al.*, 2014; Turetsky *et al.*, 2014; Tveit *et al.*, 2015). Warming increases rates of respiration, directly driving CH_4 production (*e.g.,* Yvon-Durocher *et al.*, 2012). Although, this is somewhat hindered by a simultaneous rise in CH_4-consuming methanotrophs (*e.g.,* Kip *et al.*, 2010; van Winden *et al.*, 2012, 2020; Hofmann *et al.*, 2016). Temperature also positively correlates with primary productivity, and microbial activity relies on a constant supply of organic matter (*i.e.* substrate availability) (*e.g.,* Valentine, Holland and Schimel, 1994; Joabsson and Christensen, 2001). Furthermore, current warming is thawing permafrost in subglacial regions and exposing CH_4 reservoirs (*e.g.,* Anderson *et al.*, 2010), liberating trapped gas (*e.g.,* Lamarche-Gagnon *et al.*, 2019) and promoting methanogenesis (*e.g.,* see Schuur *et al.*, 2015 and references therein).

Overall, wetter and warmer conditions will likely exacerbate biogenic CH_4 emissions, thus strengthening the positive methane cycle feedback. Indeed, sedimentary deposits indicate that wetlands were more widespread during the early Paleogene (*e.g.,* Sloan *et al.*, 1992; Beerling *et al.*, 2009), and this global distribution was modelled to emit ~4 times the pre-industrial amount of CH_4 (*e.g.,* Beerling *et al.*, 2009, 2011; see Wilton *et al.*, 2019 and references therein). For the PETM, a larger amplitude in the CIE of terrestrial archives compared to marine archives (McInerney and Wing, 2011) could be reflecting the (wet)land-derived contribution of ^{13}C-depleted biogenic CH_4. Although it has mostly been attributed to greater fractionation due to wetter conditions (*e.g.,* Bowen *et al.*, 2004; Pagani, Pedentchouk, *et al.*, 2006; Sluijs *et al.*, 2008), changes in vegetation (*e.g.,* Smith, Wing and Freeman, 2007), and high atmospheric CO_2 concentrations (see Cui *et al.*, 2021 and references therein). Evidence of increased methanotrophy, albeit limited (Figure 1.6), imply a growing production and availability of CH_4 (van Winden, Reichart, *et al.*, 2012; van Winden *et al.*, 2020). Aerobic methanotrophy is inferred from the $\delta^{13}C$ of bacterial-derived hopanes and hopenes ($\delta^{13}C_{hop}$; see Section 1.4.4.1). Pancost *et al.* (2007) was the first to detect a decrease to -75 ‰ in the $\delta^{13}C_{hop}$ record at the onset of the PETM, in the Cobham Lignite from the United Kingdom. Such a drop lies outside the observed modern range (Inglis, Naafs, *et al.*, 2019). More recent studies on other PETM-aged lignite deposits, from New Zealand (Inglis *et al.*, 2021) and Arctic Canada (Blumenberg *et al.*, 2024), exhibit similarly low $\delta^{13}C_{hop}$ values, with a minima of -60 ‰ and -50 ‰, respectively. However, hopanes and hopenes themselves are not source-specific, therefore other compounds may help trace the presence of methanotrophs and/or methanogens directly. This has been undertaken at the Cobham Lignite (Talbot, Bischoff, *et al.*, 2016), where they have identified methanotroph-specific bacteriohopanepolyols (BHPs; see Section 1.4.4.1). However, this is the only PETM-aged site, to date, that has detected these compounds. Therefore, the preservation potential of BHPs is poorly constrained.

1.4 A Lipid Biomarker Approach

Biomarkers are organic compounds (*e.g.,* proteins, carbohydrates, and lipids) with a known biological precursor (Peters, Walters and Moldowan, 2005). Lipids preserve over very long timescales (up to 10^9 years) and in a range of sedimentary archives. Thus, these molecular fossils are a unique 'tool' for investigating past changes in the climate, ecosystems, and biogeochemical cycles (Figure 1.4; Pancost and Boot, 2004). This thesis utilises the abundance, distribution, and isotopic composition of a suite of lipid biomarkers to reconstruct the hydrologic cycle and two key terrestrial carbon cycle feedbacks (*i.e.* OC_{petro} mobilisation and the methane cycle) during the early Paleogene. The following sections summarise lipid biomarker proxies for: the hydrologic cycle (see Section 1.4.1); vegetation (see Section

1.4.2); OC_{petro} mobilisation (see Section 1.4.3); and the methane cycle (see Section 1.4.4), and existing early Paleogene localities that have these records (see Section 1.4.5).

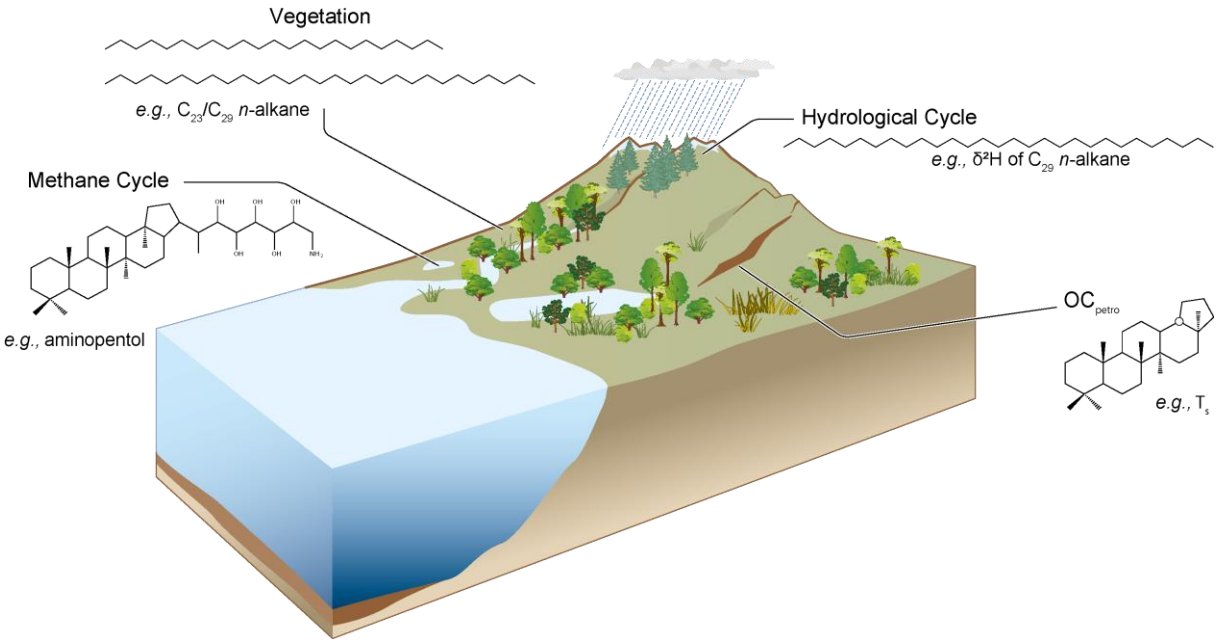

Figure 1.4 **Lipid biomarker approaches for reconstructing the past.** Examples of compounds used as proxies for the climate (*i.e.* hydrologic cycle), ecosystem (*i.e.* vegetation), and biogeochemical cycles (*i.e.* OC_{petro} and methane cycle). Adapted from Inglis *et al.* (2022).

1.4.1 Proxies for the Hydrologic Cycle

Long-chain *n*-alkyl lipids (*i.e. n*-alkanes, *n*-alcohols, and *n*-alkanoic acids) are primarily synthesised as part of the epicuticular wax on vascular (*i.e.* 'higher') plant leaves (Eglinton and Hamilton, 1967). Consequently, the stable hydrogen isotopic composition (δ^2H) of these long-chain *n*-alkyl lipids (δ^2H_{wax}) mirror that of the surrounding environmental water (*e.g.,* Sessions *et al.*, 1999). Calibrations on modern sediments across the globe have established a correlation between δ^2H_{wax} and the δ^2H of meteoric water (δ^2H_{precip}) (*e.g.,* Daniels *et al.*, 2017; McFarlin *et al.*, 2019; see Ladd *et al.*, 2021 and references therein). The δ^2H_{precip} signature can inform on the various climatological processes, including rainfall amount and changes in the atmospheric circulation (see Bowen, 2008 and references therein). As such, δ^2H_{wax} emerged as a novel proxy to reconstruct past changes in the hydrologic cycle (*e.g.,* Sauer *et al.*, 2001), and has been used to study large-scale processes during the Quaternary (present to 2.6 Ma) (*e.g.,* Schefuß, Schouten and Schneider, 2005; Tierney *et al.*, 2008; Fornace *et al.*, 2014; Tierney, Ummenhofer and DeMenocal, 2015; Bhattacharya *et al.*, 2018). Yet, many challenges remain with this approach.

Firstly, sites with minimal diagenesis must be selected, as hydrogen exchanges with the environment at greater severity with increasing thermal maturity (Sessions *et al.*, 2004; see

Sessions, 2016 and references therein). Secondly, in order to then convert δ^2H_{wax} into δ^2H_{precip}, the relationship between the two must be well-understood. Although strongly correlated, there is an offset that varies spatially and temporally (*e.g.,* Bakkelund *et al.*, 2018; see Liu and An, 2019 and references therein). This is the result of apparent isotopic fractionation ($\varepsilon_{wax/precip}$) (see Sachse *et al.*, 2012 and references therein; Sessions, 2016), which is primarily controlled by leaf water transpiration and lipid biosynthesis, and to a lesser degree soil evaporation (Tipple and Pagani, 2013; see Inglis *et al.*, 2022 and references therein). A constant $\varepsilon_{wax/precip}$ value is typically assumed, however changes in the biosynthetic pathway alone cause δ^2H_{wax} values to differ by up to a ~70 ‰, depending on the source organism (Sachse *et al.*, 2012). All living organisms discriminate against the heavier isotopes (*i.e.* ^2H), yet the extent of this fractionation depends on their physiology (*e.g.,* Chikaraishi and Naraoka, 2003; Gao *et al.*, 2014; Gamarra, Sachse and Kahmen, 2016). Since δ^2H_{wax} can integrate a catchment-wide signal, $\varepsilon_{wax/precip}$ values have been refined for specific ecosystems (*e.g.,* Magill, Ashley and Freeman, 2013; Polissar *et al.*, 2021). Therefore, region- and time-specific reconstructions of the vegetation community may help constrain δ^2H_{precip}, and potentially offer other indirect yet valuable insights into the local hydrology.

1.4.2 Proxies for Vegetation

Both *n*-alkanes (Eglinton and Hamilton, 1967) and terpenoids (Otto and Simoneit, 2001) are examples of compound classes that vary in their distributions across different plant types. The chain length of *n*-alkyl lipids were initially widely explored for proxy development, leading to the establishment of terrigenous-aquatic ratio (TAR) (Bourbonniere and Meyers, 1996), P_{aq} (Ficken *et al.*, 2000; Mead *et al.*, 2005), and average chain length (ACL) (Bush and McInerney, 2013). These are evaluated via Equation 1.1, 1.2, and 1.3, respectively.

The TAR compares long- to short-chain *n*-alkanes, the latter associated with microbes and/or algae (Nishimura and Baker, 1986; Meyers and Ishiwatari, 1993). Hence, the TAR is often applied to determine the source composition of marine sediments.

$$TAR = (C_{27}+C_{29}+C_{31})/(C_{15}+C_{17}+C_{19}) \quad \text{(Equation 1.1)}$$

A shift to higher values (>1) correspond to increased terrigenous material and/or reduced aquatic organic matter from microbial activity and algal primary productivity. Enhanced terrestrial input could further implicate a greater amount of precipitation.

The P_{aq} ratio focuses on mid-chain *n*-alkanes (C_{21-25}), associated with aquatic plants (Ficken *et al.*, 2000).

$$P_{aq} = (C_{23}+C_{25})/(C_{23}+C_{25}+C_{29}+C_{31}) \quad \text{(Equation 1.2)}$$

Values from 0.1 to 0.4 and above 0.4 were assigned to emergent and submerged macrophytes, respectively. Emergent macrophytes could suggest a lowering of the water table. Although these original definitions were based on lacustrine environments and did not include coastal settings, Mead *et al*. (2005) proposed that the ratio was also generally relevant to estuarine systems. By including marine macrophytes, the classifications were then modified to ~0.4–0.6 and >0.6. However, the P_{aq} ratio is less applicable in peats, where *Sphagnum* moss share a close chain-length distribution to aquatic macrophytes (*e.g.,* Naafs *et al.*, 2019).

The ACL ratio employs long-chain *n*-alkyl lipids, and was put forward as a proxy to differentiate between major higher plant groups (Bush and McInerney, 2013). This is evaluated via the following equation:

$$ACL = \sum(C_n \times n) / \sum(C_n) \qquad \text{(Equation 1.3)}$$

where *n* refers to odd numbered long-chain *n*-alkanes.

Numerous studies have used the ACL ratio as a proxy to distinguish plant types (*e.g.,* Kawamura and Ishimura, 2003; Rommerskirchen *et al*., 2003; Sachse, Radke and Gleixner, 2006). However, as well as being described as a 'broad-brush parameter' (Bush and McInerney, 2013), meta-analyses discovered that ACL values are even highly variable within the same phylogenetic group (*e.g.,* Diefendorf *et al.*, 2011). Therefore, the chain-length ratios should be limited to low-diversity settings. For example, in boreal *Sphagnum* moss-dominated peats, the C_{23}/C_{29} or C_{23}/C_{31} *n*-alkane ratios can reliably detect *Sphagnum* moss (*i.e.* C_{23}) (*e.g.,* Inglis *et al.*, 2015). Graminoids have also been reported to have a prevalence of C_{33} and C_{35} *n*-alkane (Bush and McInerney, 2013). These homologs may be more useful in low-latitude regions where tropical trees produce both C_{29} and C_{31} *n*-alkanes at substantially higher amounts (*e.g.,* Schefuß *et al*., 2003; Garcin *et al*., 2014).

Chain-length based reconstructions could also be corroborated by analysing the $\delta^{13}C$ of *n*-alkanes ($\delta^{13}C_{wax}$). The $\delta^{13}C_{wax}$ reflects plant types with fundamental biochemical differences, for example some submerged macrophytes are more enriched in ^{13}C than emerged macrophytes (see Naafs *et al*., 2019 and references therein). Similarly, $\delta^{13}C_{wax}$ can identify distinct carbon fixation pathways, as C4 plants are more enriched in ^{13}C than C3 plants (*e.g.,* Huang *et al.*, 2001), although a greater range in the $\delta^{13}C_{wax}$ of the latter introduces uncertainty (*e.g.,* Diefendorf *et al.*, 2010). Whilst C4 plants were not present during the early Paleogene, tandem measurements (*i.e.* $\delta^{2}H_{wax}$ and $\delta^{13}C_{wax}$) have been applied to correct the $\varepsilon_{wax/precip}$ value for shifts in their relative abundance over the last ~23 myrs (*e.g.,* Tipple and Pagani, 2010; Tierney, Pausata and De Menocal, 2017; Windler *et al.*, 2020; Windler, Tierney and Anchukaitis, 2021). Two dominant groups within woody C3 plants (*i.e.* angiosperms and gymnosperms) may also be discerned from $\delta^{13}C_{wax}$. Angiosperms are

reported to be ~2 to 3 ‰ more depleted in ^{13}C than in gymnosperms (*e.g.,* Diefendorf *et al.*, 2010). Triterpenoids and diterpenoids can further confirm the presence of angiosperms and gymnosperms, respectively, although the selective loss of triterpenoids in sediments results in an overestimation of gymnosperms in the geologic record (*e.g.,* Diefendorf, Freeman and Wing, 2014). However, caution should be taken with small differences in the $\delta^{13}C_{wax}$ values, as they can also be influenced by environmental conditions, such as temperature (*e.g.,* Pedentchouk *et al.*, 2008), light intensity (*i.e.* 'canopy effect'; Graham *et al.*, 2014), atmospheric composition (*e.g.,* Hare and Lavergne, 2021; Polissar *et al.*, 2021), and even MAP (*e.g.,* see Diefendorf and Freimuth, 2017 and references therein).

1.4.3 Proxies for OC_{petro} Mobilisation

Lipids are subject to defunctionalisation, isomerisation, catagenesis, and/or aromatisation with increasing thermal maturity from early diagenesis towards peak oil generation (Peters, Walters and Moldowan, 2005). The ratios between various structures and stereoisomers have long been utilised as thermal maturity proxies in the field of petroleum geochemistry (*e.g.,* Mackenzie *et al*., 1980; Farrimond, Taylor and Telnás, 1998). However, these ratios can also be used to trace the mobilisation and subsequent burial of OC_{petro} in the geologic record. The following will describe *n*-alkane- and hopane-based thermal maturity ratios.

1.4.3.1 *n*-Alkane-based Thermal Maturity Ratios

Modern plants and sediments contain long-chain *n*-alkanes with an odd-over-even preference (Eglinton and Hamilton, 1967), however this is progressively lost during diagenesis.

This shift away from a dominance of odd-over-even long-chain *n*-alkanes is captured by the odd-to-even predominance (OEP) ratio (Scalan and Smith, 1970) and the carbon preference index (CPI) (Bush and McInerney, 2013). There are a multiple ways of calculating CPI (*e.g.,* Marzi, Torkelson and Olson, 1993). Equation 1.5 presents it as originally defined by Bray and Evans (1961).

$$OEP=\left[\frac{C_i + 6C_{i+2} + C_{i+4}}{4C_{i+1} + 4C_{i+3}}\right]^{(-1)^{i+1}} \qquad \text{(Equation 1.4)}$$

$$CPI=\frac{1}{2}\left[\left(\frac{\sum_{odd}(C_{25\text{-}31})}{\sum_{even}(C_{26\text{-}32})}\right) + \left(\frac{\sum_{odd}(C_{27\text{-}33})}{\sum_{even}(C_{26\text{-}32})}\right)\right] \qquad \text{(Equation 1.5)}$$

High CPI values (>3–30) indicate modern sediments or relatively thermally immature organic matter (Diefendorf and Freimuth, 2017). In contrast, mature organic matter (*e.g.,* coal and oil) exhibits low CPI values (~1). CPI values <1 are less common, and typify low-maturity source rocks from carbonates or hypersaline environments.

1.4.3.2 Hopane-based Thermal Maturity Ratios

Hopanes (and hopenes) are diagenetic forms of hopanoids, which are produced by a wide diversity of bacteria, as part of their cell membrane, and hence ubiquitous in a range of environments (Kusch and Rush, 2022). In fact, they have been referred to as 'the most abundant natural products on Earth' (Ourisson and Albrecht, 1992).

With the exception of *Frankia* spp. (Rosa-Putra *et al*., 2001), all bacteria synthesise hopanoids with a 17β, 21β configuration. However, this changes to a more stable βα and αβ configuration during early diagenesis and peak oil generation, respectively (Mackenzie *et al*., 1980; Farrimond, Taylor and Telnás, 1998) (Figure 1.5). The shift from ββ to αβ is expressed via the following equation (sometimes referred in literature as 'hopanoid isomerisation'):

$$\alpha\beta/(\alpha\beta + \beta\beta) \qquad \text{(Equation 1.6)}$$

Higher thermal maturity is marked by values closer to 1. This equation is applied to hopanes that contain both isomers (*i.e.* mostly $C_{29\text{-}31}$ hopanes). However, caution should be taken when interpreting sediments with input from peats, as C_{31} αβ isomers dominate the hopane distribution within acidic environments (Inglis *et al*., 2018).

The shift from βα (also referred to as moretane; M) to the more stable αβ (also referred to as hopane; H) is assessed via the following equation (sometimes referred in literature as 'moretane/hopane ratio'):

$$\beta\alpha/(\beta\alpha + \alpha\beta) \qquad \text{(Equation 1.7)}$$

This equation is most commonly applied to C_{30} hopane (*e.g.,* French *et al*., 2012), and less commonly applied to C_{29} hopane (Peters, Walters and Moldowan, 2005). Values closer to ~0 indicate higher thermal maturity and oil generation.

The C_{29} αβ hopane (also referred to as norhopane; N) is more thermally stable than C_{30} αβ hopane. This is assessed via the following equation (sometimes referred in literature as 'norhopane/hopane ratio'):

$$C_{29}\ \alpha\beta/C_{30}\ \alpha\beta \qquad \text{(Equation 1.8)}$$

As well as a thermal maturity proxy, this ratio has been utilised to differentiate between anoxic carbonate or marl source rocks (>1) vs. clay-rich (<1) source rocks (Peters, Walters and Moldowan, 2005).

Toward the early stages of oil generation (Figure 1.5), there is a change in stereochemistry at the C-22 position, from the biologically favoured 22R configuration to a near equal mix of 22R and 22S (Mackenzie *et al*., 1980; Farrimond, Taylor and Telnás, 1998; Peters, Walters

and Moldowan, 2005). This is expressed via the following equation (sometimes referred in literature as 'homohopane isomerisation'):

$$S/(S + R) \qquad \text{(Equation 1.9)}$$

This equation is applied to $C_{31\text{-}35}$ hopanes (also referred to as homohopanes), and approaches maximum (equilibrium) values of ~0.6 as thermal maturity increases and oil is generated.

At the late stage of oil generation (Figure 1.5), C_{27} hopanes shift in the position of a D-ring methyl group, from C-18 (17α(H),22,29,30-trisnorhopane; T_m) to C-17 (18α(H),22,29,30-trisnorneohopane; T_s) (Farrimond, Taylor and Telnás, 1998; Peters, Walters and Moldowan, 2005). This is expressed via the following equation:

$$T_s/(T_s + T_m) \qquad \text{(Equation 1.10)}$$

T_m refers to 'maturable' (*i.e.* less stable), whereas T_s denotes 'stable'. Values closer to 1 indicate higher thermal maturity, although the oxicity of the depositional environment also has a notable influence (Peters, Walters and Moldowan, 2005).

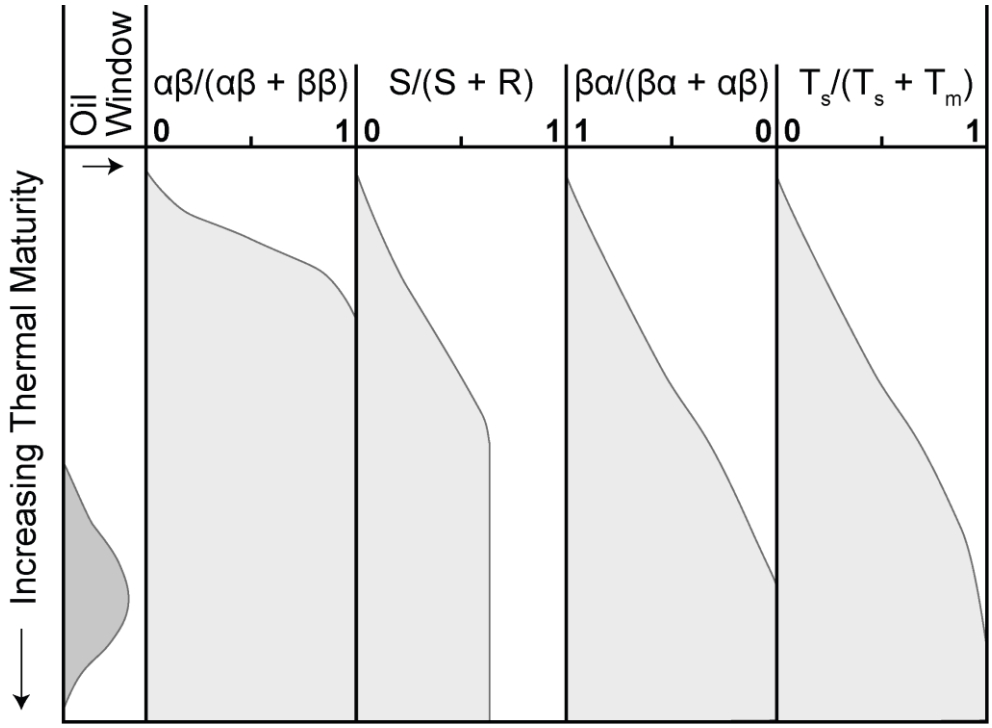

Figure 1.5 **Examples of hopane-based thermal maturity ratios.** Ordered from left to right, representing transformations that occur during early diagenesis to increasing thermal maturity until oil generation.

The hopane-based thermal maturity ratios discussed above represent different stages of maturity relative to the oil window (Figure 1.5). Therefore, a multi-ratio approach allows further information on the degree of thermal maturation. However, as noted, changes in the

lithofacies and/or depositional environment also affect the hopane distribution and should be considered (Peters, Walters and Moldowan, 2005). In addition, for its application to fingerprint OC_{petro} delivery, study sites must be carefully selected. Most importantly, sediments should be relatively thermally immature as extensive post-depositional diagenesis may conceal allochthonous contributions of OC_{petro}.

1.4.4 Proxies for the Methane Cycle

Lipids and their $\delta^{13}C$ signature can be utilised to infer the microbial community composition, and reveal insights into biogeochemical cycles (*e.g.,* see Pancost, 2024 and references therein). Two key microorganisms that are involved in regulating biogenic CH_4 fluxes are methanogens (see Section 1.4.4.2) and methanotrophs (see Section 1.4.4.1) (see Wilkes, 2020 and references therein). Methanogens are phylogenetically diverse prokaryotes that belong within the Archaea domain (see Thauer *et al.*, 2008 and references therein). They are responsible for generating CH_4 via methanogenesis, a type of anaerobic respiration that occurs at the last stages of microbial organic matter decomposition (see Thauer, 1998 and references therein). On the other hand, CH_4 can be oxidised via methanotrophy. This is undertaken by methanotrophs that perform aerobic methane oxidation (AMO) and anaerobic oxidation of methane (AOM) (*e.g.,* Hanson and Hanson, 1996).

1.4.4.1 Methanotrophy

Analysing the $\delta^{13}C$ of hopanoids provides an approach to trace methane oxidising bacteria (MOB) that are responsible for AMO (Pancost and Sinninghe Damsté, 2003). The $\delta^{13}C$ of hopanoids are primarily determined by the $\delta^{13}C$ of the substrate, the metabolic pathway used to assimilate carbon, and the organism's source ecology (*e.g.,* Hayes, 1993). Heterotrophs that consume organic substrates (*e.g.,* organic acids and sugars) will yield a hopanoid $\delta^{13}C$ signal that is similar to its food source (~-20 to -30 ‰), whereas MOB are characterised by much lower and more variable values (~-40 to -60 ‰, and up to -100 ‰; Pancost and Sinninghe Damsté, 2003). A recent survey of peatlands from different geographic regions showed that the $\delta^{13}C$ of the C_{31} hopane – one of the most abundant hopanoids in peats – spans a relatively narrow range (-22 to -35 ‰; Inglis, Naafs, *et al.*, 2019), and is enriched in ^{13}C compared to bulk organic matter and co-occurring long-chain *n*-alkanes. This suggests that C_{31} hopane is derived from heterotrophic organisms and has limited utility as a methanotroph-specific biomarker. In contrast, other hopanoids (*e.g.,* hop-22(29)-ene, also known as diploptene) yield lower $\delta^{13}C$ values (*e.g.,* up to -45 ‰; Inglis, Naafs, *et al.*, 2019), indicating that in some settings these compounds can be derived from a mix of bacterial sources consuming both ^{13}C-enriched carbohydrates and ^{13}C-depleted substrates (*i.e.* CH_4). Hopanoid $\delta^{13}C$ values of ~-60 ‰ to ~-80 ‰ have also been found in modern- (*e.g.,* Naeher *et al.*, 2014), Holocene- (*e.g.,* Naeher *et al.*, 2014; Elvert *et al.*, 2016), and Eocene- (*e.g.,*

Freeman *et al.*, 1990; Collister *et al.*, 1992) aged lake deposits. These values are considerably lower than in modern peats and implies more vigorous CH_4 consumption in lakes.

The analyses of BHPs, hopanoids with a polyfunctionalised side chain (*e.g.,* Neunlist and Rohmer, 1985), and specifically those with an amine functionality at the terminal C-35 position (amino-BHPs) (*e.g.,* see Talbot *et al.*, 2014 and references therein), provides an alternative means to reconstruct aerobic methanotrophy. Amino-BHPs include 35-aminobacteriohopane-30,31,32,33,34-pentol (aminopentol) and 35-aminobacteriohopane-31,32,33,34-tetrol (aminotetrol). Both compounds are present in terrestrial environments (see Rush *et al.*, 2016 and references therein), especially peats (*e.g.,* van Winden, Talbot, *et al.*, 2012) and lakes (*e.g.,* Talbot and Farrimond, 2007), and in some rare examples can persist in the geologic record for more than ~50 Ma (*e.g.,* Talbot *et al.*, 2016). As such, they have been used to reconstruct aerobic methanotrophy during the Quaternary (*e.g.,* Talbot *et al.*, 2014) and PETM (Talbot *et al.*, 2016). However, under unfavourable conditions for preservation, diagenesis results in the loss of the functionalised side-chain and eventual transformation of amino-BHPs into hopanes and hopenes.

Methanotrophy can also occur via AOM, which is performed by a consortium of anaerobic methanotrophic archaea (known as anaerobic methanotrophs; ANME) and sulphate-reducing bacteria (Hinrichs *et al.*, 1999). AMNE produce diagnostic isoGDGT distributions, with a high abundance of GDGT-0 to -3 relative to crenarchaeol (Pancost *et al.*, 2000). This is captured in the Methane Index (Zhang *et al.*, 2011), whereby high values (>0.5) suggest extensive anaerobic methanotrophy. This ratio is mainly used in marine settings, yet has applicability in terrestrial settings where AOM is elevated (*e.g.,* freshwater wetlands). To confirm the presence of AOM, the $\delta^{13}C$ of other compounds can be analysed (*e.g.,* pentamethylicosane and crocetane).

1.4.4.2 Methanogenesis

Methanogens synthesise diether and/or tetraether lipids (Schouten, Hopmans and Sinninghe Damsté, 2013). Archaeol (2,3-diphytanyl-O-sn-glycerol) is the most common archaeal lipid in cultured methanogens (Koga and Morii, 2007; Bauersachs *et al.*, 2015), and shows promise as a proxy for methanogenesis (Pancost *et al.*, 2011; Zheng *et al.*, 2014). Archaeol has been applied to trace methanogens in Holocene-aged peats in China, and exhibits a minimum in methanogenesis between ~6 and 4 kyrs (Zheng *et al.*, 2014). However, direct estimates of methanogen biomass based on archaeol should be made with caution, as there can be differing concentrations of archaeol per methanogen cell (McCartney *et al.*, 2013). The acyclic isoGDGT (*i.e.* GDGT-0) is also prevalent in methanogens (Koga *et al.*, 1993; Schouten, Hopmans and Sinninghe Damsté, 2013; Bauersachs *et al.*, 2015) and may provide complementary information on methanogenesis. However, both archaeol and GDGT-

0 have diverse source organisms, perhaps limiting their utility. In contrast, a subset of methanogens (*i.e. Methanococcus* and *Methanosarcina*) are known to synthesise *sn*-2-hydroxyarchaeol (Koga *et al.*, 1993). They are structurally similar to archaeol, however contain a hydroxyl group at the C-3 position on the *sn*-2 phytanyl chain (Hinrichs *et al.*, 2000). Due to the labile nature of *sn*-2-hydroxyarchaeol, this compound could be a proxy for living methanogen biomass (Pancost *et al.*, 2011).

There is also growing evidence that methanogens may synthesise unusual butanetriol and pentanetriol dibiphytanyl glycerol tetraethers (BGDTs and PDGTs, respectively). BGDTs and PDGTs have been identified in different environments, including marine sediments (Zhu *et al.*, 2014), wetlands (*e.g.,* Blewett *et al.*, 2020), and peats (*e.g.,* Yang *et al.*, 2019). Similar to the other archaeal lipids (*i.e.* archaeol and GDGT-0), both compounds increase in concentration below the anoxic layer (*e.g.,* catotelm) and are nearly absent from oxygenated layers (e.g., acrotelm). This is consistent with an anaerobic archaea origin and the fact that only cultures of the methanogen order Methanomassiliicoccales have been observed to synthesise BGDTs and PDGTs (Becker *et al.*, 2016). These compounds, alongside other minor GDGTs (Bauersachs *et al.*, 2015), are promising methanogen-specific biomarkers that warrant further study. Another recent finding is the ubiquity of glycerol monoalkyl glycerol tetraether (GMGT, also known as 'H-GDGT') in peats (Naafs, McCormick, *et al.*, 2018) and, more crucially, its occurrence in the oxic-anoxic boundary (Yang *et al.*, 2019; Blewett *et al.*, 2020). However, cultures have implicated GMGTs in a broader array of archaea, not all necessarily methanogens (see Naafs *et al.*, 2018 and references therein).

1.4.5 Existing Early Paleogene Records

Numerous lipid biomarker records are available from early Paleogene localities, however those that investigate biogeochemical cycles are much fewer. Figure 1.6 presents the key δ^2H_{wax} records that this thesis discusses, however is not an exhaustive compilation of all existing studies on the hydrologic cycle during the early Paleogene. On the other hand, there are currently only three sites that have utilised lipid biomarker thermal maturity ratios and $\delta^{13}C$ of hopanoids to reconstruct OC_{petro} mobilisation (Lyons *et al.*, 2019) and methane cycling (Pancost *et al.*, 2007; Inglis *et al.*, 2021; Blumenberg *et al.*, 2024) during the PETM, respectively.

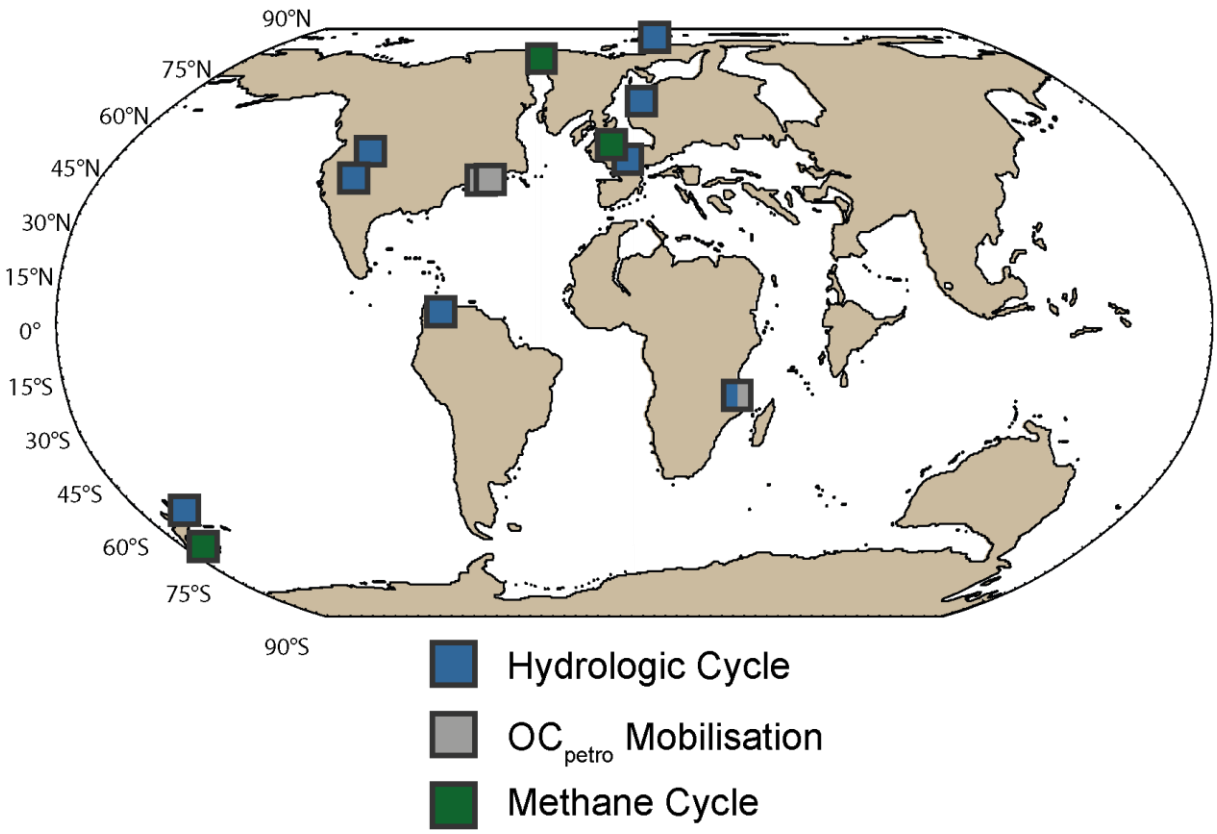

Figure 1.6 **Location of early Paleogene sites with lipid biomarker records that investigate the hydrologic cycle (blue), OC_{petro} mobilisation (grey), and the methane cycle (green).** The sites include: ACEX (central Arctic Ocean; Pagani, Pedentchouk, *et al.*, 2006), ODP Site 913 (East Greenland; Inglis, Carmichael, *et al.*, 2020), Vasterival (France; Garel *et al.*, 2013), Bighorn Basin (United States; Smith, Wing and Freeman, 2007), Green River Formation (United States; Elson *et al.*, 2022), Mar2X (Venezuela; Jaramillo *et al.*, 2010), TDP Site 14 (Tanzania; Handley *et al.*, 2008; Carmichael *et al.*, 2017), and Kumara-2 (New Zealand; Handley, Crouch and Pancost, 2011), for the hydrologic cycle; TDP Site 14 (Tanzania; Handley *et al.*, 2012), SDB (Atlantic Coastal Plain; Lyons *et al.*, 2019), and CamDor (Atlantic Coastal Plain; Lyons *et al.*, 2019), for OC_{petro} mobilisation; and Cobham Lignite (United Kingdom; Pancost *et al.*, 2007), Otaio River (New Zealand; Inglis *et al.*, 2021), and Stenkul Fiord (Arctic Canada; Blumenberg *et al.*, 2024), for the methane cycle. Palaeogeographic reconstructions of 56 Ma, adapted from Carmichael *et al.* (2017).

1.5 Scope, Aims, and Outline of the Thesis

The impact of global warming on various biogeochemical cycles is poorly understood, especially in the terrestrial realm. Both the sign and magnitude of change is disputed, and GCMs do not fully incorporate the complex relationships and feedback mechanisms. This major gap in our understanding impedes accurate predictions of future climate change. The

emergence of new lipid biomarker-based proxies have allowed for such processes to be investigated in the geologic record. This thesis focuses on the hothouse worlds of the early Paleogene (*i.e.* within the Paleocene to Eocene; ~66–34 Ma), including a hyperthermal event (*e.g.,* PETM), as they are the closest analogue and ideal testbeds for climate models. The overarching aims are:

Reconstruct the hydrologic cycle in the tropics during the early Paleogene

Our current understanding of the hydrologic cycle during the early Paleogene is mostly restricted to sites from the high-latitudes. These studies indicate enhanced poleward moisture transport and an intensification of the hydrologic cycle. However, the response of the tropics (<15ºN/S) is limited to a single site that exhibits only a brief 'snapshot' in time.

Determine the role of OC_{petro} within the global carbon cycle during the PETM

Recent work on modern systems have highlighted that CO_2 released from OC_{petro} oxidation can rival that of volcanic emissions. Therefore, understanding the sensitivity of this positive feedback mechanism is crucial. Yet, only one study has fingerprinted OC_{petro} during the PETM. This study also delivers first-order estimates for the oxidation of OC_{petro}, however direct quantification have not been possible due to the lack of proxies.

Investigate novel lipid biomarkers and their association with the methane cycle during the PETM

CH_4 is a potent GHG, yet has been largely overlooked in the geological context. Bacteriohopanepolyols (BHPs) have shown promise as biomarkers for methanotrophs, however only one study has identified them in the PETM. New methodological advancements have led to the discovery of previously undetectable BHPs, and these novel compounds have yet been reported in the geologic record.

To achieve these aims, **Chapter 3** presents a new tropical δ^2H_{wax} record, from Cerrejón Mine in Colombia, spanning the latest Paleocene. The chain-length distribution and $\delta^{13}C_{wax}$ of *n*-alkanes are utilised to identify the potential impact of diagenesis and vegetation change on the δ^2H_{wax} record. First-order estimates of δ^2H_{precip} values are then calculated and compared to water isotope-enabled model simulations, aiding in interpretations of the hydrologic cycle during the early Paleogene.

Global warming and an intensification of the hydrologic cycle may result in the terrestrial realm acting as a net CO_2 source, amplifying future climate change. In order to investigate whether this occurred in past, Chapter 4 to 6 focus on contributing several new records that reconstruct terrestrial carbon cycle feedbacks during the PETM.

In **Chapter 4**, existing and new lipid biomarker thermal maturity ratios are collated to create the first global dataset of OC_{petro} in PETM-aged shallow marine sites. A two-endmember mixing model is used to calculate OC_{petro} burial fluxes, which are reported as mass accumulation rates (MARs). The compilation is then evaluated for spatial and temporal patterns in OC_{petro} MARs during the PETM. However, this does not provide constraints on the fraction of OC_{petro} that oxidised into CO_2. Therefore, **Chapter 5** focuses on exploring novel approaches (*i.e.* Raman spectroscopy) to quantify OC_{petro} oxidation in the past. This chapter employs two of the sites that exhibited contrasting trends in Chapter 4. Raman spectroscopy has been utilised to assess OC_{petro} oxidation in modern settings. Chapter 5 presents the first application of this approach to the PETM.

Chapter 6 investigates the methane cycle, another important component of the terrestrial carbon cycle. A previous study has inferred enhanced methanotrophy from $\delta^{13}C_{hop}$ values in a southern high-latitude PETM-aged site, Otaio River from New Zealand. However, these compounds are not diagnostic and can derive from other organisms. This chapter explores whether a suite of BHPs can be used as complementary tracers for methane oxidation in the past.

Finally, **Chapter 7** provides a synopsis of the mains findings of this thesis and recommends research topics for future work.

Chapter 2 Methodology

The following chapter describes key methods applied to prepare terrestrial and marine sediments for bulk geochemical (see Section 2.2) and organic geochemical (see Section 2.3) analyses. Section 2.4 outlines relevant analytical instruments and their methods utilised at the University of Southampton, Raman Spectroscopy (see Section 2.4.4) and UHPLC-HRMS (see Section 2.4.5) analyses were undertaken at the Manchester Metropolitan University and the Royal Netherlands Institute for Sea Research (NIOZ), respectively. Information on study sites and materials (*i.e.* age controls), as well as any adaptations to the methodology, can be found in more detail within each chapter.

2.1 Sediment Preparation

Sediments were firstly freeze-dried or placed in a 50 °C overnight, then powdered with a mortar and pestle or Planetary Mill Pulverisette 5 (Fritsch), for 2 min at 300 rpm (Sparkes *et al*., 2013), to homogenise the sample. Between samples, the mortar and pestle were washed with Decon 90, then rinsed with dichloromethane (DCM) and methanol (MeOH). The agate mill and balls were cleaned with isopropanol. Some of the sediments required a prior step using a hammer to break it into smaller fragments.

2.2 Bulk Geochemistry

Powdered sediments were dissolved in 10% hydrochloric acid (HCl) and left for 24 hours to eliminate any inorganic carbon. The sediments were then washed in Milli-Q to remove the HCl. This was achieved by adding an equal quantity of Milli-Q to each sample and then centrifuging at 5,200 rpm for ~5–10 min. A syphon was then used to remove the Milli-Q, and this was repeated until the pH values were close to neutral. After drying in a 50 ºC oven, the samples were weighed into clean tin capsules on a Sartorius ME5 micro balance. For sediments that appear to be organic-rich (*i.e.* dark-coloured) vs. organic-lean (*i.e.* light-coloured or sandy sediments), an initial ~10 mg and ~30 mg were used for analyses, respectively.

2.3 Organic Geochemistry

Between ~1–2 g of the freeze-dried and homogenised sediments were weighed for extraction, separation, and/or purification. The following section discusses all the procedures utilised throughout this work. However, every chapter used a different combination of procedures based on what was most appropriate for the lipids being investigated. The efficacy was tested for each new methodology, by comparing the concentration of a pure

internal standard (I.S.) with an I.S. in a sample, and typically yielded >75 % recovery. Furthermore, a blank was processed with every set of samples to ensure that any sources of contamination could be identified.

2.3.1 Extractions

2.3.1.1 ASE Extraction

The Accelerated Solvent Extractor (ASE) uses organic solvents at high temperatures and pressures to extract compounds from solid samples. Lipids were extracted using a Thermo 350 ASE, with a solvent mixture comprised of DCM:MeOH (9:1, *v:v*). The programme followed the settings: pre-heat = 5 min; heat = 5 min; static = 5 min; pressure = 10.34 MPa; flush = 70%; purge = 300 s; cycles = 3. The acquired total lipid extracts (TLE) were then dried with a Genevac EZ-2 centrifugal evaporation system, in preparation for storage or the next step (see Section 2.3.2).

2.3.1.2 Bligh and Dyer Extraction

The Bligh and Dyer extraction (Bligh and Dyer, 1959) technique is much less destructive and thus maximises the yield of BHPs. Therefore, BHPs were extracted using a modified Bligh and Dyer. Firstly, the samples were ultrasonicated for 15 min with a solvent mixture consisting of MeOH:DCM:phosphate buffer (2:1:0.8, *v:v:v*), centrifuged for 0.5 min at 3,000 rpm, and the supernatant collected through pre-extracted cotton wool. This was repeated a further 2 times, however with 10 min of ultrasonication. Secondly, extra DCM and phosphate buffer were added to the combined supernatant to obtain a new ratio of MeOH:DCM:phosphate buffer (1:1:0.9, *v:v:v*), and incorporated using a vortex mixer. Clean biphasic separations were then achieved after the samples were centrifuged for 0.5 min at 2,600 rpm, and the DCM layers were transferred. Finally, the aqueous phases were then washed with just DCM a further 2 times, from which the DCM layers were transferred and subsequently combined. The aforementioned procedure was repeated on the same solid residue, however with trichloroacetic acid (TCA) in replacement of the phosphate buffer for the first solvent mixture. In the end, the two extracts were combined to acquire the Bligh Dyer extracts (BDE). As BHPs are more unstable, the BDE were dried under a gentle continuous flow of N_2 and stored below -20 °C.

2.3.2 Column Chromatography

2.3.2.1 Silica Column

Column chromatography is a method to separate the TLE into specific compound classes. The most commonly applied procedure uses aluminium oxide or activated silica gel columns

with different solvent mixtures. Here, a silica column is used to create three-fractions: aliphatic (*e.g., n*-alkanes, hopanes, steranes etc.), aromatic (*e.g.*, PAH, unsaturated compounds etc.), and polar (*e.g., n*-alkanoic acids, *n*-alcohols, GDGTs etc.). Glass pipettes packed with glass wool were furnaced and filled with activated (*i.e.* dried overnight at 100 °C) silica gel. The solvents used to elute each fraction were: hexane (Hex; 4 mL), Hex:DCM (3:1, *v:v*; 4 mL), and Hex:MeOH (1:2, *v:v*; 4 mL), respectively. Firstly, the columns were conditioned with 2 dead volumes (~3 mL) of Hex. The TLE were then loaded onto the column using 5 drops (~0.25 mL), which is repeated 3 times and followed by 2 dead volumes (~3 mL) directly added to the column. All the fractions were dried with a N_2 blower at 40 °C.

2.3.2.2 'Hybrid' Column

The 'Hybrid' column allows for the additional separation of the *n*-alkanoic acids ('fatty' acids) from the TLE. Overall, this method creates five-fractions: aliphatic, ketone (*e.g.,* alkenone etc.), alcohols (*e.g., n*-alkanols; sterols; diols; GDGTs etc.), fatty acids, and pigments. Following Section 2.3.2.1, glass pipettes packed with glass wool were furnace. However, the solid phase was half aminopropyl silica gel (LC-NH_2) and half 5 % deactivated silica gel. The solvents used were: Hex (4 mL), DCM, DCM:isopropanol (IPA) (2:1, *v:v*; 4 mL), 4% acetic acid in DCM(4 mL), and MeOH(4 mL), respectively. The columns were conditioned and the TLE loaded using the same procedure as in Section 2.3.2.1. However, the last 2 solvents were directly added to the column, assuming that most of the TLE was rinsed and added to the column with the first 3 solvents. All the fractions were then dried with a N_2 blower at ~40 °C.

2.3.3 Removal of Elemental Sulphur

High concentrations of elemental sulphur should be removed from samples as it can both damage the analytical instruments and obscure the chromatogram. Sulphur was identified by visible crystals in the vial and/or confirmed by evaluating the mass spectra (Figure 2.1). In summary, extracted copper balls were added to the fraction and left for 24 hrs. Between each use, the copper was cleaned using ~37 % HCl, Milli-Q, and then rinsed with MeOH and DCM.

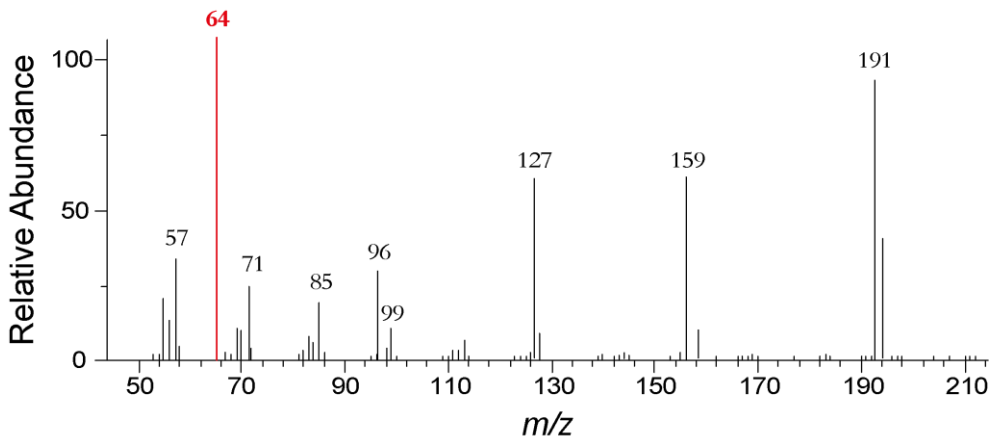

Figure 2.1 Example mass spectrum with mass-to-charge ratio (*m/z*) 64, diagnostic of sulphur dioxide.

2.3.4 Urea Adduction

Urea adduction is a molecular sieving technique that can separate coeluting compounds based on their size and stereochemistry. The straight-chain/acyclic *n*-alkanes get incorporated in the urea crystals (*i.e.* the adduct fraction), whereas the branched/cyclic hopanes are too stereochemically 'bulky' to fit and so remain (*i.e.* non-adduct fraction). This procedure may also extract *n*-alkanes from any unresolved complex mixtures (UCM), partially reducing the UCM-to-signal ratio, which should ideally be lower than 1:3. Firstly, 200 µL of urea (10 % in MeOH), acetone, and Hex were added to the aliphatic fractions and placed in a freezer for ~30–60 min. The samples were dried with a N_2 blower at <40 °C to prevent loss of low-molecular weight compounds. The non-adduct fractions were extracted and transferred with a total of ~4 mL of Hex, or until the Hex was clear. The urea crystals were then dissolved in 500 µL of Milli-Q and MeOH. Finally, 1 mL of Hex was added to extract the adduct compounds and the sample vortexed to induce a phase separation, from which the Hex was transferred. This was repeated a further 3 times, so that a total of ~4 mL of Hex was acquired. Both fractions were then dried with a N_2 blower.

2.3.5 Derivatisation

2.3.5.1 Silylation

In order to analyse functional compounds (*e.g.,* alcohols and fatty acids) via gas chromatography (GC), they must be derivatised. Alcohol groups are silylated to create trimethylsilyl (TMS) ethers. This method is undertaken just before the samples are injected into the analytical instruments, as silylated compounds vary in stability depending on the sample matrix. 25 µL of *N,O*-Bis(TMS)trifluoroacetamide (BSTFA) and pyridine are added to the alcohol fraction. This is then heated to 60 °C for 1 hour, cooled for 10-15 min, and dried with a N_2 blower.

2.3.5.2 Methylation

Acids are methylated to the methyl ester derivatives. 100 µL of BF_3-MeOH is added to the fatty acid fraction. This is then heated to 60 °C for 30 min. After cooled (~10–15 min), ~1 mL of Milli-Q and ~2 mL of DCM are added to the sample and vortexed. Once settled, the DCM containing the fatty acid methyl esters (FAME) are extracted. This is repeated until the DCM is clear. Any residual Milli-Q in the DCM is removed using a sodium sulphate (Na_2SO_4) column.

2.3.6 Internal Standard and Sample Preparation

Prior to extraction, an appropriate concentration of I.S. was added to each sample. By adding the I.S. at the beginning, the efficacy of the whole procedure can be calculated. Bromohexadecane and 9-bromophenanthrene was used for the aliphatic and aromatic fractions, respectively. The appropriate concentrations of sample was then re-suspended in Hex or ethyl acetate (EtAc) prior to analyses.

2.4 Analytical Instrumentation

2.4.1 EA-IRMS

The bulk elemental concentrations and isotopic compositions, for organic carbon and nitrogen, were performed on an Elementar vario ISOTOPE select elemental analyser (EA) interfaced with a thermal conductivity detector (TCD) and an Isoprime 100 continuous flow isotope ratio mass spectrometer (IRMS), respectively. Samples were combusted at 950 °C with addition of pure oxygen. The resulting NOx and CO_2 gases were reduced to N_2 and CO_2 in the reduction column, which was held at 550 °C. Quality control, to ensure consistency in the data, involved analysing a high organic content sediment standard (HOCS; Elemental Microanalysis Ltd.). The standard deviation was then calculated to determine the analytical precision of the run. For the normalisation of the isotope ratios, the United States Geological Survey (USGS) 40 and 41 are used as international reference materials.

2.4.2 GC-FID and GC-MS

Most of the lipids investigated in this thesis are volatile and thus GC-amenable. A ThermoFisher Trace 1310 GC with a flame ionisation detector (FID) was used to first assess the relative abundance. This allowed the appropriate concentration to be determined for the GC-mass spectrometry (MS). A ThermoFisher Trace 1310 GC coupled to a Thermo TSQ8000 Triple Quadrupole MS was then used to characterise complex mixtures of analytes. For every run, 1 µL of sample was injected. Helium was used in both GCs as the

carrier gas, and separation was achieved with a DB-5 column (30 m × 0.25 mm i.d. 0.25 µm film thickness). The GC-FID temperature program started at 40 °C for 2 min and ramped up to 130 °C at 4 °C min^{-1}. A temperatures of 310 °C was then kept for a final isothermal time of 15 min to remove all the solvents. The GC-MS program started at 70 °C for 1 min, and increased to 130 °C at 20 °C min^{-1}, followed by 300 °C at 4 °C min^{-1}, which was then held for 20 min. MS scans occurred between mass-to-charge ratio (*m/z*) 50 to 650 Da, and the ionisation energy was 70 eV. For some samples with low concentrations, selected ion monitoring (SIM) was used.

2.4.3 GC-IRMS

Compound-specific isotope analysis (CSIA), namely carbon and hydrogen, was undertaken on a ThermoFisher Trace 1310 GC coupled to a Thermo Delta V Plus IRMS and equipped with a GC Isolink and Conflo IV. The GC oven followed the set up described above (see Section 2.4.2). The combustion reactor was maintained at 1000 °C and 1400 °C for carbon and hydrogen, respectively. For hydrogen analysis, much higher concentrations of analytes was required. In addition, as part of quality control, the H_3 factor was calculated prior to each sequence, to correct for protonation reactions occurring within the ion source (Sessions *et al.*, 1999). Results were typically below 3 ppm V^{-1}. Samples were run in triplicates and normalised for variations in response by comparing to odd numbered *n*-alkanes (C_{17-25}) with a known isotopic composition (the A7 standard reference material; obtained from Arndt Schimmelman, Indiana University, USA). This standard was analysed 4 times prior and 3 times post each sample batch (n = 3).

2.4.4 Raman Spectroscopy

The crystallinity of carbonaceous materials were assessed with an InVia Raman spectrometer (Renishaw). The samples were systematically scanned using a 50x magnification microscope. All carbonaceous particles were first determined by brief exposure to a 514 nm Ar-ion laser (2 s; measurement window 1050–1915 cm^{-1}). Those confirmed were further inspected and photographed prior to a final spectrum being measured by long exposure (60 s; measurement window 800–2200 cm^{-1}). Laser power was kept low enough (estimated to be <6 mW) to cause no noticeable thermal alterations to the targets.

2.4.5 UHPLC-HRMS

BHP analysis was performed on an Agilent 1290 Infinity I ultra-high-performance liquid chromatography (UHPLC) coupled to Q Exactive orbitrap high resolution tandem mass spectrometry ($HRMS^2$), equipped with a heated electrospray ionisation (HESI) probe (ThermoFisher Scientific). The methods are outlined in Hopmans *et al.* (2021). To

summarise, separation was achieved with an Acquity C_{18} BEH column (2.1 x 150 mm, 1.7 µm particle; Waters) and solvent (A) MeOH:H_2O:formic acid:14.8 M NH_{3aq} (85:15:0.12:0.04, *v:v*) and (B) MeOH:IPA:formic acid:14.8 M NH_{3aq} (1:1:0.12:0.04, *v:v*), at a flow rate of 0.2 mL min $^{-1}$. The gradient program started with 95 % of A for 3 min, to 40 % and 100 % of B at 12 and 50 min, respectively, ending at 80 min. The analytes were detected with positive ion monitoring between mass-to-charge ratio (*m/z*) 350–2000 Da (resolution of 70,000 ppm at *m/z* 200). This was followed by data-dependent MS^2 (resolution of 17,500 ppm) of the 10 most abundant ions and dynamic exclusion (6 s) within 3 ppm mass tolerance, and an inclusion list of 165 calculated exact masses of BHPs was also used. Optimal fragmentation was achieved with a stepped normalised collision energy of 22.5 and 40.

2.5 Lipid Identification

The lipids were identified based on retention times, fragmentation patterns, comparison to a known standard (an in-house reference oil; North Sea Oil-1), and library matches. The peak areas from the GC-MS were integrated and calculated using the software Xcalibur. Lipids are typically referred in relative abundance to other lipids, however the data in this thesis can also be converted to concentrations (µg per g of sediment) based on the I.S. peak areas. Peaks that were present with low signal, or a noise-to-signal ratio greater than 1:3, were noted to be below detection (b.d.). Data from the GC-IRMS was processed on the software Isodat. A comparison study of both automatic and manual integrations on Isodat showed that auto integrations yielded more precise results, although peaks were checked and manually corrected. The peak height must be at least 50 % of the reference peaks. Standard deviation (s.d.) for $\delta^{13}C$ should ideally be below 0.5 ‰, and for $\delta^{2}H$ below 6 ‰. Final results are expressed relative to Vienna PeeDee Belemnite (VPDB) for carbon and Vienna Standard Mean Ocean Water (VSMOW) for hydrogen.

Chapter 3 The Hydrological Response of the Tropics to Hothouse Climates of the Past

Abstract

State-of-the-art general circulation models (GCMs) predict that future warming will result in an intensification of the current hydrologic cycle, yet large uncertainties remain in the response of the tropics (<15°N/S). The geologic record can provide a unique insight into how the hydrologic cycle operated in the past. The hydrogen isotopic composition of long-chain *n*-alkanes (δ^2H_{wax}) have previously been utilised to evaluate the hydrologic cycle during the 'hothouse' climate of the early Paleogene (*i.e.* within the Paleocene to Eocene; ~66–34 Ma), and suggest increased rainfall in the tropics with global warming. However, this is based on a single deposit, Mar2X in Venezuela, which may not be regionally representative. Here, we investigate a new sedimentary sequence that spans the latest Paleocene (~57–56 Ma), from Cerrejón Mine in Colombia. A δ^2H_{wax} record is generated to infer changes in the amount of precipitation. δ^2H_{wax} values range from -114.3 ‰ to -175.6 ‰, exhibiting larger-than-expected fluctuations during the latest Paleocene. Assuming a net fractionation factor of -121 ‰, first-order estimations of δ^2H of precipitation (δ^2H_{precip}) vary between -13 ‰ and -52 ‰. This is consistent with the late Paleocene δ^2H_{precip} values from Mar2X (-9 ‰ to -38 ‰), although there is greater variability at Cerrejón Mine. The wide range of δ^2H_{precip} values indicate that rainfall intensity changed dramatically during the latest Paleocene. However, this contrasts with water isotope-enabled climate model simulations (iCESM1.2) that suggest a much narrower range of δ^2H_{precip} values, highlighting potential issues with the proxy- and/or model-based reconstructions.

Chapter 3 to be submitted. **Hollingsworth, E.H.,** Jaramillo, C.A., Carvalho, M.R., Cramwinckel, M.J., and Inglis, G.N. The Hydrological Response of the Tropics to Hothouse Climates of the Past.

3.1 Introduction

Understanding how the hydrologic cycle may respond to future warming is vital. The latest generation of general circulation models (GCMs) within the Coupled Model Intercomparison Project Phase 6 (CMIP6), predicts a 'wet gets wetter' and 'dry gets drier' response (Chou and Neelin, 2004; Held and Soden, 2006), and it is 'very likely' that precipitation will increase over the tropical rain belt (Lee *et al.*, 2021). However, this paradigm does not apply over land (*e.g.,* Greve *et al.*, 2014; Byrne and O'Gorman, 2015), and GCMs exhibit regional-scale variability across the tropics (<15°N/S) (Lee *et al.*, 2021). In fact, even the sign of change is inconsistent in some tropical regions, despite attempts through successive CMIP phases to reduce biases (*e.g.,* 'double-ITCZ bias'; Fiedler *et al.*, 2020).

The geologic record offers a unique opportunity to elucidate the response of the tropical hydrologic cycle to warming (*e.g.,* Tierney *et al.*, 2020). There have been many investigations on the 'hothouse' climate of the early Paleogene (*i.e.* Paleocene to Eocene; ~66–34 Ma). This time interval is unprecedented over the last 66 Ma (Westerhold *et al.*, 2020), with a peak global mean surface temperature of 35.2 °C (Evans *et al.*, 2024). However, early Paleogene-aged sediments from the tropics are scarce (Appendix I), and most of these studies have focused on a transient global warming event, known as the Paleocene-Eocene Thermal Maximum (PETM; ~56 Ma) (see Carmichael *et al.*, 2017 and references therein), or the Eocene (Inglis, Carmichael, *et al.*, 2020; Elson *et al.*, 2022; Inglis, Toney, *et al.*, 2022). However, insights into the background state of the late Paleocene are important to fully contextualise the perturbations observed during the PETM.

The hydrogen isotopic composition of long-chain *n*-alkanes (δ^2H_{wax}) can be used to evaluate past changes in the hydrologic cycle (*e.g.,* Sauer *et al.*, 2001). Long-chain *n*-alkanes are primarily synthesised as part of the epicuticular wax on vascular (*i.e.* 'higher') plant leaves (Eglinton and Hamilton, 1967). da Silveira Lobo Sternberg (1988), first demonstrated that modern δ^2H_{wax} values mirror that of its surrounding environmental water. Subsequent calibration studies have established the relationship between δ^2H_{wax} and the δ^2H of meteoric water (δ^2H_{precip}) globally (*e.g.,* Daniels *et al.*, 2017; McFarlin *et al.*, 2019; see Ladd *et al.*, 2021 and references therein). The δ^2H_{precip} signature varies both spatially and temporally, as it is controlled by multiple climatological processes (see Bowen, 2008 and references therein). As such, interpreting δ^2H_{precip} is complex, although a wealth of information can be derived. Monitoring of the present-day distribution highlights that there are distinct spatial patterns. On a global-scale, the high-latitudes and large continental interiors exhibit lower δ^2H_{precip} values due to the predominant effects of Rayleigh distillation during the transport of atmospheric water vapour (*e.g.,* Liu, Bowen and Welker, 2010). Similarly, extratropical regions are mostly influenced by the strong variability in temperature (*e.g.,* Dansgaard, 1964; Bowen, 2008). In contrast, the tropics are both proximal to the source of water and

characterised by stable temperatures, and therefore δ^2H_{precip} is driven by seasonality in the hydrologic cycle. In other words, lower δ^2H_{precip} values in the tropics indicate an increase in the amount of rainfall (*i.e.* 'amount effect'; Dansgaard, 1964; Bowen, 2008), although drastic changes in the atmospheric circulation and/or evaporation rates may overprint this signal.

Existing tropical δ^2H_{wax} records from the early Paleogene are limited to one site in Venezuela (Mar2X; Jaramillo *et al.*, 2010). The δ^2H_{wax} record exhibits ^{2}H-depletion (~20–40 ‰) at the onset of the PETM, indicating an enhanced amount effect (*i.e.* more precipitation). Models corroborate a wetter tropics during the PETM (*e.g.,* Winguth *et al.*, 2010; Carmichael *et al.*, 2016; Cramwinckel *et al.*, 2023). However, variability in the δ^2H_{wax} record prior to the PETM are of comparable magnitude (~30 ‰), implying a dynamic hydrologic cycle during the late Paleocene. Here, we present a new tropical δ^2H_{wax} record from Cerrejón Mine in Colombia. The deposits broadly date within the late Paleocene to early Eocene (Jaramillo *et al.*, 2007). Prior to first-order estimations of δ^2H_{precip}, the chain-length distribution and carbon isotopic composition of *n*-alkanes ($\delta^{13}C_{wax}$) are utilised to assess the application of δ^2H_{wax} as a proxy for this site. Subsequent interpretations of the δ^2H_{precip} record are aided with comparisons to model-derived δ^2H_{precip} values (*e.g.,* Lee *et al.*, 2007; Nusbaumer *et al.*, 2017).

3.2 Material and Methods

3.2.1 Site Description and Age Controls

The Cerrejón Mine is located in the Rancheria River Valley, eastern Colombia (Figure 3.1), and is the largest open-cast coal mine in the world (Jaramillo *et al.*, 2007). Here, samples (*n* = 293) were obtained from the Annex Pit by Prof. Carlos Jaramillo.

The sampled section spans ~250 m, from the upper Cerrejón Formation to the base of the overlying Tabaco Formation (Appendix II). The deposits mostly comprise of laminated mudstones and siltstones, with bioturbation and abundant plant fossils, interspersed by coal seams and sandstone (Jaramillo *et al.*, 2007). The lithofacies and floral composition indicate an overall fluvial-influenced coastal environment (Jaramillo *et al.*, 2007). An inundation event above coal 155 (Appendix II) was inferred from the presence of dinoflagellate cysts. At the top of the Cerrejón Formation, a fining-upward succession, from conglomeratic coarse-grained sandstone, has been suggested as the filling of channel structures cutting alluvial plains (Jaramillo *et al.*, 2007).

The ages of the Cerrejón and Tabaco Formation were proposed as late Paleocene and (early) Eocene, respectively (Jaramillo *et al.*, 2007). A composite biostratigraphical record, including 70 sites in the region and encompassing the whole Cenozoic, has since determined 18 palynological zonations (Jaramillo, Rueda and Torres, 2011). These zones were defined by a constrained optimisation and graphic correlation method, and calibrated with

foraminifera, $\delta^{13}C$, and magnetostratigraphy data (Jaramillo, Rueda and Torres, 2011). The Cerrejón Formation coincides with two tie-points, the first and last appearance of *Foveotricolpites perforates* at 59 Ma and 56.1 Ma, respectively (Jaramillo, Rueda and Torres, 2011). Therefore, the sampled section in this study can be broadly placed after 59 Ma and up to the Eocene-aged Tabaco Formation.

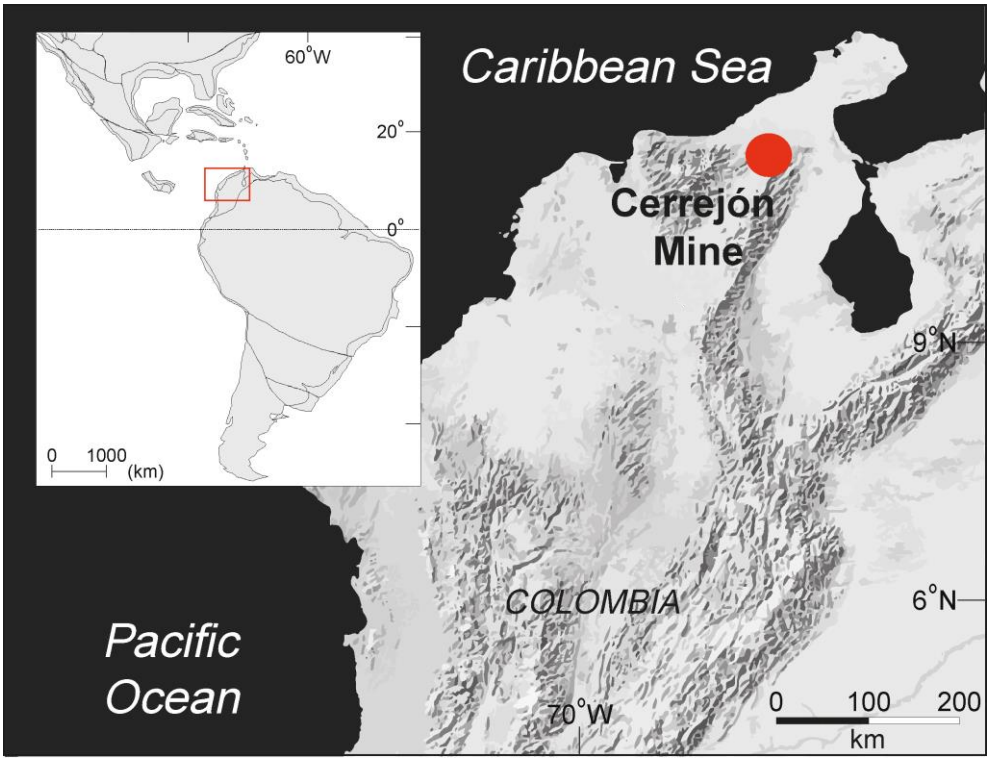

Figure 3.1 The present-day location of Cerrejón Mine, Eastern Colombia (11.3°N, 72.41°W). The insert shows the late Paleocene palaeogeographic map. Adapted from Jaramillo *et al.* (2010).

3.2.2 Bulk Geochemistry

First, sediments were homogenised with a mortar and pestle (see Section 2.1). A total of 87 samples were processed for bulk geochemical analyses (see Section 2.2). The stable carbon isotopic composition of bulk organic carbon ($\delta^{13}C_{org}$) has been published from two cores in the lower section of the 1 km thick Cerrejón Formation (WRV-04752 and WRV-04774; Appendix II), and can be accessed within Jaramillo *et al*. (2007). Here, we expand the $\delta^{13}C_{org}$ and total organic carbon (TOC) record further into the upper Cerrejón Formation. Based on lithological observations, between ~10–30 mg of samples were used for analyses. The data was acquired from an Elementar vario ISOTOPE select elemental analyser coupled with Isoprime 100 isotope ratio mass spectrometer (EA-IRMS; see Section 2.4.1). In total, 31 samples were re-weighed for analyses, as carbon concentrations fell over or under the calibration range of the EA. To test for cyclicity in the $\delta^{13}C_{org}$ record, spectral analysis was undertaken in the depth domain. The Nyquist frequency was first confirmed satisfied (*i.e.*

there are 2 samples per 'theorised' cycle), and the record detrended and linearly interpolated on a 1 cm scale to create equal spacing. The multitaper method (MTM) was then applied using R Package Astrochron (Meyers, 2014).

3.2.3 Organic Geochemistry

For biomarker analyses, samples from the coal seams were targeted (n = 44), as a pilot run (n = 20) determined a low concentration of analytes in the non-coal deposits. The organic geochemistry procedure is fully described in Section 2.3. In summary, ~2 g of sediment were extracted using a Thermo 350 Accelerated Solvent Extractor (ASE), with DCM:MeOH (9:1, *v:v*) (see Section 2.3.1.1). The extracts were then separated into five fractions (see Section 2.3.2.2), with the exception of the samples from the pilot run which were separated into three fractions (see Section 2.3.2.1). The apolar fraction of 17 samples required removal of elemental sulphur (see Section 2.3.3). Moreover, those with TOC values >0.7 % (n = 21) were urea adducted (see Section 2.3.4), to separate the *n*-alkanes for compound-specific isotope analysis (CSIA). The apolar fractions were re-suspended in hexane, and characterised using gas chromatography-mass spectrometry (GC-MS; see Section 2.4.2). Compounds were identified based on retention times, fragmentation patterns, and comparison to an in-house standard. CSIA, including carbon and hydrogen, were performed using a GC coupled to an isotope ratio mass spectrometer (GC-IRMS; see Section 2.4.3). A total of 11 samples were re-suspended in ethyl acetate and manually injected, to acquire the concentration necessary for δ^2H analyses. Peak height must be at least 50 % of the reference peaks. Standard deviation (s.d.) should ideally be below 0.5 ‰ and 6 ‰ for $\delta^{13}C$ and δ^2H, respectively.

3.2.4 *n*-Alkane-based Chain-Length Ratios

The carbon preference index (CPI; see Section 1.4.3.1) is used to assess whether δ^2H_{wax} values are affected by diagenesis. The terrigenous-aquatic ratio (TAR) (Bourbonniere and Meyers, 1996), P_{aq} (Ficken *et al.*, 2000; Mead *et al.*, 2005), and average chain length (ACL) (Bush and McInerney, 2013) (see Section 1.4.2) provide insight into the vegetation community composition. For the ACL ratio, n refers to odd numbered *n*-alkanes from C_{25} to C_{33}.

3.2.5 Water Isotope-Enabled Model Simulations

Modelled δ^2H_{precip} values were obtained via isotope-enabled Community Earth System Model version 1.2 (iCESM1.2; Zhu, Poulsen and Tierney, 2019; Zhu *et al.*, 2020), following a slightly updated version of the available script (https://github.com/NCAR/iCESM1.2). In summary, simulations were run with atmospheric CO_2 concentrations of 1x, 3x, 6x, and 9x

that of the pre-industrial (PI) value (284.7 ppmv). For the Eocene simulations, the boundary conditions remained constant, including the palaeogeography, land-sea mask, vegetation distribution, non-CO_2 GHG concentrations, soil properties, aerosols, solar constant, and orbital parameters, following the Deep-Time Model Intercomparison Project (DeepMIP) protocol (Herold *et al.*, 2014; Lunt *et al.*, 2017). The δ^2H of seawater was initialised from a constant value of -8.0 ‰, to account for the absence of ice sheets (Hollis *et al.*, 2019). Individual grid cells have a horizontal resolution of 1.9 × 2.5° (latitude × longitude) for the atmosphere and land component, and a nominal 1° for the ocean and sea ice component. The δ^2H_{precip} values were acquired from the closest grid corner to Cerrejón Mine (Figure 3.8).

3.3 Results

3.3.1 Bulk Geochemistry

Figure 3.2a presents a high-resolution bulk $\delta^{13}C_{org}$ record from this study (closed symbols), alongside the published data (open symbols) from cores WRV-04752 and WRV-04774 (Jaramillo *et al.*, 2007). Overall, $\delta^{13}C_{org}$ values range between -24.3 ‰ and -27.8 ‰, with the lowest value at 66.69 m (closed symbols; Figure 3.2a). There are large fluctuations throughout the record, but a LOESS regression reveals an overall decrease upsection. This likely represents the global declining trend characteristic of the latest Paleocene (*e.g.,* Westerhold *et al.*, 2020). In general, TOC values are very low (<1 %), but 17 out of the 85 samples are >1 % (Figure 3.2b).

3.3.2 Organic Geochemistry

The apolar fractions typically contain short- (C_{13-19}), mid- (C_{21-25}), and long-chain (C_{27-35}) *n*-alkanes (*e.g.,* Figure 3.2c). In addition, 75 % of the samples comprise of hopanes, ranging from C_{27} to C_{35} (*e.g.,* Figure 3.2c). Variations of the αβ, βα, and ββ isomers at the C-17 and C-21 position, and the R and S stereochemistry at the C-22 position, are available for C_{27}, C_{29}, C_{30}, and C_{31}, and C_{31} to C_{33} hopanes, respectively. C_{32} ββ hopane is not observed in any of the samples, and C_{33-35} hopanes are only found in the αβ configuration.

The chain-length distribution of *n*-alkanes are shown in Figure 3.3. In total, 9 samples throughout the record have CPI values >3, with a maximum of 8.6 at 40.42 m, and none of the data points are <1 (Figure 3.3b). The average CPI value is 2.9, and the record does not correlate with TOC (R^2 <0.1). The average value for TAR, P_{aq}, and ACL is 2, 0.7, and 27.3, respectively. The TAR and P_{aq} present an overall trend and fluctuations (Figure 3.3c-d) that are in slight anti-phase with each other (R^2 = 0.4). Although the TAR record appears to have a positive relationship with TOC, the correlation is not strong (R^2 <0.2). Similar to TAR, the

ACL record exhibits an overall decrease upsection, from a maximum of 29.4 at 225.41 m to a minimum of 25 at 39.36 m (Appendix III).

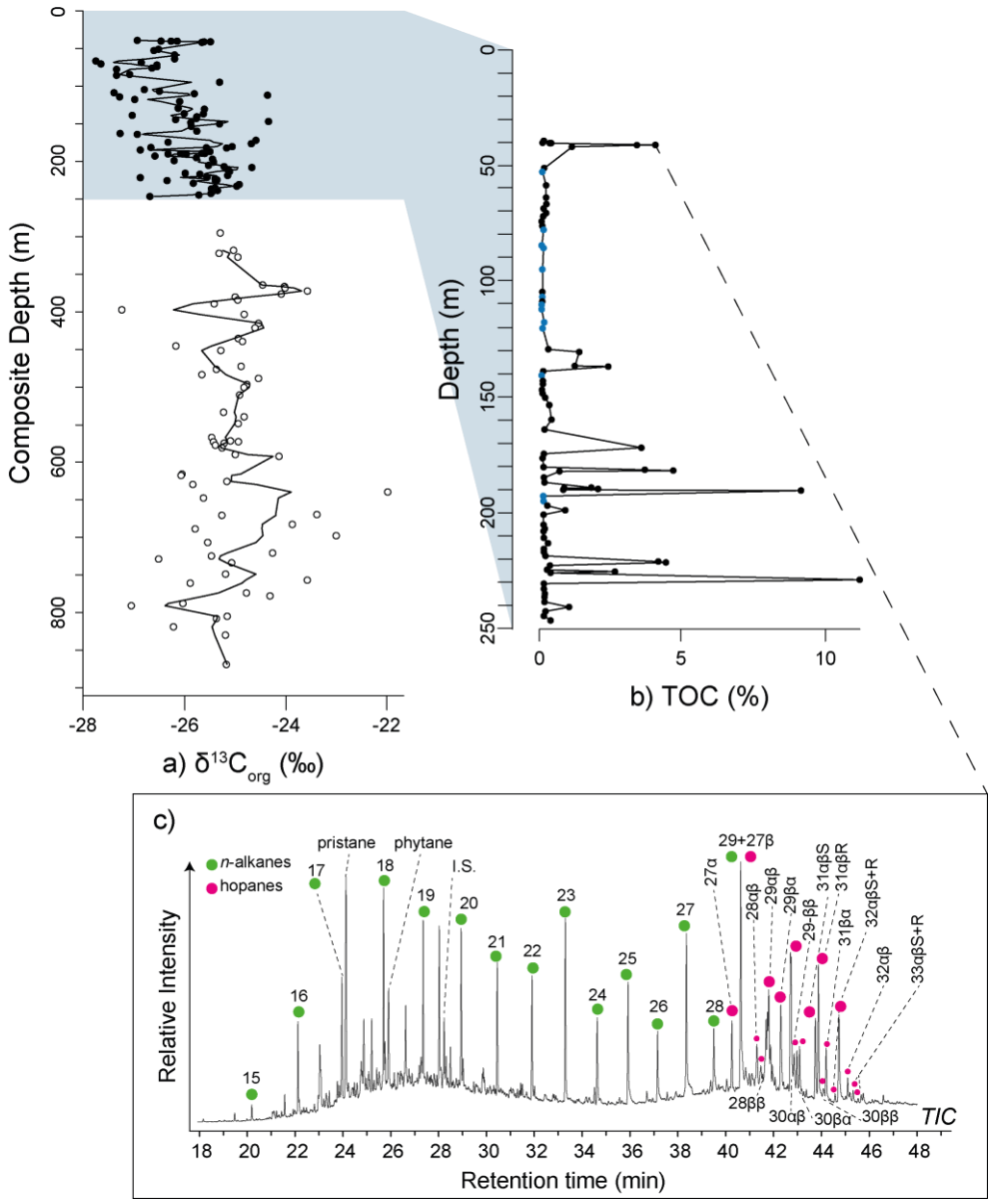

Figure 3.2 Bulk sediment (a) $\delta^{13}C$ of organic carbon ($\delta^{13}C_{org}$), and (b) total organic carbon (TOC) from Cerrejón Mine. The closed symbols are from this study and the open symbols are from Jaramillo *et al.* (2007). The solid line in panel (a) is a LOESS curve fitted with a span of 0.05, using R Package stats (R Core Team, 2021). The blue symbols within panel (b) are TOC measurements (n = 13) that fell under the calibration range. (c) an example chromatogram from a sample at 41.17 m, prior to urea adduction. The *n*-alkanes (green) and hopanes (pink) are highlighted on the total ion chromatogram (TIC). The numbers signify the carbon chain-length.

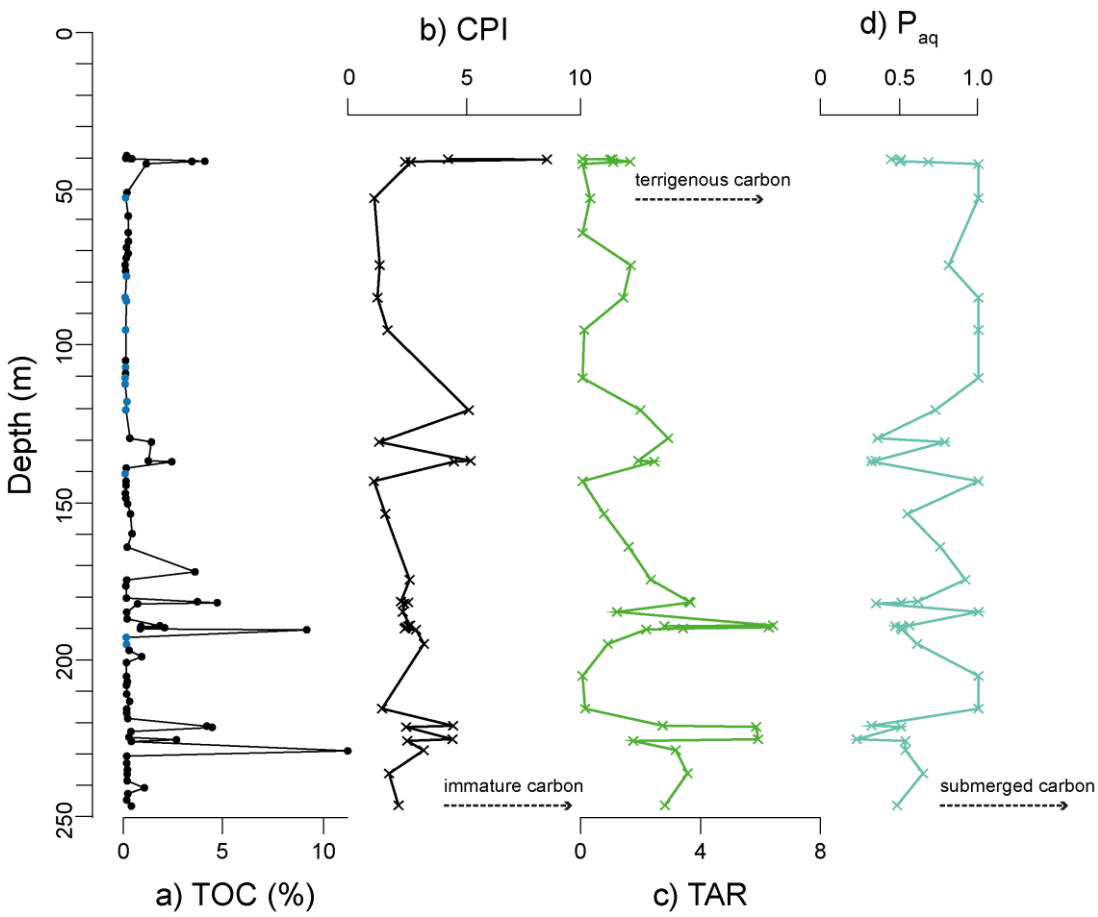

Figure 3.3 *n*-Alkane-based chain-length ratios from Cerrejón Mine. (a) bulk sediment total organic carbon (TOC), (b) carbon preference index (CPI), (c) terrigenous-aquatic ratio (TAR), and (d) P_{aq}. The blue symbols within panel (b) are TOC measurements that fell under the calibration range.

From the samples targeted for CSIA (n = 21), 19 and 16 apolar fractions had the required concentrations to obtain $\delta^{13}C_{wax}$ and $\delta^{2}H_{wax}$ values, respectively. The s.d. for the $\delta^{13}C_{wax}$ dataset were consistently <0.4 ‰, however the $\delta^{2}H_{wax}$ dataset contained s.d. that exceeded 6 ‰. Typically, the higher the number of replicates the lower the s.d. value (Polissar and D'Andrea, 2014). However, in this study, the s.d. for $\delta^{2}H_{wax}$ were likely skewed by the third run, due to there not being enough analytes. Therefore, only duplicate measurements were used for $\delta^{2}H_{wax}$, and any samples that still had s.d. higher than 10 ‰ were excluded.

Figure 3.4 presents the average $\delta^{13}C_{wax}$ and $\delta^{2}H_{wax}$ values for the odd numbered long- (C_{27-33}) and mid- (C_{21-25}) chain *n*-alkanes. The $\delta^{13}C_{wax}$ records are ^{13}C-depleted compared to the bulk $\delta^{13}C_{org}$ values (Figure 3.4a). The long-chain *n*-alkanes range from -29.8 ‰ to -34.6 ‰, whereas the mid-chain *n*-alkanes are ^{13}C-enriched relative to the long-chain *n*-alkanes (-26.3 ‰ and -30.3 ‰; Figure 3.4b) and exhibit values closer to the $\delta^{13}C_{org}$ record. In contrast, the range in $\delta^{2}H_{wax}$ values are very similar between the long- (from -114.3 and -175.6 ‰) and mid- (from -175.8 ‰ and -119.9 ‰) chain *n*-alkanes (Figure 3.4c). The long- and mid-chain *n*-alkanes do not correlate in both the $\delta^{13}C_{wax}$ and $\delta^{2}H_{wax}$ records (R^2 <0.1). However, there is a stronger correlation in the $\delta^{2}H_{wax}$ records below ~150 m.

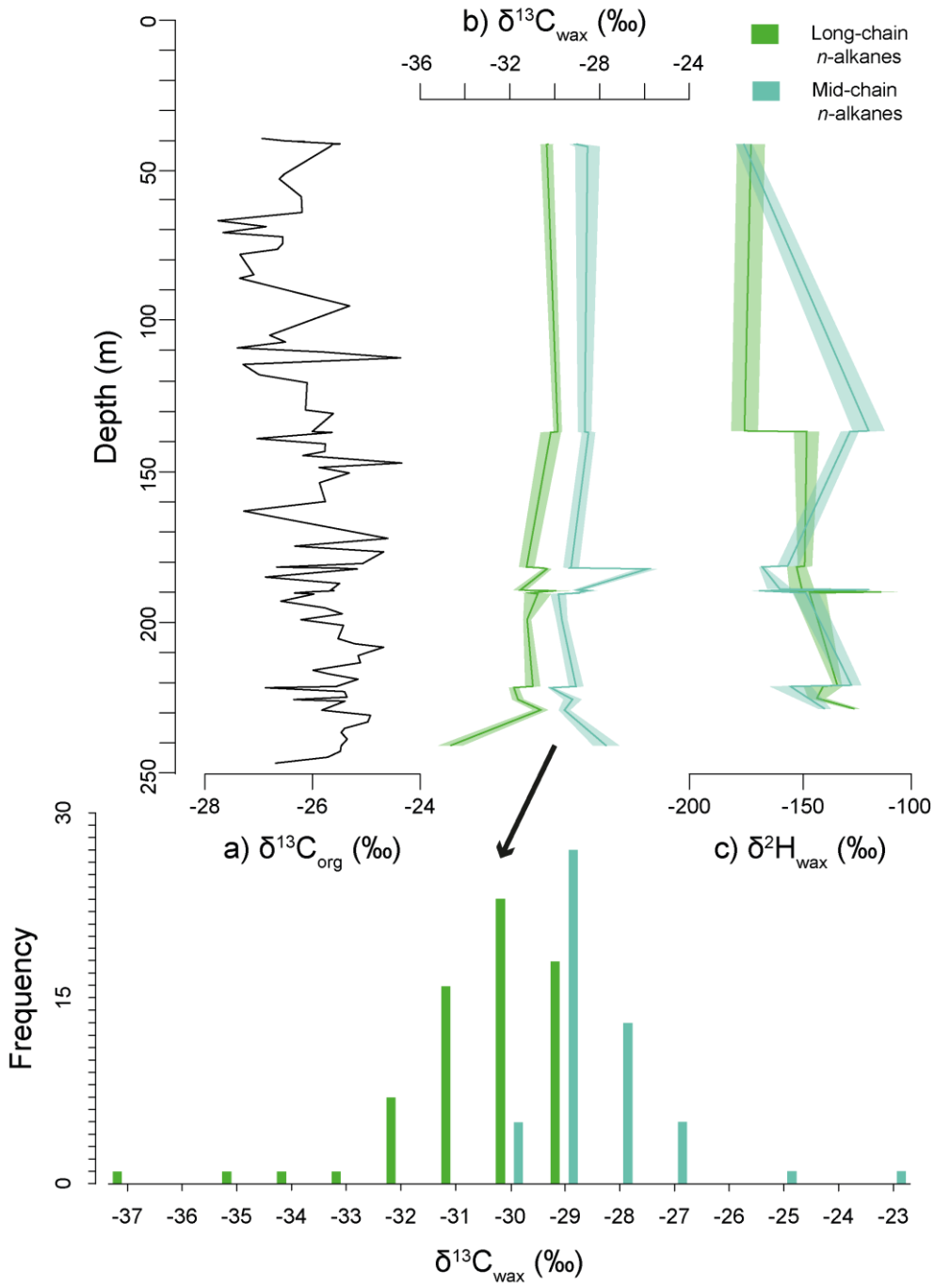

Figure 3.4 The CSIA of odd numbered long- (C_{27-33}) and mid- (C_{21-25}) chain *n*-alkanes from Cerrejón Mine. (a) bulk sediment $\delta^{13}C$ of organic carbon ($\delta^{13}C_{org}$), (b) average $\delta^{13}C$ of long- and mid-chain *n*-alkanes ($\delta^{13}C_{wax}$), and (c) average $\delta^{2}H$ of long- and mid-chain *n*-alkanes ($\delta^{2}H_{wax}$). The shading within panels (b) and (c) represents the error range, defined as 1 s.d. of the triplicate and duplicate measurements, respectively. Note that the resolution of the $\delta^{13}C_{wax}$ (n = 18) and $\delta^{2}H_{wax}$ (n = 14) are much lower than the $\delta^{13}C_{org}$ record. The insert bar chart shows the frequency (*i.e.* number of samples) distribution of $\delta^{13}C_{wax}$ values based on long- and mid-chain *n*-alkanes.

3.4 Discussion

3.4.1 Orbital Variability during the Latest Paleocene

Existing bulk geochemical proxy records (*e.g.,* $\delta^{13}C$ and $\delta^{18}O$) from the late Paleocene and early Eocene show cyclicity on orbital timescales (*e.g.,* Barnet *et al.*, 2019, 2020). These records suggest that the long (405-kyr) and short (100-kyr) eccentricity bands are the most dominant. Potential cyclicity was previously observed in the Cerrejón Formation, from changes in the abundance of major palynomorph groups (Jaramillo *et al.*, 2007). Spectral analysis was therefore attempted on the stratigraphical log. However, as the thickness of the deposits are within the same order-of-magnitude as stochastic processes, it may convolute with other climate forcings (Morón *et al.*, 2007). Interestingly, the high-resolution bulk $\delta^{13}C_{org}$ record of this study presents what appears to be regular alternations (Figure 3.4a). Identifying orbital variation could help place this study section in a more precise temporal position, but also aid in interpreting the $\delta^{2}H_{wax}$ record (*e.g.,* Walters *et al.*, 2023; Campbell *et al.*, 2024).

Here, we undertake spectral analyses on the new $\delta^{13}C_{org}$ record. The MTM power spectra exhibits two weak peaks around 10 m and 20 m (Figure 3.5). With continuous subsidence of the basin and no significant hiatuses, an assumed linear sedimentation rate (LSR) between the two available tie points narrows the age of this study section to ~57–56 Ma. The decline in the $\delta^{13}C_{org}$ record upsection, supports that this sedimentary sequence likely represents the latest Paleocene (*e.g.,* Westerhold *et al.*, 2020). According to this first-order age model, the two peaks in the MTM power spectra correspond to ~40 kyrs (*i.e.* obliquity) and ~80 kyrs. Obliquity only causes very small differences in seasonal insolation over the low-latitudes. As such, strong obliquity signals in the tropics have been attributed to high-latitude processes, for example the evolution of glaciers (see Bosmans *et al.*, 2015 and references therein). Yet, the latest Paleocene is thought to be ice-free, which may be why other records that span across the late Paleocene and early Eocene show very little or no power in the obliquity band (see Zeebe *et al.*, 2017 and references therein). Therefore, other mechanisms are required to explain the potential obliquity signal in the Cerrejón Formation (Figure 3.5), and we tentatively suggest that this is due to obliquity-induced changes in the tropical atmospheric circulation (*e.g.,* Bosmans *et al.*, 2015). However, we note that the spectral analysis is based on an age model with only two tie points and assumes a LSR. The latter does not consider the probable differences in accumulation rates between the distinct lithologies. Thus, future work to improve the age model is required to confirm orbital variability during the latest Paleocene.

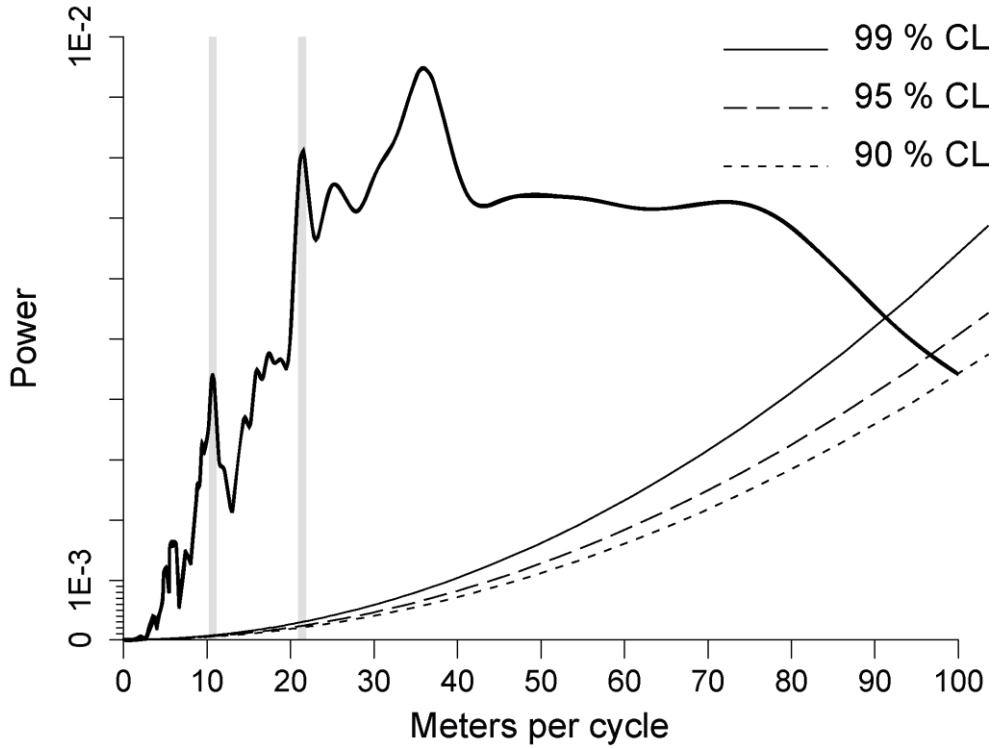

Figure 3.5 The MTM power spectrum for the $\delta^{13}C_{org}$ record in this study, in metres per cycle (m^{-1}). The grey bands mark two peaks around 10 m and 20 m. CL; confidence level.

3.4.2 Impact of Diagenesis and Vegetation Change upon the δ^2H_{wax} record

In order to identify potential biases in the δ^2H_{wax} record of this study, we utilise the chain-length distribution of *n*-alkanes to assess the impact of (i) diagenesis and (ii) vegetation change. The extent of post-depositional diagenesis is important to determine as the hydrogen atoms, although covalently bound to carbon, can exchange with the environmental water when burial temperatures exceed 100 °C (Sessions *et al.*, 2004; see Sessions, 2016 and references therein). The presence of hopanes with the αβ configuration suggests some early diagenesis (Peters, Walters and Moldowan, 2005), however average CPI values (2.9) are consistent with relatively unaltered organic matter (>3–30; Diefendorf and Freimuth, 2017). Thus, the long-chain *n*-alkanes from Cerrejón Mine have mostly retained their biological odd-over-even predominance, indicating that the δ^2H_{wax} values are not overly affected by diagenetic alterations. In contrast, the δ^2H_{wax} record from the other existing early Paleogene-aged tropical sedimentary sequence (Mar2X), exhibits much lower CPI values (<1.5; Jaramillo *et al.*, 2010). Therefore, the Mar2X record may be biased by post-depositional diagenesis.

The vegetation community also impacts the δ^2H_{wax} values. Organisms with different physiologies have varying degrees of discrimination against the heavier isotope (*i.e.* ^2H)

(*e.g.,* Chikaraishi and Naraoka, 2003; Gao *et al.*, 2014; Gamarra, Sachse and Kahmen, 2016). In fact, the lipid biosynthetic pathways alone can cause a ~70 ‰ difference in the δ^2H_{wax} values (Sachse *et al.*, 2012). The palynology of the Cerrejón Formation, reveals that there was an overall dominance of tropical plants that thrive in wet environments during the late Paleocene (Jaramillo *et al.*, 2007). The presence of certain species were associated with modern wetland areas behind mangroves, near the upper limit of tidal influences. Jaramillo *et al.* (2007) noted that there were no obvious long-term trends in the floral composition. However, the *n*-alkane-based chain-length ratios of this study exhibits a gradual change. Specifically, there is an overall shift towards shorter chain-lengths upsection, with a decrease in the TAR (Figure 3.3c) and ACL ratio (Appendix III), and an increase in P_{aq} values (Figure 3.3d). TAR discriminates between long- and short-chain *n*-alkanes, the latter assigned to microbes and/or algae (Nishimura and Baker, 1986; Meyers and Ishiwatari, 1993). Hence, a decline implies fewer higher plants and potentially enhanced aquatic primary productivity. In coastal settings, such as inferred for the Cerrejón Formation, the P_{aq} ratio can differentiate between submerged (>0.6) and emergent (~0.4–0.6) macrophytes (Mead *et al.*, 2005).

The $\delta^{13}C_{wax}$ record can also provide useful insight into vegetation types, and further confirm interpretations based on chain-length ratios. The long-chain *n*-alkanes all co-vary (R^2 >0.65), suggesting that they have a similar source (Figure 3.6). On the other hand, the lack of correlation between the $\delta^{13}C_{wax}$ values of the long- and shorter chain *n*-alkanes, also observed in moderns settings (*e.g.,* Diefendorf *et al.*, 2011; Inglis, Naafs, *et al.*, 2019), signifies that they likely derive from a different source (Figure 3.6). The mid-chain *n*-alkanes are consistently ~4 ‰ enriched, relative to the long-chain *n*-alkanes (Figure 3.4b). As submerged macrophytes use ^{13}C-enriched bicarbonate as their substrates (see Naafs *et al.*, 2019 and references therein), this may explain the distinct range in $\delta^{13}C_{wax}$ values of the mid-chain *n*-alkanes. This is also agrees with the greater presence of submerged plants as indicated by the high P_{aq} values. Thus, reconstructions of the hydrologic cycle should be limited to the δ^2H_{wax} of long-chain *n*-alkanes. However, the TAR (Figure 3.3c) and ACL (Appendix III) values also fluctuate dramatically. In addition, palynomorph abundances also highlight that the coal and non-coal samples have significantly different floral compositions in the Cerrejón Formation (Jaramillo *et al.*, 2007), for example there is a more homogenous assemblage in the coal seams. This is indicative of a tropical swamp, which requires niche morphospecies that are adapted to permanently waterlogged conditions (Jaramillo *et al.*, 2007). In contrast, there is a diverse range of fungi, palms, ferns, Moraceae, and Araceae in the non-coal samples. As such, the vegetation community, in particular with the changing depositional environments, must be considered for the δ^2H_{wax} record.

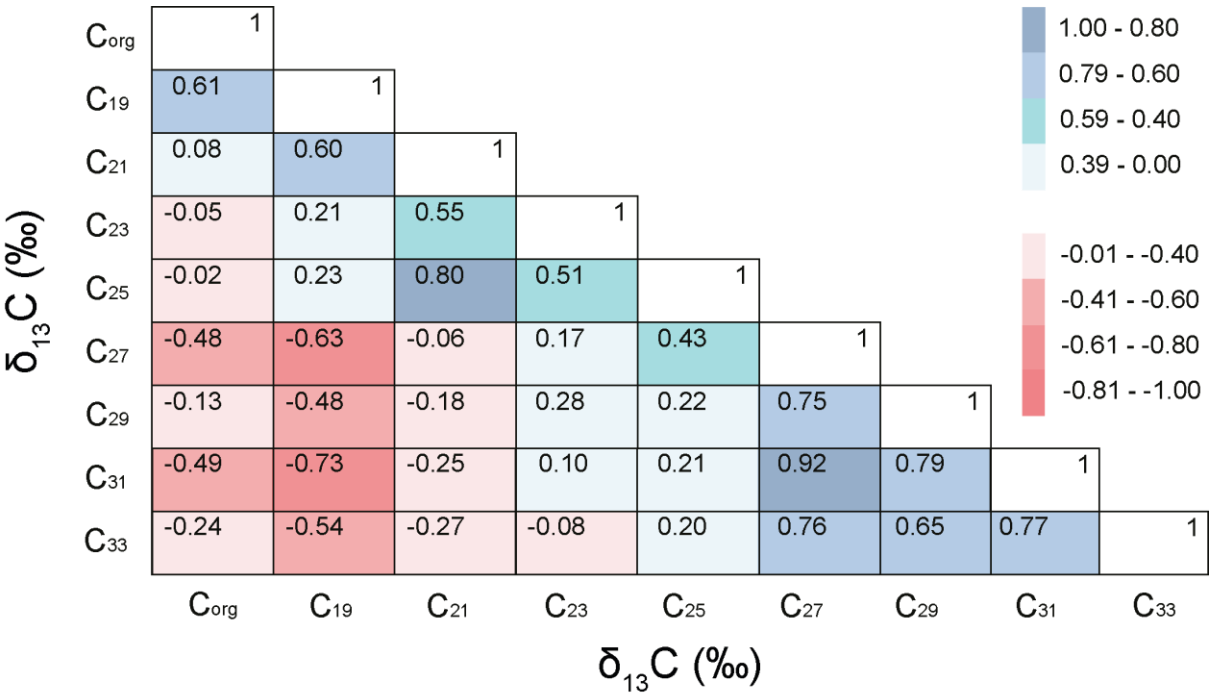

Figure 3.6 Correlation matrix between the $\delta^{13}C$ of odd numbered *n*-alkanes from C_{19} to C_{33}, and the LOESS curve of the bulk sediment $\delta^{13}C$ of organic carbon ($\delta^{13}C_{org}$).

3.4.3 The Hydrologic Cycle in the Tropics during the Latest Paleocene

To convert δ^2H_{wax} into δ^2H_{precip} requires defining the apparent isotopic fractionation ($\varepsilon_{wax/precip}$) value (see Sachse *et al.*, 2012 and references therein; Sessions, 2016). This varies both through space and time (*e.g.,* Bakkelund *et al.*, 2018; see Liu and An, 2019 and references therein), as a result of mostly leaf/soil water evaporation and lipid biosynthesis. However, in warm and humid conditions, ^2H-enrichment from transpiration is thought to be minimal (*e.g.,* Feakins *et al.*, 2016). A study on the size of leaf fossils collected across the Cerrejón Formation confirms high mean annual precipitation during the late Paleocene (3,240 mm; Wing *et al.*, 2009), suggesting that evaporation has a limited impact on δ^2H_{precip} values. However, the local vegetation community and its evolution must be accounted for (see Section 3.4.2).

Here, a net fractionation factor of -121 ‰ was assumed for first-order estimations of δ^2H_{precip}. This is based on the $\varepsilon_{wax/precip}$ value for C_{29} *n*-alkanes, acquired from the most up-to-date global dataset of modern systems (McFarlin *et al.*, 2019), and represents C3 plants as the C4 carbon fixation pathway did not evolve until the Miocene (*e.g.,* Edwards *et al.*, 2010). The value is consistent with past publications (*e.g.,* Sachse *et al.*, 2012), and also falls between fractionation factors that were previously used for the Eocene (~-110 ‰; Inglis, Carmichael, *et al.*, 2020; Elson *et al.*, 2022) and PETM (-130 ‰; Pagani, Pedentchouk, *et al.*, 2006; Handley, Crouch and Pancost, 2011; Handley *et al.*, 2012). For comparison with our compiled latest Paleocene δ^2H_{precip} data (Figure 3.7a), we applied the same fractionation

factor (-121 ‰) to the existing δ^2H_{wax} record from Mar2X (Jaramillo *et al.*, 2010). This site is just 50 km east of Cerrejón Mine, but encompasses the late Paleocene, PETM, and early Eocene (Figure 3.7b) (see Appendix IV for the trends in depth).

At the Cerrejón Mine, δ^2H_{precip} ranges between -13 ‰ to -52 ‰ (Figure 3.7a), with an average value of -23 ‰. This is very consistent with the average value from the late Paleocene at Mar2X (-22 ‰; Figure 3.7b). Although Mar 2X is only based on 3 data points, the similarities indicate that both records may be unaffected by post-depositional diagenesis (see Section 3.4.2). The late Paleocene δ^2H_{precip} values from the two sites are ^2H-enriched compared to the PETM (-42 ‰ to -58 ‰) and early Eocene (-47 ‰ to -54 ‰) intervals from Mar2X, signifying relatively more rainfall during the PETM and early Eocene (Figure 3.7b). However, the ranges of δ^2H_{precip} values are much greater during the late Paleocene, especially at Cerrejón Mine. An unstable hydrologic cycle has been previously proposed for the early-to-middle Eocene (*e.g.,* Inglis, Carmichael*, et al.*, 2020), with δ^2H_{precip} values varying dramatically (~80 ‰) over multi-million year timescales. However, there are currently no other studies that have reported a dynamic hydrologic cycle during the latest Paleocene.

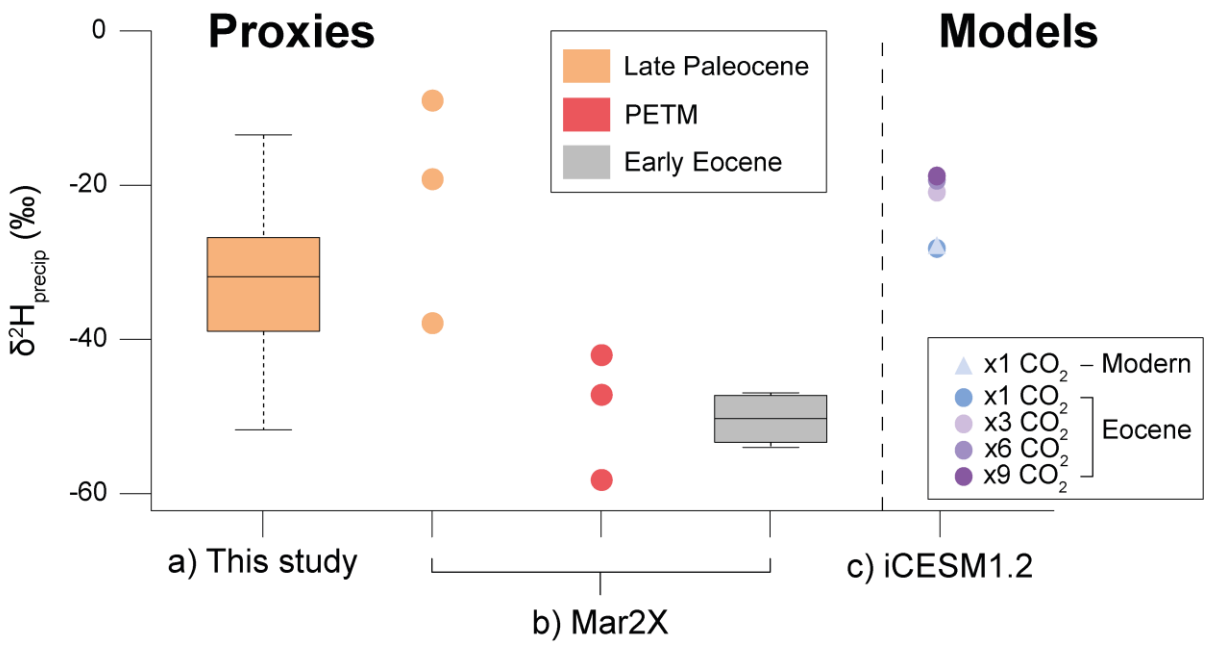

Figure 3.7 Proxy- and model-derived δ^2H of precipitation (δ^2H_{precip}) values in the tropics during the early Paleogene. The proxy-derived δ^2H_{precip} estimates from (a) Cerrejón Mine and (b) Mar2X, are inferred from C_{29} *n*-alkanes. Time intervals are as follows: late Paleocene (orange), Paleocene-Eocene Thermal Maximum (PETM) (pink), and early Eocene (grey). The solid line and box represents the median value and 25th to 75th percentiles, respectively. (c) model-derived δ^2H_{precip} estimates from iCESM1.2 (Zhu, Poulsen and Tierney, 2019; Zhu *et al.*, 2020), under atmospheric CO_2 concentrations of 1x the pre-industrial (PI) value in the modern simulation (triangle) and 1x 3x, 6x, and 9x the PI value in the Eocene simulation (circle).

To explore whether the ^{2}H-depletion during the PETM can be explained by changes in climate states, we compare our results to the model-derived data obtained from iCESM1.2. The simulations include a range of atmospheric CO_2 concentrations (1x, 3x, 6x, and 9x, the PI value; Zhu, Poulsen and Tierney, 2019; Zhu *et al*., 2020), under Eocene boundary conditions. Interestingly, at this site, the model-derived δ^2H_{precip} values become progressively more ^{2}H-enriched with higher atmospheric CO_2 concentrations (Figure 3.7c), implying enhanced aridity with greater atmospheric CO_2 levels. This is contradictory to the predicted wetter tropics with global warming (Lee *et al*., 2021). Moreover, plant fossil evidence (Jaramillo *et al*., 2007; Wing *et al*., 2009) and increasing P_{aq} values (Figure 3.3d) from Cerrejón Mine indicate a rising water table and/or waterlogged environment. Therefore, the more arid conditions inferred from iCESM1.2 is likely the result of the location of Cerrejón Mine, on the northern edge of the Intertropical Convergence Zone (ITCZ) (Figure 3.8). This highlights the sensitivity of δ^2H_{precip} to the precise positioning of the study site (*i.e.* the palaeogeography and rotation frame used) and ITCZ. The latter is crucial to constrain as the ITCZ migrates seasonally and studies have shown that it narrowed with the elevated temperatures of the PETM (Tierney *et al*., 2022; Cramwinckel *et al*., 2023). Furthermore, complex nonlinear responses of, for example, the South American monsoon are potentially not fully incorporated in the model (*e.g.,* Acosta *et al*., 2022).

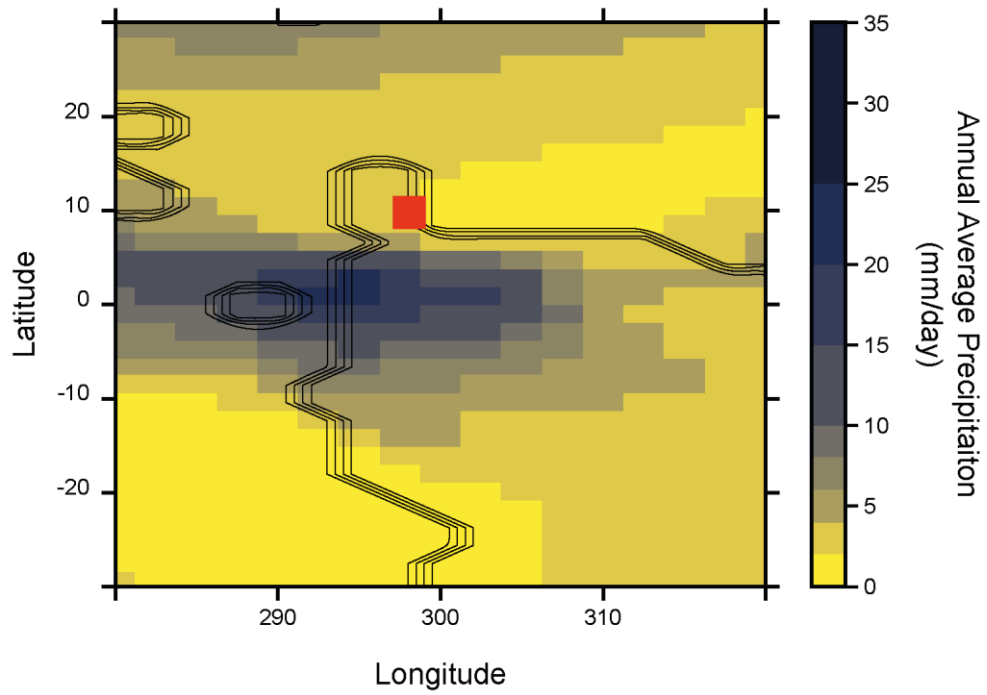

Figure 3.8 Annual average precipitation (mm/day) estimates from iCESM1.2 (Zhu, Poulsen and Tierney, 2019; Zhu *et al*., 2020), under atmospheric CO_2 concentrations of 6x the pre-industrial (PI) value in the Eocene simulation. The continent-ocean boundary (black solid line) and the grid cell (red rectangle) is displayed, with the upper left corner representing the closest grid corner to Cerrejón Mine.

Another discrepancy between the proxy- and model-derived data is that the 3x, 6x, and 9x CO_2 simulations exhibit a remarkably narrow range in δ^2H_{precip} values (-19 ‰ to -21 ‰; Figure 3.7c). The much larger and variable proxy-based results from the late Paleocene (-13 ‰ to -52 ‰; Figure 3.7a) may be due to shifts in the vegetation community (see Section 3.4.2). Further work on pollen-corrected δ^2H_{precip} estimations would help reduce this bias (Feakins, 2013). In addition, the timescales captured in the two approaches are likely causing the difference observed, with the model typically averaging the climate over a relatively short duration (~10^2–10^3 years; Zhu, Poulsen and Tierney, 2019; Zhu *et al.*, 2020). This may also explain why the δ^2H_{precip} value is more ^2H-enriched in the modern simulation (-28 ‰; Figure 3.7c) compared to the present-day annual average at the current location of Cerrejón Mine (-36 ± 4 ‰, with 95 % confidence; Bowen and Revenaugh, 2003; Bowen, 2024), with an assumed altitude of 0 m. The model additionally only represents a 'snapshot' of an equilibrium climate state, although studies have shown that fluctuations in the δ^2H_{wax} record could be driven by orbital variability (Walters *et al.*, 2023). However, the 1x CO_2 simulations under modern and Eocene boundary conditions produce similar δ^2H_{precip} values (Figure 3.7c). This suggests that the other non-CO_2 variables (*i.e.* palaeogeography, land-sea mask, vegetation distribution, PI non-CO_2 GHG concentrations, soil properties, aerosols, solar constant, and orbital parameters) have a minor impact on δ^2H_{precip}.

3.5 Conclusion

Overall, the new sedimentary sequence from Cerrejón Mine has provided an opportunity to evaluate the hydrological response of the tropics during warmer climates. First-order estimations of δ^2H_{precip} reveal a wide range of values that could indicate a more dynamic hydrologic cycle in the tropics during the latest Paleocene. Although this is consistent with the late Paleocene record from nearby Mar2X, the water isotope-enabled climate model simulations (iCESM1.2) present a contrasting narrow range in δ^2H_{precip} values. The issue may lie with unreliable proxy-based δ^2H_{precip} values due to the effects of vegetation change. To exclude this, further work to generate pollen-corrected δ^2H_{precip} estimations is required. However, the timescale and orbital periodicities captured by the model is also important to consider. In addition, the simulations with higher atmospheric CO_2 concentrations exhibit relatively more ^2H-enriched values. This highlights the sensitivity of δ^2H_{precip} to the location of the study site and ITCZ, or that monsoon systems may be poorly represented in iCESM1.2.

Chapter 4 Spatial and Temporal Patterns in Petrogenic Organic Carbon Mobilisation during the Paleocene-Eocene Thermal Maximum

Abstract

The Paleocene-Eocene Thermal Maximum (PETM) was a transient global warming event and is recognised in the geologic record by a prolonged negative carbon isotope excursion (CIE). The onset of the CIE was due to a rapid influx of ^{13}C-depleted carbon into the ocean-atmosphere system. However, the mechanisms required to sustain the negative CIE remains unclear. Enhanced mobilisation and oxidation of petrogenic organic carbon (OC_{petro}) has been invoked to explain elevated atmospheric carbon dioxide concentrations during the body of the CIE. However, existing evidence is limited to three sites from the mid-latitudes and subtropics. Here, we determine whether: (i) enhanced mobilisation and subsequent burial of OC_{petro} in marine sediments was a global phenomenon; and (ii) whether it occurred throughout the PETM. To achieve this, we utilise a lipid biomarker approach to trace and quantify OC_{petro} burial in a global compilation of PETM-aged shallow marine sites (n = 7, including five new sites). Our results confirm that OC_{petro} mass accumulation rates (MARs) increased within the subtropics and mid-latitudes during the PETM, consistent with evidence of higher physical erosion rates and intense episodic rainfall events. High-latitude sites do not exhibit drastic changes in the source of organic carbon during the PETM and OC_{petro} MARs increase slightly or remain constant, perhaps due a more stable hydrological regime. Crucially, we also demonstrate that OC_{petro} MARs remained elevated during the recovery phase of the PETM. Although OC_{petro} oxidation was likely an important positive feedback mechanism throughout the PETM, we show that this feedback was both spatially and temporally variable.

Chapter 4 published in *Paleoceanography and Paleoclimatology*. **Hollingsworth, E.H.**, Elling, F.J., Badger, M.P.S., Pancost, R.D., Dickson, A.J., Rees-Owen, R.L., Papadomanolaki, N.M., Pearson, A., Sluijs, A., Freeman, K.H., Baczynski, A.A., Foster, G.L., Whiteside, J.H., and Inglis, G.N. 2024. Spatial and Temporal Patterns in Petrogenic Organic Carbon Mobilization During the Paleocene-Eocene Thermal Maximum. 39(2). https://doi.org/10.1029/2023PA004773. EHH wrote the original draft and all co-authors contributed to reviewing and editing. EHH, FJE, MPSB, AJD, RLR-O, NMP, and GNI carried out organic geochemical analyses.

4.1 Introduction

Climate and tectonics have modulated the flux of carbon to and from terrestrial reservoirs over geological timescales. Early studies predominantly focused on understanding the role of inorganic carbon, for example, carbon dioxide (CO_2) released from solid Earth degassing vs. CO_2 drawdown from silicate weathering (*e.g.,* Walker, Hays and Kasting, 1981; Berner, Lasaga and Garrels, 1983; Berner and Caldeira, 1997). However, the past two decades have highlighted the importance of the terrestrial organic carbon cycle as a climate feedback mechanism (Hilton and West, 2020). Whether it acts as a positive or negative feedback mechanism largely depends on whether the organic carbon (OC) is 'biospheric' (OC_{bio}), representing relatively recent thermally immature organic carbon (10^2–10^4 years old; *e.g.,* vegetation and soils), or 'petrogenic' (OC_{petro}), representing ancient rock-derived and thermally mature organic carbon (>10^6 years old; *e.g.,* organic carbon-rich shales). Erosion, mobilisation, and the subsequent burial of OC_{bio} in marine sediments helps to sequester CO_2 (Stallard, 1998; Berhe *et al.*, 2007). In contrast, exhumation and oxidation of OC_{petro} during lateral transport from land-to-sea can release CO_2 (Petsch, Berner and Eglinton, 2000). In modern settings, up to ~90 % of OC_{petro} is oxidised in large catchments such as the Amazon and Himalayan range (*e.g.,* Galy *et al.*, 2008; Bouchez *et al.*, 2010), whereas a lower proportion (~10–40 %) of OC_{petro} is oxidised in mountain basins with steep rivers (*e.g.,* Hilton *et al.*, 2011, 2014). Crucially, regardless of individual catchment dynamics, OC_{petro} has the potential to oxidise and increase atmospheric CO_2 concentrations.

Several studies have quantified the mobilisation and burial of OC_{petro} in modern systems (*e.g.,* Blair *et al.*, 2003; Galy *et al.*, 2007; Hilton *et al.*, 2010, 2011; Smith *et al.*, 2013; see Galy, Peucker-Ehrenbrink and Eglinton, 2015 and references therein; Clark *et al.*, 2017, 2022; see Hilton and West, 2020 and references therein; see Eglinton *et al.*, 2021 and references therein) and Quaternary sediments (*e.g.,* Kao *et al.*, 2008, 2014; Hilton *et al.*, 2015; Hefter, Naafs and Zhang, 2017). These studies show that erosion and transport of OC_{petro} is largely controlled by a combination of geomorphic and climatic processes (*e.g.,* Hilton, 2017; Eglinton *et al.*, 2021). For example, extreme rainfall events can trigger bedrock landslides (*e.g.,* Hilton, Galy and Hovius, 2008) and/or create deeply incised gullies (*e.g.,* Leithold, Blair and Perkey, 2006), both of which can expose OC_{petro} to oxidation. However, clastic sediments from hyperpycnal flows and turbidites can act to enhance the preservation of OC_{petro} (*e.g.,* Hilton *et al.*, 2011; Bouchez *et al.*, 2014). As climate models indicate an intensification of the hydrologic cycle in response to rising atmospheric CO_2 levels and global temperatures (Lee *et al.*, 2021), the delivery of OC_{petro} to the oceans will likely be enhanced in the future. However, such predictions are based on present-day observations and/or past climate states that span lower-than-modern atmospheric CO_2 concentrations (*e.g.,* Kao *et al.*, 2008; Hilton and West, 2020).

The geologic record enables investigations into high CO_2 states of the past, providing unique insights into how terrestrial carbon cycle processes may operate in the future. Many studies have focused on the Paleocene-Eocene Thermal Maximum (PETM; ~56 Ma) (McInerney and Wing, 2011), a transient carbon cycle perturbation characterised by global warming (~4–6 °C; Inglis, Bragg*, et al.*, 2020; Tierney *et al.*, 2022) and an intensified hydrologic cycle (see Carmichael *et al.*, 2017 and references therein). The PETM is identified in the geologic record by a negative carbon isotope excursion (CIE) (−4 ± 0.4 ‰; Elling *et al.*, 2019). The onset of the PETM is on the order-of-millennia (Zeebe *et al.*, 2014; Kirtland Turner, 2018) and is followed by sustained low and stable carbon isotopic composition ($\delta^{13}C$) values for ~94–170 thousand years (kyrs) (Zeebe and Lourens, 2019), referred to as the 'body' of the CIE (Bowen *et al.*, 2006). The body is then followed by a long recovery of ~50–120 kyrs (Zeebe, Zachos and Dickens, 2009; Murphy, Farley and Zachos, 2010; Bowen, 2013), which is further divided into Phase I (initial rapid rise in $\delta^{13}C$) and Phase II (final gradual rise in $\delta^{13}C$) (Röhl *et al.*, 2007).

The onset of the CIE was the result of a rapid influx of ^{13}C-depleted carbon from one or more reservoirs outside the active global exogenic carbon pool (Dickens, Castillo and Walker, 1997). Proposed reservoirs include submarine methane hydrates (Dickens *et al.*, 1995; Dickens, 2011), terrestrial organic carbon (Kurtz *et al.*, 2003; Deconto *et al.*, 2012; Bowen, 2013), and volcanic carbon related to the North Atlantic Igneous Province (Svensen *et al.*, 2004; Storey, Duncan and Swisher, 2007; Gutjahr *et al.*, 2017; M. T. Jones *et al.*, 2019). Less explored are the mechanisms responsible for the prolonged body of the CIE. This feature requires continual input of ^{13}C-depleted carbon (*e.g.,* Zeebe, Zachos and Dickens, 2009), thus several feedback mechanisms (either acting individually or in combination) have been proposed. This includes a slow dissociation of oceanic methane hydrates (Zeebe, 2013), pulsed releases of thermogenic methane from vent complexes (*e.g.,* Frieling *et al.*, 2016; Kirtland Turner, 2018), and/or 'leaky' terrestrial organic carbon reservoirs (Bowen, 2013). Alternatively, recent work suggests that CO_2 released from OC_{petro} oxidation could explain the extended body of the CIE (Lyons *et al.*, 2019). This theory is based on evidence of an order-of-magnitude increase in the delivery of OC_{petro} to the oceans, ~10–20 kyrs after the onset of the PETM. However, this study was limited to the mid-latitudes (Atlantic Coastal Plain) and subtropics (Tanzania) (see Section 1.4.5), and therefore may not be globally representative. It is also unclear whether enhanced mobilisation of OC_{petro} was a persistent feature throughout the PETM or restricted to the body interval.

Here, we use lipid biomarker thermal maturity ratios to fingerprint OC_{petro} burial in a global compilation of PETM-aged shallow marine sites (n = 7, including five new sites). Lipid biomarkers undergo various structural alterations with increasing thermal maturity (*e.g.,* defunctionalisation, isomerisation, catagenesis, and aromatisation; Peters, Walters and Moldowan, 2005), and thus can be used to assess the proportion of OC_{petro} in marine

sediments (Lyons *et al.*, 2019). We focus on thermally immature shallow marine sediments as they are 'hotspots' for terrestrial organic carbon input (Bianchi *et al.*, 2018). We quantify OC_{petro} burial fluxes before and during the PETM, using a two-endmember mixing model. Overall, we aim to determine whether: (i) enhanced mobilisation and subsequent burial of OC_{petro} in the ocean was a global phenomenon; and (ii) whether it occurred throughout the PETM.

4.2 Methods

4.2.1 Data Compilation

New *n*-alkane- and hopane-based thermal maturity ratios were acquired from the following PETM-aged shallow marine sites: the International Ocean Drilling Program Expedition 302 Site M0004A (or the Arctic Coring Expedition; 'ACEX'), the Ocean Drilling Program Site 1172 Hole D ('ODP Site 1172'), 'Kheu River', ODP Leg 174AX Ancora Site Hole A/B ('Ancora'), and the Tanzania Drilling Project Site 14 Hole A ('TDP Site 14') (Figure 4.1). Additional information (*e.g.,* palaeodepth) and a brief description of the lithology for each site can be found within Appendix V and Appendix VI, respectively. We also compile *n*-alkane- and hopane-based thermal maturity ratios from the following published PETM-aged shallow marine sites: TDP Site 14 (Handley *et al.*, 2012; Carmichael *et al.*, 2017), South Dover Bridge ('SDB') (Lyons *et al.*, 2019), and Cambridge-Dorchester Airport ('CamDor') (Lyons *et al.*, 2019) (Figure 4.1). Other published biomarker records are available for PETM-aged shallow marine sites, however these sequences are dominated by autochthonous OC_{petro} and show evidence for post-depositional diagenesis (Handley, Crouch and Pancost, 2011; Cui *et al.*, 2021).

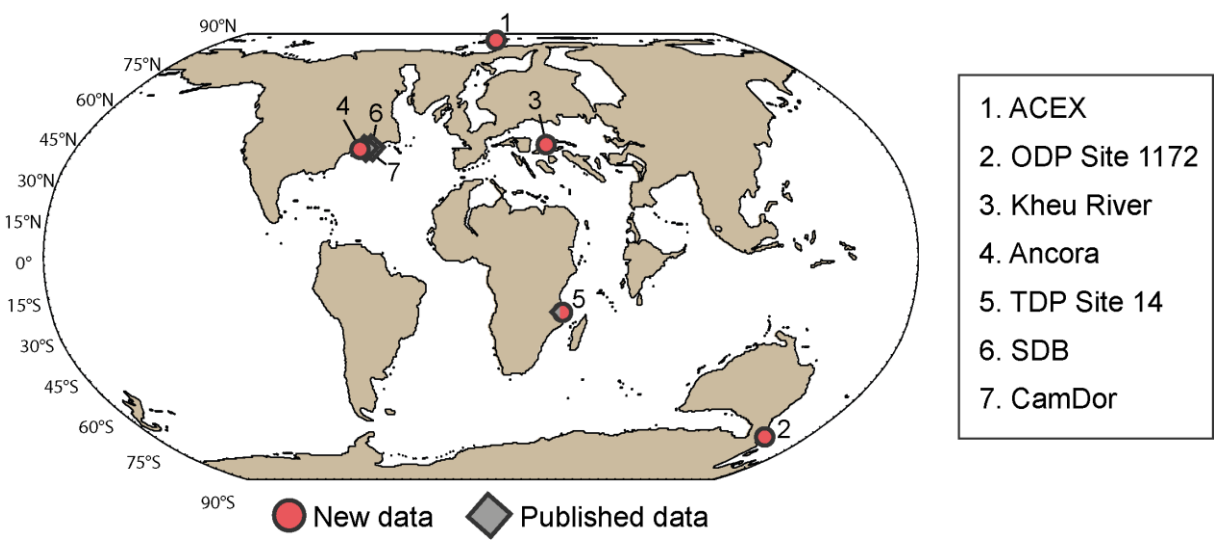

Figure 4.1 Location of sites with new data (1–5) and published data (5–7). Palaeogeographic reconstructions of 56 Ma, adapted from Carmichael *et al.* (2017).

4.2.2 Organic Geochemistry

For this study, samples from ACEX (*n* = 94), ODP Site 1172 (*n* = 41), and Ancora (*n* = 42) were freeze dried, homogenised, and extracted using a MARS5 microwave-assisted extraction system, with: (i) dichloromethane:methanol (DCM:MeOH; 1:1, *v:v*), (ii) DCM:MeOH (9:1, *v:v*), and (iii) DCM, at Harvard University (Elling *et al*., 2019). Each solvent mixture was heated for 30 min to 100 °C, followed by a hold time of 20 min. The extracts from the three steps were combined into a total lipid extract (TLE) and further divided into five fractions (following Polik, Elling and Pearson, 2018). At the University of Southampton, extracted copper was added to the apolar fractions for 24 hr to remove elemental sulphur (see Section 2.3.3). The apolar fractions were then redissolved in hexane (Hex) and the organic-rich samples were first analysed using gas chromatography with a flame ionisation detector (GC-FID; see Section 2.4.2) to assess concentrations. Following this, all the samples were analysed using a GC coupled to a mass spectrometer (GC-MS; see Section 2.4.2). Compound identification was based on retention times, fragmentation patterns, and comparison to an in-house standard.

Kheu River samples (*n* = 39) were extracted at the University of Bristol by ultrasonicating homogenised samples sequentially with DCM, DCM:MeOH (1:1, *v:v*), and MeOH. Elemental sulphur was removed from the combined TLE using activated copper turnings. An activated silica column with saturated ammonia in chloroform and chloroform:acetic acid (100:1, *v:v*) was used to separate the neutral and acid fraction, respectively. The apolar fraction was split from the neutral fraction by elution with Hex:DCM (9:1, *v:v*) and separation on an alumina column. The apolar fractions were then analysed at the University of Bristol on a Thermoquest Finnigan Trace GC interfaced with a Thermoquest Finnigan Trace MS. The GC was fitted with a fused capillary column (50 m × 0.32 mm i.d.) and the carrier gas was helium. The samples were suspended in ethyl acetate (EtAc) and injected at 70 °C. The temperature program increased to 130 °C (20 °C min^{-1}), then 300 °C (4 °C min^{-1}), and finally remained isothermal for 20 min. The MS operated with an electron ionisation source at 70 eV, scanning over *m/z* ranges of 50–850 Da. The compounds were integrated on the total ion chromatogram (TIC).

Additional samples (*n* = 12) from TDP Site 14 were homogenised and extracted at the University of Bristol. Extractions were achieved via Soxhlet apparatus overnight, using DCM:MeOH (2:1, *v:v*). The TLE was suspended in Hex:DCM (9:1, *v:v*) and separated by alumina column chromatography. Co-eluting compounds and/or unresolved complex mixtures were reduced with urea adduction (following Pancost *et al.*, 2008). Elemental sulphur was removed using extracted copper turnings. The apolar fractions were analysed at the University of Bristol on the same GC-MS as used for Kheu River. The GC was fitted with a CPsil-5CB column (Agilent Technologies, dimethylpolysiloxane stationary phase) and the

carrier gas was helium. The samples were injected in EtAc at 70 °C. The temperature program increased to 130 °C (20 °C min^{-1}), then 300 °C (4 °C min^{-1}), and finally held for 25 min. The MS operated with an electron ionisation source at 70 eV, scanning over *m/z* ranges of 50–850 Da. The compounds were integrated on the TIC or using the appropriate mass fragment (*e.g., m/z* 191).

4.2.3 A Lipid Biomarker Approach

This study utilises several *n*-alkane and hopane-based thermal maturity ratios (see Section 1.4.3). In summary, long-chain *n*-alkanes progressively lose their odd-over-even preference during diagenesis (Eglinton and Hamilton, 1967). This is captured by the carbon preference index (CPI) (Bray and Evans, 1961). As sites with extensive post-depositional diagenesis were excluded, values closer to 1 likely suggest input of thermally mature allochthonous organic matter (*e.g.,* OC_{petro}). The hopane-based thermal maturity ratios include $C_{29\text{-}31}$ αβ/(αβ + ββ), $C_{29\text{-}30}$ βα/(βα + αβ), C_{29} αβ/C_{30} αβ, $C_{31\text{-}35}$ S/(S + R), and $T_s/(T_s + T_m)$ (see Section 1.4.3.2). We use a multi-ratio approach as each ratio corresponds to different stages of maturity from early diagenesis towards the generation of oil, thus enabling insight on the degree of thermal maturation. Higher values indicate greater thermal maturity, with the exception of βα/(βα + αβ). However, hopane distributions also vary depending on the lithofacies and/or depositional environment (Peters, Walters and Moldowan, 2005). Therefore, without knowledge of the source rocks at each locality, comparison between the sites should be undertaken with caution.

4.2.4 Two-Endmember Mixing Model

The fraction of OC_{petro} (f_{petro}) was calculated for each hopane-based thermal maturity ratio (X_{mix}; Table 4.1), following the two-endmember mixing model from Lyons *et al*. (2019):

$$X_{mix} = f_{petro} \times X_{petro} + \left(1 - f_{petro}\right) \times X_{background} \qquad \text{(Equation 4.1)}$$

where $X_{background}$ and X_{petro} is the defined immature and mature endmembers, respectively. The endmembers for $C_{31\text{-}35}$ S/(S + R) ratio follow the definitions in Lyons *et al*. (2019), where $X_{background}$ is the contemporaneous carbon value of 0 and X_{petro} is the most thermally mature value of 0.6. The endmembers for $C_{29\text{-}30}$ βα/(βα + αβ) ratio also follow the definitions in Lyons *et al*. (2019), where $X_{background}$ is 1 and X_{petro} is 0. For this study, the endmembers of the αβ/(αβ + ββ) ratio was defined as 0 for $X_{background}$ and 1 for X_{petro}. Note that C_{29} αβ/C_{30} αβ and $T_s/(T_s + T_m)$ ratios were excluded due to their strong dependence on the source rock and/or depositional environment (Peters, Walters and Moldowan, 2005).

Table 4.1 Variables used to calculate f_{petro}.

Site	X_{mix}	LSR (cm kyr^{-1})				Organic carbon content (%) References
		Pre-PETM	Core PETM	Recovery PETM		
				Phase I	Phase II	
ACEX[a]	C_{30-31} αβ/(αβ + ββ) C_{31} S/(S + R) C_{30} βα/(βα + αβ)	1	Min: 3.8 Max: 6.2			TOC Elling *et al.* (2019)
ODP Site 1172[b]	C_{30-31} αβ/(αβ + ββ) C_{31} S/(S + R) C_{30} βα/(βα + αβ)	0.57	Min: 0.4 Max: 0.5	Not available		C_{org} Papadomanol-aki, Sluijs and Slomp (2022)
Kheu River[c]	C_{29-31} αβ/(αβ + ββ) C_{29-30} βα/(βα + αβ)	0.3	1.9			C_{org} Dickson *et al.* (2014)
Ancora[d]	C_{30-31} αβ/(αβ + ββ) C_{31} S/(S + R) C_{30} βα/(βα + αβ)	0.8	11.2 and 4.3	1.3	8.4	TOC Elling *et al.* (2019)
TDP Site 14[e]	C_{29-31} αβ/(αβ + ββ) C_{31-35} S/(S + R) C_{29-30} βα/(βα + αβ)	Min: 0.5 Max: 2	Min: 3.5 Max: 14	NA		C_{org} Aze *et al.* (2014)
SDB[f]	C_{31} S/(S + R) C_{29} βα/(βα + αβ)*	Min: 1.03 Max: 2.4	14	21.3	21.3	TOC Lyons *et al.* (2019)
CamDor[f]	C_{29} βα/(βα + αβ)* C_{31-32} S/(S + R)*	Min: 1.03 Max: 2.4	14			TOC Lyons *et al.* (2019)

Note. a-f References for LSR. *f_{petro} calculated in Lyons *et al*. (2019).
[a]Sluijs, *Röhl, et al*. (2008). [b]Sluijs *et al.* (2011). [c]John *et al.* (2008). [d]Stassen, Thomas and Speijer (2012). [e]Lyons *et al*. (2019). [f]Doubrawa *et al.* (2022).

4.2.5 Mass Accumulation Rates

The mass accumulation rate (MAR; in gC cm^{-2} kyr^{-1}) of OC_{petro} was calculated for all the new and published f_{petro} data, following Lyons *et al*. (2019):

$$MAR = LSR \times \rho \times f_{petro} \times \frac{TOC}{100} \quad \text{(Equation 4.2)}$$

where LSR is the linear sedimentation rate (cm kyr^{-1}), ρ is the dry bulk density (g cm^{-3}), and TOC is the total organic carbon (TOC) or C_{org} (%) (Table 4.1). As published bulk density values are only available for one site (ODP Site 1172), a constant ρ value of 1.8 g cm^{-3} was assumed across all the sites (following Dunkley Jones *et al*., 2018). However, we acknowledge that changes in dry bulk density may influence absolute MARs, especially in sites with major lithological changes (Appendix VI). The TOC values and LSR were acquired for each location from the published studies (Table 4.1). C_{org} records from ODP Site 1172 (Papadomanolaki, Sluijs and Slomp, 2022) and TDP Site 14 (Aze *et al.*, 2014) were linearly

interpolated to match the depths of the biomarker data, using R Package Astrochron (Meyers, 2014). LSR estimates were obtained (where possible) for three key time intervals: (i) pre-PETM (Paleocene), (ii) the 'core' (onset and body of the CIE) of the PETM, (iii) and the recovery of the PETM (Appendix VI). This was available for all the sites with the exception of ODP Site 1172, which lacks the recovery interval. Note that the recovery at Ancora and SDB were further divided into: (iiia) Phase I, and (iiib) Phase II. Kheu River does not have LSR data, thus estimates were taken from the nearby Aktumsuk section (Uzbekistan; John *et al.*, 2008). Both Kheu River and Aktumsuk comprise of shallow marine deposits that exhibits TOC values from ~0.1 % pre-PETM to a maximum of ~8.5 % during the PETM (Bolle *et al.*, 2000; Dickson *et al.*, 2014). Similarly, LSRs from within the core interval of SDB was assumed to be the same for the entire PETM section at CamDor (following Lyons *et al.*, 2019).

4.3 Results

4.3.1 Thermal Maturity Ratios

4.3.1.1 ACEX

The apolar fraction contains short- (C_{15-19}), mid- (C_{21-25}), and long- (C_{27-33}) chain *n*-alkanes, and C_{27} to C_{32} hopanes (including αβ, βα, and ββ isomers). Both the CPI (ranging from ~1 to 3; Figure 4.2b) and hopane-based thermal maturity ratios exhibit relatively stable trends throughout the sequence, suggesting that the organic carbon source did not distinctly change. Note that potential information may be missing due poor core recovery between ~388 and 384.5 mcd (Sluijs *et al.*, 2006). However, C_{30} αβ/(αβ + ββ) (Figure 4.2c), C_{31} S/(S + R) (Figure 4.2d), and $T_s/(T_s + T_m)$ (Figure 4.2f) values slightly increase (*i.e.* higher thermal maturity) between pre-PETM and the core of the PETM, by an average of 0.01, 0.01, and 0.08, respectively. These indices then decline during the recovery interval. C_{31} αβ/(αβ + ββ) and C_{30} βα/(βα + αβ) ratios (Figure 4.2c) exhibit the opposite trend, with lower thermal maturity during the core interval and the C_{30} βα/(βα + αβ) ratio (Figure 4.2e) continuing to decline into the recovery of the PETM.

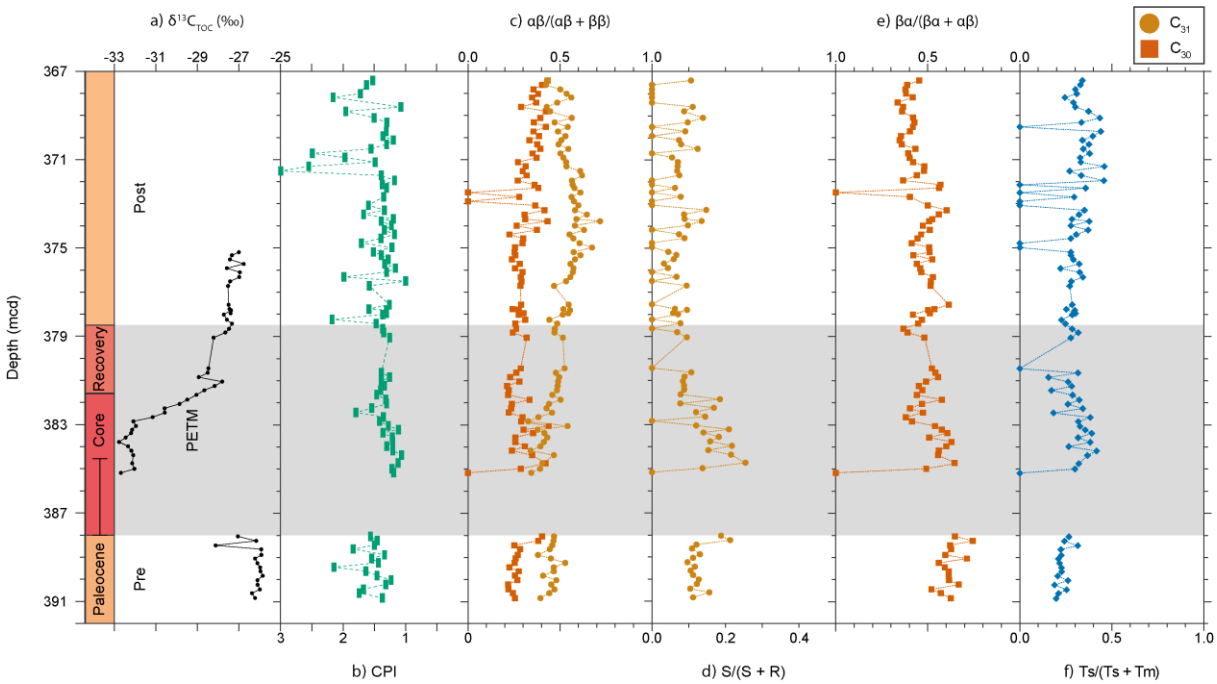

Figure 4.2 Thermal maturity ratios at ACEX. Note some of the axis (CPI and βα/(βα + αβ)) are reversed to reflect increasing thermal maturity toward the right. (a) bulk sediment $\delta^{13}C$ of total organic carbon ($\delta^{13}C_{TOC}$) (Elling *et al.*, 2019), (b) CPI (this study), (c) αβ/(αβ + ββ) ratios (this study), (d) S/(S + R) ratio (this study), (e) βα/(βα + αβ) ratio (this study), and (f) Ts/(Ts + Tm) ratio (this study). The PETM interval (including the core and recovery) is highlighted by grey shading, and a core gap is present from ~388 to 384.5 mcd (Sluijs *et al.*, 2006).

4.3.1.2 ODP Site 1172

The apolar fraction contains C_{16-34} *n*-alkanes and the CPI has a mean value of 2.8. Samples with CPI >3 (*i.e.* relatively low thermal maturity), are mostly constrained to the pre-PETM interval (Figure 4.3b). Hopanes range from C_{27} to C_{32} (including αβ, βα, and ββ isomers), and the thermal maturity ratios exhibit a relatively stable trend throughout the sequence. However, the C_{31} S/(S + R) ratio slightly increases by 0.09 during the core interval and into the recovery of the PETM (Figure 4.3d), suggesting potential input of thermally mature organic carbon. C_{30} αβ/(αβ + ββ) (Figure 4.3c), C_{31} αβ/(αβ + ββ) (Figure 4.3c), and C_{30} βα/(βα + αβ) (Figure 4.3e) values exhibit the opposite behaviour, shifting toward relatively thermally immature values during the core of the PETM, by an average of 0.19, 0.22, and 0.07, respectively. During the recovery, C_{30} αβ/(αβ + ββ) (Figure 4.3c), C_{31} αβ/(αβ + ββ) (Figure 4.3c), and C_{30} βα/(βα + αβ) (Figure 4.3e) ratios return to relatively more thermally mature values.

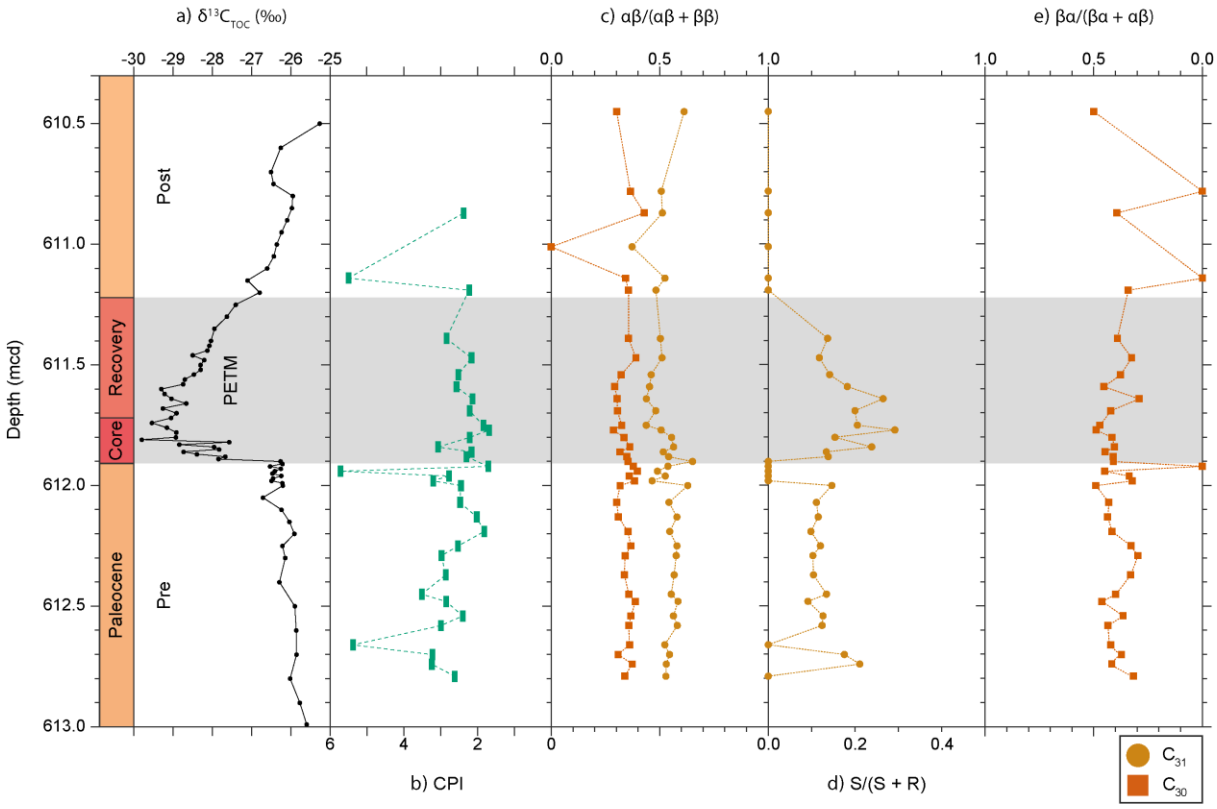

Figure 4.3 Thermal maturity ratios at ODP Site 1172. Note some of the axis (CPI and βα/(βα + αβ)) are reversed to reflect increasing thermal maturity toward the right. (a) bulk sediment $\delta^{13}C$ of total organic carbon ($\delta^{13}C_{TOC}$) (Sluijs *et al.*, 2011), (b) CPI (this study), (c) αβ/(αβ + ββ) ratios (this study), (d) S/(S + R) ratio (this study), and (e) βα/(βα + αβ) ratio (this study). The PETM interval (including the core and recovery) is highlighted by grey shading.

4.3.1.3 Kheu River

C_{16-35} *n*-alkanes were identified in the apolar fraction, in addition to C_{27} to C_{31} hopanes (including αβ, βα, and ββ isomers). Prior to the PETM and during the recovery, the CPI drops below 1 (Figure 4.4b), which may suggest input of low-maturity source rocks from carbonates or hypersaline environments. The CPI also oscillate drastically between ~1 and ~3 within the lower depths of the core of the PETM (~0–50 cm; Figure 4.4b). This section of high variability is also reflected in the C_{29} αβ/C_{30} αβ (Figure 4.4d) and C_{29} βα/(βα + αβ) (Figure 4.4e) ratios, suggesting rapid changes in the organic carbon source. However, it may also represent greater sampling resolution within the PETM. Overall, the average of all the thermal maturity ratios exhibit lower thermal maturity during the core interval. In addition, the C_{29} αβ/C_{30} αβ ratio present values >1 during the PETM (Figure 4.4d), potentially indicating input from clay-rich source rocks. With the exception of $T_s/(T_s + T_m)$ (Figure 4.4f), all of the ratios increase in higher thermal maturity during the recovery to either higher than pre-PETM (*i.e.* C_{29} αβ/C_{30} αβ) and C_{29-30} βα/(βα + αβ) ratios) or near pre-PETM values (*i.e.* C_{29-31} αβ/(αβ + ββ) ratio).

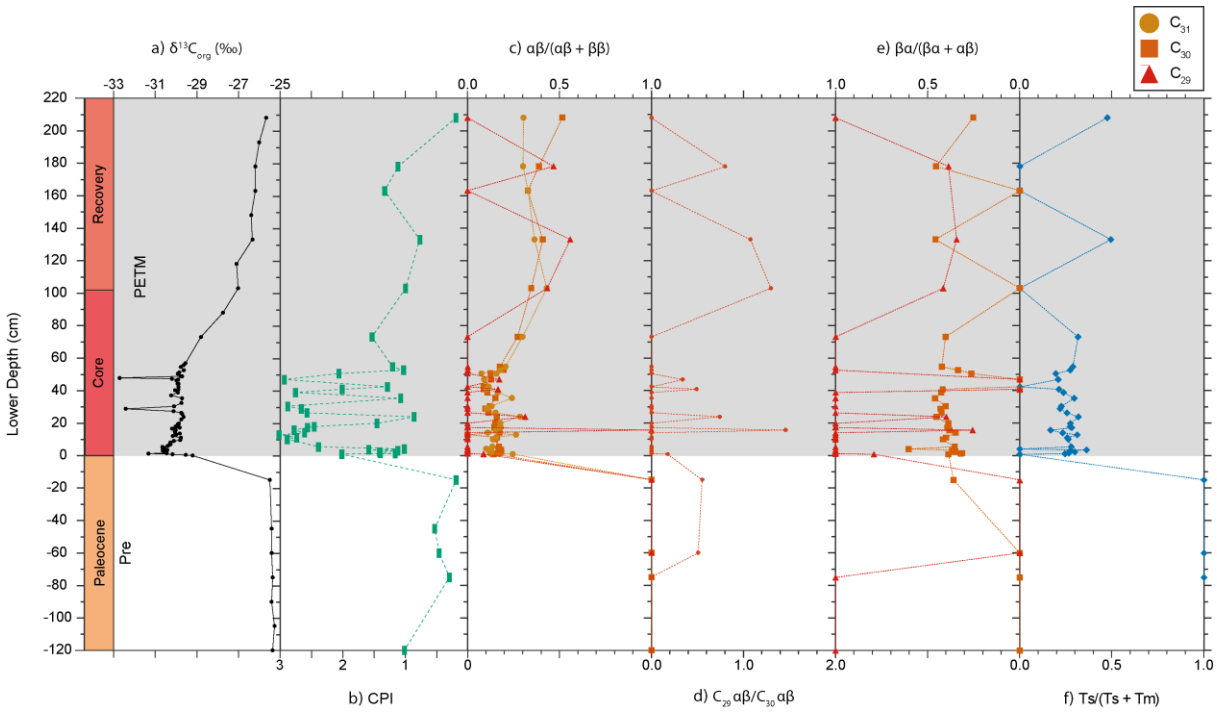

Figure 4.4 Thermal maturity ratios at Kheu River. Note some of the axis (CPI and βα/(βα + αβ)) are reversed to reflect increasing thermal maturity toward the right. (a) bulk sediment $\delta^{13}C$ of organic carbon ($\delta^{13}C_{org}$) (Dickson *et al.*, 2014), (b) CPI (this study), (c) αβ/(αβ + ββ) ratios (this study), (d) C_{29} αβ/C_{30} αβ ratio (this study), (e) βα/(βα + αβ) ratios (this study), and (f) Ts/(Ts + Tm) ratio (this study). The PETM interval (including the core and recovery) is highlighted by grey shading.

4.3.1.4 Ancora

The apolar fraction contains $C_{15\text{-}34}$ *n*-alkanes and C_{27} to C_{31} hopanes (including αβ, βα, and ββ isomers). CPI ranges from 1 to 2.2 and the pre-PETM and PETM interval are comparable (Figure 4.5b). Similarly, $C_{30\text{-}31}$ αβ/(αβ + ββ) values remain relatively constant, albeit exhibiting a very slight decline by an average of 0.01–0.03 (*i.e.* decreasing thermal maturity; Figure 4.5c). On the other hand, C_{31} S/(S + R) (Figure 4.5d) and C_{30} βα/(βα + αβ) (Figure 4.5e) values peak toward higher thermal maturity during the core of the PETM, reaching a maximum of 0.38 and 0.04, respectively. C_{31} S/(S + R) values exhibit a drastic shift during the PETM (Figure 4.5d) and there is a near equal mix of 22S and 22R isomers, suggesting potential transient input of thermally mature organic carbon. Changes in the C_{31} S/(S + R) ratio and C_{30} βα/(βα + αβ) ratio do not occur synchronously, instead C_{31} S/(S + R) values lag behind by ~1.5 mcd.

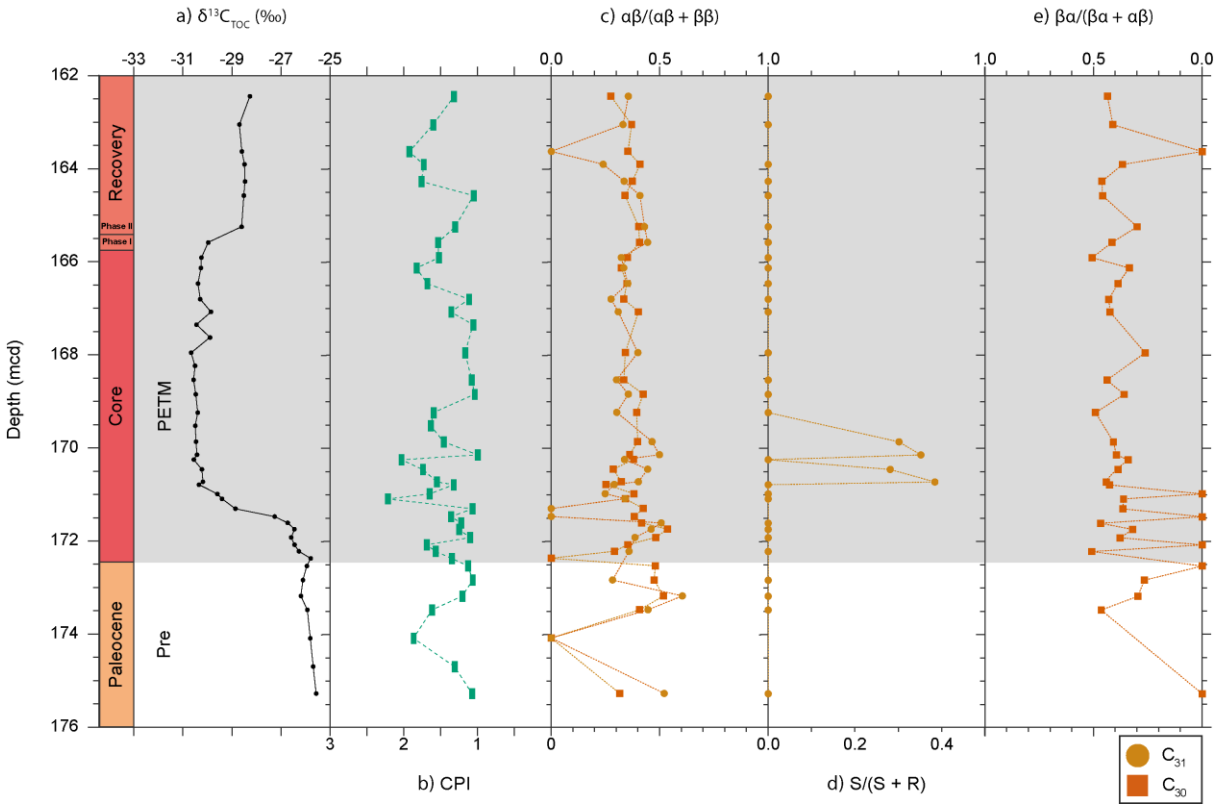

Figure 4.5 Thermal maturity ratios at Ancora. Note some of the axis (CPI and βα/(βα + αβ)) are reversed to reflect increasing thermal maturity toward the right. (a) bulk sediment $\delta^{13}C$ of total organic carbon ($\delta^{13}C_{TOC}$) (Elling *et al.*, 2019), (b) CPI (this study), (c) αβ/(αβ + ββ) ratios (this study), (d) S/(S + R) ratio (this study), and (e) βα/(βα + αβ) ratio (this study). The PETM interval (including the core and recovery) is highlighted by grey shading.

4.3.1.5 TDP Site 14

$C_{16\text{-}33}$ *n*-alkanes and C_{27} to C_{35} hopanes (including αβ, βα, and ββ isomers) were identified in the apolar fraction. The CPI remains >3 (*i.e.* low thermal maturity), with the exception of five data points which occur during the core of the PETM (Figure 4.6b). Most noticeable is the large variability in the hopane-based thermal maturity ratios pre-PETM and for the first ~4 m of the core of the PETM. In the upper ~5 m of the core of the PETM, the ratios are more stable and in general agreement. This interval mostly exhibits more thermally mature values than during the pre-PETM section (*e.g.,* C_{31} αβ/(αβ + ββ) increases by an average of 0.5; Figure 4.6c), suggesting a potential shift to an input of thermally mature organic carbon. For example, $C_{29\text{-}31}$ αβ/(αβ + ββ) values are close to its mature endmember of 1 (Figure 4.6c).

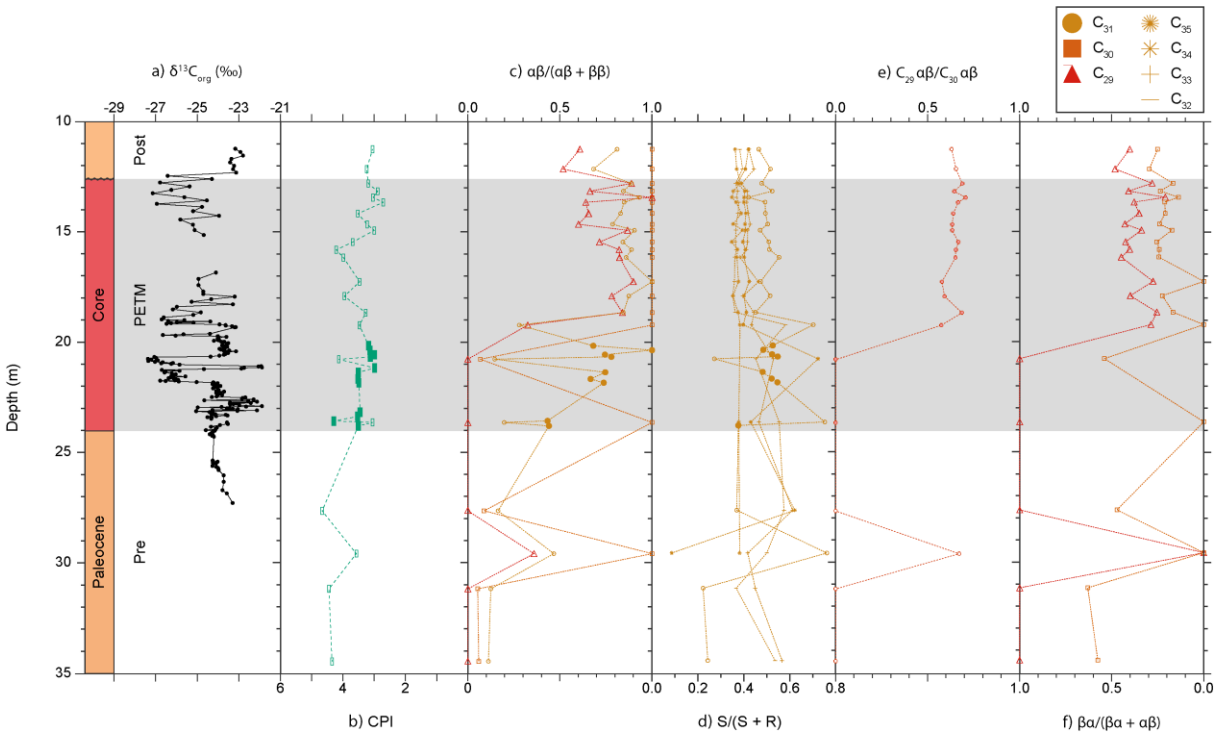

Figure 4.6 Thermal maturity ratios at TDP Site 14. Note some of the axis (CPI and βα/(βα + αβ)) are reversed to reflect increasing thermal maturity toward the right. (a) bulk sediment $\delta^{13}C$ of organic carbon ($\delta^{13}C_{org}$) (Aze *et al.*, 2014), (b) CPI (this study; Handley *et al.*, 2012), (c) αβ/(αβ + ββ) ratios (this study; Handley *et al.*, 2012), (d) S/(S + R) ratios (this study; Handley *et al.*, 2012), (e) C_{29} αβ/C_{30} αβ ratio (Handley *et al.*, 2012), and (f) βα/(βα + αβ) ratios (Handley *et al.*, 2012). The closed symbols are from this study and the open symbols are from Handley *et al.* (2012). The PETM interval (including the core) is highlighted by grey shading, and an unconformity truncates the CIE at 12.6 m.

4.3.2 OC_{petro} Mass Accumulation Rates

The OC_{petro} MARs were acquired from all the sites and grouped (where possible) into the key time intervals: (i) pre-PETM (Paleocene), (ii) the core (onset and body of the CIE) of the PETM, (iii) the recovery of the PETM, (iiia) Phase I of the recovery, and (iiib) Phase II of the recovery (Appendix VI). To enable comparison between sites, we calculated the fold change in mean OC_{petro} MARs between pre-PETM and during the PETM (*i.e.* including the core and recovery of the PETM) (Figure 4.7). Overall, most of the sites display an increase in OC_{petro} MARs during the PETM (ACEX: 7×10^{-2} gC cm^{-2} kyr^{-1}, Kheu River: 3×10^{-2} gC cm^{-2} kyr^{-1}, Ancora: 2×10^{-2} gC cm^{-2} kyr^{-1}, SDB: 6×10^{-2} gC cm^{-2} kyr^{-1}, CamDor: 8×10^{-3} gC cm^{-2} kyr^{-1}, and TDP Site 14: 8×10^{-3} gC cm^{-2} kyr^{-1}). However, the sites with the largest increase are restricted to the mid-latitudes (*i.e.* Kheu River, Ancora, and SDB). In contrast, ODP Site 1172 exhibits a decrease (3×10^{-4} gC cm^{-2} kyr^{-1}) in OC_{petro} MAR during the PETM.

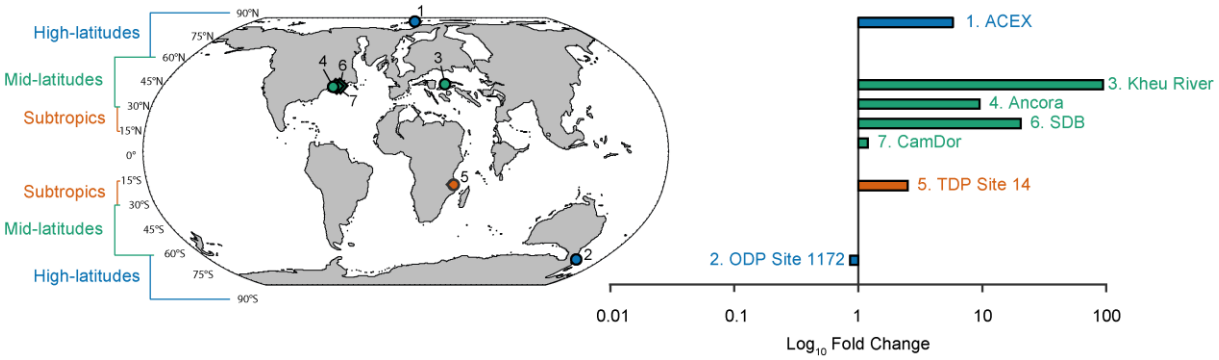

Figure 4.7 Log_{10} fold change in mean OC_{petro} mass accumulation rates (MARs) between pre-PETM and during the PETM (*i.e.* including the core and recovery of the PETM). The latitudes are defined as: high (>60°N/S), mid- (30–60°N/S), and subtropics (15–30°N/S) (Appendix V).

4.4 Discussion

4.4.1 Enhanced OC_{petro} Mass Accumulation Rates in the Subtropics and Mid-Latitudes during the PETM

A previous study from Tanzania (TDP Site 14) reported a relative increase in thermally mature αβ hopanes during the PETM (Handley *et al.*, 2012; Carmichael *et al.*, 2017). Here, we present new hopane-based thermal maturity data that reveals rapidly fluctuating values within the first ~4 m of the core of the PETM (Figure 4.6). Similar patterns were observed in the bulk $\delta^{13}C$ of organic carbon ($\delta^{13}C_{org}$) (Figure 4.6a), the *n*-alkane $\delta^{13}C$ record, the chain-length distribution of *n*-alkanes, and the branched and isoprenoid tetraether (BIT) index (Appendix VII). The $\delta^{13}C_{org}$ and *n*-alkane $\delta^{13}C$ records were previously suggested to reflect episodic reworking of older (pre-PETM) material rather than changes in the atmospheric carbon reservoir (Handley *et al.*, 2008; Aze *et al.*, 2014). The hopane-based thermal maturity ratios within this study confirms this variable delivery of OC_{petro}. In contrast, the upper ~5 m of the core of the PETM exhibits more stability in the hopane-based thermal maturity ratios (Handley *et al.*, 2012; Carmichael *et al.*, 2017), $\delta^{13}C_{org}$ values, and *n*-alkane $\delta^{13}C$ values (Handley *et al.*, 2008; Aze *et al.*, 2014), indicating a switch from an episodic to persistent delivery of OC_{petro}. The hopane-based thermal maturity ratios also indicate that the OC_{petro} within this interval is of higher thermal maturity. During the PETM, a rise in thermally mature hopanes and LSRs increases OC_{petro} MAR by an average of 8×10^{-3} gC cm^{-2} kyr^{-1} (Figure 4.7). Enhanced OC_{petro} MAR is consistent with a shift from predominantly marine organic carbon to a terrestrial organic carbon source (*e.g.,* an increase in the abundance of long-chain *n*-alkanes produced by vascular plants and brGDGTs produced by soil bacteria; (Handley *et al.*, 2008, 2012; Carmichael *et al.*, 2017). Whilst there is greater LSR and terrigenous material during the PETM, C_{org} values declined. This drop was attributed to the

larger contribution of clay (Handley *et al.*, 2012). Evidence includes an abundance of kaolinite, suggestive of intensified physical erosion (John *et al.*, 2012), and high Li/Al combined with low Na/Al, suggestive of exhumation of older weathered clay. These additional proxies also indicate processes that support an increase in the mobilisation and accumulation of OC_{petro} during the PETM.

Similar to Tanzania, Ancora exhibits an increase in the average OC_{petro} MAR (by 2×10^{-2} gC cm^{-2} kyr^{-1}) during the PETM (Figure 4.7). This value falls within the average OC_{petro} MARs estimated at two other sites from the Atlantic Coastal Plain (*i.e.* SDB: 6×10^{-2} gC cm^{-2} kyr^{-1} and CamDor: 8×10^{-3} gC cm^{-2} kyr^{-1}; Figure 4.7). However, the higher OC_{petro} MAR is largely driven by a shift in LSR from 0.8 cm kyr^{-1} (pre-PETM) to 11.28 cm kyr^{-1} (PETM) (Table 4.1; Stassen, Thomas and Speijer, 2012), and thus any uncertainty in the LSRs will also be reflected in the MAR estimates. The higher OC_{petro} MAR is consistent with evidence of terrestrial input to the Atlantic Coastal Plain during the PETM, including a higher abundance of kaolinite (Gibson, Bybell and Mason, 2000), detrital magnetic minerals (Kopp *et al.*, 2009), charcoal, seed pods, and terrestrial spores (Self-Trail *et al.*, 2017). In addition, there is an increase in the terrigenous-aquatic ratio (see Section 1.4.2) (Lyons *et al.*, 2019). Indirect evidence includes changes in the marine microfossil assemblage toward benthic foraminifera (Self-Trail *et al.*, 2017) and dinoflagellates (Sluijs and Brinkhuis, 2009) that can tolerate brackish water with high sediment input. However, with the exception of the abrupt peaks of C_{31} S/(S + R) at ~169–171 mcd (Figure 4.5d) and C_{30} βα/(βα + αβ) at ~171–173 mcd (Figure 4.5e), the thermal maturity ratios at Ancora are relatively stable compared to SDB and CamDor (Lyons *et al.*, 2019). Unlike Ancora, SDB and CamDor are characterised by a 6 ‰ increase in $\delta^{13}C_{org}$ values during the PETM (Lyons *et al.*, 2019), which was argued to represent reworking of older (pre-PETM) material and not an increase in primary productivity (Lyons *et al.*, 2019). This ^{13}C enrichment is not observed at Ancora (Elling *et al.*, 2019) and is consistent with the relatively stable thermal maturity ratios during the PETM (Figure 4.5a).

The average OC_{petro} MAR at Kheu River exhibit an increase (by 3×10^{-2} gC cm^{-2} kyr^{-1}) during the PETM (Figure 4.7), driven by an order-of-magnitude rise in C_{org} values from an average background level of ~0.1 wt. % (pre- and post-PETM) to ~4.4 wt. % (Dickson *et al.*, 2014). However, in contrast to the sites discussed thus far, thermal maturity ratios at Kheu River shift to immature values during the core of the PETM (Figure 4.4). During the PETM, the *n*-alkane distribution is dominated by long-chain homologs characteristic of vascular plants (Dickson *et al.*, 2014). It can therefore be argued that the shift observed in the thermal maturity ratios is mostly due to enhanced input of the OC_{bio} (*i.e.* immature hopanes such as ββ isomers) transported from land, although in situ production cannot be dismissed. An increase in the Chemical Index of Alteration (CIA) and spike in Ti/Al during the PETM not only corroborates evidence for terrestrial input but possibly erosion of older (pre-PETM) material (Dickson *et al.*, 2014). As such, both OC_{petro} and (to a larger extent) OC_{bio} were likely

delivered to this site. OC_{bio} burial may negate CO_2 released via enhanced OC_{petro} oxidation (*e.g.,* John *et al.*, 2008; Sluijs, Röhl, *et al.*, 2008; Bowen and Zachos, 2010; Kaya *et al.*, 2022; Papadomanolaki, Sluijs and Slomp, 2022). Therefore, understanding whether the Kheu River region was a net carbon source or sink requires further investigations, and this study highlights the need to quantify both OC_{bio} and OC_{petro} in marine sediments. Regardless, the subtropical and mid-latitudinal sites all exhibit an increase in OC_{petro} MARs during the PETM, and thus suggests that OC_{petro} oxidation may provide an additional source of CO_2.

4.4.2 Limited Change in Organic Carbon Sources in the High-Latitudes during the PETM

In the subtropics and mid-latitudes, average OC_{petro} MARs increased between 8×10^{-3} and 6×10^{-2} gC cm^{-2} kyr^{-1} during the PETM for a given site (see Section 4.4.1). In the high-latitudes, OC_{petro} MARs in the Arctic (ACEX) and the southwest Pacific Ocean (ODP Site 1172) either increase (by 7×10^{-2} gC cm^{-2} kyr^{-1}) or decrease (by 3×10^{-4} gC cm^{-2} kyr^{-1}), respectively (Figure 4.7). The decline observed at ODP Site 1172 is due to a small drop in C_{org} values and LSRs. The marked rise at ACEX is mostly driven by a peak in TOC values, from a minimum of 1.3 % (pre-PETM) to a maximum of 4.9 % (core PETM) (Elling *et al.*, 2019). Absolute abundances of palynomorphs from ACEX suggest that there is a mixture of marine and terrestrial organic matter (Sluijs, *Röhl, et al.*, 2008). However, both sites, with the exception of the C_{31} S/(S + R) ratio at ODP Site 1172 (Figure 4.3d), have stable thermal maturity ratios throughout the record. This indicates that although the supply of organic carbon increased during the PETM, the organic carbon source did not distinctly change. Intriguingly, there is an antiphase relationship between C_{30} αβ/(αβ + ββ) and C_{31} αβ/(αβ + ββ) at ACEX (Figure 4.2c), perhaps suggesting subtle changes in the organic carbon source during the PETM. Decoupling between the C_{30} and C_{31} indices could be due to a greater input of acidic peats, which are dominated by C_{31} αβ hopanes but lack abundant C_{30} αβ isomers (Inglis *et al.*, 2018). The contribution of OC_{bio} from acidic peats at ACEX has also been inferred from brGDGTs (Sluijs *et al.*, 2020).

4.4.3 Climate Exerts Primary Control on OC_{petro} Mobilisation during the PETM

Various factors may explain why some shallow marine sediments are characterised by enhanced delivery of OC_{petro} during the PETM. Present-day observations have identified a strong link between rainfall and efficient erosion/transfer of organic carbon from land-to-sea (*e.g.,* Hilton, 2017; Eglinton *et al.*, 2021). In the subtropics, evidence for changes in the hydrologic cycle during the PETM are scarce. Previous work at TDP Site 14 revealed that the hydrogen isotopic composition of *n*-alkanes (δ^2H_{wax}) increased during the PETM, which was inferred to represent a shift towards more arid climate conditions (Handley *et al.*, 2008; Carmichael *et al.*, 2017). Enhanced aridity could lead to minimal vegetation cover, hindering

soil development, and maximising the potential for erosion and mobilisation of OC_{petro} (*e.g.,* Leithold, Blair and Perkey, 2006; Hilton, Galy and Hovius, 2008). Furthermore, there are large fluctuations in δ^2H_{wax} values, which may indicate oscillations between dry and wet climate states and/or an increase in extreme precipitation events (Handley *et al.*, 2008; Carmichael *et al.*, 2017). Modelling studies over subtropical Africa during the PETM support the latter (Carmichael, Pancost and Lunt, 2018). Episodic and intense rainfall on a landscape prone to erosion would explain the highly variable delivery of different organic carbon sources, as shown by the hopane-based thermal maturity data (this study), $\delta^{13}C_{org}$ values, and *n*-alkane $\delta^{13}C$ values (Handley *et al.*, 2008; Aze *et al.*, 2014).

Analogous to TDP Site 14, Kheu River also exhibits high variability in the thermal maturity ratios (*e.g.,* CPI, C_{29} αβ/C_{30} αβ, and C_{29} βα/(βα + αβ); Figure 4.4), chain-length distribution of *n*-alkanes, BIT index, grain-size, and CIA during the PETM (Dickson *et al.*, 2014). Although two brief intervals of marine transgression have been noted in this region (Shcherbinina *et al.*, 2016), the biomarker records are more variable and thus appear to be more consistent with episodic changes in precipitation. There are multiple lines of evidence associating other mid-latitude sites with increased transient and extreme rainfall events during the PETM, for example the deposition of conglomerates in the Pyrenees (Schmitz and Pujalte, 2003, 2007; Chen *et al.*, 2018), changes in paleosol weathering indices, and the abundance and composition of nodules in the Bighorn Basin (*e.g.,* Kraus and Riggins, 2007; Kraus *et al.*, 2013). There is also evidence for greater freshwater runoff in the Atlantic Coastal Plain (*i.e.* Ancora, SDB, and CamDor) during the PETM, with the development of a river-dominated shelf referred to as the 'Appalachian Amazon' (Kopp *et al.*, 2009; Self-Trail *et al.*, 2017; Doubrawa *et al.*, 2022). This is consistent with high-resolution climate models that suggest the western Atlantic region was dominated by an increase in extratropical cyclones and more extreme rainfall events (Kiehl *et al.*, 2021; Rush *et al.*, 2021; Shields *et al.*, 2021). Although the hydrologic cycle likely exerted a first-order control on the mobilisation of terrestrial organic carbon, other ecological and/or geological controls could have also been important. For example, the dominance of OC_{bio} at Kheu River may reflect abundant vegetation cover (*e.g.,* Goñi *et al.*, 2013). On the other hand, the dominance of OC_{petro} at TDP Site 14 may reflect greater availability of OC_{petro}-rich rock and/or exacerbated erosion of OC_{petro} caused by limited soil development (*e.g.,* Hilton *et al.*, 2011).

Model simulations indicate an increase in precipitation in the high-latitudes for a PETM-type warming event (*e.g.,* Winguth *et al.*, 2010; Carmichael *et al.*, 2016; Cramwinckel *et al.*, 2023). Proxies also reconstruct northern and southern high-latitudes to be wetter at the onset of the PETM (*e.g.,* evidence from palynomorphs; Sluijs *et al.*, 2006; Willard *et al.*, 2019; Korasidis *et al.*, 2022, fossilised plants; Harding *et al.*, 2011, δ^2H_{wax}; Pagani, Pedentchouk, *et al.*, 2006, and clay-mineralogy; Robert and Kennett, 1994; Kaiho *et al.*, 1996; Dypvik *et al.*, 2011). Yet, biomarker evidence from high-latitude sites (*i.e.* ACEX and ODP Site 1172) indicate limited

changes in the source of organic carbon during the PETM. This suggests that in order to exhume and mobilise OC_{petro}, changes in rainfall seasonality and frequency of extreme precipitation events may be required (see Section 4.4.1). Alternatively, there may be other feedback mechanisms and/or more regional controls beyond the hydrologic cycle. In modern systems, local geomorphic processes play a strong role in regulating OC_{petro} transport from land-to-sea (*e.g.,* Hilton and West, 2020). Variability in OC_{petro} MARs could also be attributed to changes in sea level during the PETM. Indeed, various studies have suggested marine transgression during the PETM, including: ACEX (Sluijs *et al*., 2006), ODP Site 1172 (Sluijs *et al*., 2011), Kheu River (Shcherbinina *et al.*, 2016), the Atlantic Coastal Plain (John *et al.*, 2008), and elsewhere (see Sluijs, Brinkhuis, *et al.*, 2008 and references therein; see Li *et al.*, 2020 and references therein; Jiang *et al.*, 2023). However, the reduced supply of terrestrial organic carbon into the marine realm, expected with sea level rise, is rarely observed (*e.g.,* Sluijs *et al.*, 2014) and most PETM sites are characterised by enhanced terrigenous material during the PETM (see Carmichael *et al*., 2017 and references therein).

4.4.4 Timing and Implications for CO_2 Release during the PETM

Enhanced OC_{petro} delivery was suggested to have occurred ~10–20 kyrs after the onset of the PETM (*i.e.* within the body of the CIE) by Lyons *et al*. (2019). Here, we confirm that elevated OC_{petro} MARs occurred within the core of the PETM at several other sites (*i.e.* ACEX, Kheu River, Ancora; Figure 4.8). However, the exact timing within the core (*i.e.* onset or body) cannot be determined due to the lack of robust age constraints. The sites where the recovery phases were defined (*i.e.* ACEX, Kheu River, Ancora, and SDB) enable insight into whether enhanced OC_{petro} MARs continued after the core interval or recovered to pre-PETM values. Interestingly, at both Ancora and SDB, median OC_{petro} MARs are higher than the core of the PETM in Phase II and I, respectively (Figure 4.8). The decrease in OC_{petro} MAR during Phase I of the recovery at Ancora is only based on a single data point. Although an increase in OC_{petro} MARs during the recovery is not observed at ACEX and Kheu River, values do not return to pre-PETM levels. This suggests that at certain localities, terrestrial organic carbon cycle perturbations continued into the recovery phase. If OC_{petro} was oxidised, it may have provided an additional source of CO_2 during the recovery. In this scenario, other negative feedback mechanisms are required to negate the additional carbon released and help assist in the recovery of the PETM. Several processes have been proposed, such as silicate weathering (Penman *et al*., 2014) and/or enhanced OC_{bio} burial, either on land (Bowen and Zachos, 2010; Bowen, 2013) or within the ocean (John *et al.*, 2008; Ma *et al.*, 2014). Exacerbated weathering and erosion during the PETM (Pogge von Strandmann *et al.*, 2021) may increase nutrient delivery from land-to-sea, stimulating primary productivity and therefore OC_{bio} burial (Kaya *et al.*, 2022; Papadomanolaki, Sluijs and Slomp, 2022).

However, the origin of sequestered organic carbon in ocean sediments (*i.e.* terrestrial vs. marine) remain a major source of uncertainty.

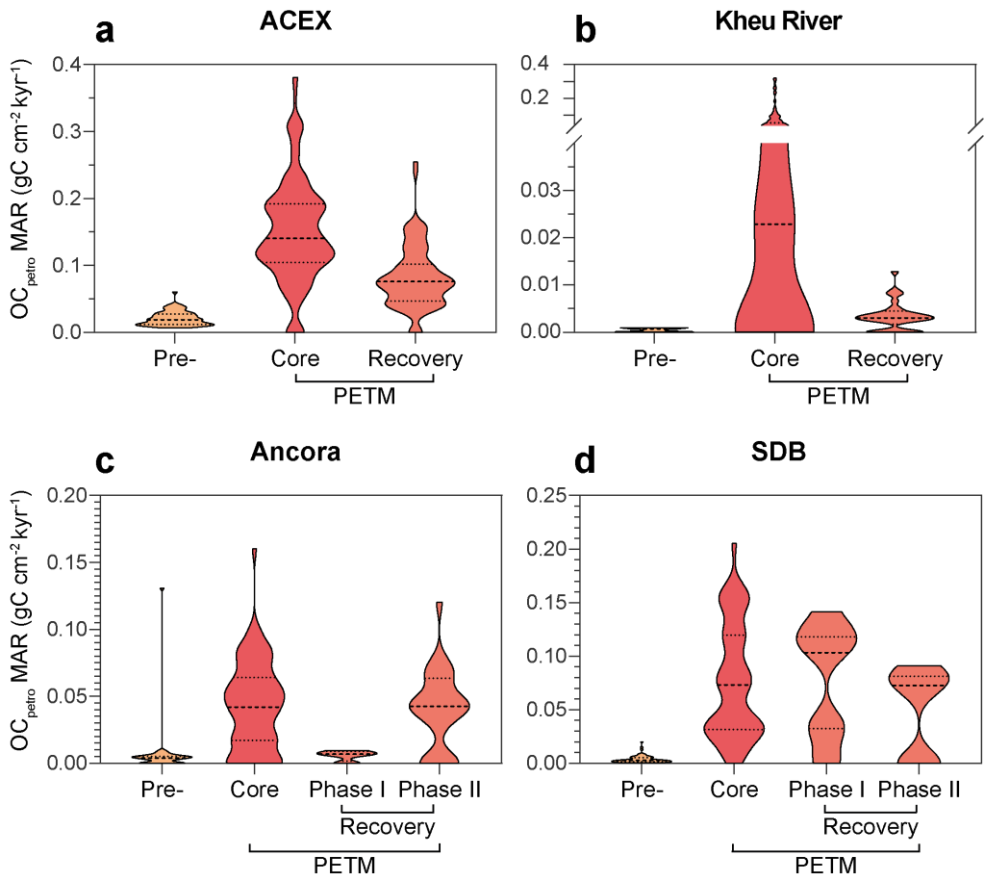

Figure 4.8 Violin plots of OC_{petro} MARs (gC cm^{-2} kyr^{-1}) for the defined time intervals of sites with the recovery phase (a) ACEX, (b) Kheu River, (c) Ancora, and (d) SDB. The thick dashed line represents the median and the thin dashed line extends from the 25th to 75th percentiles. Note the discontinuous y-axis and two different scales in panel (b).

Overall, Lyons *et al*. (2019) inferred between 10^2 and 10^4 PgC was released as CO_2 globally due to oxidation of OC_{petro} during the PETM. This assumed that the three sites (*i.e.* SDB, CamDor, and TDP Site 14) are globally representative. However, this study demonstrates that enhanced OC_{petro} MARs were mostly restricted to the subtropics and mid-latitudes, suggesting that global estimates may be lower than previously inferred. In addition, the maximum value of 10^4 PgC assumed that 85 % of OC_{petro} was oxidised. However, increased erosion of clastic sediments can aid the preservation of OC_{petro} (*e.g.,* Burdige, 2007; Bouchez *et al*., 2014). Furthermore, intense precipitation events (characteristic of the subtropics and mid-latitudes; *e.g.,* Schmitz and Pujalte, 2003, 2007; Kraus and Riggins, 2007; Handley *et al*., 2008; Kraus *et al*., 2013; Carmichael *et al*., 2017; Kiehl *et al*., 2021; Rush *et al*., 2021; Shields *et al*., 2021) may decrease the transfer time of OC_{petro} from source to sink, thereby reducing the possibility for oxidation (*e.g.,* Hilton *et al*., 2011). However, it is important to consider that shallow marine sites will likely integrate an expansive catchment area, which

incorporate slow meandering rivers as well as steep mountainous rivers. In the former system, the extent of OC_{petro} oxidised could be as high as ~90 % (*e.g.,* Galy *et al.*, 2008; Bouchez *et al.*, 2010). This is especially likely at sites where large freshwater input was evident, such as the Atlantic Coastal Plain (Kopp *et al.*, 2009; Self-Trail *et al.*, 2017; Doubrawa *et al.*, 2022). We also demonstrate that CO_2 release may have continued into the recovery of the PETM, suggesting that other feedback mechanisms (*e.g.,* OC_{bio} burial) were necessary to aid in the recovery of the Earth's climate system. To constrain global estimates of CO_2 emitted from OC_{petro} oxidation, further work is required to elucidate these uncertainties. Raman spectroscopy could help identify the oxidation efficiency based on the degree of highly degradable organic carbon vs. recalcitrant organic carbon (see Chapter 5), whilst palaeo-digital elevation models may provide further insight on sediment routing systems and transit time during the PETM (Lyster *et al.*, 2020).

4.5 Conclusion

This study uses a multi-biomarker approach to reconstruct the mobilisation of OC_{petro} during the PETM. We find widespread evidence for enhanced OC_{petro} mass accumulation rates (MARs) in the subtropics and mid-latitudes during the PETM. In this region, we argue that extreme rainfall events exacerbated erosion, mobilisation, and burial of OC_{petro} in the marine realm. In addition, we demonstrate that high OC_{petro} MARs persisted into the recovery phase of the PETM. However, the high-latitude sites do not exhibit a distinct change in the source of organic carbon during the PETM. This may be due to a more stable hydrological regime and/or additional controls, such as geomorphic processes or sea level change. Overall, OC_{petro} oxidation likely acted as an additional source of CO_2 during the PETM. However, further work is needed to determine the exact contributions of OC_{petro} as a positive feedback mechanism during the PETM and other hyperthermals.

Chapter 5 Enhanced Petrogenic Organic Carbon Oxidation during the Paleocene-Eocene Thermal Maximum

Abstract

The Paleocene-Eocene Thermal Maximum (PETM; ~56 Ma) is a hyperthermal event associated with the rapid input of carbon into the ocean-atmosphere system. Previous studies show that there was a greater delivery of petrogenic organic carbon (OC_{petro}) into the marine realm during the PETM. The oxidation of this OC_{petro} may have released additional carbon dioxide (CO_2), thereby prolonging the PETM. However, proxy-based estimates of OC_{petro} oxidation are unavailable due to the lack of suitable techniques. Raman spectroscopy is used to evaluate OC_{petro} oxidation in modern settings. For the first time, we explore whether Raman spectroscopy can evaluate OC_{petro} oxidation during the PETM. In the mid-Atlantic Coastal Plain, there is a shift from disordered to graphitised carbon. This is consistent with enhanced oxidation of disordered OC_{petro} and intensified physical erosion. In the Arctic Ocean, the distribution of graphitised carbon vs. disordered carbon does not change, suggesting limited variability in weathering intensity. Overall, this study provides the first evidence of increased OC_{petro} oxidation during the PETM, although it was likely not globally uniform. Our work also highlights the utility of Raman spectroscopy as a novel 'tool' to reconstruct OC_{petro} oxidation in the past.

Chapter 5 published in *Geochemical Perspective Letters*. **Hollingsworth, E.H.**, Sparkes, R.B., Self-Trail, J.M., Foster, G.L., and Inglis, G.N. Enhanced petrogenic organic carbon oxidation during the Paleocene-Eocene thermal maximum, *Geochemical Perspective Letters*. 33. https://doi.org/10.7185/geochemlet.2444. EHH wrote the original draft and all co-authors contributed to reviewing and editing. EHH and RBS carried out geochemical and data analyses, respectively.

5.1 Introduction

At the Paleocene-Eocene boundary, an abrupt carbon cycle perturbation gave rise to a global warming event (~4–6 °C; Tierney *et al.*, 2022), known as the Paleocene-Eocene Thermal Maximum (PETM; ~56 Ma). The initial flux of carbon occurred within ~3–21 kyrs (the onset of the PETM; see Kirtland Turner, 2018 and references therein), yet the PETM persisted for a further 170 ± 30 kyrs (the 'body' of the PETM; Zeebe and Lourens, 2019). The long duration of the PETM can be reproduced in carbon cycle models but requires a continuous source of carbon into the ocean-atmosphere system and/or additional feedbacks (*e.g.,* Bowen, 2013). Proposed mechanisms for the additional source include the slow dissociation of oceanic methane hydrates (*e.g.,* Zeebe, 2013), pulsed emissions from hydrothermal vent complexes (Frieling *et al.*, 2016; see Jin *et al.*, 2024 and references therein), and the oxidation of soil organic carbon (*e.g.,* Bowen, 2013) or petrogenic organic carbon (OC_{petro}) (Lyons *et al.*, 2019).

Biomarker thermal maturity ratios can fingerprint OC_{petro} that has been subject to relatively low burial temperature (<165 °C). Changes in biomarker thermal maturity ratios from a global compilation of shallow-marine sediments indicate greater delivery of OC_{petro} into the ocean during the PETM (Chapter 4; Lyons *et al.*, 2019). Based on modern observations (*e.g.,* Hilton and West, 2020; Soulet *et al.*, 2021), it is likely that the increased erosion rates and higher temperatures during the PETM enhanced OC_{petro} oxidation. However, constraining the fraction of OC_{petro} that was oxidised to CO_2 (*i.e.* the oxidation efficiency) remains challenging in the geologic record due to an insufficiency of proxies. In order to calculate the mass of OC_{petro}-derived CO_2 released during the body of the PETM, Lyons *et al.* (2019) used the present-day lower and upper bounds in oxidation efficiency (15–85 %; Bouchez *et al.*, 2010; Hilton *et al.*, 2011, 2014). This resulted in a wide range of estimates that span two orders-of-magnitude (10^2–10^4 PgC; Lyons *et al.*, 2019). To reduce the uncertainty, new techniques are required to determine OC_{petro} oxidation efficiency in the past. This will help reveal whether OC_{petro} oxidation is an important positive feedback mechanism during hyperthermals, and thus its potential role in future climate change.

Here, we explore the utility of Raman spectroscopy as a novel 'tool' to reconstruct OC_{petro} oxidation in the geologic record. Raman spectroscopy is a non-destructive technique that assesses nm-scale differences in the crystallinity of carbonaceous materials. This enables the distinction between highly crystalline (*i.e.* graphite) to amorphous (*i.e.* disordered) carbon, and can therefore detect OC_{petro} that formed at burial temperatures up to 650 °C (Beyssac *et al.*, 2002; Henry *et al.*, 2019). As the porous structure of disordered carbon makes it more susceptible to oxidation, a shift towards a dominance of graphitised carbon downstream has been suggested to indicate high OC_{petro} oxidation efficiency (Figure 5.1). This has been used to evaluate OC_{petro} oxidation in modern settings (*e.g.,* Galy *et al.*, 2008;

Bouchez *et al.*, 2010), however has rarely been applied in a geological context. Canfield *et al.* (2021) employed this approach in the Proterozoic, but this was with the aim to reconstruct atmospheric oxygen concentrations. Here, we employ Raman spectroscopy to identify OC_{petro} in PETM-aged sediments, and evaluate changes in OC_{petro} oxidation during the PETM.

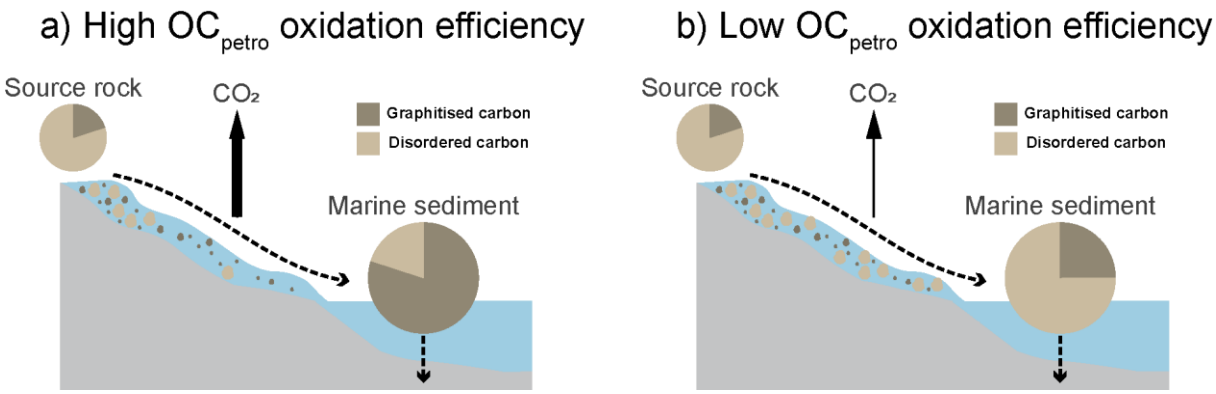

Figure 5.1 A simplified schematic illustrating the Raman spectroscopy approach to evaluating OC_{petro} oxidation. Marine sediment composition with (a) a dominance of graphitised carbon (dark brown) and (b) graphitised and disordered carbon (light brown), indicating a high and low OC_{petro} oxidation efficiency, respectively. Given that OC_{petro} oxidation is a source of CO_2, this correlates with a (a) high and (b) low CO_2 flux.

5.2 Material and Methods

We investigated two shallow-marine sites that exhibit higher OC_{petro} mass accummulation rates (MARs) during the PETM (Chapter 4). The South Dover Bridge ('SDB') core was drilled in the Salisbury Embayment (mid-Atlantic Coastal Plain; Figure 5.2; *e.g.,* Self-Trail, 2011; Self-Trail *et al.*, 2012) and shows a drastic increase in OC_{petro} delivery during the PETM (Lyons *et al.*, 2019). International Ocean Drilling Program Expedition 302 Site M0004A ('ACEX'), is located at the Lomonosov Ridge (central Arctic Ocean; Figure 5.2; *e.g.,* Backman *et al.*, 2006) and indicates minimal change in organic carbon source(s) during the PETM (Chapter 4).

Figure 5.2 Location of the Arctic Coring Expedition (ACEX; 82.81°N, 66.91°E) and South Dover Bridge (SDB; 41.39°N, 59.48°W) during the PETM (palaeo-latitudes based on mantle reference frame; Hollis *et al.*, 2019). Top panel: representation of the palaeogeography of the Northern Hemisphere 56 Ma, adapted from Carmichael *et al.* (2017). Bottom panel: the mid-Atlantic Coastal Plain with the modern coastline and Fall Line (brown dashed line), adapted from Bralower *et al.* (2018).

We follow the methodology outlined in Sparkes *et al*. (2013), which was specifically developed to facilitate Raman Spectroscopy of sedimentary rocks. Overall, 36 samples from SDB and 12 samples from ACEX were processed. Firstly, wet sediments were either freeze-dried or placed in a 50 ºC oven overnight (Appendix VIII Table 4). The samples were then ground to a fine powder with a Planetary Mill Pulverisette 5 (Fritsch) (see Section 2.1). The analyses were undertaken at the Manchester Metropolitan University with an InVia Raman spectrometer (Renishaw) (see Section 2.4.5). In summary, the homogenised samples were compressed between two glass slides to create a 1 cm^2 area which can be rastered at regular spaced intervals. Once a carbonaceous particle was confirmed, a spectrum was produced from long exposure to a 514 nm Ar-ion laser (60 s; measurement window 800–2200 cm^{-1}). To increase the chance that the data is representative of the population, 10 spectra were collected for each sample. The peaks in each spectrum were fitted using an updated script (https://github.com/robertsparkes/raman-fitting/releases/tag/v1.1.5) of the automated process described in Sparkes *et al*. (2013), and manually checked for inconsistencies.

5.3 Results

In total, 360 spectra from SDB and 120 spectra from ACEX were collected. The automated process resulted in only 7 spectra from SDB and 1 spectrum from ACEX being excluded due to a noise-to-signal ratio greater than 1:3. In previous studies, spectra were characterised as either: (i) highly graphitised carbon; (ii) mildly graphitised carbon; (iii) intermediate carbon; or (iv) disordered carbon (Sparkes *et al*., 2013). Spectra from highly graphitised carbon have a single sharp peak at 1580 cm^{-1} (G peak; Figure 5.3e). Disordered carbon has a wider 'G band' at approximately 1600 cm^{-1}, produced by a convolution of the G (1580 cm^{-1}) and D2 (1620 cm^{-1}) peaks, alongside other peaks signifying disorder (D1; 1350 cm^{-1}, D3; 1500 cm^{-1}, and D4; 1200 cm^{-1}; Figure 5.3f). Our data suggests a bimodal distribution (Figure 5.3e,f), and as such, spectra were categorised as either graphitised or disordered carbon (Figure 5.3a-d; Appendix VIII Table 3 and 4). This separation was based on peak burial temperatures, which were calibrated using the R2 and RA2 peak area ratio, and not the sum of peak width (G + D1 + D2) (see Sparkes *et al*., 2013).

At SDB, there is a mixture of both graphitised and disordered carbon in the Pre-PETM interval (including the pre-onset excursion; POE) and 'Core' PETM (including the onset, body, and Recovery interval) (Figure 5.3a,b). Compared to the Pre-PETM, the PETM exhibits a statistically highly significant (P <0.001) increase in the mean percentage of graphitised carbon (33 %; Appendix IX Figure 5a). However, this shift does not occur until ~1.5 m above the onset of the PETM (Figure 5.4b). At ACEX, there is a dominance of disordered carbon in the Pre-PETM interval and Core PETM (Figure 5.3c,d), and no statistically significant (P ≥0.1) change throughout the record (Figure 5.5b; Appendix IX Figure 5c). Both sites show a higher percentage of graphitised carbon in the Recovery and Post-PETM intervals than in the Pre-PETM interval (Appendix IX Figure 5a,c).

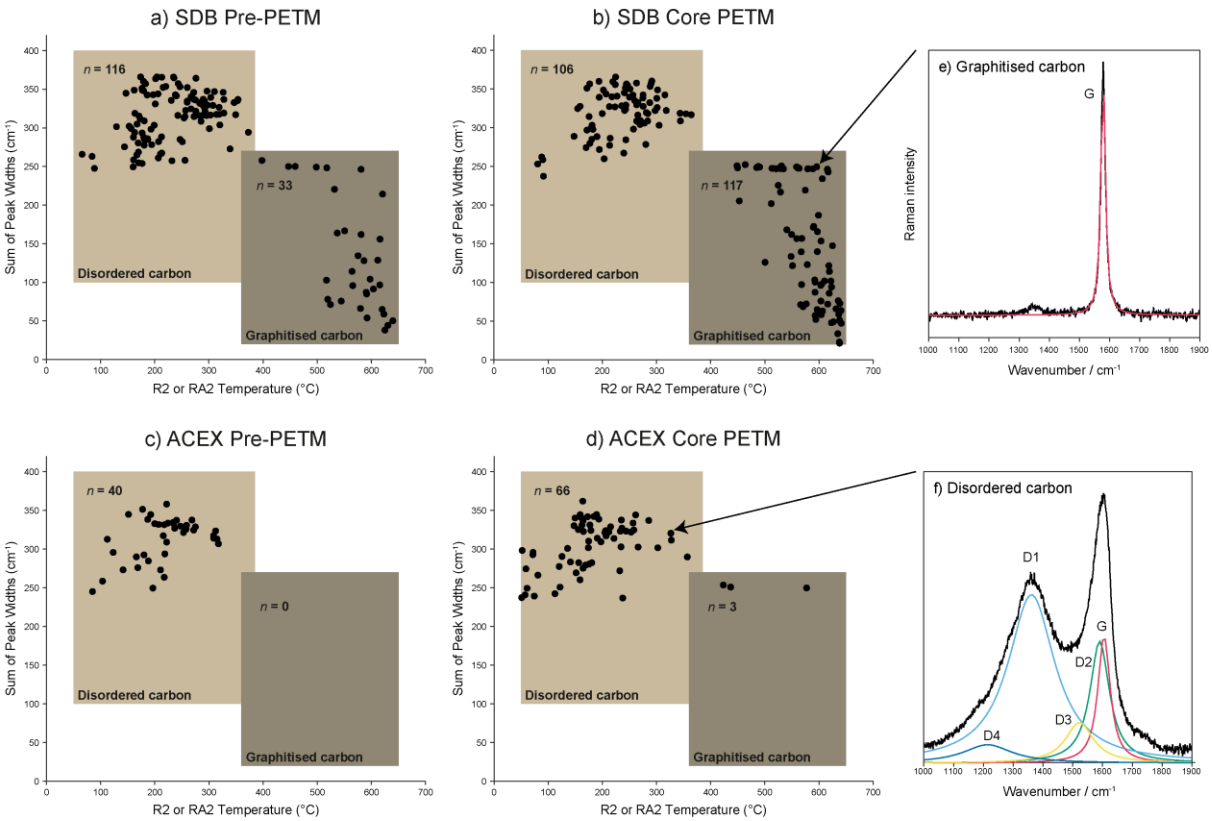

Figure 5.3 'Sparkes' plots combining data from the Pre-PETM interval (including the pre-onset excursion; POE) vs. Core PETM (including the onset, body, and Recovery interval; see Chapter 4 and references therein) at (a-b) SDB and (c-d) ACEX. The spectra are categorised into either graphitised carbon (dark brown) or disordered carbon (light brown). Examples of Raman spectra (black) with fitted peaks (coloured) for (e) graphitised carbon, from a SDB sample at 200.28 m (indicated by arrow), and (f) disordered carbon, from an ACEX sample at 385.11 mcd (indicated by arrow). Spectra have had a linear background removed during the automated process, and the fitted peaks include: G (1580 cm^{-1}), D1 (1350 cm^{-1}), D2 (1620 cm^{-1}),s D3 (1500 cm^{-1}), and D4 (1200 cm^{-1}) (Sparkes *et al.*, 2013).

To assess whether our semi-quantitative method (*i.e.* 10 spectra per sample) can accurately represent the population, four samples from SDB were analysed in duplicates (Figure 5.4b; Appendix VIII Table 3). With the exception of 202.37 m (s.d. = 35 %), the measurements yielded similar values (average s.d. = 7 %). However, interpretations of small-scale variability (*e.g.,* <14 %) should be made with caution and we recommend that future studies increase the number of spectra per sample.

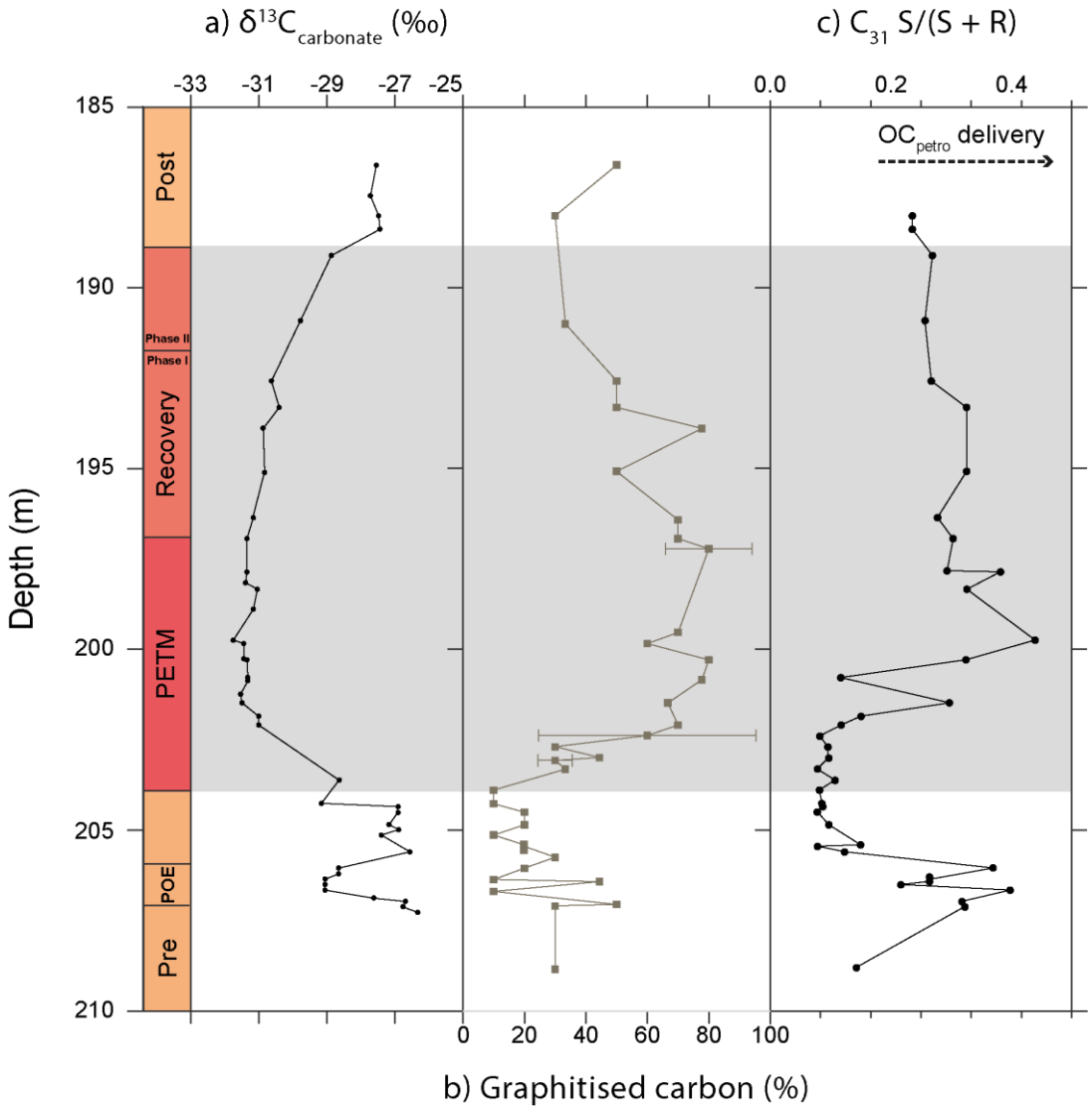

Figure 5.4 The SDB record of (a) bulk sediment $\delta^{13}C$ of carbonates ($\delta^{13}C_{carbonates}$) (Lyons *et al.*, 2019), (b) percentage graphitised carbon (this study), and (c) C_{31} homohopane 22S/(22S + 22R) ratio (Lyons *et al.*, 2019). The error bars within panel (b) represent 1 s.d. of the duplicate measurements, with the exception of the sample at 205.12 m (s.d. = 0 %). The time intervals are as follows: Pre-PETM, PETM (onset/body), Recovery Phase I, Recovery Phase II, and Post-PETM, based on Chapter 4 and references therein. The POE in the Pre-PETM interval is isolated using the definition from Babila *et al*. (2022).

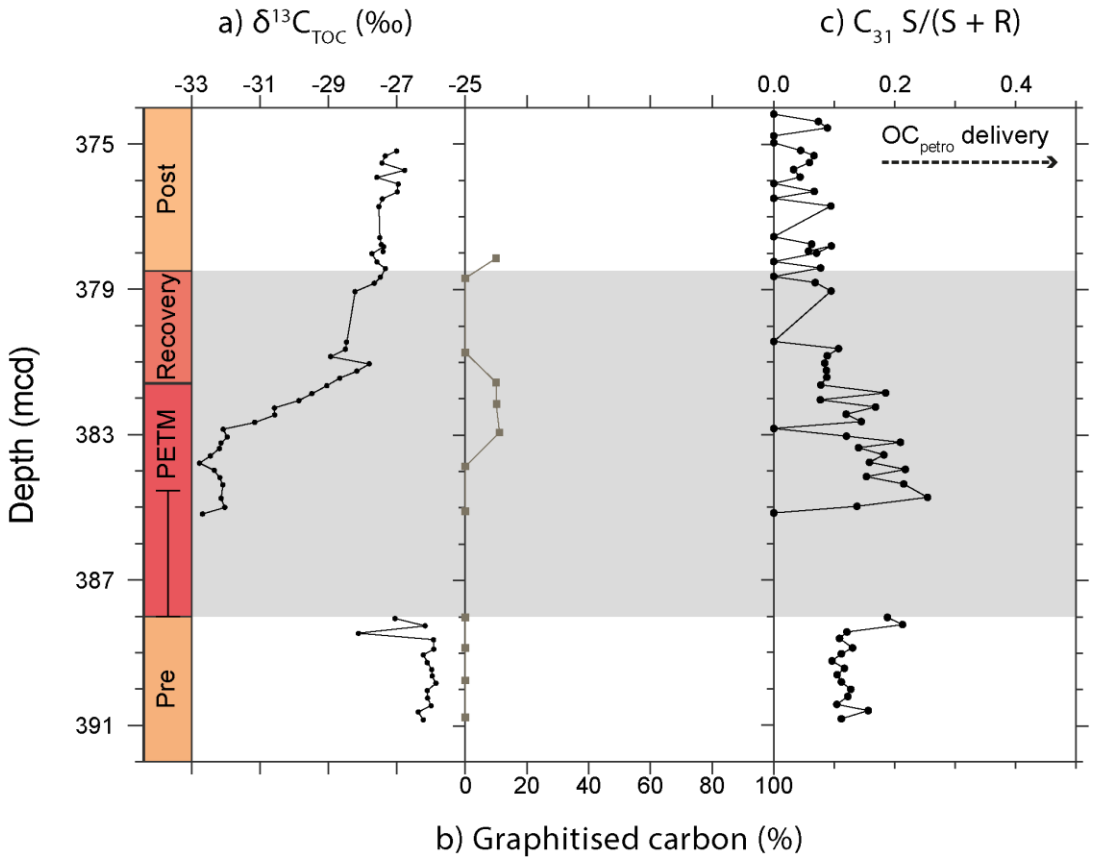

Figure 5.5 The ACEX record of (a) bulk sediment $\delta^{13}C$ of total organic carbon ($\delta^{13}C_{TOC}$) (Elling *et al*., 2019), (b) percentage graphitised carbon (this study), and (c) C_{31} homohopane 22S/(22S + 22R) ratio (Chapter 4). The time intervals are as follows: Pre-PETM, PETM (onset/body), Recovery, and Post-PETM, based on Chapter 4 and references therein. Note the core gap from ~388–384.5 mcd (Sluijs *et al*., 2006).

5.4 Discussion

5.4.1 Fingerprinting OC_{petro} Delivery during the PETM

Raman spectroscopy has most commonly been used to fingerprint OC_{petro} in modern river catchments and continental shelves (*e.g.,* Galy *et al*., 2008; Bouchez *et al*., 2010; Sparkes *et al*., 2018, 2020; Sun *et al*., 2022). Thus, we first compare our results to biomarker thermal maturity ratios from the same PETM-aged shallow-marine cores (Chapter 4; Lyons *et al.*, 2019). The C_{31} homohopane 22S/(22S + 22R) ratio is plotted alongside the percentage of graphitised carbon at SDB (Figure 5.4c; Appendix IX Figure 5b) and ACEX (Figure 5.5c; Appendix IX Figure 5d). Higher C_{31} S/(S + R) values suggest greater delivery of OC_{petro}, with values closer to 0.6 indicating input of OC_{petro} formed during early stages of the oil window (see Section 1.4.3.2).

Overall, there are similarities between the percentage of graphitised carbon and the C_{31} S/(S + R) ratio at both sites, whereby SDB exhibits large fluctuations (Figure 5.4) and ACEX shows relatively low and stable values (Figure 5.5). At SDB, the percentage of graphitised carbon and C_{31} S/(S + R) ratio increases between the Pre-PETM interval and both the POE and PETM intervals (Appendix IX Figure 5a,b). The ~1.5 m lag within the PETM interval in the percentage of graphitised carbon (Figure 5.4b) is also reflected in the C_{31} S/(S + R) ratio (Figure 5.4c) and the stable carbon isotopic composition of bulk organic carbon ($\delta^{13}C_{org}$) (Lyons *et al.*, 2019), suggesting a delayed response of ~10–20 kyrs. This confirms that Raman spectroscopy can be applied to fingerprint OC_{petro} delivery in the past, and could be particularly powerful in permitting the inclusion of study sites with post-depositional diagenesis (Sparkes *et al.*, 2020). Our new data supports previous findings indicating enhanced OC_{petro} delivery at SDB (Lyons *et al.*, 2019) and no drastic changes in organic carbon source(s) at ACEX (Chapter 4) during the PETM. Assuming that the graphitised carbon and thermally mature biomarkers at SDB came from the same source, the increase in graphitised OC_{petro} MAR during the PETM is calculated to be 2 x 10^{-2} gC cm^{-2} kyr^{-1} (based on Chapter 4).

5.4.2 Characterising and Identifying the Potential Sources of OC_{petro}

Kopp *et al.* (2009) initially hypothesised that Cretaceous-aged upland deposits, such as the Potomac Group, could have been a source of sediment to the Salisbury Embayment during the PETM (*e.g.,* Schneider-Mor and Bowen, 2013). Indeed, similarities were found with the biomarker thermal maturity ratios from the Raritan Formation of the upper Potomac Group and the PETM-aged SDB core (Lyons *et al.*, 2019). In addition, the $\delta^{13}C_{org}$ values and source rock properties (*e.g.,* T_{max}) are comparable (Lyons *et al.*, 2019). As the percentage of graphitised carbon (Figure 5.4b; Appendix IX Figure 5a) and the C_{31} S/(S + R) ratios (Figure 5.4c; Appendix IX Figure 5b) follow a similar trend, this suggests that the graphitised OC_{petro} may have also been sourced from the Raritan Formation. However, the presence of graphitised OC_{petro} implies burial temperatures (~350–650 °C; Beyssac *et al.*, 2002) that should severly diminish or completely destroy biomarkers (Peters, Walters and Moldowan, 2005). Therefore, the graphitised OC_{petro} was likely reworked into the Raritan Formation and subsequently re-exhumed alongside the thermally mature biomarkers during the PETM. This is consistent with present-day observations of graphite particles surviving transport over thousands of kilometres (*e.g.,* Galy *et al.*, 2008) and persisting over multiple erosion cycles (*e.g.,* Jehlicka and Rouzaud, 1990; Sparkes *et al.*, 2020). Decoupling between the percentage of graphitised carbon and the C_{31} S/(S + R) ratios during the POE could signify two distinct sources of OC_{petro} (Figure 5.4b,c; Appendix IX Figure 5a,b).

At ACEX, the relative abundance of disordered carbon (Figure 5.5b; Appendix IX Figure 5c) and low C_{31} S/(S + R) values (Figure 5.5c; Appendix IX Figure 5d) throughout the record

indicates that the OC_{petro} is derived from a more thermally immature source rock (*i.e.* protolith). This is consistent with the excellent preservation of pollen and spores (Sluijs, Röhl, *et al.*, 2008), and the presence of biomarkers diagnostic of peats and/or lignite deposits (*e.g.,* C_{31} αβ hopanes; Chapter 4), in these sediments. The dominance of disordered carbon also implies limited availability of graphite-rich source rocks.

5.4.3 Evaluating OC_{petro} Oxidation during the PETM

The mid-Atlantic Coastal Plain during the PETM has been referred to as the 'Appalachian Amazon' due to similarities with sediments from the modern Amazon shelf, including features indicative of hyperpycnal flow (Self-Trail *et al.*, 2017), and the presence of kaolinite (Gibson, Bybell and Mason, 2000) and magnetofossils (see Kopp *et al.*, 2009 and references therein). Present-day observations of two Amazon tributaries show the preferential oxidation of the less recalcitrant disordered OC_{petro} and a consequential relative increase in graphite downstream (Bouchez *et al.*, 2010). The Amazon is mostly supplied by low-grade metamorphic rocks from the Andes, which are subject to a long residence time within the extensive meandering rivers typical of large catchments. This results in the estimated loss of up to ~90 % of OC_{petro} during transport (Bouchez *et al.*, 2010; see Dellinger *et al.*, 2023 and references therein). The progressive shift towards more graphite along the land-to-sea transect is also seen in modern rivers that have a contribution of high-grade metamorphic rocks, such as in the Himalayas (Beyssac *et al.*, 2004). However, the Himalayas have more efficient sediment routing systems that promote burial of OC_{petro} in the Bengal Fan (Galy *et al.*, 2007).

As the Amazon shelf is the closest analogue for the mid-Atlantic Coastal Plain, we argue that the shift from a dominance of disordered to graphitised carbon at SDB represents enhanced oxidation of disordered OC_{petro} during the PETM. Furthermore, Lyons *et al.* (2019) implied OC_{petro} oxidation from the higher Oxygen Index within the body of the PETM at SDB relative to the Raritan Formation. We note that the oxidation and/or deposition of OC_{petro} can also occur in floodplains (*e.g.,* Scheingross *et al.*, 2021). However, this would lead to the loss of all types of OC_{petro} from the fluvial load, thus maintaining an equal distribution of graphitised carbon vs. disordered carbon between the Pre-PETM and PETM intervals. An average ~5 °C of warming during the PETM (Tierney *et al.*, 2022) may have also caused OC_{petro} oxidation to increase by one-fold, based on observations made by Soulet *et al.* (2021) in modern river catchments.

At SDB, there is a pronounced ~20 fold increase in linear sedimentation rates, and higher OC_{petro} MAR, during the PETM (Lyons *et al.*, 2019). Given the widespread evidence for intense precipitation events (see Carmichael *et al.*, 2017 and references therein) and exacerbated erosion rates (*e.g.,* John *et al.*, 2008), greater exhumation of graphitised OC_{petro}

can also explain the shift from a dominance of disordered to graphitised carbon. For example, a more active palaeo-Potomac river could have sourced new graphite-rich rocks from regions in the Appalachian Mountains (*e.g.,* Poag and Sevon, 1989; Kopp *et al.*, 2009). On the other hand, multiple sites in the Atlantic Coastal Plain reveal that the POE was a smaller-scale carbon cycle perturbation than compared to the PETM (Sluijs *et al.*, 2007; Self-Trail *et al.*, 2012; Elling *et al.*, 2019; see Babila *et al.*, 2022 and references therein). The warming excursion, detected in some temperature proxies, is also much less severe (Inglis *et al.*, 2023). Therefore, the lower magnitude change in the relative abundance of graphitised carbon during the POE would imply a lower oxidation efficiency and/or abated physical erosion (Figure 5.4b; Appendix IX Figure 5a). However, there is a distinct shift towards more thermally mature biomarkers within the POE, indicating some input of OC_{petro} from a more thermally immature source rock. Overall, the role of OC_{petro} oxidation during the POE remains unclear, but can be addressed by investigating other marginal sites where the POE has been identified (*e.g.,* Tasman Sea; Elling *et al.*, 2019).

At ACEX, intense precipitation may have countered warming-induced OC_{petro} oxidation by decreasing residence time in the rivers and/or amplifying floodplain storage. Higher sedimentation rates also promote the burial and preservation of organic matter (Galy *et al.*, 2007). However, the limited presence of graphite in this system could suppress signals that indicate changes in the oxidation of disordered OC_{petro}.

5.5 Conclusion

This study explores whether Raman spectroscopy can be used to reconstruct OC_{petro} oxidation in the past. Our results show a shift from a dominance of disordered to graphitised carbon at SDB, indicating that OC_{petro} oxidation acted as a positive feedback mechanism in the mid-Atlantic Coastal Plain during the PETM. However, data from the Arctic Ocean suggests that this process may not be globally uniform. Moreover, the smaller increase in graphitised carbon within the POE implicates that a larger climate aberration, such as the PETM, is required. This study shows the utility of Raman spectroscopy to fingerprint OC_{petro} delivery and – when combined with biomarker thermal maturity ratios – help diversify the type of OC_{petro} that can be characterised. As this approach detects more recalcitrant forms of OC_{petro} (*i.e.* graphite), it additionally expands the number of sites that can be analysed. Our study also highlights the potential for Raman spectroscopy to reconstruct OC_{petro} oxidation in the geological past.

Chapter 6 Investigating Past Methane Cycle Perturbations through the Lens of Novel Polyfunctionalised Hopanoids

Abstract

Methane (CH_4) is an essential component of the carbon cycle, and ice core records indicate that atmospheric CH_4 concentrations have oscillated on orbital timescales. Yet, ice core records are limited to the 'icehouse' conditions of the last 800 kyrs. Therefore, we do not understand how the methane cycle may respond to future global warming. Enhanced methane cycling has been inferred during past 'hothouse' climates, notably the Paleocene-Eocene Thermal Maximum (PETM; ~56 Ma). This is based on a shift towards lower values in the carbon isotopic composition of bacterial-derived hopanoids ($\delta^{13}C_{hop}$). However, these compounds have multiple source organisms (*e.g.,* methanotrophs, photoautotrophs, and heterotrophs), and the $\delta^{13}C_{hop}$ value can also reflect changes between methanotrophs and their metabolic pathway used to assimilate carbon. In contrast, bacteriohopanepolyols (BHPs) are polyfunctionalised hopanoids that may be a more diagnostic tracer of methanotrophs. BHPs have been reported in one PETM-aged deposit, but their preservation potential is unclear. Here, we aim to: (i) determine the preservation of novel BHPs during the PETM; and (ii) explore their potential as a proxy to reconstruct past methane cycle dynamics. To achieve this, we examine the presence of BHPs at Otaio River (New Zealand). The Otaio River deposits are in part formed by the development of wetlands, environments currently associated with increasing methane emissions. We identify a total of 16 BHPs, 6 of which are reported for the first time in sediments as old as the PETM. The prevalence of complex BHPs, such as bacteriohopane-31,32,33,334-tetrol cyclitol ether (BHT-CE) suggests excellent preservation. Interestingly, 35-aminobacteriohopane-30,31,32,33,34-pentol (aminopentol) increases during the PETM and coincides with the very negative $\delta^{13}C_{hop}$ values. This supports the utility of aminopentol as a proxy for methane cycling during transient warming events. Overall, our study presents the most diverse BHP profile found thus far in sedimentary deposits from over ~50 Ma, and demonstrates the opportunity to apply BHPs to unravel past changes in the methane cycle and microbial ecology.

Chapter 6 is currently in preparation for *Geochemica et Cosmochimica Acta*. **Hollingsworth, E.H.,** Rush, D., Hopmans, E.C., Kennedy, E.M., Pancost, R.D., and Inglis, G.N. Investigating Past Methane Cycle Perturbations Through the Lens of Novel Polyfunctionalised Hopanoids.

6.1 Introduction

Atmospheric methane (CH_4) concentrations have risen from pre-industrial levels of 700–750 ppb to ~1100 ppb today (Nisbet *et al.*, 2019). This is predominantly due to anthropogenic activity, namely agriculture and fossil fuel exploitation exacerbating the generation of biogenic and thermogenic and/or pyrogenic CH_4, respectively (Canadell *et al.*, 2021). On the centennial-scale, CH_4 is a far more potent greenhouse gas (GHG) than CO_2 (Forster *et al.*, 2021). As such, there is an urgency to prioritise the reduction of CH_4 emissions and develop new carbon removal technologies (*e.g.,* Abernethy *et al.*, 2021; Ocko *et al.*, 2021). However, this requires a holistic view of the methane cycle, accounting for natural sources and understanding how it may respond to future climate change.

Present-day observations indicate that biogenic and pyrogenic CH_4 fluxes are the most likely to be affected by evolving climate regimes (*e.g.,* Dean *et al.*, 2018). Global warming is exposing biogenic CH_4 reservoirs in subglacial regions (*e.g.,* Anderson *et al.*, 2010; see Schuur *et al.*, 2015 and references therein; Lamarche-Gagnon *et al.*, 2019). Moreover, higher temperatures enhance rates of microbial activity, therefore increasing the production of CH_4 from methanogens (*e.g.,* Yvon-Durocher *et al.*, 2012; Olefeldt *et al.*, 2013; Chu *et al.*, 2014; Turetsky *et al.*, 2014; Tveit *et al.*, 2015). CH_4 can then be directly emitted into the atmosphere or consumed and released as CO_2 via the oxidation of CH_4 by methanotrophs (*e.g.,* Kip *et al.*, 2010; van Winden, Reichart, *et al.*, 2012; Hofmann *et al.*, 2016; van Winden *et al.*, 2020). In addition to warming, an intensified hydrologic cycle could amplify both pyrogenic and biogenic CH_4 contributions. Droughts induce biomass burning events, releasing pyrogenic CH_4 (*e.g.,* Saito *et al.*, 2016; Wilson *et al.*, 2016; Ribeiro *et al.*, 2018). In contrast, wetter conditions lead to anoxic environments that favour methanogenesis, such as wetlands. In fact, wetlands are currently the largest source of naturally-derived CH_4 (~25–35 % of the total combined natural and anthropogenic sources), resulting in proportionally higher uncertainty in its future role in the carbon cycle (Saunois *et al.*, 2020). More efficient CH_4 oxidation has also been observed in peatlands subject to wet and dry cycles (*e.g.,* Huang *et al.*, 2018; Inglis, Naafs, *et al.*, 2019).

Long term observations spanning different climate states can help offer new insights into varying responses of the methane cycle (*e.g.,* Tierney *et al.*, 2020). However, continuous measurements of atmospheric CH_4 concentrations are only available for the last ~40 years (Lan, Thoning and Dlugokencky, 2024). Ice cores extend the record back a further 800 kyrs, and demonstrates a positive correlation with the eccentricity-paced climate amelioration of the interglacial periods (Delmotte *et al.*, 2004; Loulergue *et al.*, 2008). The stable carbon isotopic composition ($\delta^{13}C$) of CH_4 identified a dominantly biogenic source, as they are ^{13}C-depleted (~-60 ‰) compared to those originating from thermogenic (~-44 ‰) or pyrogenic (~-21 ‰) processes (*e.g.,* Bock *et al.*, 2017; Dyonisius *et al.*, 2020). This highlights the long-

standing importance of wetlands, which likely grew in spatial extent due to the retreat of ice sheets in the northern high-latitudes (*e.g.,* Schmidt, Shindell and Harder, 2004; Smith *et al.*, 2004) and/or the superimposed precession-forced shifts in the ITCZ and monsoon systems over the tropics (*e.g.,* Blunier *et al.*, 1995; Loulergue *et al.*, 2008). However, ice cores represent the colder-than-modern conditions of the Quaternary epoch (2.6 Ma to present).

Studies on more analogous 'hothouse' climates are scarce due to the paucity of appropriate archives (*i.e.* terrestrial deposits) and proxies for the methane cycle. However, the $\delta^{13}C$ of bacterial-derived hopanoids ($\delta^{13}C_{hop}$), specifically the diagenetic forms (*e.g.,* hopanes and hopenes), have been used to infer changes in aerobic methanotrophy in the past, including the Paleocene-Eocene Thermal Maximum (PETM; ~56 Ma). Lignite deposits from the United Kingdom (Cobham Lignite; Pancost *et al.*, 2007), New Zealand (Otaio River; Inglis *et al.*, 2021), and Arctic Canada (Stenkul Fiord; Blumenberg *et al.*, 2024) (see Section 1.4.5) all exhibit a decline in $\delta^{13}C_{hop}$ values during the PETM, reflecting enhanced aerobic methanotrophy and thus availability of CH_4 for the microbial community (*e.g.,* van Winden, Reichart, *et al.*, 2012; van Winden *et al.*, 2020). This ranges from a minima of -50 ‰ at Stenkul Fiord (Blumenberg *et al.*, 2024) to -76 ‰ at Cobham Lignite (Pancost *et al.*, 2007), both of which lie outside the observed modern range of peatlands (Inglis, *Naafs, et al.*, 2019). At Otaio River and Cobham Lignite, the $\delta^{13}C_{hop}$ excursion mostly occurred during the onset of the PETM (Pancost *et al.*, 2007; Inglis *et al.*, 2021). On the other hand, this is less pronounced at Stenkul Fiord, and Blumenberg *et al.* (2024) suggested that methanotrophy may have been elevated before and after the PETM. Hopanoids are synthesised by a wide array of bacteria, including cyanobacteria, heterotrophs, and methanotrophs (Rohmer, Bouvier-Nave and Ourisson, 1984). As such, the $\delta^{13}C_{hop}$ could reflect a mix of sources, limiting the utility of hopanes and hopenes as biomarkers for methanotrophy. Changes in the metabolic pathway used to assimilate carbon can also exert a control upon $\delta^{13}C_{hop}$, with Type I (Gammaproteobacteria) methanotrophs characterised by relatively low $\delta^{13}C_{hop}$ values compared to Type II (Alphaproteobacteria) methanotrophs. Therefore, additional techniques are required to assess methane cycling in the past.

Bacteriohopanepolyols (BHPs) are hopanoids with a polyfunctionalised side chain (*e.g.,* Rohmer, Bouvier-Nave and Ourisson, 1984). The most frequently reported is bacteriohopane-32,33,34,35-tetrol (BHT). However, a diverse suite of new structures have since been discovered, including several that correspond to specific source organisms (*e.g.,* see Talbot and Farrimond, 2007 and references therein; Talbot *et al.*, 2008). BHPs with an amine functionality at the terminal C-35 position (amino-BHPs) are associated with aerobic methanotrophs (see Talbot *et al.*, 2014 and references therein). Yet, the analyses of BHPs in pre-Quaternary-aged sediments have been limited to a few studies and restricted to a single BHP (BHT; Bednarczyk *et al.*, 2005; van Dongen *et al.*, 2006). BHPs were initially thought to be unstable, rapidly losing their functional groups and transforming to hopanes and hopenes

during the earliest stages of diagenesis. However, Talbot *et al.* (2016) recently reported amino-BHPs in the Cobham Lignite (~56 Ma), extending the application of complex BHPs as far back as the PETM. Since Talbot *et al.* (2016), methodological advancements have allowed the separation of previously undetected BHPs with novel side chains (Hopmans *et al.*, 2021). The distribution of these compounds may be used to further assess specific bacterial metabolisms (see Kusch and Rush, 2022 and references therein).

Here, we examine the presence of BHPs at the PETM-aged Otaio River site. This site is characterised by wetland and marginal marine deposits, which are ideal for investigating the methane cycle. Furthermore, a published $\delta^{13}C_{hop}$ record (Inglis *et al.*, 2021) allows for the validity of BHPs as methanotroph biomarkers to be evaluated. Overall, we aim to: (i) determine the preservation of novel BHPs during the PETM; and (ii) explore their potential as a proxy to reconstruct past methane cycle dynamics.

6.2 Material and Methods

6.2.1 Site Description and Age Controls

The Otaio River is located on the South Island of New Zealand (Figure 6.1a). Here, samples were obtained by Dr. Liz Kennedy from an exposed ~55 m section consisting of the Broken River Formation and the Kauru Formation (Forsythe, 2001).

Lithological observations of the Broken River Formation note mixed sandstone and mudstone, interspersed with ~10-50 cm and >1 m thick lignites throughout the succession (Inglis *et al.*, 2021) (Figure 6.1b). The former is characterised by relatively low (<6 %) total organic carbon (TOC) values, with signs of burrowing and the presence of dinoflagellate cysts (Pancost *et al.*, 2013). This indicates an overall low-energy estuarine or deltaic setting, and has been referred to as the 'marine interbeds' (Inglis *et al.*, 2021). In contrast, the 'lignites' have relatively high (>20 %, but up to ~70 %) TOC values, reflecting shifts to coastal wetland environments (Inglis *et al.*, 2021). Furthermore, the recovery of pristine plant fossils implies conditions that would favour the preservation of BHPs (Pancost *et al.*, 2013). This is corroborated with evidence of low thermal maturity, from *n*-alkane- (*i.e.* carbon preference index; CPI) and hopane- (*i.e.* $C_{27\text{-}32}$ ββ/(αβ + βα + ββ)) based thermal maturity ratios (Inglis *et al.*, 2021).

Palynological evidence suggests that the Broken River Formation encompasses both the late Paleocene and early Eocene (Pancost *et al.*, 2013), estimated to span ~56 to 48.9 Ma (Naafs, Rohrssen, *et al.*, 2018). During this time interval (~55 Ma) the latitude and longitude of the site was 56.1°S and 163.7°W, respectively (Huber and Caballero, 2011; Hollis *et al.*, 2012). The transition from Paleocene to Eocene (*i.e.* the PETM) is captured in the Broken River Formation (5.5 m), identified by a transient negative carbon isotope excursion (CIE) in

the $\delta^{13}C$ of bulk organic carbon ($\delta^{13}C_{org}$) and long-chain *n*-alkanes ($\delta^{13}C_{wax}$) (Inglis *et al.*, 2021). There is also an acme of the dinoflagellate cyst *Apectodinium augustum* (Figure 6.1b), the biostratigraphic marker for the PETM, during a marine incursion following the CIE (9.5–11.7 m; Pancost *et al.*, 2013). Although the CIE does not fully recover, the occurrence of a dinoflagellate cyst typically seen post-PETM (*i.e. Rhombodinium subtile*) signifies the termination of the PETM (17.45 m) (Figure 6.1b). Finally, a shift at ~41.5 m delineates the boundary between the Broken River Formation and the overlying Eocene-aged Kauru Formation. The presence of marine fauna (Marwick, 1960), glauconite, intense bioturbation, and a relatively low branched and isoprenoid tetraether (BIT) index value (~0.56) at ~41.5 m, all suggest marine deposition (Inglis *et al.*, 2021).

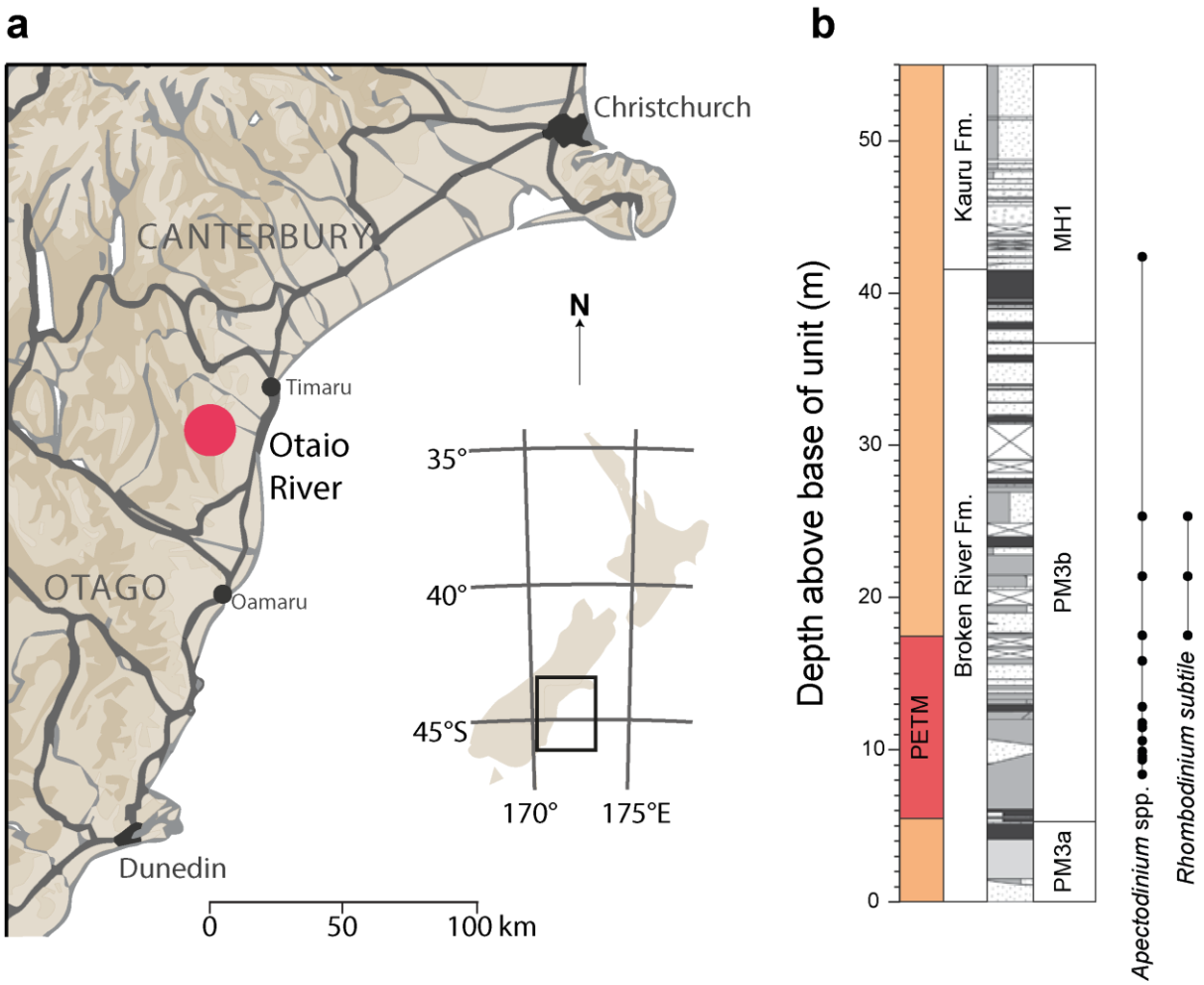

Figure 6.1 (a) present-day location of Otaio River, on the South Island of New Zealand. (b) a stratigraphical log of the Broken River Formation and Kaura Formation. Miospore zones and key biostratigrahic markers are also shown. Adapted from Inglis *et al.* (2021). FM.; Formation.

6.2.2 Bulk Geochemistry

A total of 39 samples were firstly freeze-dried and crushed with a ceramic mortar and pestle. Low-resolution (*n* = 24) TOC and $\delta^{13}C_{org}$ records have been generated previously within

Inglis *et al*. (2021). To increase the sampling resolution, we undertook additional bulk geochemical analyses on 15 samples. We follow the procedure described in detail in Section 2.2. In summary, 10 % hydrochloric acid (HCl) was added to the powdered sediments to remove inorganic carbon then dried in a 50 °C oven. Based on the available TOC dataset, an initial ~10 mg of samples were used for analyses. The TOC and $\delta^{13}C_{org}$ values were then acquired from an Elementar vario ISOTOPE select elemental analyser coupled with Isoprime 100 isotope ratio mass spectrometer (EA-IRMS; see Section 2.4.1). In total, 8 samples were re-weighed to ~0.5–1.5 mg (n = 6) and ~15–30 mg (n = 2) for analyses, due to carbon concentrations falling over or under the calibration range of the elemental analyser, respectively.

6.2.3 Organic Geochemistry

All the samples (n = 39) were freeze-dried, crushed, extracted, and analysed for underivatised BHPs at the Royal Netherlands Institute for Sea Research (NIOZ).

6.2.3.1 Bligh and Dyer Extraction

The extraction procedure for BHPs followed a modified Bligh and Dyer (see Section 2.3.1.2). In summary, ~1 or 2 g of sediment were weighed depending on whether it has relatively high (>20 %) or low (<6 %) TOC values, respectively. The samples were then ultrasonicated for 15 min with a solvent mixture consisting of methanol (MeOH), dichloromethane (DCM), and phosphate buffer (2:1:0.8, *v:v:v*). After centrifugation, the supernatants were collected and the whole procedure was repeated a further 2 times. Extra DCM and phosphate buffer was added to obtain a new ratio of MeOH:DCM:phosphate buffer (1:1:0.9, *v:v:v*) and achieve a biphasic separation, from which the DCM layers were collected. The aqueous phase was washed with just DCM two more times. The aforementioned procedure was repeated on the same solid residue, however with trichloroacetic acid (TCA) in replacement of the phosphate buffer for the first solvent mixture. The two extracts were combined into one Bligh Dyer extract (BDE), dried under a continuous flow of N_2 and stored at -20 °C until analysis.

6.2.3.2 UHPLC-HRMS Analyses

For analysis, ~2 mg of BDE was transferred using DCM:MeOH (1:1, *v:v*) and dried. This aliquot was filtered through a 0.45 µm regenerated cellulose syringe filter (4 mm diameter; Grace Alltech) with 200 µl of a deuterated diacylglyceryltrimethylhomoserine (DGTS-d9; Avanti® Polar Lipids), added as an internal standard (I.S.), and LC-MS grade MeOH:DCM (9:1, *v:v*) for rinsing. Once dried, the filtered sample was resuspended with 200 µl of the LC-MS grade MeOH:DCM (9:1, *v:v*) and 50 µl was transferred for analysis. The analyses were performed on an Agilent 1290 Infinity I ultra-high-performance liquid chromatography (UHPLC) coupled to Q Exactive orbitrap high resolution tandem mass spectrometry

($HRMS^2$), equipped with a heated electrospray ionisation (HESI) probe (ThermoFisher Scientific) (see Section 2.4.4).

6.2.3.3 Identification and Semi-Quantification

The advancement in the analysis of BHPs via UHPLC-HRMS, has led to an expansion in the range of structures that can be detected (Hopmans *et al.*, 2021). As such, we applied a targeted approach for identification, based on BHPs found in the Cobham Lignite (Talbot, Bischoff, *et al*., 2016) and those that are commonly associated with the methane cycle (Table 6.1).

Most BHPs were identified using the retention times and exact masses displayed within the partial mass chromatograms and supplementary data of Hopmans *et al.* (2021). The different stereoisomers of BHT (*i.e.* BHT-34R and BHT-x) and the position of the methylation on BHPs were separated by retention time, following Schwartz-Narbonne *et al*. (2020) and Hopmans *et al.* (2021), respectively. We further confirmed our identifications by at least examining one MS^2 spectrum for the diagnostic fragments of each parent ion (Hopmans *et al.*, 2021). For the N-formylated-amino-BHPs, the retention times, exact masses, and an example of an MS^2 spectrum for N-formylated aminopentol can be found in Richter *et al.* (2023). See Appendix XI for the retention times, exact masses, and MS^2 spectra of anhydro BHPs.

A summed mass chromatogram with varying combinations of the protonated ($[M+H]^+$), ammoniated ($[M+NH_4]^+$), and/or sodiated ($[M+Na]^+$) adducts (within 5 ppm mass accuracy) were used for integrating BHP peak areas (Table 6.1). Peaks lower than the signal threshold ($<1 \times 10^5$) were typically excluded from integration but noted to be below detection (b.d.). The I.S. peak areas were also integrated and the average of the total dataset calculated. This average I.S. value was then used to normalise for variations in the response factor between samples, caused by both matrix effects and deviations in the performance of the MS. The subsequent corrected BHP peak areas (response unit; RU) were also further normalised for variations in TOC values, and reported as RU per g of OC. This is summarised in the following equation:

$$\left[\left(\frac{\text{Average I.S. peak areas}}{\text{I.S. peak area}}\right) \times \text{BHP peak area}\right] \times \left[\text{weight of sediment} \times \left(\frac{\text{TOC}}{100}\right)\right] \qquad \text{(Equation 6.1)}$$

Since we only have a ‘surrogate’ standard, the BHPs are mostly discussed in the context of relative abundance. Interpretations of RU per g of OC are restricted to this study, where samples were analysed together. Future work requires fully constraining the ionisation efficiencies of individual BHPs and/or synthesising an authentic standard to attain absolute concentrations (Hopmans *et al.*, 2021). Until then, caution should be taken when making quantitative comparisons with other sites.

Table 6.1 List of targeted BHPs (and their abbreviated names), grouped by side chains with similar moieties (see Appendix X for BHP structures). Combinations of the protonated ($[M+H]^+$), ammoniated ($[M+NH_4]^+$), and/or sodiated ($[M+Na]^+$) adducts were used for integrations.

Side chain configurations	BHPs	Adducts
hydroxy-BHPs	*bacteriohopane-32,33,34,35-tetrol (BHT) BHT-34R BHT-x 2Me-BHT 3Me-BHT *BHT cyclitol ether (-CE) 3Me-BHT-CE bacteriohopane-31,32,33,34,35-pentol (BHpentol) 3Me-BHpentol bacteriohopane-30,31,32,33,34,35-hexol (BHhexol) 3Me-BHhexol	$[M+NH_4]^+$, $[M+H]^+$, $[M+Na]^+$ $[M+NH_4]^+$, $[M+H]^+$, $[M+Na]^+$ $[M+NH_4]^+$, $[M+H]^+$, $[M+Na]^+$ $[M+H]^+$, $[M+Na]^+$
amino-BHPs	*35-aminobacteriohopane-32,33,34-triol (aminotriol) 3Me-aminotriol *35-aminobacteriohopane-31,32,33,34-tetrol (aminotetrol) 3Me-aminotetrol *35-aminobacteriohopane-30,31,32,33,34-pentol (aminopentol) 3Me-aminopentol	$[M+H]^+$, $[M+Na]^+$ $[M+H]^+$, $[M+Na]^+$ $[M+H]^+$, $[M+Na]^+$
MC-BHPs	35-methylcarbamate-aminotriol (MC-aminotriol) MC-aminotetrol MC-aminopentol	$[M+H]^+$, $[M+Na]^+$
ethenolamine-BHPs	ethenolamine-BHT ethenolamine-BHpentol ethenolamine-BHhexol	$[M+H]^+$
N-formylated-amino-BHPs	N-formylated aminotriol N-formylated aminotetrol N-formylated aminopentol	
anhydro BHPs	*anhydro-BHT *2Me-anhydro-BHT *3Me-anhydro-BHT *3,31Me-anhydro-BHT[a] *anhydro-BHpentol anhydro-aminotriol 3Me-anhydro-aminotriol	$[M+NH_4]^+$, $[M+H]^+$, $[M+Na]^+$ $[M+NH_4]^+$, $[M+H]^+$, $[M+Na]^+$ $[M+NH_4]^+$, $[M+H]^+$, $[M+Na]^+$ $[M+NH_4]^+$, $[M+H]^+$, $[M+Na]^+$ $[M+NH_4]^+$, $[M+H]^+$, $[M+Na]^+$ $[M+H]^+$, $[M+Na]^+$ $[M+H]^+$, $[M+Na]^+$

Note. *BHPs discovered in the Cobham Lignite, with [a]a tentative placement of a methyl on the C-31 position (Talbot, Bischoff, *et al.*, 2016).

The following discussion also refers to BHPs individually and by their side chain configuration (Table 6.1). A further distinction is made between the anhydro BHPs and the rest of the BHPs (*i.e.* non-anhydro BHPs), based on evidence that the former are diagenetic products (*e.g.,* Eickhoff *et al.*, 2014). To test this grouping and identify other relationships, potentially beyond structural differences, we applied principal component analysis (PCA) using R Package stats (R Core Team, 2021). The BHP dataset was first normalised per sample (*i.e.*

relative abundances) and then per compound, in order to standardise the relative abundances and assess variance equally.

6.3 Results

6.3.1 Bulk Geochemistry

Overall, the TOC record at Otaio River reveals a wide range of values, from a minimum of 0.2 % to a maximum of 71.6 % (Figure 6.2a). The lower half of the section (~0–25 m) exhibits more frequent fluctuations. Between 29 and 41.15 m, is an interval with consistently high TOC values, averaging at 60.3 %. Above 49.15 m the TOC values remains close to 0 %, however there are only three samples in the upper 10 m of the section (~45–55 m).

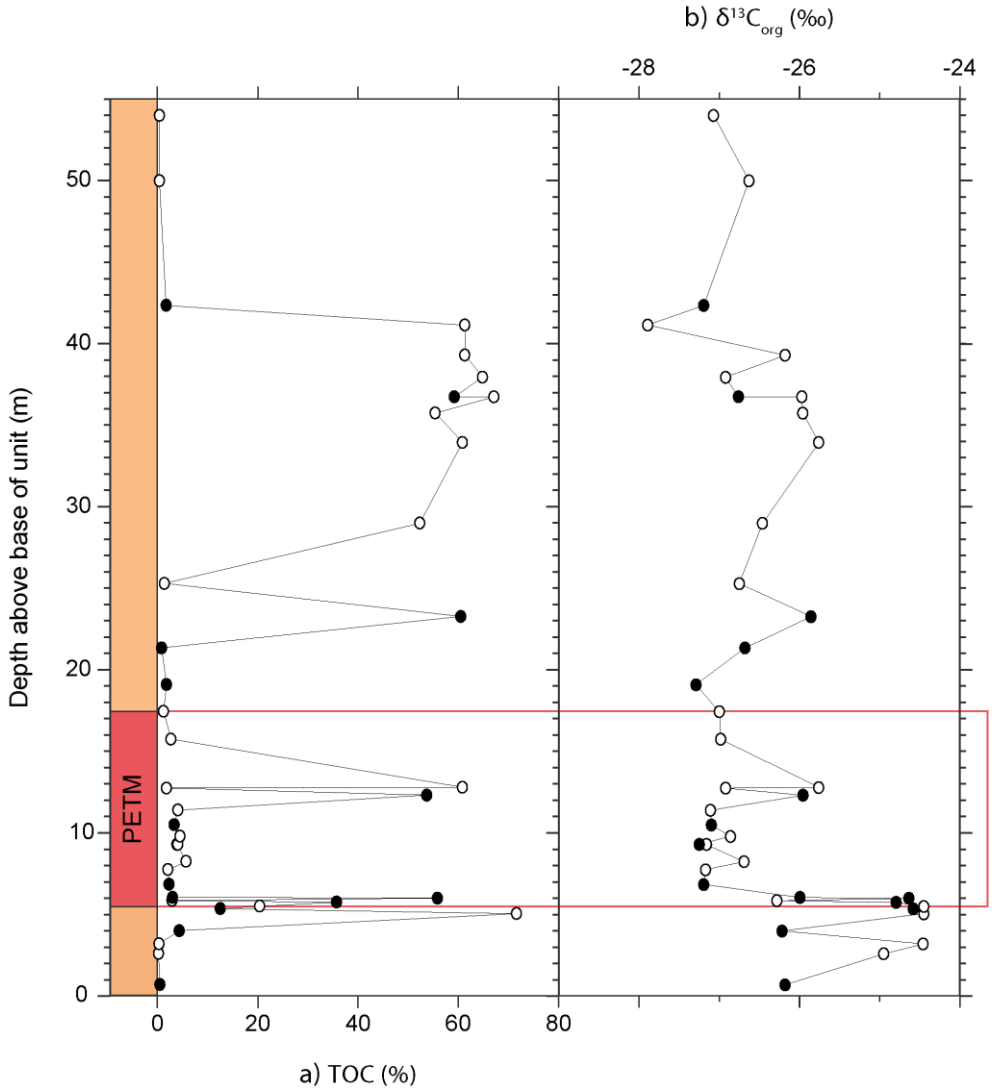

Figure 6.2 Bulk sediment (a) total organic carbon (TOC), and (b) $\delta^{13}C$ of organic carbon ($\delta^{13}C_{org}$) at Otaio River. The closed symbols are from this study and the open symbols are from Inglis *et al.* (2021). The core PETM is outlined by a pink box.

The $\delta^{13}C_{org}$ results from this study (closed symbol; Figure 6.2a) closely follow the trends seen in the published record of Inglis *et al.* (2021) (open symbol; Figure 6.2b). This is with the exception of two data points at 0.7 m and 4 m, that present a negative shift of ~1 ‰ away from the average pre-PETM $\delta^{13}C_{org}$ value. However, these excursions are not as large as the CIE, which was identified to be ~2 ‰ (Inglis *et al.*, 2021). This ~2 ‰ CIE defined the onset of the PETM at 5.5 m. Using the expanded dataset, we document a greater CIE (2.6 ‰) than previously reported, from -24.6 ‰ (at 6 m) to -27.2 ‰ (at 6.85 m) (Figure 6.2b).

6.3.2 Polyfunctionalised Hopanoids

6.3.2.1 Distribution of BHPs

Of the 33 targeted BHPs, 16 were identified at Otaio River (Figure 6.3). In general, anhydro BHPs are the most dominant of the different side chain configurations, making up 80% of the total BHP profile (Figure 6.3). Within this group, anhydro-BHT (38 %) and anhydro-aminotriol (23 %) have the highest relative abundances. The remainder of the anhydro BHPs are comprised of 3Me-anhydro-BHT and anhydro-BHpentol (7 %), 2Me-anhydro-BHT and 3,31Me-anhydro-BHT (2 %), and 3Me-anhydro-aminotriol (0.5 %).

For the non-anhydro BHPs, aminotriol and BHT-CE are the most dominant (7 %), followed by BHT (3 %) and 3Me-aminotriol (2 %). The rest of the non-anhydro BHPs have very low relative abundances (<1 %). However, it is worth noting the presence of two isomers of BHT, with a clear prevalence of BHT-x over BHT-34R, in addition to aminopentol, MC-aminotriol, and ethenolamine-BHT. Both MC-aminotriol and ethenolamine-BHT were only present in peaks just below the 1×10^5 signal threshold, however are included as they have shown potential as methanotroph biomarkers (Richter *et al.*, 2023). On the other hand, 2Me-BHT and 3Me-BHT are excluded from this study as they are only in one sample and therefore cannot provide insight into changes in distribution across the Otaio River section. This is in addition to 3Me-BHT-CE, aminotetrol, MC-aminotriol, and N-formulated aminotriol, which were found based on retention times and exact masses but lacked an MS^2 (*i.e.* MC-aminotriol) or had an MS^2 that was not sufficiently diagnostic for confirming identification.

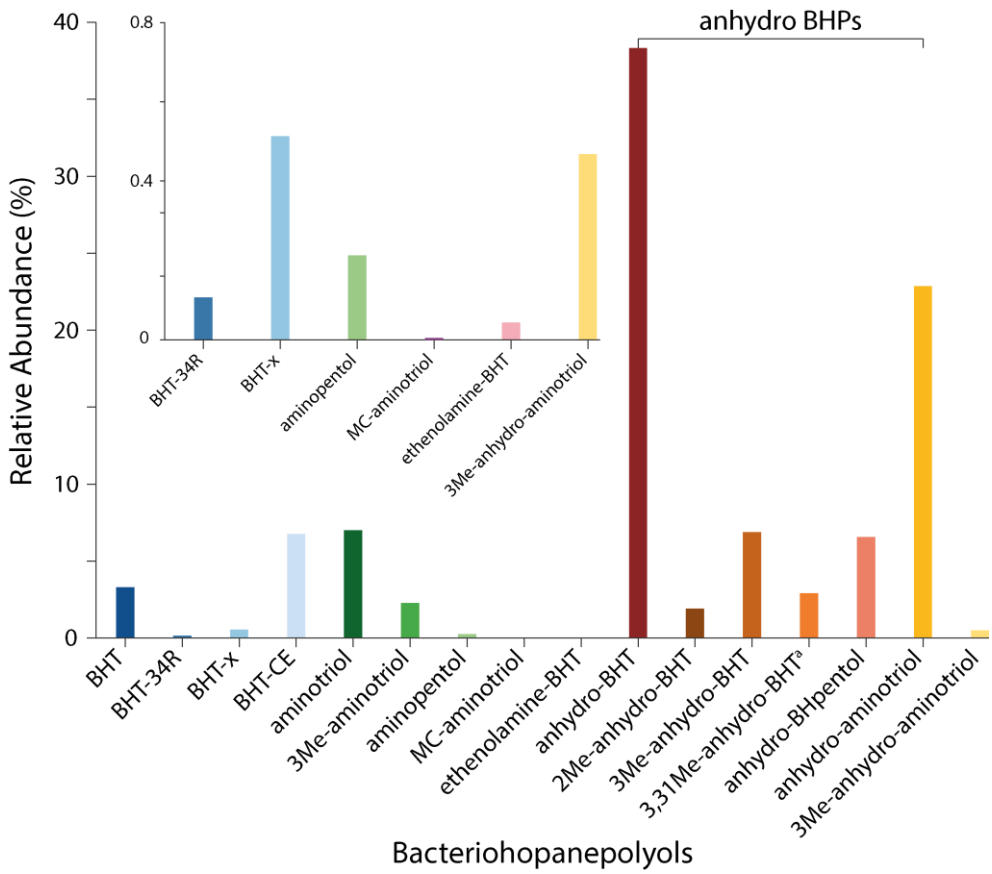

Figure 6.3 The total bacteriohopanepolyols (BHPs) profile and their relative abundances (%) at Otaio River. The insert bar chart shows BHPs with relative abundances <1 %. The BHPs are ordered by their side chain configuration. [a]refers to the tentative placement of a methyl on the C-31 position (Talbot, Bischoff, *et al.*, 2016).

6.3.2.2 BHP Profiles across the Otaio River Section

The total BHP abundance markedly varies across the Otaio River section (Figure 6.4a). See Appendix XII for individual BHP abundances in response unit (RU) per g of OC. Prior to the PETM (from 0 to 5.35 m), anhydro BHPs comprise an average of 85 % of the BHP profile, whereas the non-anhydro BHPs only account for 15 %. This changes during the PETM (from 5.5 to 17.45 m) to an average of 71 % and 29 %, respectively. At 12.75 m, the non-anhydro BHPs make up a combined 64 % majority. The shift from pre-PETM to the PETM is most likely driven by an increase in BHT-CE (Appendix XII), and to a lesser degree aminotriol (Figure 6.3). BHT-CE exhibits the greatest variability (s.d. = 7 × 10^9 RU per g of OC; Appendix X), with the exception of anhydro-BHT and anhydro-aminotriol. On the other hand, BHT remains relatively constant and 3Me-aminotriol presents a slight decline (Appendix XII). There is also a decrease in anhydro-BHT (Appendix XII), and to a smaller degree 3Me-anhydro BHT (Figure 6.3). However, anhydro-aminotriol, and the less prevalent anhydro-BHpentol (Figure 6.3), exhibits an increase at the PETM and at the base of the section (Appendix XII). Following the PETM, there appears to be a return to the late Paleocene distribution of BHPs (Figure 6.4b). A distinct interval between 29 and 41.15 m, has very low

total BHP abundance, with a maximum of 3 × 10^{10} RU per g of OC. Most of the BHPs show a decline, with the exception of a few BHPs (*i.e.* 2Me-, 3Me-, and 3,31Me-anhydro-BHT) that increase between 33.95 to 41.15 m (Appendix XII). There is also a dominance of anhydro BHPs in this interval (Figure 6.4a), which is likely due the complete absence of BHT-CE (Appendix XII).

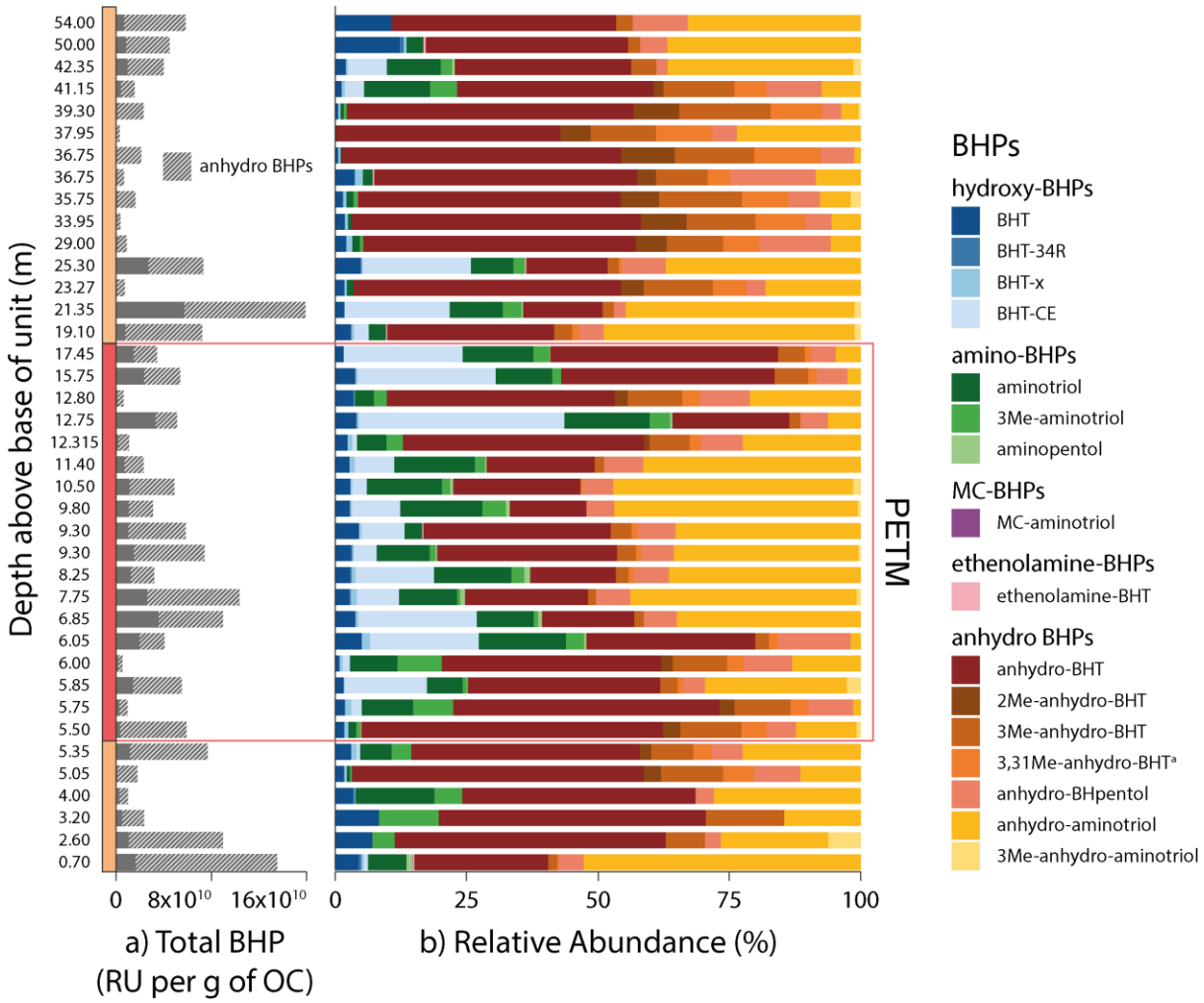

Figure 6.4 The bacteriohopanepolyols (BHPs) profiles across the Otaio River section (note that the y-axis is not on a continuous scale). (a) abundance of total BHP in response unit (RU) per g of OC, with the proportion of anhydro BHPs highlighted by diagonal lines, and (b) relative abundances (%) of individual BHPs, within each sample. The BHPs are grouped by their side chain configuration, and [a]refers to the tentative placement of a methyl on the C-31 position (Talbot, Bischoff, *et al.*, 2016). The core PETM is outlined by a pink box.

6.3.2.3 Principal Component Analysis

The first two principal components explains 51 % of the total variance in the BHP dataset (34.1 % and 16.9 % on PC1 and PC2, respectively; Figure 6.5). Most of the anhydro BHPs (red label; Figure 6.5), with the exception of anhydro-aminotriol and 3Me-anhydro-aminotriol, positively score on PC1. These anhydro BHPs are generally found in samples with high TOC

values (light blue points; Figure 6.5). On the other hand, the non-anhydro BHPs negatively score on PC1 and are in samples with low TOC values (dark blue points; Figure 6.5). This suggests that changes in the TOC record drives most of the variability seen in the BHP dataset. Within the non-anhydro BHPs, the amino-BHPs cluster together with a negative score on PC2 (green label; Figure 6.5). However, this relationship is mostly caused by the occurrence of MC-aminotriol and ethenolamine-BHT in three samples (purple and pink label, respectively; Figure 6.5). The variable influencing PC2 is unknown, but it is clearly separate to the TOC record and mostly changes in samples with low TOC values.

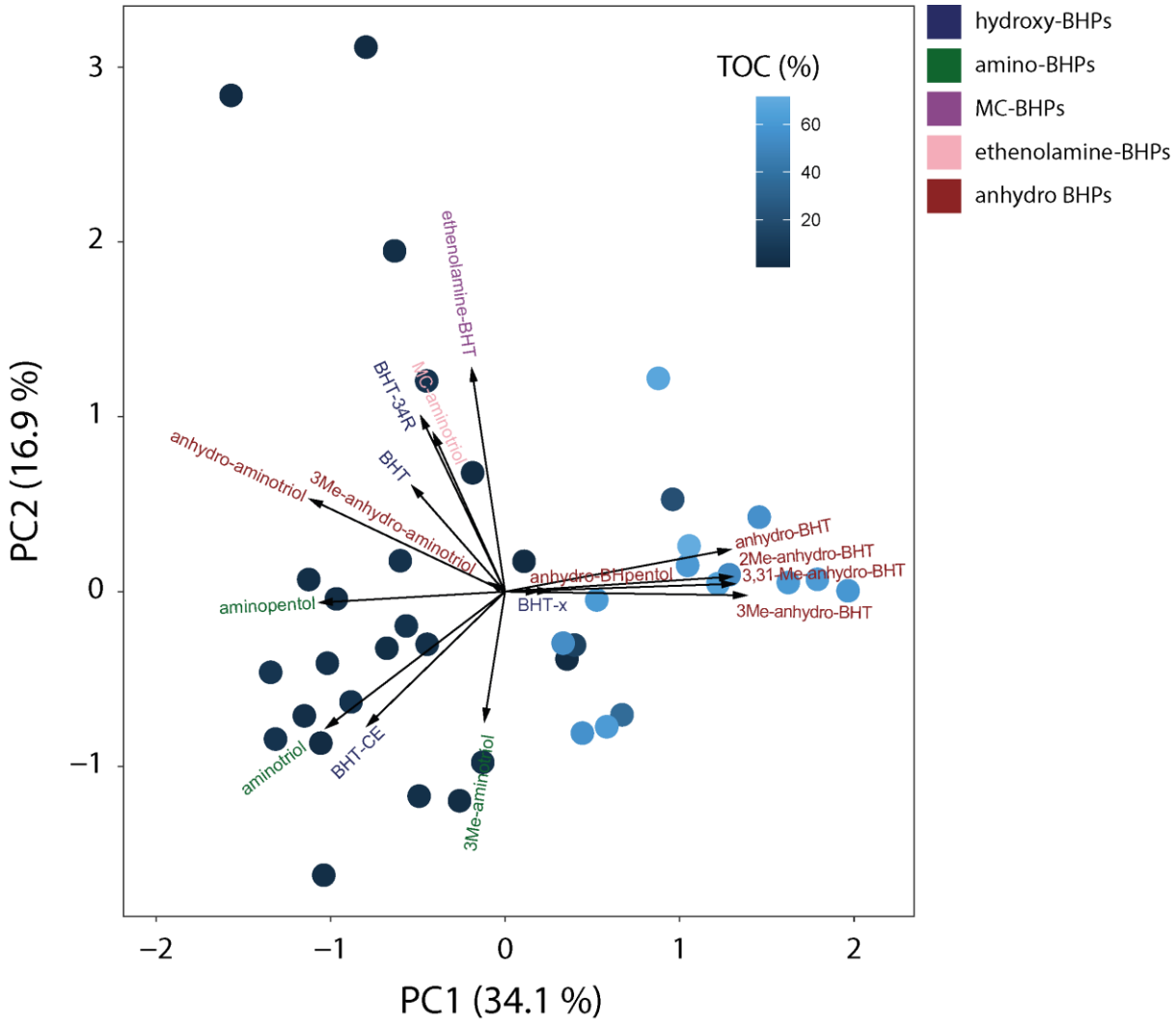

Figure 6.5 Principal Component Analysis (PCA) biplot of the BHP dataset from Otaio River. The colour of the labels group the BHPs by their side chain configurations. The colour of the points indicates the TOC values, which are on a continuous scale from low (dark blue) to high (light blue).

6.4 Discussion

6.4.1 The Origin of BHPs at Otaio River

6.4.1.1 Modern or Past?

The application of BHPs at Otaio River relies upon the assumption that they represent remnants of the past, and not the modern, microbial community. There is evidence showing that bacteria can thrive ~2 km below the ocean floor (*e.g.,* Inagaki *et al.*, 2015). Although we cannot fully preclude the possibility of BHP input from recently living bacteria, this study is focused upon methane oxidising bacteria (MOB), which are typically aerobic and thus unlikely to be derived from subsurface (*i.e.* anoxic) production. Furthermore, there are observations that suggest that the BHPs are not of modern origin.

Firstly, there is a pronounced trend in the $\delta^{13}C_{hop}$ record across the Otaio River section (Inglis *et al.*, 2021), that does not change with lithological variability (*i.e.* marine interbeds vs. lignite) (Figure 6.1b). Following the arguments made by Pancost *et al.* (2007), for Cobham Lignite, this trend reflects a 'true' signal. Namely, both sites present a marked decrease in $\delta^{13}C_{hop}$ values that only occurs during the onset of the PETM. The non-anhydro BHPs are also influenced by a variable unrelated to lithology (Figure 6.5). Specifically, BHT-34R, aminopentol, MC-aminotriol, and ethenolamine-BHT abundances do not show a statistically significant (P >0.005) correlation to lithology. As will become evident in Section 6.4.2, these BHPs exhibit distinct fluctuations, supporting a past origin of BHPs at Otaio River.

Secondly, anhydro BHPs are the most dominant of the side chain configurations at Otaio River (Figure 6.3). Anhydro BHPs are thought to be early diagenetic products of other BHPs, and not from modern production (*e.g.,* Eickhoff *et al.*, 2014). Moreover, their prevalence is characteristic of geologic sediments (*e.g.,* Talbot *et al.*, 2016). The PCA biplot further confirms that the anhydro BHPs are distinct from the rest of the BHPs (Figure 6.5). However, Otaio River also contains a wide diversity of non-anhydro BHPs that might not be expected in such old deposits. For instance, at Cobham Lignite, only BHT and the three amino-BHPs were discovered (Talbot, Bischoff, *et al.*, 2016), whereas, in this study, two isomers of BHT, BHT-CE, 3Me-aminotriol, MC-aminotriol, and ethenolamine-BHT are additionally found (Figure 6.3). These compounds are reported for the first time in PETM-aged sediments. Based on heat degradation experiments, Osborne (2016) concluded that the 'weaker' ether bond in BHT-CE could lead to a preferential early degradation into BHT. Talbot *et al.* (2016) thus used the absence of BHT-CE at Cobham Lignite as evidence against a modern origin of BHPs. However, there is also a lack of correlation between BHT and BHT-CE at Otaio River (R^2 <0.1; Appendix XIII Figure 8), and BHT-CE has been identified in Quaternary-aged deposits (*e.g.,* Cooke, Talbot and Wagner, 2008; Handley *et al.*, 2010). Therefore, the

prevalence of complex BHPs (*i.e.* BHT-CE and amino-BHPs), despite their high degree of functionality, likely suggests ideal preservation conditions rather than subsurface production at Otaio River. This agrees with evidence of lower thermal maturity, indicated by an average CPI value of 6.1 (Inglis *et al.*, 2021).

6.4.1.2 Potential Source Organisms

Amongst the non-anhydro BHPs, the compounds with the highest relative abundances at Otaio River are aminotriol, BHT-CE, and BHT (Figure 6.3). In modern settings, this distribution has been associated with a heterotrophic bacterial population (Talbot, Mcclymont, *et al.*, 2016). Yet, BHT is derived from a diverse range of prokaryotes (*e.g.,* Rohmer, Bouvier-Nave and Ourisson, 1984) and found ubiquitously (*e.g.,* Talbot *et al.,* 2003), limiting its utility as a biomarker. Indeed, Otaio River is characterised by the lack of a discernible pattern in the changes of BHT with depth (Figure 6.4b). On the other hand, BHT-CE exhibits two peaks during the PETM (6.85 and 12.75 m), as well as one post-PETM (21.35 m; Figure 6.4b). However, similar to BHT, BHT-CE has been found in multiple cultures, including methanotrophs, methylotrophs, purple non-sulphur bacteria, acetic acid bacteria, and cyanobacteria (see Eickhoff *et al.*, 2013 and references therein). The genes required for the formation of BHT-CE are known (*hpnJ;* Belin *et al.*, 2018), however no studies have applied bioinformatics analysis (*i.e.* a Basic Local Alignment Search Tool; BLAST). As such, the true extent of organisms that are capable of synthesising BHT-CE remains undiscovered.

In contrast to BHT and BHT-CE, amino-BHPs are specifically associated with aerobic MOB (see Talbot *et al.*, 2014; Talbot, Bischoff, *et al*., 2016 and references therein). Within MOB cultures, there is a distinct divide in the distribution of amino-BHPs between Type I and Type II methanotrophs. Type I preferentially synthesises aminopentol (*e.g.,* Neunlist and Rohmer, 1985; Cvejic *et al.*, 2000; Talbot *et al.*, 2001), with aminotriol and aminotetrol produced in trace amounts (*e.g.,* Kusch and Rush, 2022). However, not all species synthesise aminopentol (*e.g.,* Rush *et al.*, 2016), and it was recently identified in non-MOB (*e.g.,* Kolouchová *et al.*, 2021; Elling *et al.*, 2022). Type II primarily synthesises a mix of aminotriol and aminotetrol (*e.g.,* Rohmer, Bouvier-Nave and Ourisson, 1984; Talbot *et al.*, 2008; van Winden, Talbot, *et al.*, 2012). Sulphate-reducing bacteria (SRB) are the only other known sources of aminotetrol, and one species was found with low levels of aminopentol (see Blumenberg *et al.*, 2012 and references therein). Aminotriol, on the other hand, has many producers including non-MOB (Talbot and Farrimond, 2007; see Talbot *et al*., 2008 and references therein). This may explain the consistent prevalence of aminotriol, alongside BHT and BHT-CE, throughout the Otaio River section (Figure 6.4b). The Cobham Lignite is characterised by similar relative abundances of aminotriol and aminotetrol (Talbot, Bischoff, *et al*., 2016). The ratio between these two compounds were suggested to be more indicative

of a population of aerobic MOB rather than a SRB. Intriguingly, there is a complete lack of aminotetrol at Otaio River, which helps exclude SRB as a potential source (*e.g.,* Blumenberg *et al.*, 2012). Consequently, aminopentol at Otaio River may signify a dominance of the Type I over Type II methanotrophs. Overall, the total BHP profile at Otaio River indicates a likely role of both heterotrophy and Type I regulated aerobic methanotrophy.

The most relatively abundant BHP at Otaio River is anhydro-BHT (Figure 6.3). This was also reported to be the case in the other two available studies on pre-Quaternary-aged sediments (van Dongen *et al.*, 2006; Talbot, Bischoff, *et al.*, 2016). The formation of anhydro-BHT has been proposed to be from the dehydration and cyclisation of the BHT side chain (*e.g.,* Bednarczyk *et al.*, 2005; Talbot *et al.*, 2005), and/or the loss of the adenine moiety from adenosylhopane (*e.g.,* Cooke, Talbot and Wagner, 2008). Bradley *et al.* (2010) speculated that anhydro-BHT may be an 'accidental' product caused by a reductive loss of phosphate from a phosphorylated intermediate created during the conversion of adenosylhopane to ribosylhopane. The latter an essential biosynthetic step, by the gene *hpnG,* for the generation of all BHPs (see Belin *et al.*, 2018 and references therein). However, an increase in anhydro-BHT is observed in sediments at depth (*e.g.,* Bednarczyk *et al.*, 2005; Saito and Suzuki, 2007). This is often concurrent with a decrease in BHT, suggesting that anhydro-BHT may indeed be sourced from BHT (*e.g.,* Cooke, Talbot and Wagner, 2008; Handley *et al.*, 2010; Blumenberg *et al.*, 2013), although the opposite is seen when comparing active microbial mats vs. relict microbial mats (Drozd, Evans and Summons, 2023). Moreover, experiments that induced acid catalysis (Schaeffer *et al.*, 2008) and simulated diagenetic conditions (*e.g.,* Eickhoff *et al.*, 2014; Osborne, 2016) have confirmed the transformation of BHT and/or BHT-CE to anhydro-BHT. At Otaio River, where the whole section has undergone a relatively similar degree of diagenesis, the trend with depth will not be apparent. However, BHT and anhydro-BHT abundances exhibits a positive correlation (R^2 = 0.4; Appendix XIII Figure 9), indicating a potential shared source. This is not as prominent with BHT-CE (R^2 <0.1; Appendix XIII Figure 10), although aminotriol and 3Me-aminotriol show a stronger correlation with their anhydro BHP homologues (R^2 = 0.6 and 0.3, respectively; Appendix XIII Figure 11 and 12). Yet, it is curious that there is a dearth of 2Me- and 3Me-BHTs when 2Me- and 3Me-anhydro-BHTs are present (Figure 6.3). Future work is required to better understand the diagenetic products of BHPs. If an anhydro BHP can be linked to a precursor compound, they could also be used to identify source organisms. In the geologic record, where these degraded but more recalcitrant forms dominate (*e.g.,* Talbot *et al.*, 2016), this would allow the opportunity to use BHPs in an extensive way as achieved in modern settings. However, in order to trace bacterial metabolisms, the precursor BHP must also be source-specific.

6.4.2 Controls on the Abundance and Distribution of BHPs across the Otaio River Section

6.4.2.1 Importance of Depositional Environment

The abundance and distribution of BHPs changes markedly across the Otaio River section (Figure 6.4a). There is a negative correlation between the total BHP abundance and TOC values (R^2 = 0.4; Appendix XIII Figure 14). Additionally, the distribution is strongly influenced by lithological variability (Figure 6.5). In particular, the anhydro BHPs, with the exception of 2Me-anhydro-BHT and 3Me-anhydro-aminotriol, all correlate to lithology with a statistically high significance ($P < 0.001$). These observations suggest that the depositional environment exerts a first-order control on BHP variations.

In the lignites, there are less BHPs per g of OC. This is especially noticeable between 29 and 41.15 m, where TOC values average at 60.28 % (Figure 6.2a) and the total BHP abundance does not exceed 3×10^{10} RU per g of OC (Figure 6.4a). Wetland deposits are typically dominated by a supply of plant-derived organic matter, hence the relatively smaller contribution of BHPs in the organic carbon pool within the lignites. Modern tropical wetlands are further characterised by enhanced rates of primary productivity and degradation (Pancost, 2024). Although Otaio River has a paleo-latitude of 56.1°S (Huber and Caballero, 2011; Hollis *et al.*, 2012), proxy-based mean annual air temperature reconstructions indicate tropical conditions during the PETM (~20–26 ° C; Inglis *et al.*, 2021). The exacerbated degradation rates also explains the distribution of non-anhydro BHPs vs. anhydro BHPs in the lignites, with a comparatively lower or higher proportion, respectively (Figure 6.6b). This was similarly observed in the lignite layers at Cobham Lignite (Talbot, Bischoff, *et al.*, 2016).

The marine interbeds, on the other hand, have more BHPs per g of OC and a 20 % higher proportion of the non-anhydro BHPs (Figure 6.6a). A larger relative abundance of 'biohopanoids', as referred to in Talbot *et al.* (2016), was also noted in the non-lignite layers at Cobham Lignite. Since the non-lignite layers are composed of fine-grained clay with low permeability, enhanced preservation was reasoned (Talbot, Bischoff, *et al.*, 2016). However, both the anhydro and non-anhydro BHPs increase in the marine interbeds at Otaio River (Appendix XII). In fact, all of the BHPs have a higher relative abundance, with the exception of 2Me-anhydro-BHT, which is curiously only present in the lignites, and 3,31Me-anhydro-BHT (Figure 6.6). This suggests that there is a greater input of BHPs and thus its transformation products, as well as enhanced preservation.

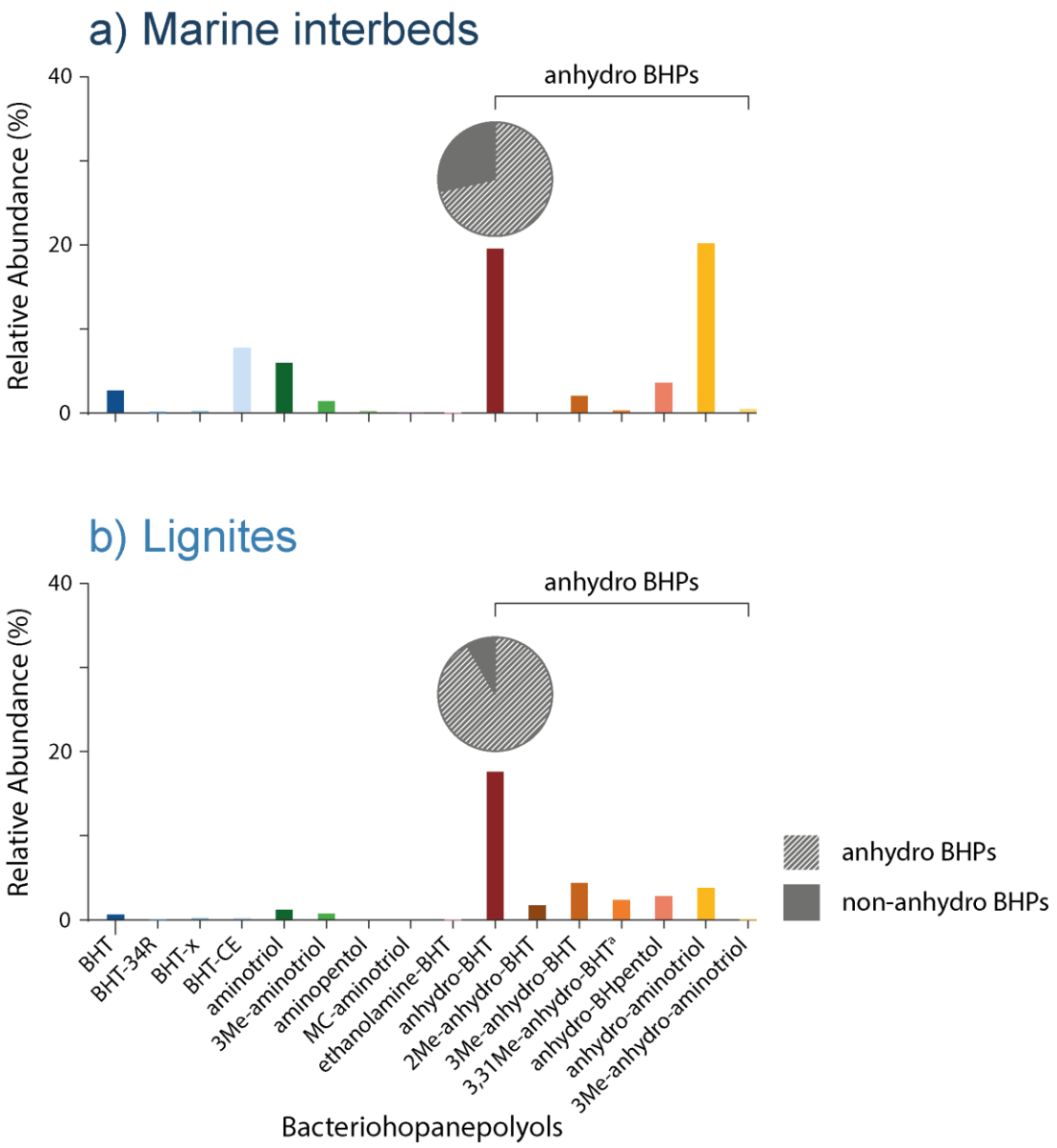

Figure 6.6 The total bacteriohopanepolyols (BHPs) profile and their relative abundances (%) in the (a) marine interbeds and (b) lignites at Otaio River. The pie charts show the proportion of anhydro BHPs (solid colour) vs. non-anhydro BHPs (diagonal lines). The BHPs are ordered by their side chain configuration. [a]refers to the tentative placement of a methyl on the C-31 position (Talbot, Bischoff, *et al.*, 2016).

6.4.2.2 Terrestrial Input in the Marine Interbeds

To investigate whether the greater abundance of BHPs in the marine interbeds at Otaio River is due to export from terrestrial regions or in situ marine production, we exploit two stereoisomers of BHT (*i.e.* BHT-34R and BHT-x). BHT-x, also known as BHT-II (*e.g.,* Kusch *et al.*, 2018) and named for its unknown stereochemistry, has exclusively been reported in *Ca.* Scalindua, a marine anaerobic ammonium oxidation (anammox) bacteria (Rush *et al.*, 2014; Schwartz-Narbonne *et al.*, 2020). Paired 16S genomic sequencing and the distribution of ladderane lipid further solidified BHT-x as a biomarker for marine anammox (van Kemenade *et al.*, 2022). As such, it has been used as a proxy to investigate the marine

nitrogen cycle, as far back as the Pliocene (*e.g.,* Rush *et al.*, 2019; Zindorf *et al.*, 2020; van Kemenade *et al.*, 2023), although its application is complicated by mechanisms of lateral transport (van Kemenade *et al.*, 2022). On the other hand, BHT-34R has five known producers to date, including three aerobic heterotrophic bacteria (*Frankia* spp.; Rosa-Putra *et al.*, 2001, *Acetobacter pasteurianus* and *Komagataeibacter xylinus*; Peiseler and Rohmer, 1992), an aerobic Type II methanotroph (*Methylocella palustris*; van Winden, Talbot, *et al.*, 2012), and a freshwater anammox bacteria (*Ca.* Brocadia; Schwartz-Narbonne *et al.*, 2020). However, environmental (*e.g.,* Hemingway *et al.*, 2018; Lengger *et al.*, 2019; Elling *et al.*, 2021) and in vitro (Schwartz-Narbonne *et al.*, 2023) studies have identified that BHT-34R, as well as BHT-x, from anammox bacteria can be distinguished by low $\delta^{13}C$ values. Regardless of the multiple potential sources, all the known producers of BHT-34R are terrestrial. Therefore, the distribution of BHT-34R vs. BHT-x in the marine interbeds may be able to differentiate between terrestrial input vs. marine input, respectively.

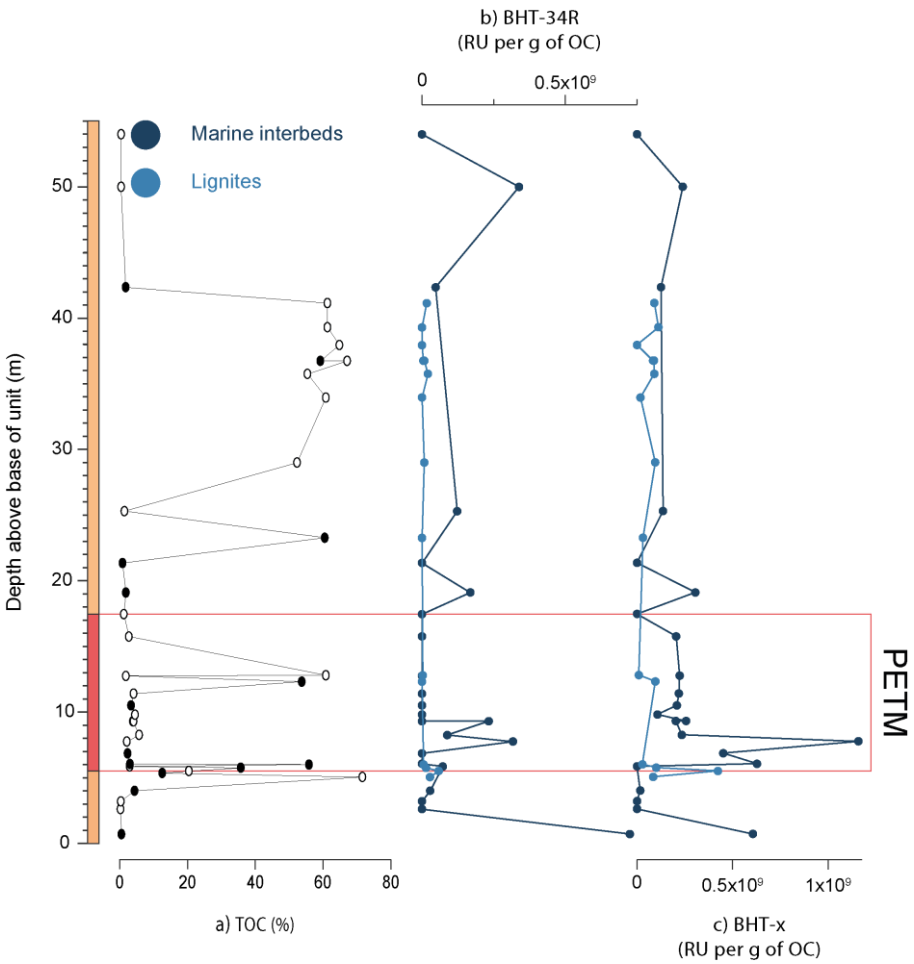

Figure 6.7 The Otaio River section with (a) total organic carbon (TOC), and the abundances of (b) BHT-34R and (c) BHT-x, in response unit (RU) per g of OC. The closed symbols are from this study and the open symbols are from Inglis et al. (2021). The BHP abundances are separated into marine interbeds (dark blue) and lignites (light blue). The core PETM is outlined by a pink box.

Overall, both these compounds are observed at Otaio River, with a greater relative abundance of BHT-x compared to BHT-34R (Figure 6.3). Although BHT (*i.e.* BHT-34S) was discovered at Cobham Lignite, the isomers were not detected due to analytical constraints (Talbot, Bischoff, *et al.*, 2016). Fluctuations in BHT-34R and BHT-x, within the marine interbeds, correlate at specific depths across the Otaio River section (Figure 6.7b-c), which could indicate simultaneous increases in both terrestrial and marine input. However, this argument is complicated by the fact that BHT-x is also counterintuitively present in the lignites (Figure 6.7c). *Ca.* Scalindua can tolerate relatively high salinity (Okabe *et al.*, 2024), and BHT-x has been found in multiple environments with such conditions (Kusch *et al.*, 2021). Therefore, this supports that the lignites at Otaio River represent a coastal (brackish) wetland, whereby BHT-x is transported by the tide and/or produced in situ.

The relatively lower abundance of BHT-34R in the lignites at Otaio River is also counterintuitive due to its inferred terrestrial origin (Figure 6.7b). Furthermore, the complete lack of aminopentol is unexpected (Figure 6.6), especially considering that it only occurs in the lignite layers at Cobham Lignite (Talbot, Bischoff, *et al.*, 2016). The lignites at Otaio River may only be capturing a very local signal within the wetland, compared to fluvial or marine deposits that encompass a wider catchment. Interestingly, in addition to aminopentol, MC-aminotriol is also only found in the marine interbeds at Otaio River (Figure 6.6). MC-aminotriol was recently discovered in cultures of a few Type I methanotroph genera (*e.g.,* Talbot *et al.*, 2001; Rush *et al.*, 2016). Type I methanotrophs are typically isolated from aquatic systems (see Kusch and Rush, 2022 and references therein). Therefore, the existence of both aminopentol and MC-aminotriol in the marine interbeds at Otaio River should be unsurprising. Yet paradoxically, the distribution of BHPs in modern marine settings are often associated with a low abundance of aminopentol, and dominated by a range of novel MC-BHPs (Rush *et al.*, 2016) and aminotriol (*e.g.,* Talbot *et al.*, 2014; Osborne, 2016; Rush *et al.*, 2016). Since MC-BHPs are sparsely reported elsewhere (*e.g.,* Smit, 2021), they were put forwards as a biomarker for methanotrophy in the marine realm, where the presence of aminopentol is not favoured (Rush *et al.*, 2016), and in lakes (Richter *et al.*, 2023). Aminopentol, on the other hand, have mostly been found in the modern terrestrial realm (see Rush *et al.*, 2016 and references therein), such as peats (*e.g.,* van Winden, Talbot, *et al.*, 2012) and lakes (*e.g.,* Talbot and Farrimond, 2007). Observations of aminopentol in near-shore marine sediments (*e.g.,* Zhu *et al.*, 2010; Wagner *et al.*, 2014; Spencer-Jones *et al.*, 2015; De Jonge *et al.*, 2016; Rush *et al.*, 2016) have thus been linked to export of organic matter from land, and hence their concentrations with depth used as a proxy to reconstruct wetland methane cycling during the Quaternary (*e.g.,* Talbot *et al.*, 2014; Rush *et al.*, 2016; Schefuß *et al.*, 2016; Spencer-Jones, Wagner and Talbot, 2017).

Considering that the marine interbeds at Otaio River contain aminopentol and smaller quantities of MC-aminotriol and aminotriol, this supports both terrestrial and marine input.

Input of terrestrial organic matter is consistent with the prevalence of pollen, spores, and leaf fossils at Otaio River (Pancost *et al*., 2013). Moreover, there is a dominance of plant- (*i.e. n*-alkanes) and soil- (*i.e.* branched glycerol dialkyl glycerol tetraethers; brGDGTs) derived biomarkers, the latter resulting in a high average branched and isoprenoid tetraether (BIT) index of 0.95 (Inglis *et al.*, 2021). Overall, the greater abundance and structural diversity in the marine interbeds at Otaio River is likely due export from terrestrial regions and in situ marine production. Other studies have also made this argument for marine sediments with similar observations in the abundance and distribution of BHPs (*e.g.,* Handley *et al.*, 2010; Wagner *et al.*, 2014). Therefore, the BHPs within the marine interbeds at Otaio River may reflect changes occurring in the terrestrial realm.

6.4.2.3 A Methane Cycle Perturbation during the PETM

Although the abundance and distribution of BHPs at Otaio River are primarily controlled by the depositional environment and terrestrial input, there are also distinct fluctuations superimposed on these variables. In particular, the relative abundance of non-anhydro BHPs within the marine interbeds and lignites are higher in the core PETM, by 7 % and 22 %, respectively (Figure 6.4a). This drastic change in the proportion of non-anhydro BHPs between the latest Paleocene and PETM lignites is not observed at Cobham Lignite (Talbot, Bischoff, *et al*., 2016). These non-anhydro BHPs could reveal information on other variables that are influencing the microbial community composition. This includes, for example, the role of temperature, pH, hydrology, and/or biogeochemistry on the production and preservation of BHPs. To investigate methane cycling, we primarily focus on BHPs that change in abundance with the $\delta^{13}C_{hop}$ record (Figure 6.8).

Interestingly, the highest abundance of aminopentol, aminotriol, and anhydro-aminotriol (Figure 6.8b-d) occur during the PETM and coincide with the most negative $\delta^{13}C_{hop}$ values (-60.9 ‰) at 6.85 m (Figure 6.8a). This is with the exception of the increase at 0.7 m and 21.35 m (Figure 6.8b-d), which is in part exaggerated as a result of very low TOC values combined with relatively large BHP peak areas. All three BHPs exhibit fluctuations within the marine interbeds that correlate at specific depths across the Otaio River section (Figure 6.8b-d). Although, aminotriol has lower source-specificity, and is found in organisms other than methanotrophs, the PCA biplot reveals a potential relationship with aminopentol (Figure 6.5). Similarly, anhydro-aminotriol behaves very differently to the other anhydro BHPs (Figure 6.5), and there is a likely link with aminotriol (Appendix XIII Figure 12).Taken together, the evidence imply that these BHPs may share a common source during certain intervals.

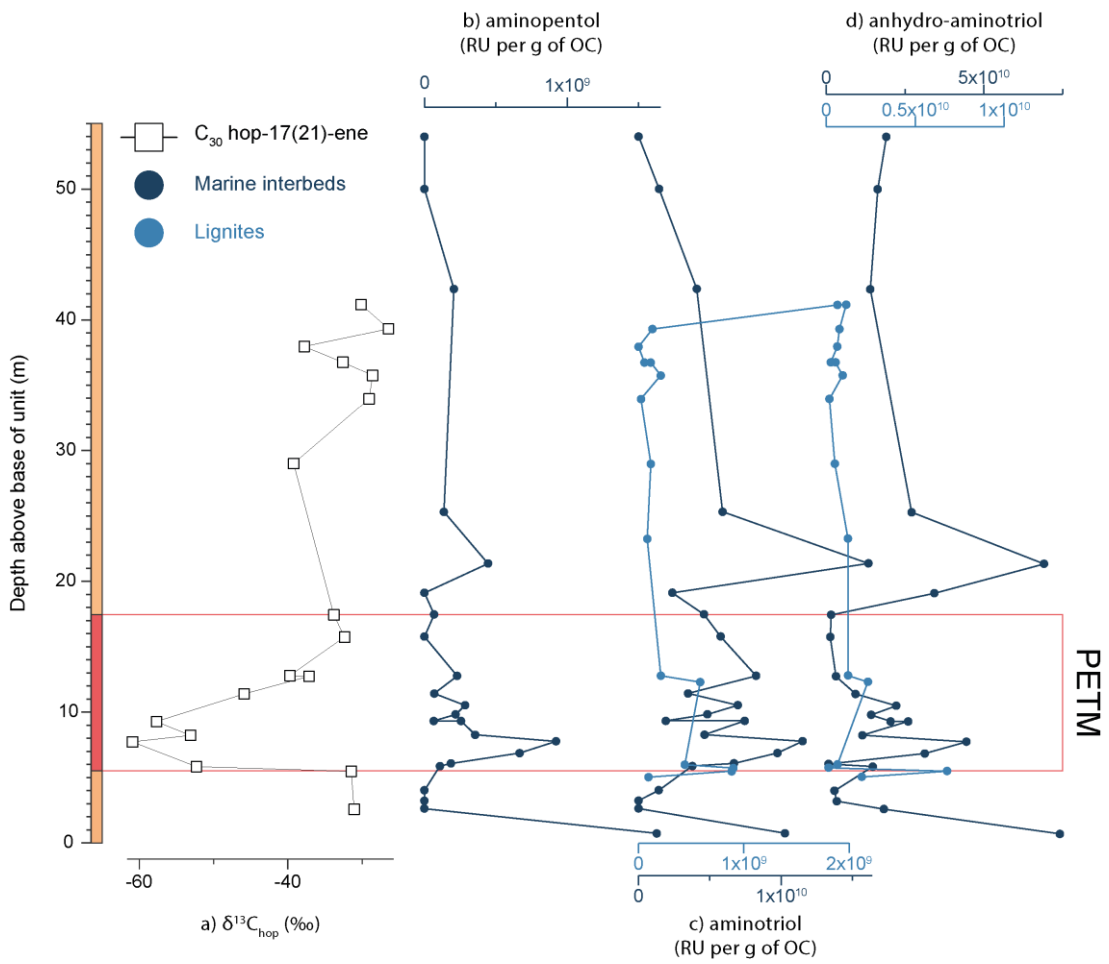

Figure 6.8 The Otaio River section with (a) the $\delta^{13}C$ of C_{30} hop-17(21)-ene (Inglis *et al.*, 2021), and the abundances of (b) aminopentol, (c) aminotriol, and (d) anhydro-aminotriol, in response unit (RU) per g of OC. The BHP abundances are separated into marine interbeds (dark blue) and lignites (light blue), with the exception of aminopentol which are only present in the marine interbeds. Note the two distinctly different scales for the marine interbeds vs. lignites. The core PETM is outlined by a pink box.

The findings here are remarkably comparable to the Cobham Lignite study (Talbot, Bischoff, *et al.*, 2016), where an increase in the relative abundance of aminopentol was noted at the onset of the CIE, with a maxima of 4 % (Talbot, Bischoff, *et al.*, 2016). Although this peak is greater than observed at Otaio River (1.7 %; Figure 6.4b), and in modern peats (Kim *et al.*, 2011; van Winden, Talbot, *et al.*, 2012; Talbot, Mcclymont, *et al.*, 2016), the comparison of sites with varying diversity should be undertaken with caution. Furthermore, the highest relative abundance in aminopentol at Cobham Lignite does not coincide with the most ^{13}C-depleted sample. Aminotriol and anhydro-aminotriol at Cobham Lignite also increases at the onset of the CIE, yet are not discussed in detail as there are peaks of a similar magnitude prior to and after the CIE (Talbot, Bischoff, *et al.*, 2016). This additionally applies to aminopentol (Talbot, Bischoff, *et al.*, 2016), whereas the change is more pronounced at Otaio River (Figure 6.8b). In fact, at Otaio River, the relative abundance of aminopentol is on

average twice as high in the core PETM compared to pre- and post-PETM (Figure 6.4b). Moreover, there is a consistent presence of aminopentol and a lack of aminotetrol throughout the Otaio River section. This suggests that the $\delta^{13}C_{hop}$ excursion reflects enhanced methanotrophy, and not a shift between Type I and Type II methanotrophs and their distinct metabolic pathways (van Winden *et al.*, 2010). Overall, this study supports previous findings of a methane cycle perturbation at Otaio River during the PETM (Inglis *et al.*, 2021). BHPs have only been examined in one other PETM-aged deposit (*i.e.* Cobham Lignite; Talbot *et al.*, 2016), however there are many similarities between the BHP trends, and both sites validate aminopentol as a biomarker for Type I methanotrophs. Cobham Lignite has additional evidence of methanogenesis during the PETM (based on GDGT-0; Inglis, Farnsworth, *et al.*, 2019), perhaps indicating enhanced CH_4 production, as well as CH_4 oxidation. This study further highlights the importance of assessing the full suite of BHPs, and their degradation products, as other compounds may also trace changes in the methane cycle.

6.4.3 Other Potential Biomarkers for Methanotrophy?

Since Otaio River exhibits enhanced aerobic methanotrophy during the PETM (inferred via $\delta^{13}C_{hop}$ and aminopentol), we can use this site to explore other potential BHP-based proxies for CH_4 oxidation. Similar to aminopentol, 3Me homologues of BHPs, especially amino-BHPs, have long served as biomarkers of Type I methanotrophs (*e.g.,* Neunlist and Rohmer, 1985; Zundel and Rohmer, 1985; Cvejic *et al.*, 2000; Talbot *et al.*, 2001). 3Me-amino-BHPs were not detected at Cobham Lignite (Talbot, Bischoff, *et al.*, 2016). At Otaio River, only 3Me-aminotriol is present, but with a relative abundance higher than aminopentol and closer to BHT. 3Me-anhydro-aminotriol is also plotted alongside 3Me-aminotriol (Figure 6.9b-c), as they correlate (Appendix XIII Figure 13) and the latter behaves differently to the other anhydro BHPs (Figure 6.5). Both the BHPs do not exhibit an increase, within the marine interbeds, at the onset of the PETM (Figure 6.9b-c), indicating that they are insensitive to changes in methane cycling. However, the highest abundance of 3Me-aminotriol in the lignites does occur within the core PETM (note the difference in scale; Figure 6.9b). Compared to 3Me-aminotetrol and 3Me-aminopentol, 3Me-aminotriol was only recently reported in cultures of Type I methanotrophs (Banta, Wei and Welander, 2015). However, BLAST analyses of the gene responsible for C-3 methylation in hopanoids (*hpnR*) has highlighted the widespread ability of non-MOB that can methylate at the C-3 position (*e.g.,* acetic acid bacteria and Actinobacteria), as well as methanotrophs that cannot (Welander and Summons, 2012; Mayer *et al.*, 2021). Regardless of the exact source, 3Me-BHPs have been suggested to promote cell survival during the late stationary phase for methanotrophs living in high CH_4 and low O_2 conditions (Welander and Summons, 2012). The influence of high temperatures in triggering the production of aminopentol and 3Me-aminopentol was

similarly observed (Osborne *et al.*, 2017). As such, the presence of 3Me-aminotriol in the lignites at Otaio River likely signifies a CH_4-rich environment, which is consistent with the evidence of enhanced aerobic methanotrophy during the PETM.

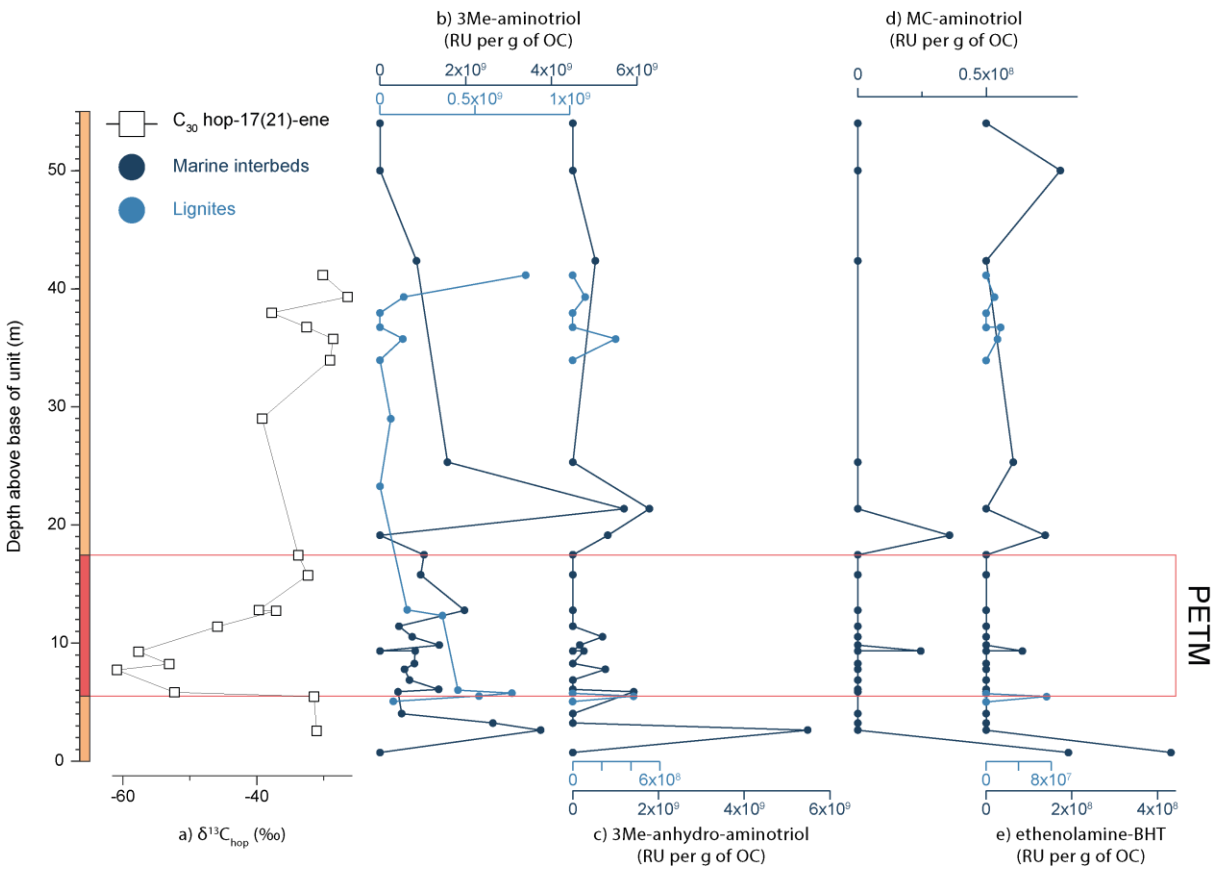

Figure 6.9 The Otaio River section with (a) the $\delta^{13}C$ of C_{30} hop-17(21)-ene (Inglis *et al.*, 2021), and the abundances of (b) 3Me-aminotriol, (c) 3Me-anhydro-aminotriol, (d) MC-aminotriol, and (e) ethenolamine-BHT, in response unit (RU) per g of OC. The BHP records are separated into marine interbeds (dark blue) and lignites (light blue), with the exception of MC-aminotriol, which are only present in the marine interbeds. Note the two distinctly different scales for the marine interbeds vs. lignites. The core PETM is outlined by a pink box.

A range of other novel BHPs have also shown promise as a complementary biomarker to aminopentol. Ethenolamine-BHT was recently found in a co-culture that included a lacustrine Type I methanotroph genus (*Methylobacter* sp.; Richter *et al.*, 2023). At Otaio River, MC-aminotriol and ethenolamine-BHT are not present during the PETM, with the exception of one minor peak in a marine interbed (9.3 m; Figure 6.9d-e). The overall low relative abundance of the novel BHPs makes it difficult to infer whether this is the result of reduced methanotrophy. However, MC-aminotriol and ethenolamine-BHT appear together but separate to the amino-BHPs in the PCA biplot (Figure 6.5), potentially signifying a different source. Indeed, MC-aminotriol was recently reported in a culture of nitrate-oxidising bacteria

(*Nitrococcus mobilis* and *Nitrobacter vulgaris*) under specific growth conditions (Elling *et al.*, 2022). Thus, future work is required to further confirm the ubiquity of these novel BHPs.

6.5 Conclusion

This study explores the abundance and distribution of BHPs at Otaio River (New Zealand). We identify a range of complex and novel BHPs that are reported for the first time in sediments as old as the PETM. The detection of a wide array of BHPs at Otaio River has been possible due to analytical developments. However, we also show that BHPs can be found well-preserved. We find a peak in aminopentol, concomitant with the most negative $\delta^{13}C_{hop}$ value during the PETM. Since there is a lack of aminotetrol throughout the Otaio River section, this suggests that the $\delta^{13}C_{hop}$ excursion reflects enhanced methanotrophy and is not influenced by a shift in the methanotroph community. The increase in aminopentol during the PETM has now been observed at two sites, further supporting the utility of aminopentol as a proxy for methanotrophs in the past. Overall, this study demonstrates the potential for BHPs to not only reconstruct methane cycle dynamics, but possibly a range of other environmental controls.

Chapter 7 Conclusion

7.1 Outcomes of the Thesis

This thesis addresses a major gap in our understanding on how the hydrologic cycle and associated terrestrial carbon cycle feedbacks may respond to future global warming. In particular, it shows the potential for the terrestrial realm to become a source of carbon (Bowen, 2013). A lipid biomarker approach was utilised to investigate the hothouse worlds (*i.e.* Paleocene and Eocene; ~66–34 Ma) and a hyperthermal event (*e.g.,* PETM) of the past. Firstly, several new terrestrial and marine records are developed, reconstructing both the hydrologic cycle in the tropics (see Section 7.1.1) and the mobilisation of OC_{petro} globally (see Section 7.1.2), during the latest Paleocene and PETM, respectively. Secondly, novel 'tools' are explored as proxies to identify the role of OC_{petro} and the methane cycle as positive feedback mechanisms during the PETM. This includes Raman spectroscopy for the oxidation of OC_{petro} (see Section 7.1.2) and BHPs for the oxidation of CH_4 (see Section 7.1.3). The following section summarises the main outcomes of Chapter 3 to 6, along with an overall outlook of the thesis (see Section 7.3). Additionally, recommendations for future work are suggested in Section 7.2.

7.1.1 A Dynamic Hydrologic Cycle in the Tropics during the Latest Paleocene

Most studies on the hydrologic cycle during hothouse climates are from the high-latitudes, and are restricted to the PETM (see Carmichael *et al*., 2017 and references therein) or Eocene (*e.g.,* Inglis, Carmichael, *et al.*, 2020; Elson *et al*., 2022; Inglis, Toney, *et al*., 2022). A δ^2H_{wax} record from a single tropical site in Venezuela (Mar2X; Jaramillo *et al.*, 2010) exhibits a wide range of values, potentially indicating a dynamic hydrologic cycle during the late Paleocene. **Chapter 3** investigates a new terrestrial sedimentary sequence, from Cerrejón Mine in Colombia, and establishes a tropical δ^2H_{wax} record.

First, a high-resolution bulk $\delta^{13}C_{org}$ record was generated and confirms that the section spans the latest Paleocene (~57–56 Ma), excluding the PETM. Spectral analysis reveals a potential obliquity signal, however the age model is only based on two tie points and assumes a LSR. The chain-length distribution and $\delta^{13}C_{wax}$ of n-alkanes imply minimal effects of post-depositional diagenesis at this site, but the vegetation community does change and may therefore bias the δ^2H_{wax} record. First-order estimates of δ^2H_{precip} were calculated for Cerrejón Mine (Chapter 3) and Mar2X (Jaramillo *et al.*, 2010), using a net fractionation factor of -121 ‰ (McFarlin *et al*., 2019). The two sites present similar δ^2H_{precip} values for the late Paleocene, with an average of -23 ‰ and -22 ‰, for Cerrejón Mine and Mar2X, respectively. A wide range of δ^2H_{precip} values, especially at Cerrejón Mine, also supports a dynamic

hydrologic cycle during the late Paleocene. In order to aid in interpretations, these results were compared to δ^2H_{precip} values acquired from water isotope-enabled model simulations (iCESM1.2). Interestingly, although the simulations comprise a range of atmospheric CO_2 concentrations (1x, 3x, 6x, and 9x, the PI value; Zhu, Poulsen and Tierney, 2019; Zhu *et al.*, 2020), the model-derived data varies much less and displays progressively more ^2H-enriched values with higher CO_2 levels. This highlights an issue with either the proxy- and/or model-based reconstructions, for example iCESM1.2 may not accurately represent orbital variability and/or the evolution of the ITCZ.

7.1.2 Enhanced OC_{petro} Mobilisation and Oxidation during the PETM

A recent study identified an order-of-magnitude increase in the delivery of OC_{petro} to the oceans, and argued that this may have been responsible for the long duration of the PETM (Lyons *et al.*, 2019). To determine whether this was a global phenomenon, and the timing within the PETM, **Chapter 4** utilises lipid biomarker thermal maturity ratios to fingerprint OC_{petro} in a global compilation of PETM-aged shallow marine sites. Deposits with evidence of extensive post-depositional diagenesis were excluded, resulting in a total of seven sites, including five new records.

The compilation revealed spatial heterogeneity in the response of thermal maturity ratios during the PETM. The most pronounced shifts towards thermally mature values are restricted to the subtropics and mid-latitudes, with the exception of one of the sites in the Atlantic Coastal Plain (Ancora) and Kheu River. Similar to Ancora, the high-latitude sites exhibit relatively stable trends in the thermal maturity ratios, implying that there were no distinct changes in the source of organic carbon. In contrast, Kheu River presents a shift towards thermally immature values during the PETM. Although this is the only site to show such a trend, it highlights the importance to consider the contribution of OC_{bio}, as a greater burial of OC_{bio} relative to OC_{petro} would result in a net carbon sink.

OC_{petro} mass accumulation rates (MARs) were calculated using a two-endmember mixing model. Overall, most sites are characterised by enhanced OC_{petro} MARs during the PETM. Several of these records, especially two sites from the Atlantic Coastal Plain (Ancora and SDB), indicate elevated OC_{petro} MAR into the recovery phases of the PETM. In addition, Tanzania and Kheu River present rapid fluctuations in the thermal maturity ratios. Episodic reworking at Tanzania, rather than changes in the atmospheric carbon reservoir, was previously suggested to explain oscillations in the $\delta^{13}C_{org}$ and $\delta^{13}C_{wax}$ records (Handley *et al.*, 2008; Aze *et al.*, 2014). The subtropics and mid-latitudes have also been associated with an increase in extreme precipitation events during the PETM. This is based on multiple evidence from proxies (*e.g.,* Carmichael *et al.*, 2017; Chen *et al.*, 2018) and models (*e.g.,* Carmichael, Pancost and Lunt, 2018; Rush *et al.*, 2021). Intermittent and intense rainfall on

land with minimal vegetation cover or soil development would explain the highly variable input of OC_{petro} observed in the thermal maturity ratios at Tanzania. Beyond the control of the hydrologic cycle on OC_{petro} MARs, local geomorphic processes also likely regulated the mobilisation of OC_{petro} (Hilton and West, 2020).

However, to determine the role of OC_{petro} within the global carbon cycle, requires constraining the fraction that oxidised into CO_2. Lyons *et al*. (2019) estimated a wide range (10^2 to 10^4 PgC) in the mass of OC_{petro}-derived carbon emitted globally during the PETM. This was based upon the extensive range of oxidation efficiencies observed in the present-day, from 15 % in erosive mountain basins to 85 % in large catchments such as the Amazon and Himalayan range (Bouchez *et al.*, 2010; Hilton *et al.*, 2011, 2014). Therefore, new techniques are required to reconstruct oxidation efficiencies in the past. Raman spectroscopy has been applied to assess OC_{petro} oxidation in modern settings (*e.g.,* Galy *et al.*, 2008; Bouchez *et al.*, 2010), but rarely in a geological context. Thus, **Chapter 5** focuses on exploring this approach in two of the PETM-aged shallow marine sites that exhibited contrasting trends in Chapter 4.

Overall, the Raman spectroscopy results are very consistent with the thermal maturity ratios (Chapter 4). The mid-Atlantic Coastal Plain site (SDB) presents large shifts, with an increase in thermally mature values and graphitised carbon during the PETM suggesting greater OC_{petro} delivery. The graphitised carbon was likely reworked into Cretaceous-aged deposits (*e.g.,* Sparkes *et al*., 2020), such as the Raritan Formation, and was subsequently eroded during the PETM. On the other hand, the Arctic Ocean site (ACEX) shows low and stable values, indicating a continuous source of thermally immature and disordered carbon throughout the record. Assuming that the modern Amazon shelf is a close analogue for the mid-Atlantic Coastal Plain (*e.g.,* Bouchez *et al.*, 2010), the increase in graphitised OC_{petro} during the PETM reflects the preferential oxidation of the more labile disordered OC_{petro}. This provides the first evidence of an enhanced oxidation efficiency during the PETM, although data from the Arctic Ocean implies that this may not be globally uniform.

7.1.3 The Utility of BHPs as a Proxy for the Methane Cycle in the Geologic Past

Very negative $\delta^{13}C_{hop}$ values during the PETM have been attributed to a perturbation in the methane cycle (Pancost *et al.*, 2007; Inglis *et al.*, 2021; Blumenberg *et al.*, 2024). However, the $\delta^{13}C_{hop}$ signature can be influenced by multiple source organisms, including methanotrophs, photoautotrophs, and heterotrophs. As Type I methanotrophs typically exhibit more ^{13}C-depleted values than Type II methanotrophs, this could also represent a shift in the methanotroph community. In contrast, BHPs are source-specific and can be derived from Type I or Type II methanotrophs. BHPs have been reported in samples as old as ~50 Ma (*e.g.,* Talbot *et al.*, 2016), but only in sites with exceptional preservation. Recent advancements in the analysis of BHPs via UHPLC-HRMS, have led to the discovery of a

diverse suite of new structures (Hopmans *et al.*, 2021). To determine the preservation and potential for these novel BHPs to trace methanotrophy in the past, **Chapter 6** examines the abundance and distribution of BHPs at Otaio River in New Zealand.

The diverse range of complex and novel BHPs detected, demonstrates excellent preservation potential of BHPs. This is especially the case in the marine deposits, which also exhibit evidence of export from terrestrial regions, as well as in situ marine production (*e.g.,* Handley *et al.*, 2010; Wagner *et al.*, 2014). Based on an assemblage comprised mostly of anhydro BHPs (*e.g.,* Eickhoff *et al.*, 2014), and distinct trends in the abundances and distributions of non-anhydro BHPs, the BHPs at Otaio River are likely representative of past microbial life and not of modern origin. The BHP profile at Otaio River is indicative of a largely heterotrophic bacterial population. The presence of aminopentol but lack of aminotetrol signifies the dominance of Type I over Type II methanotrophs. The ratio between aminopentol and aminotetrol is constant throughout the Otaio River section, confirming that the negative excursion in the $\delta^{13}C_{hop}$ record is not due to changes in the microbial community composition, but instead reflects enhanced AMO. Overall, the abundance of aminopentol, aminotriol, and anhydro-aminotriol increases with decreasing $\delta^{13}C_{hop}$ values. Remarkably, this is also observed in the other available study on PETM-aged sediments (Talbot, Bischoff, *et al.*, 2016). This validates the utility of aminopentol as a proxy for methane cycling during transient warming events.

7.2 Future work

7.2.1 Pollen-Corrected δ^2H_{precip} Estimates for the Tropics during the Latest Paleocene

First-order estimates of δ^2H_{precip} were calculated for the tropics during the latest Paleocene (Chapter 3). However, this does not account for vegetation change, which was previously evidenced by shifts in the floral composition (Jaramillo *et al.*, 2007, 2010), and suggested by the chain-length distribution of *n*-alkanes in Chapter 3. Studies have utilised $\delta^{13}C_{wax}$ to refine $\varepsilon_{wax/precip}$ values for specific vegetation types (*e.g.,* Tipple and Pagani, 2010; Tierney, Pausata and De Menocal, 2017; Windler *et al.*, 2020; Windler, Tierney and Anchukaitis, 2021) or for whole ecosystems (*e.g.,* Magill, Ashley and Freeman, 2013; Polissar *et al.*, 2021). However, tandem measurements of $\delta^{13}C_{wax}$ and δ^2H_{wax} have most commonly been used to correct for the contribution C4 plants (*e.g.,* Tipple and Pagani, 2010; Tierney, Pausata and De Menocal, 2017; Windler *et al.*, 2020; Windler, Tierney and Anchukaitis, 2021), which is not relevant for the early Paleogene as this carbon fixation pathway had not yet evolved. Similarly, $\delta^{13}C_{wax}$ can distinguish between two groups of woody C3 plants (*i.e.* angiosperm and gymnosperms; Diefendorf *et al.*, 2010), that were also found to have distinct $\varepsilon_{wax/precip}$ values. However, this has only been reported in semi-desert environments (Pedentchouk *et al.*, 2008).

Pollen data from the same samples could help refine δ^2H_{precip} estimates from Cerrejón Mine (Chapter 3). Insights from pollen records can be used to calculate plant-specific fractionation factors (Feakins, 2013). This has been successfully applied to the Miocene (Feakins, 2013) and Eocene (Inglis, Carmichael, *et al.*, 2020), and showed that vegetation isotope effects may cause up to 30‰ difference in values. However, this is only possible when appropriate modern analogues are available. In addition, biases in production, transportation, and/or preservation of palynomorphs must be considered (Feakins, 2013; Inglis, Carmichael, *et al.*, 2020; Inglis, Toney, *et al.*, 2022). Pollen from the upper Cerrejón Formation section is currently being processed and counted, at the Smithsonian Tropical Research Institute. Further work should focus on utilising this data to corroborate the trends in the proxy-derived δ^2H_{precip} records from the tropics (Chapter 3).

An unstable hydrologic cycle during the latest Paleocene can also be supported with new sites and/or proxies. However, future work should prioritise developing high-resolution δ^2H_{wax} records with robust age models. This is necessary to identify spatial synchronicity, timing of events, and leads and lags in the hydrologic cycle and response of the terrestrial realm (*e.g.,* Inglis, Toney, *et al.*, 2022). Moreover, in addition to advancing km-scale climate models (Slingo *et al*., 2022), expanding the number of δ^2H_{wax} records, especially in the lower latitudes, may reveal regional-scale patterns. With vulnerable communities living in low-lying coastal areas, it is crucial to understand how the tropical hydrologic cycle will evolve with increasing temperatures in the future (*e.g.,* Hoegh-Guldberg *et al.*, 2019).

7.2.2 Determining the Role of OC_{bio} within the Global Carbon Cycle during the PETM

Chapter 4 and 5 revealed that an intensified hydrologic cycle and global warming exacerbated the role of OC_{petro} oxidation as a carbon source during the PETM. However, this thesis does not investigate the mechanisms associated with carbon sinks. Organic carbon can also be categorised into the 'biospheric' (OC_{bio}) pool, which represents thermally immature organic carbon (10^2–10^4 years old), such as from vegetation and soils. If this OC_{bio} is deposited into the ocean, carbon is sequestered on geological timescales (*e.g.,* Stallard, 1998; Berhe *et al.*, 2007; Hilton *et al.*, 2008, 2012). This is thought to exceed the mass of carbon removed via silicate weathering (Hilton and West, 2020). Present-day observations show that erosion increases the delivery of OC_{bio} from land-to-sea (*e.g.,* Hilton *et al*., 2008; Hilton, Meunier, *et al*., 2011; Ramos Scharrón, Castellanos and Restrepo, 2012; Clark *et al*., 2013, 2016, 2017; Wang *et al*., 2019). Although, beyond a certain threshold there is a greater relative abundance of OC_{petro} (*e.g.,* Blair *et al*., 2003; Komada, Druffel and Trumbore, 2004; Hilton *et al*., 2015; Hilton and West, 2020).

Preceding the PETM, reduced organic carbon burial has been inferred (*e.g.,* Armstrong Mckay and Lenton, 2018), whereas a strengthening of this negative feedback mechanism has been used to explain the rapid recovery phase and termination of the PETM (*e.g.,* Kaya *et al.*, 2022; Papadomanolaki, Sluijs and Slomp, 2022). The latter is suggested over carbonate burial from silicate weathering, which takes place over much longer timescales (*e.g.,* Bowen and Zachos, 2010; Bowen, 2013). A greater accumulation of sediments with high TOC values, especially in continental margins and restricted basins, also signify efficient sequestering of organic carbon (*e.g.,* John *et al.*, 2008; Sluijs, Röhl, *et al.*, 2008; Dunkley Jones *et al.*, 2018). Furthermore, there is evidence that conditions favoured preservation of organic matter (*i.e.* deoxygenation and water column stratification; Clarkson *et al.*, 2021; see Papadomanolaki, Sluijs and Slomp, 2022 and references therein). However, determining the source (*i.e.* terrestrial vs. marine) of this organic carbon remains a major challenge (*e.g.,* Inglis, Toney, *et al.*, 2022). There are signs of both terrigenous material (*e.g.,* see Carmichael *et al.*, 2017 and references therein; Self-Trail *et al.*, 2017; Lyons *et al.*, 2019) and enhanced marine primary productivity/export (*e.g.,* Ma *et al.*, 2014). In fact, they may have worked in tandem, with erosion and weathering on land increasing nutrient availability in the ocean (*e.g.,* Pogge von Strandmann *et al.*, 2021). Biomarkers have been utilised to identify OC_{bio} in marine sediments, by tracing thermally unaltered plant- and soil-derived organic matter (*e.g.,* Inglis, Toney, *et al.*, 2022). Therefore, future studies should quantify the mobilisation of both OC_{petro} and OC_{bio}. These insights are necessary to provide a holistic view of the global carbon cycle and put into context how organic carbon modulated atmospheric CO_2 during the PETM.

7.2.3 Quantifying CO_2 Release via OC_{petro} Oxidation in the Geologic Past

In modern systems, OC_{petro} is distinguished from OC_{bio} by bulk or compound-specific radiocarbon (^{14}C) (*e.g.,* Bouchez *et al.*, 2010; Galy, Peucker-Ehrenbrink and Eglinton, 2015; Hilton *et al.*, 2015; Scheingross *et al.*, 2021). The analysis of ^{14}C has also been used to track in situ production of CO_2 from weathering (*e.g.,* Soulet *et al.*, 2021). However, due to the relatively short half-life (5,730 years), ^{14}C is not applicable to the geologic record beyond ~60 kyrs. Recent work has applied rhenium and its isotopic composition to trace oxidative weathering processes in the present-day (*e.g.,* Zondervan *et al.*, 2023). Although this approach may be applicable to the past, potential other influences on rhenium isotopes are not yet fully constrained.

Chapter 5 demonstrated the utility of Raman spectroscopy as an alternative qualitative approach to reconstruct oxidation efficiencies in the past. However, future work is required to validate the method in modern settings with different weathering intensities. This may aid in establishing a technique to quantify OC_{petro} oxidation, and subsequent CO_2 release, in the past. However, future investigations must consider the composition of source rocks, as this

determines friability and mineral associations which are important in protecting organic compounds from degradation (*e.g., Yu et al.*, 2021; Gu and Brantley, 2022). Moreover, there are still large uncertainties in our understanding of other abiotic and biotic influences on oxidation efficiency, for example temperature (*e.g.,* Soulet *et al.*, 2021), O_2 availability (*e.g.,* Scheingross *et al.*, 2021), and microbial activity (*e.g.,* Hemingway, Hilton*, et al.*, 2018).

7.2.4 Elucidating the Primary Driver of Enhanced Methane Cycling during the PETM

Evidence of enhanced aerobic methanotrophy, based on a decrease in $\delta^{13}C_{hop}$ records (Pancost *et al.*, 2007; Inglis *et al.*, 2021) and an abundance of aminopentol (Chapter 6; Talbot *et al.*, 2016), is mostly restricted to the onset of the PETM. Since these trends do not persist into the early Eocene, despite elevated temperatures, it was suggested that a rapid rather than gradual warming event is required to trigger a perturbation in the methane cycle (Inglis *et al.*, 2015, 2021). On the other hand, more negative $\delta^{13}C_{hop}$ values in a lignite deposit from Arctic Canada coincide with intervals of greater rainfall during the Eocene and Paleocene (Blumenberg *et al.*, 2024). However, neither study have reconstructed both temperature and precipitation. Therefore, future work should apply a multi-proxy approach to provide insights into the potential drivers of methane cycling. This could include establishing a $\delta^{2}H_{wax}$ record at Otaio River and/or utilising GDGTs as a temperature proxy at Stenkul Fiord (Arctic Canada).

7.2.5 Investigating Other Early Eocene Hyperthermals

This thesis has focused mostly on the PETM. However, the early Eocene encompasses multiple hyperthermals, the largest of which is the Eocene Thermal Maximum 2 (ETM2), also known as H-1 or the Elmo event (Lourens *et al.*, 2005). This was the first to occur after the PETM (~54.1 Ma), and was followed chronologically by H-2 (~54 Ma), I-1 (~53.65 Ma), I-2 (~53.55 Ma), J (~53.1 Ma), and the Eocene Thermal Maximum 3 (ETM3), also known as K or X (~52.8 Ma) (*e.g.,* Westerhold *et al.*, 2018). The exact number and nomenclature have yet to be established, and little is known due to the relatively recent discovery of these events. However, they are similarly characterised by negative CIEs, although much smaller in magnitude than the PETM (~1–2 ‰; Figure 1.2) and not always associated with a dissolution horizon (*e.g.,* Harper *et al.*, 2019). Several studies have linked the successive nature of the early Eocene hyperthermals to strong orbital forcings, specifically variations in Earth's eccentricity (*e.g.,* Lourens *et al.*, 2005; Deconto *et al.*, 2012; Kirtland Turner *et al.*, 2014; Littler *et al.*, 2014; Lauretano, Zachos and Lourens, 2018). For example, the role of eccentricity, and obliquity, were proposed to drive carbon emissions from the thawing of permafrost (*e.g.,* Deconto *et al.*, 2012). This reservoir would not have had time to 'recharge' between each hyperthermal, which would explain the progressively less pronounced CIE

across the early Eocene (*e.g.,* Deconto *et al.*, 2012). The shift in distribution of insolation caused by these external influences may have impacted the interaction of other complex carbon cycle processes. Therefore, future work should also explore transient warming events beyond the PETM, as potential analogues for future climate change. In particular, assessing whether OC_{petro} oxidation and methane cycling scales with increasing severity in climate aberrations.

7.3 Outlook

Employing a suite of lipid biomarkers, this thesis reveals the sensitivity of various biogeochemical cycles during hothouse worlds of the past. Terrestrial records from the tropics imply an unstable hydrologic cycle during the latest Paleocene. The role of positive feedback mechanisms within the terrestrial carbon cycle also appears heightened during the PETM. Widespread evidence for enhanced OC_{petro} mobilisation, and oxidation, in the past supports the growing body of work that have identified the importance of this carbon source in the present-day. Furthermore, multiple proxies suggest exacerbated methane cycling within wetland environments. Many studies have focused on reconstructing temperature and atmospheric CO_2 concentrations across the Cenozoic, yet biogeochemical cycles were previously overlooked due to the challenges of characterising these processes in the geologic record. However, new approaches to using existing techniques, such as Raman spectroscopy, and the discovery of a range of novel BHPs in PETM-aged deposits demonstrate exciting avenues for further research. The findings of this thesis implicates that temperature rise during a future hyperthermal will likely be amplified. Current estimates for a high emission/low mitigation climate scenario predicts 6.6–14.1 °C of warming by the end of the 23rd century, however GCMs do not fully incorporate potential contributions from OC_{petro} and methane oxidation to atmospheric GHGs. Therefore, the vital next step is to focus on quantifying these positive feedback mechanisms within the global carbon cycle.

Appendix I

Figure 1 Location of sites where there are proxy-based data representing an increase (blue symbol) or decrease (red symbol) in precipitation during the PETM. Palaeogeographic reconstructions of 56 Ma, adapted from Carmichael *et al.* (2017).

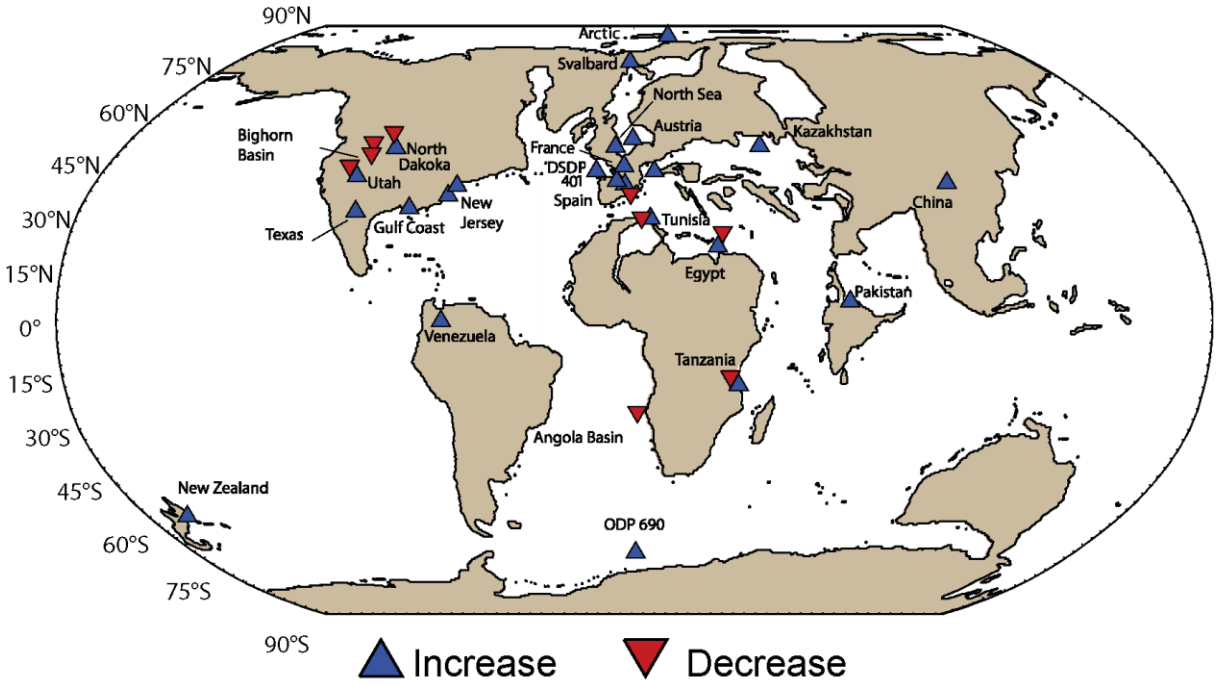

Appendix II

Figure 2 Generalised stratigraphical log of the upper Cerrejón Formation and the base of the Tabaco Formation (Chapter 3). The coals are numbered from the oldest to youngest. WRV-04774 and WRV-04752 are cores drilled by Caarbones del Cerrejón LLC. Adapted from Jaramillo *et al.* (2007).

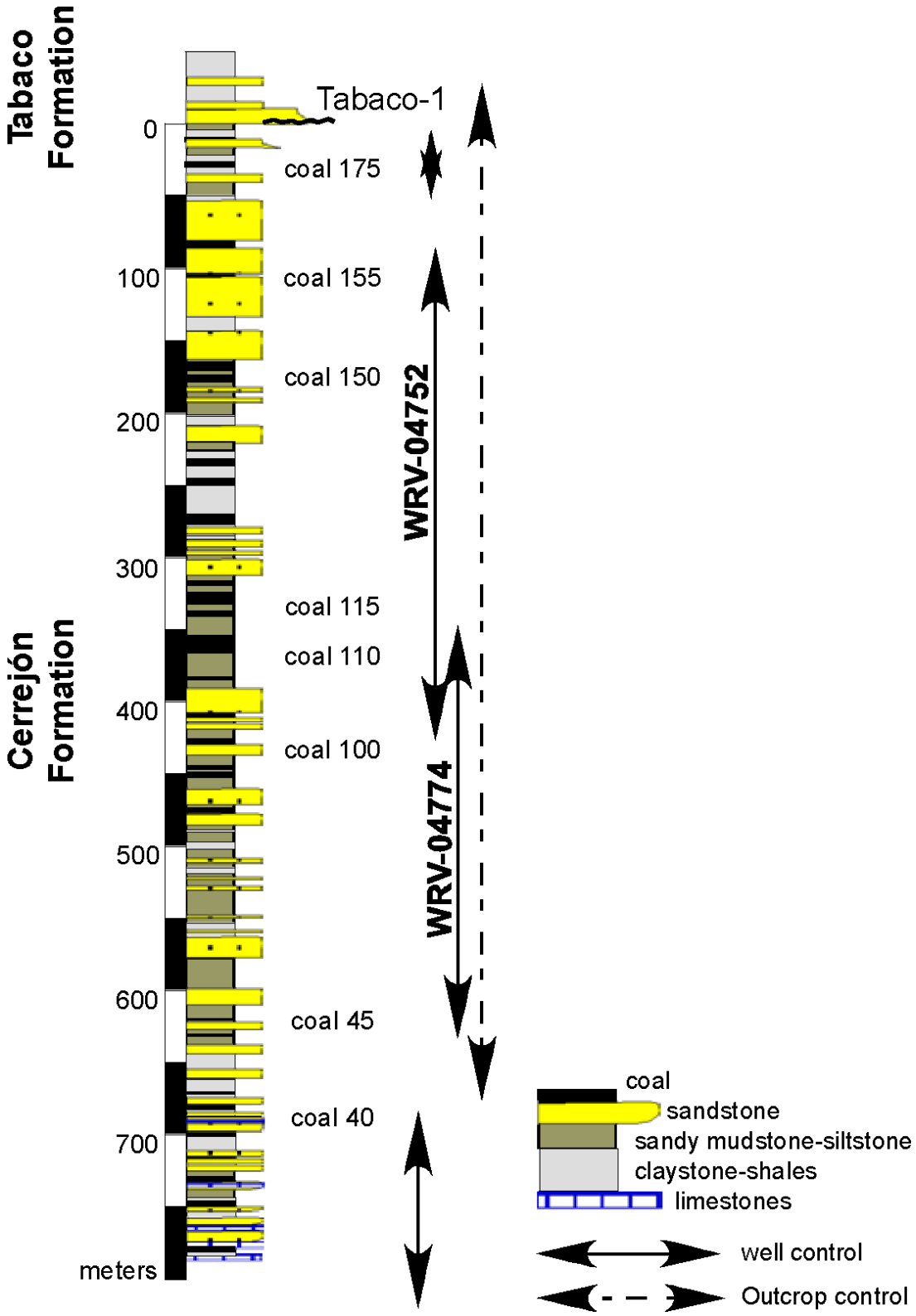

Appendix III

Table 1 The average chain length (ACL) data discussed in Chapter 3. The ACL is calculated using the equation defined by Bush and McInerney (2013). Where, *n* refers to odd numbered *n*-alkanes from C_{25} to C_{33}.

Depth (m)	ACL
39.36	25
40.4	28.5
40.42	28.1
41.17	28.4
41.27	27.9
41.97	25
52.82	26.4
74.19	26.5
84.56	25.5
94.89	25.6
110.14	25
120.4	27.7
129.42	28.1
130.6	27
136.59	28.6
136.86	28.4
143.11	25
153.51	28.5
164.05	27.1
174.54	26.3
181.48	27.8
181.8	28.1
182.13	28.3
184.8	25.7
189.15	28
189.35	28.1
189.75	28.1
190.1	27.9
190.43	28.1
195.02	27.7
205.25	25
215.66	25.4
221.1	28.6
221.5	28
225.41	29.4
225.96	27.9
228.94	27.8
236.35	27.9
246.53	28.5

Appendix IV

Figure 3 The δ^2H of precipitation (δ^2H_{precip}) from Cerrejón Mine (Chapter 3), calculated for C_{29} (white circle and dashed line) and C_{31} (black circle and solid line) *n*-alkanes. The error bars represent 1 s.d. of the duplicate measurements.

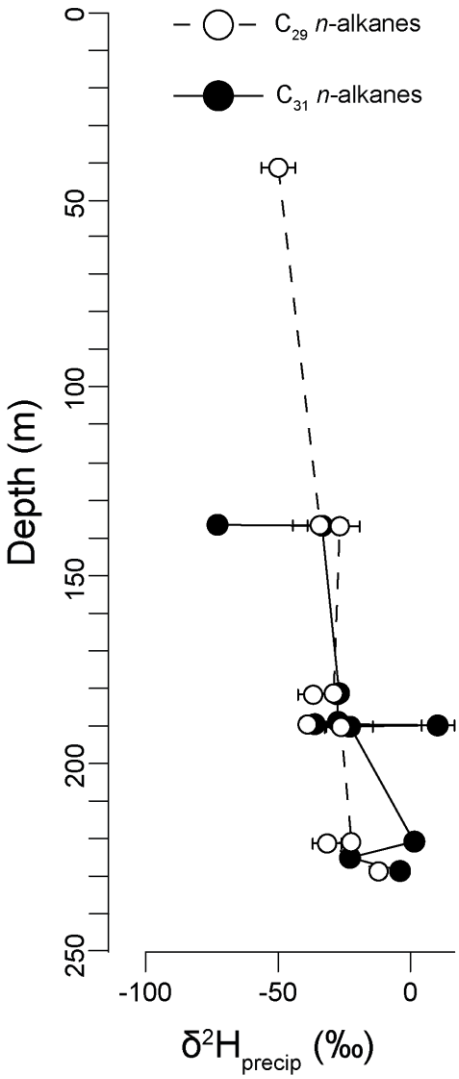

Appendix V

Table 2 Additional information on study sites in Chapter 4.

Site	Present-day location	Latitude and longitude	Palaeo-latitude and palaeo-longitude*	Palaeo-depth
ACEX[a]	Lomonosov Ridge, Central Arctic Ocean	~87°52'0''N, 136°10'38.4''E	82.81°N 66.91°E	200 m
ODP Site 1172[b]	East Tasman Plateau, southwest Pacific Ocean	44°57'0''S, 150°55'0''E	69.46°S 159.91°E	300 m
Kheu River[c]	Central Northern Caucasus		30-45°N	100–200 m
Ancora[d]	New Jersey Shelf, Atlantic Coastal Plain	39°41′31.975″N, 74°50′56.459″W	42.1°N 57.59°W	<110 m
TDP Site 14[e]	Southern Tanzania, East Africa	9°16'59.89''S, 39°30'45.04''E	17.27°S 31.85°E	300–500 m
SDB[f]	Salisbury Embayment, Atlantic Coastal Plain	38°44'49.34''N, 76°00'25.09''W	41.39°N 59.48°W	<150 m
CamDor[f]	Salisbury Embayment, Atlantic Coastal Plain	38°32'3.84''N, 76°01'44.4''W	41.39°N 59.48°W	<150 m

Note. a-f References for palaeo-depth.

[a]Sluijs, *Röhl, et al*. (2008). [b]Hollis *et al.* (2019). [c]Junium, Dickson and Uveges (2018). [d]Harris *et al.* (2010). [e]Handley *et al.* (2008). [f]Lyons *et al*. (2019).

*based on 56 Ma mantle reference frame (Hollis *et al.*, 2019).

Appendix VI

The following appendix provides a summary of the available key time intervals and linear sedimentation rates (LSRs) at each study site in Chapter 4. A further discussion for each locality outlines the previously published definitions for the key time intervals and LSRs, with descriptions of lithology.

III.1 Summary

We divide each dataset into one of the following intervals: 'pre-PETM' (Paleocene), the 'core' (onset and body of the CIE) of the PETM, the 'recovery' of the PETM, and 'post-PETM'. All four intervals occur at ACEX, ODP Site 1172, and SDB. SDB and Ancora also subdivide the recovery into 'Phase I' and 'Phase II'. Note that Ancora and Kheu River section does not include post-PETM deposits. In addition, an unconformity truncates the core of the PETM at TDP Site 14 (*i.e.* no recovery or post-PETM interval). The definition for the core of the PETM at CamDor includes the recovery (Lyons *et al.*, 2019).

LSRs were acquired for the pre-PETM intervals of all the sites. However, in most cases (*i.e.* ACEX, Kheu River, TDP Site 14, and CamDor) LSRs were only available for the entire PETM (*i.e.* including the core and the recovery of the PETM). In addition, LSR for the recovery of the PETM at ODP Site 1172 was not available. Below we provide further details for each site.

III.2 ACEX

The LSRs for this site are based on the identification of the CIE, alongside biostratigraphy utilising dinoflagellate cysts and benthic foraminifera (Sluijs, *Röhl, et al*., 2008). The LSR for the uppermost Paleocene is 1 cm kyr^{-1} (Sluijs, *Röhl, et al*., 2008). The beginning of the PETM was identified to be the top of Core 32X (~387 mcd), although this lower bound is problematic due to core recovery (Sluijs, *Röhl, et al*., 2008). The end of the PETM is within Core 29X (~378.5 mcd). Following Elling *et al*. (2019), the transition from the core to recovery of the PETM was located ~381.6 mcd. However, an LSR value of 5 ±1.2 cm kyr^{-1} was only available for the entire PETM (*i.e.* including the core and the recovery of the PETM) (Sluijs, *Röhl, et al*., 2008). The entire record is composed of organic-rich fine-grained siliclastic mudstone (Sluijs, *Röhl, et al*., 2008).

III.3 ODP Site 1172

Sediments at this site consist mainly of organic-rich clay and siltstones, and the age-model was constructed by integrating dinoflagellate cyst and magnetostratigraphy (Sluijs *et al*., 2011). The Upper Paleocene LSR is 0.57 cm kyr^{-1}, and Sluijs *et al*. (2011) defined the beginning of the PETM at ~611.9 rmbsf and the end of the PETM between 611.2 rmbsf and

611 rmbsf. The recovery phase starts at ~611.7 rmbsf, however LSR was not available for this interval. For the core PETM, LSR of 0.4–0.5 cm kyr^{-1} was estimated, although it was noted that it is likely much more variable (Sluijs *et al.*, 2011).

III.4 Kheu River

The upper Paleocene is composed of greenish marls, and the beginning of the PETM is tied to the base of a sapropel horizon (0 cm; Gavrilov, Shcherbinina and Oberhänsli, 2003). However, the sapropel is just ~75 cm thick and only spans the lower CIE. The upper CIE and the start of the recovery interval (~1.02 m; Shcherbinina *et al.*, 2016) is identified within calcareous clay deposits. The Kheu River section does not extend to post-PETM deposits and LSRs are not available. Therefore, estimates were taken from the Aktumsuk section, which were determined using magnetostratigraphy and planktonic foraminiferal zonations (Uzbekistan; John *et al.*, 2008). Although the two sites are not directly comparable, both are composed of shallow marine deposits. Furthermore, TOC values shift from ~0.1 % pre-PETM to ~8.5 % during the PETM (Bolle *et al.*, 2000; Dickson *et al.*, 2014). The pre-PETM LSR is 0.3 cm kyr^{-1} and a LSR of 1.9 cm kyr^{-1} was assumed for the entire PETM (*i.e.* including the core and the recovery of the PETM) (John *et al.*, 2008).

III.5 Ancora

The LSRs for Ancora are based on a regional correlation of core sites that have either identification of the CIE, biostratigraphy, and/or magnetostratigraphy (Stassen, Thomas and Speijer, 2012). The uppermost Paleocene LSR is 0.8cm kyr^{-1}, and this LSR estimate was used until depths 171.6–171.3 m (Stassen, Thomas and Speijer, 2012). However, we separately define the beginning of the PETM as between 172.53 m and 172.37 m (following Elling *et al.*, 2019). The recovery interval begins at 165.7 m, and was further split between Phase I and Phase II at 165.4 m (Stassen, Thomas and Speijer, 2012). The Ancora section does not extend to post-PETM deposits. The core of the PETM starts with a LSR of 11.2 cm kyr^{-1}, however there is a shift to 4.3 cm kyr^{-1} between samples 167.35 m and 167.08 m (Stassen, Thomas and Speijer, 2012). The LSR of Phase I is 1.3 cm kyr^{-1} and this increases to 8.4 cm kyr^{-1} during Phase II (Stassen, Thomas and Speijer, 2012). The PETM sediments consist of a kaolinite-rich clay layer which sits between a glauconitic quartz sand upper Paleocene section and a calcareous clay/silt lower Eocene section (Gibson, Bybell and Mason, 2000).

III.6 TDP Site 14

The PETM sediments from TDP Site 14 are mainly claystones and clayey siltstones (Nicholas *et al.*, 2006). The chronostratigraphy was established from identification of the CIE (Handley *et al.*, 2008), and biostratigraphic analyses of benthic and planktonic foraminifera, nannofossils, and dinoflagellate cysts (Nicholas *et al.*, 2006). The pre-PETM LSR ranges

from 0.5 cm kyr^{-1} to 2 cm kyr^{-1} (following Lyons *et al.*, 2019). The beginning of the PETM is ~24 mbs (Aze *et al*., 2014) and an unconformity truncates the core of the PETM at 12.6m (Handley *et al.*, 2008, 2012). The LSR for the core of the PETM ranges from 3.5 cm kyr^{-1} to 14 cm kyr^{-1} (following Lyons *et al.*, 2019).

III.7 SDB and CamDor

The SDB core is represented by glauconitic quartz sands in the upper Paleocene and silty clay during the PETM. The LSRs were determined by correlating the calcareous nannoplankton zones and the CIE records from cores across Maryland and New Jersey (Doubrawa *et al.*, 2022). Using this approach, the latest Paleocene LSR for SDB was recalculated to 1.03–2.4 cm kyr^{-1} (Doubrawa *et al.*, 2022). The beginning of the PETM at SDB was identified between 203.9 m and 204 m, at the base of the Marlboro Clay (Self-Trail *et al*., 2012; Doubrawa *et al*., 2022). The LSR for the core of the PETM was recalculated to a more conservative estimate of 14 cm kyr^{-1} (Doubrawa *et al.*, 2022). Regional change in the sedimentary regime during the core of the PETM was identified in Doubrawa *et al.* (2022), however excluded from Chapter 4. Furthermore, Phase I and II were also defined at ~196.9 m and 190.5–192 m, respectively (Self-Trail *et al*., 2012; Doubrawa *et al*., 2022). The LSR of Phase I was recalculated to 21.3 cm kyr^{-1} (Doubrawa *et al.*, 2022), and this was assumed for the Phase II interval. At CamDor, the beginning of the PETM is also assigned to the base of the Marlboro (224.15 m; Bralower *et al.,* 2018). Following Lyons *et al*. (2019), we assumed that the SDB LSRs can be used at CamDor. However, with no recovery phase defined at CamDor, 14 cm kyr^{-1} was used for the entire PETM (*i.e.* including the core and the recovery of the PETM).

Appendix VII

Figure 4 Thermal maturity ratios and other lipid biomarker approaches at TDP Site 14 (Chapter 4). Note the βα/(βα + αβ) axis is reversed to reflect increasing thermal maturity towards the right. a) $\delta^{13}C$ of *n*-alkanes: C_{25} (diamond); C_{27} (circle); C_{29} (square); and C_{31} *n*-alkane (triangle) (Aze *et al.*, 2014), b) αβ/(αβ + ββ) ratios (Chapter 4; Handley *et al.*, 2012), c) S/(S + R) ratios (Chapter 4; Handley *et al.*, 2012), d) C_{29} αβ/C_{30} αβ ratio (Handley *et al.*, 2012), e) βα/(βα + αβ) ratios (Handley *et al.*, 2012), f) average chain length (ACL) (Handley *et al.*, 2012), and g) branched and isoprenoid tetraether (BIT) index (Carmichael *et al.*, 2017). The closed symbols are from this study and the open symbols are from Handley *et al.* (2012). The PETM interval (including the core) is highlighted by grey shading, and an unconformity truncates the CIE at 12.6 m.

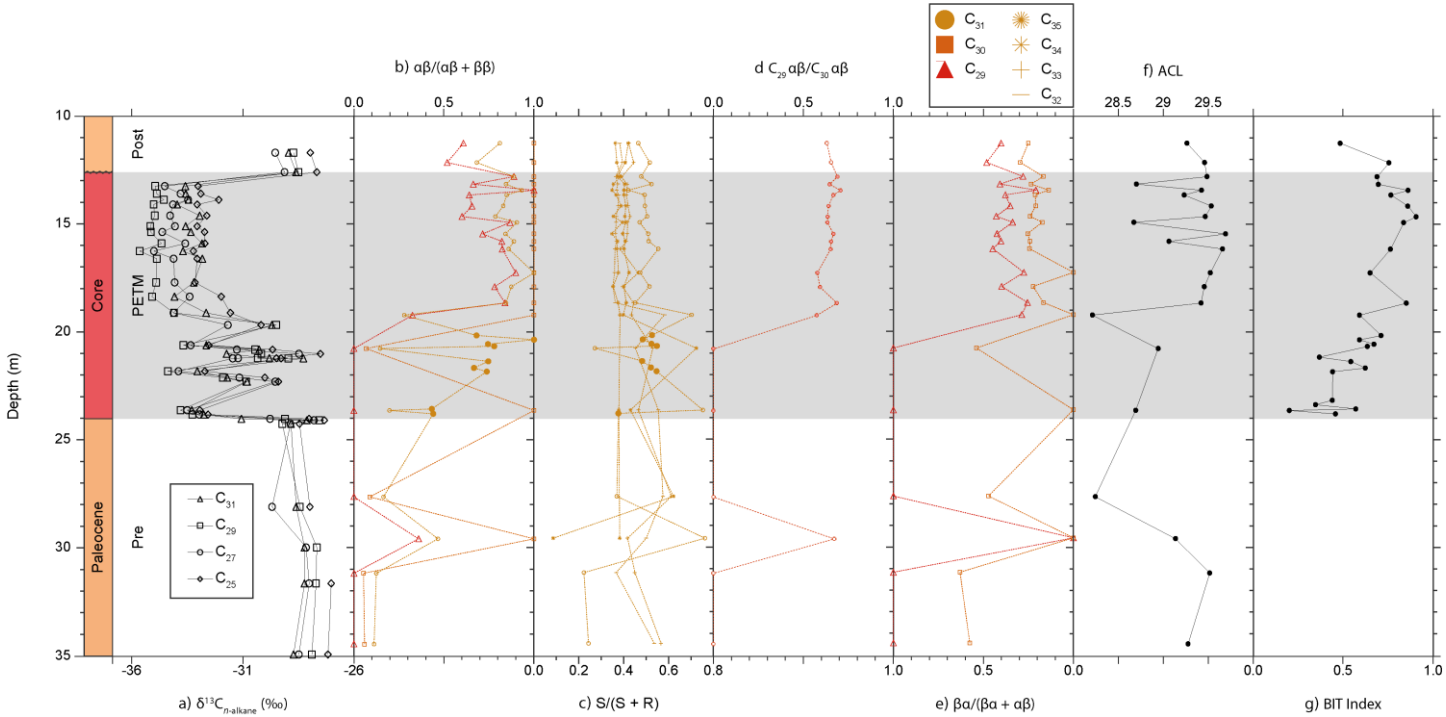

Appendix VIII

The following appendix provides all the new data presented in Chapter 5.

Table 3 Number of disordered carbon vs. graphitised carbon spectra from SDB, with duplicate results in parenthesis. The disordered and graphitised carbon were separated based on peak burial temperatures, which were calibrated using the R2 and RA2 peak area ratio (see Sparkes *et al*., 2013). The time intervals are as follows: Pre-PETM, PETM (onset/body), Recovery, and Post-PETM, based on Appendix VI and references therein. The pre-onset Excursion (POE) in the Pre-PETM interval is isolated using the definition from Babila *et al*. (2022).

Time interval	Approx. sample depth (m)	Disordered carbon	Graphitised carbon
Post-PETM	186.6	5	5
Post-PETM	188	7	3
Recovery	190.99	6	3
Recovery	192.57	5	5
Recovery	193.3	5	5
Recovery	193.88	2	7
Recovery	195.07	5	5
Recovery	196.41	3	7
PETM	196.93	3	7
PETM	197.21	2 (4)	8 (6)
PETM	199.52	3	7
PETM	199.83	4	6
PETM	200.28	2	8
PETM	200.83	2	7
PETM	201.47	3	6
PETM	202.08	3	7
PETM	202.37	4 (9)	6 (1)
PETM	202.68	7	3
PETM	202.98	5	4
PETM	203.06	7 (7)	3 (2)
PETM	203.3	6	3
PETM	203.88	9	1
Pre-PETM	204.26	9	1
Pre-PETM	204.49	8	2
Pre-PETM	204.84	8	2
Pre-PETM	205.12	9 (9)	1 (1)
Pre-PETM	205.4	8	2
Pre-PETM	205.44	8	2
Pre-PETM	205.74	7	3
POE	206.04	8	2
POE	206.35	9	1
POE	206.41	5	4
POE	206.68	9	1

POE	207.04	5	5
POE	207.08	7	3
Pre-PETM	208.83	7	3

Table 4 Number of disordered carbon vs. graphitised carbon spectra from ACEX. The disordered and graphitised carbon were separated based on peak burial temperatures, which were calibrated using the R2 and RA2 peak area ratio (see Sparkes *et al*., 2013). The time intervals are as follows: Pre-PETM, PETM (onset/body), Recovery, and Post-PETM, based on Appendix VI and references therein.

Time interval	**Depth (mcd)**	**Freeze-dried**	**Oven-dried**	**Disordered carbon**	**Graphitised carbon**
Post-PETM	378.14	Yes		9	1
Recovery	378.69		Yes	10	0
Recovery	380.73	Yes		10	0
Recovery	381.56	Yes		9	1
PETM	382.15		Yes	9	1
PETM	382.94		Yes	8	1
PETM	383.87		Yes	10	0
PETM	385.11		Yes	10	0
Pre-PETM	388.03		Yes	10	0
Pre-PETM	388.87	Yes		10	0
Pre-PETM	389.75		Yes	10	0
Pre-PETM	390.78	Yes		10	0

Appendix IX

Figure 5 Mean percentages of graphitised carbon (Chapter 5) and mean values of the C_{31} homohopane 22S/(22S+22R) ratio (Chapter 4; Lyons *et al.*, 2019), from (a-b) SDB and (c-d) ACEX. The time intervals are as follows: Pre-PETM, PETM (onset and body), Recovery, and Post-PETM (see Appendix VI and references therein). At SDB, the POE in the Pre-PETM interval is isolated using the definition from Babila *et al*. (2022). The uncertainty is displayed as the 95 % confidence interval of the mean, with error bars not included when sample size is <4.

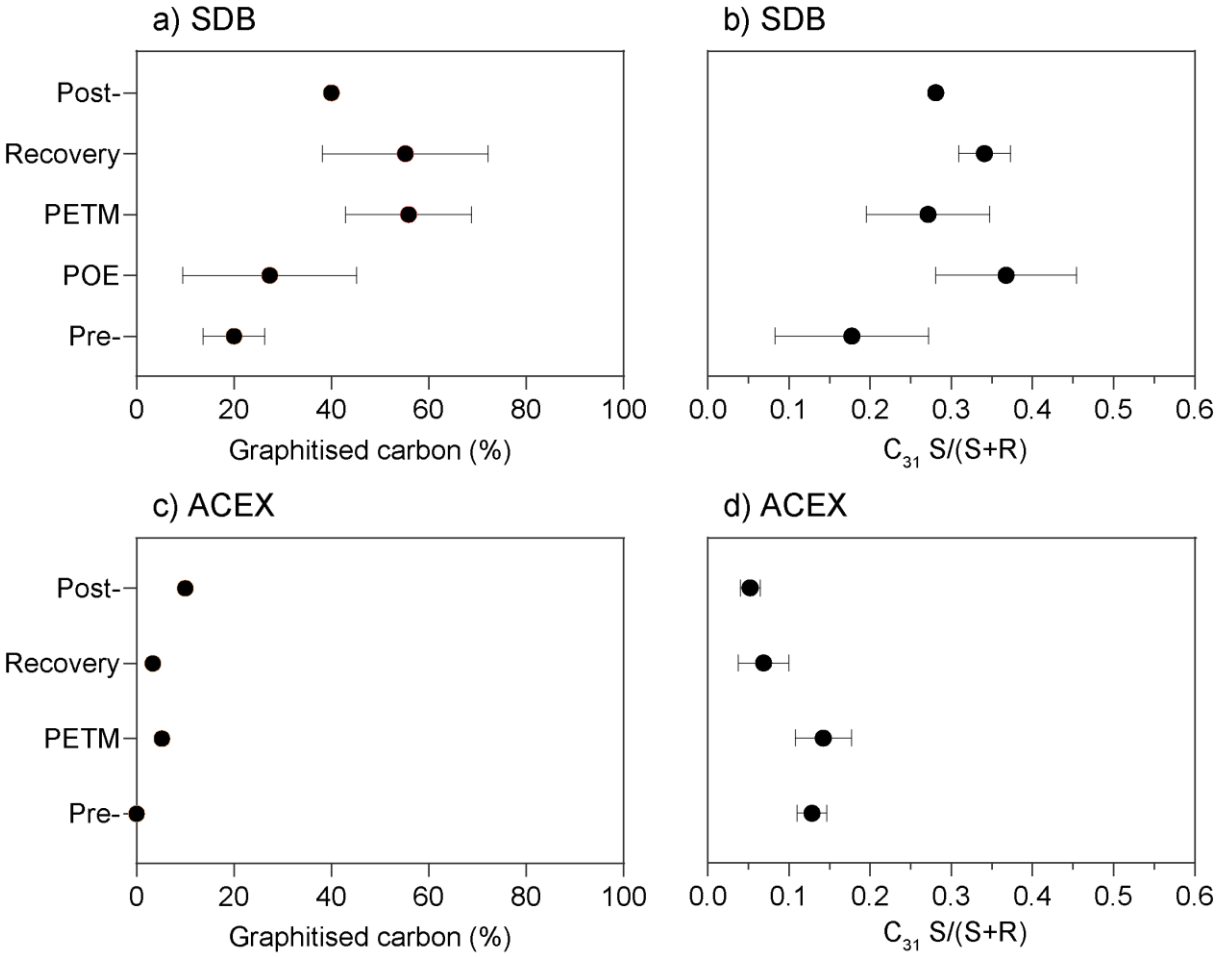

Appendix X

Figure 6 Structures of bacteriohopanepolyols (BHPs) identified in Chapter 6, including the hopane skeleton and the extended side chains. The BHPs are classified into side chain configurations with similar moieties. Hydroxy-BHPs group simple polyols, whereas amino-BHPs, MC-BHPs, and ethenolamine-BHPs have an amine, methylated carbamic acid ester, and an ethenolamine group at the C-35 position, respectively. BHT-CE and amino-BHPs are also referred to as complex BHPs. [a]refers to the tentative placement of a methyl on the C-31 position (Talbot, Bischoff, *et al*., 2016).

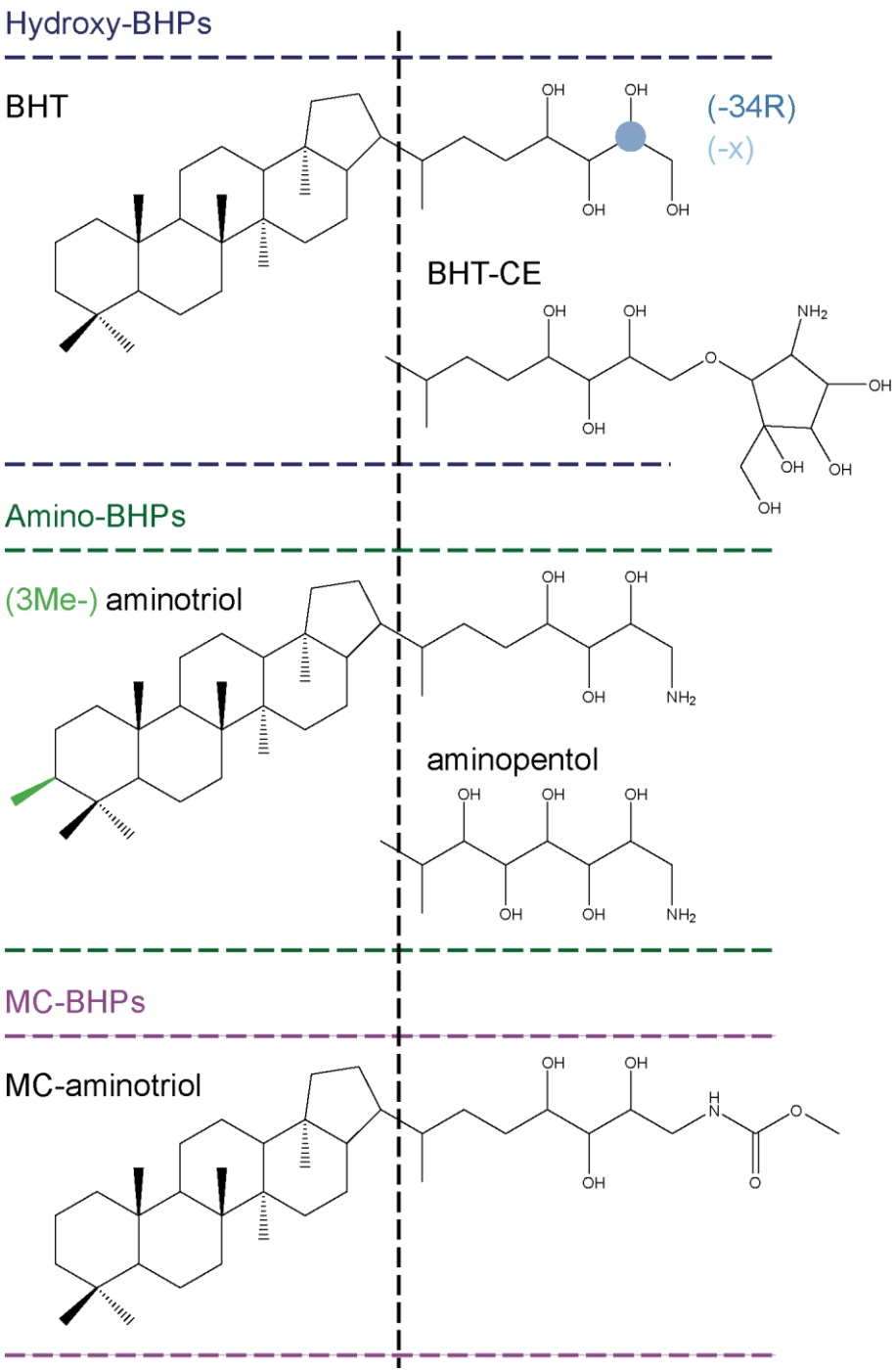

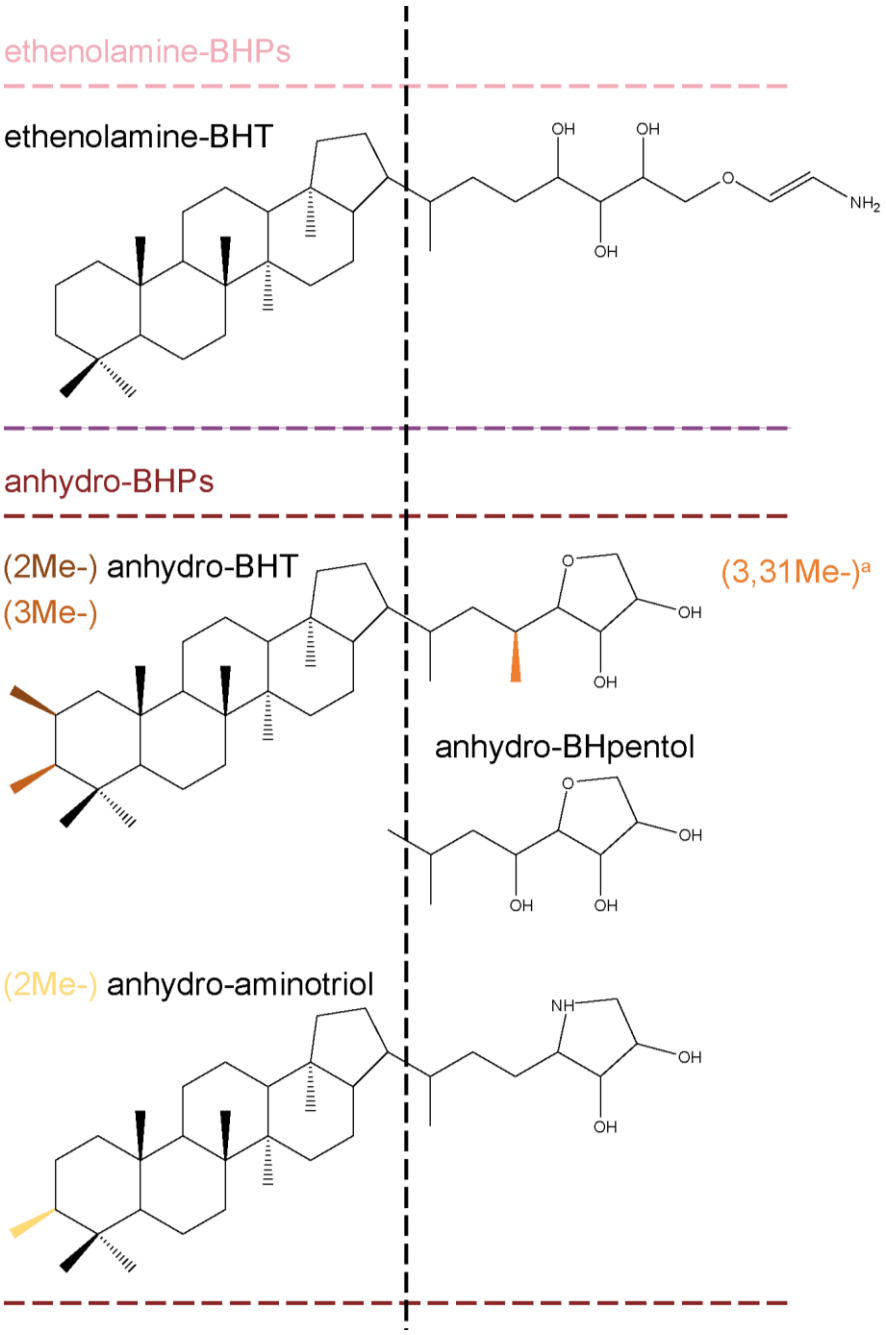
ethenolamine-BHPs
ethenolamine-BHT
OH
OH
O
NH2
OH
anhydro-BHPs
(2Me-) anhydro-BHT
(3Me-)
O
OH
OH
(3,31Me-)a
anhydro-BHpentol
O
OH
OH
OH
(2Me-) anhydro-aminotriol
NH
OH
OH

Appendix XI

Figure 7 Example extracted ion chromatograms (EICs) from a sample at 39.3 m, with the highest diversity of anhydro BHPs (Chapter 6). We report the exact masses (within 5 ppm mass accuracy) of a specific combination of the protonated ($[M+H]^+$), ammoniated ($[M+NH_4]^+$), and/or sodiated ($[M+Na]^+$) adducts used within the summed mass chromatogram for the integration of each BHP (Table 6.1). With MS^2 spectra of a) anhydro-BHT, b) 2Me-anhydro-BHT, c) 3Me-anhydro-BHT, d) 3,31Me-anhydro-BHT, e) anhydro-BHpentol, f) anhydro-aminotriol, and g) 3Me-anhydro-aminotriol. [a]refers to the tentative placement of a methyl on the C-31 position (Talbot, Bischoff, *et al.*, 2016).

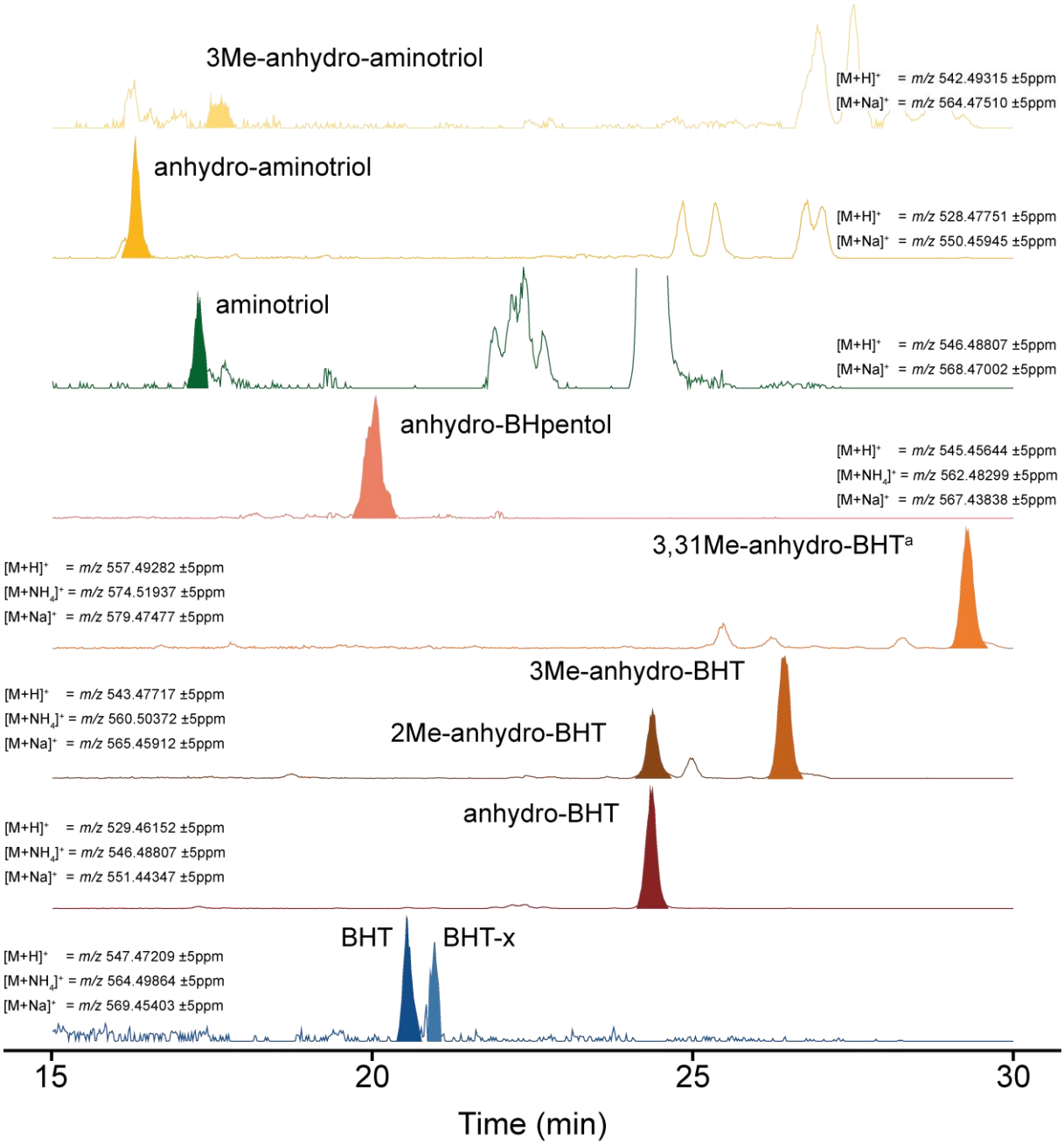

a) MS² of *m/z* 546.5, $[M+NH_4]^+$ of anhydro-BHT

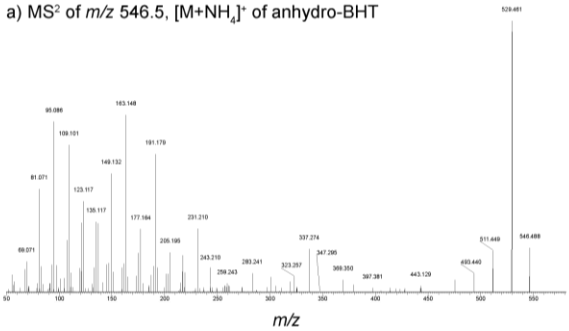

b) MS² of *m/z* 560.5, $[M+NH_4]^+$ of 2Me-anhydro-BHT

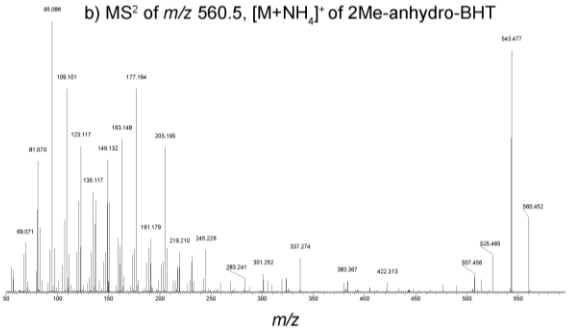

c) MS² of *m/z* 560.5, $[M+NH_4]^+$ of 3Me-anhydro-BHT

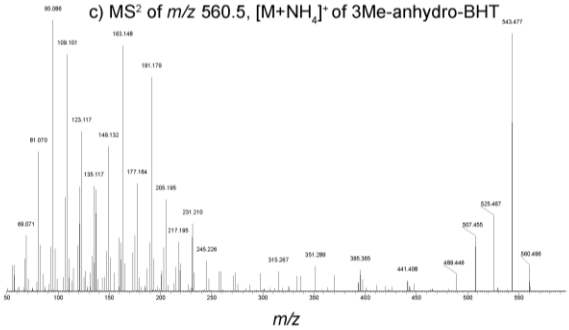

d) MS² of *m/z* 574.3, $[M+NH_4]^+$ of 3,31Me-anhydro-BHT[a]

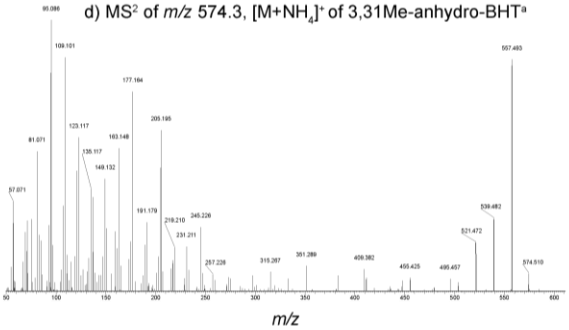

e) MS² of *m/z* 562.5, $[M+NH_4]^+$ of anhydro-BHpentol

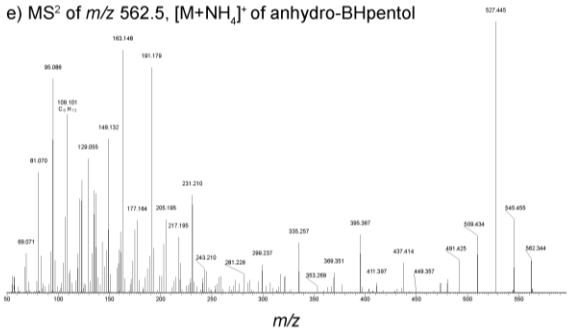

f) MS² of *m/z* 528.5, $[M+H]^+$ of anhydro-aminotriol

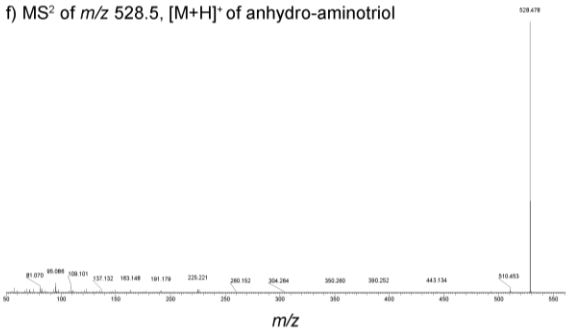

g) MS² of *m/z* 542.4, $[M+H]^+$ of 3Me-anhydro-aminotriol

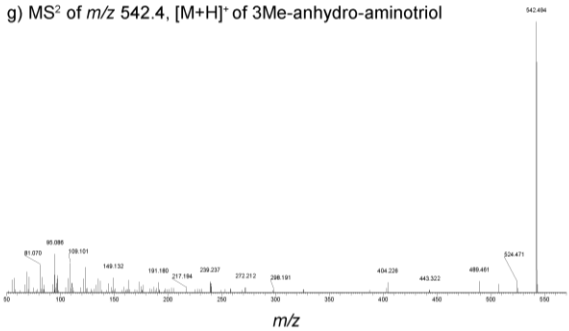

Appendix XII

Table 5 Individual BHP abundances, in response unit (RU) per g of OC, as discussed in Chapter 6.

Depth above base of unit (m)	BHT	BHT -34R	BHT -x	BHT -CE	amin otriol	3Me-amin otriol	amino pentol	MC-amin otriol	ethenol amine-BHT	anhydro -BHT	2Me-anhydro -BHT	3Me-anhydro -BHT	3,31Me-anhydro -BHT	anhydro -BH pentol	anhydro -amin otriol	3Me-anhydro -amin otriol
0.7	7×10^8	7×10^8	6×10^8	1×10^9	1×10	0	2×10^9	8×10^7	4×10^8	4×10	0	2×10^9	4×10^8	7×10^9	7×10	0
2.6	6×10^9	0	0	0	0	4×10^9	0	0	0	5×10	0	7×10^9	0	3×10^9	2×10	5×10^9
3.2	2×10^9	0	0	0	0	3×10^9	0	0	0	1×10	0	3×10^9	0	0	3×10^9	0
4	3×10^8	3×10^7	2×10^7	0	1×10^9	5×10^8	0	0	0	4×10^9	0	0	0	3×10^8	3×10^9	0
5.05	3×10^8	3×10^7	9×10^7	0	9×10^7	7×10^7	0	0	0	1×10	6×10^8	2×10^9	1×10^9	2×10^9	2×10^9	0
5.35	2×10^9	0	8×10^8	5×10^8	5×10^9	3×10^9	0	0	0	3×10	2×10^9	6×10^9	3×10^9	5×10^9	2×10	0
5.5	1×10^9	6×10^7	4×10^8	0	9×10^8	5×10^8	0	0	7×10^7	3×10	2×10^9	7×10^9	3×10^9	3×10^9	7×10^9	4×10^8
5.75	2×10^8	1×10^7	1×10^8	2×10^8	9×10^8	7×10^8	0	0	0	5×10^9	3×10^8	1×10^9	3×10^8	8×10^8	1×10^8	0
5.85	8×10^8	7×10^7	0	9×10^9	4×10^9	4×10^8	1×10^8	0	0	2×10	0	2×10^9	6×10^8	2×10^9	1×10	1×10^9
6	4×10^7	5×10^6	3×10^7	7×10^7	4×10^8	4×10^8	0	0	0	2×10^9	1×10^8	5×10^8	2×10^8	5×10^8	6×10^8	0
6.05	2×10^9	0	6×10^8	8×10^9	7×10^9	1×10^9	2×10^8	0	0	1×10	0	1×10^9	7×10^8	6×10^9	8×10^8	0
6.85	3×10^9	0	5×10^8	2×10	1×10	7×10^8	7×10^8	0	0	2×10	0	2×10^9	0	6×10^9	3×10	0
7.75	3×10^9	3×10^8	1×10^9	8×10^9	1×10	6×10^8	9×10^8	0	0	2×10	0	2×10^9	0	7×10^9	4×10	8×10^8
8.25	9×10^8	9×10^7	2×10^8	5×10^9	5×10^9	8×10^8	4×10^8	0	0	5×10^9	0	7×10^8	3×10^8	2×10^9	1×10	0
9.3	2×10^9	2×10^8	2×10^8	3×10^9	7×10^9	8×10^8	3×10^8	0	0	3×10	0	3×10^9	7×10^8	5×10^9	3×10	3×10^8

9.3	3×10^9	0	3×10^8	5×10^9	2×10^9	0	6×10^7	2×10^7	8×10^7	2×10	0	2×10^9	7×10^8	4×10^9	2×10	0
9.8	9×10^8	0	1×10^8	3×10^9	5×10^9	1×10^9	2×10^8	0	0	4×10^9	0	0	0	2×10^9	1×10	2×10^8
10.5	1×10^9	0	2×10^8	1×10^9	7×10^9	8×10^8	3×10^8	0	0	1×10	0	0	2×10^8	3×10^9	2×10	7×10^8
11.4	6×10^8	0	2×10^8	2×10^9	3×10^9	4×10^8	7×10^7	0	0	5×10^9	0	4×10^8	0	2×10^9	9×10^9	0
12.315	2×10^8	0	1×10^8	9×10^7	6×10^8	3×10^8	0	0	0	5×10^9	1×10^8	8×10^8	2×10^8	8×10^8	2×10^9	0
12.75	2×10^9	0	2×10^8	2×10	8×10^9	2×10^9	2×10^8	0	0	1×10	0	1×10^9	0	3×10^9	3×10^9	0
12.8	2×10^8	2×10^6	9×10^6	0	2×10^8	1×10^8	0	0	0	3×10^9	1×10^8	6×10^8	2×10^8	5×10^8	1×10^9	0
15.75	2×10^9	0	2×10^8	1×10	6×10^9	9×10^8	0	0	0	2×10	0	3×10^9	8×10^8	3×10^9	1×10^9	0
17.45	6×10^8	0	0	8×10^9	5×10^9	1×10^9	7×10^7	0	0	1×10	0	2×10^9	4×10^8	2×10^9	2×10^9	0
19.1	2×10^9	2×10^8	3×10^8	2×10^9	2×10^9	0	0	4×10^7	1×10^8	2×10	0	2×10^9	1×10^9	3×10^9	3×10	8×10^8
21.35	3×10^9	0	0	3×10	2×10	6×10^9	4×10^8	0	0	2×10	0	3×10^9	0	4×10^9	7×10	2×1010^9
23.27	1×10^8	0	3×10^7	0	8×10^7	0	0	0	2×10^6	3×10^9	3×10^8	9×10^8	4×10^8	2×10^8	1×10^9	0
25.3	4×10^9	1×10^8	1×10^8	2×10	6×10^9	2×10^9	1×10^8	0	6×10^7	1×10	0	2×10^9	4×10^8	6×10^9	3×10	0
29	2×10^8	8×10^6	1×10^8	0	1×10^8	6×10^7	0	0	0	4×10^9	5×10^8	9×10^8	6×10^8	1×10^9	5×10^8	0
33.95	6×10^7	0	2×107	0	2×10^7	0	0	0	0	2×10^9	3×10^8	4×10^8	3×10^8	2×10^8	2×10^8	0
35.75	2×10^8	2×10^7	9×10^7	0	2×10^8	1×10^8	0	0	1×10^7	8×10^9	1×10^9	2×10^9	1×10^9	9×10^8	9×10^8	3×10^8
36.75	2×10^8	8×10^6	9×10^7	0	1×10^8	0	0	0	2×10^7	3×10^9	2×10^8	6×10^8	3×10^8	1×10^9	5×10^8	0
36.75	1×10^8	4×10^6	8×10^7	0	6×10^7	0	0	0	0	1×10	2×10^9	3×10^9	3×10^9	1×10^9	2×10^8	0
37.95	0	0	0	0	0	0	0	0	0	1×10^9	1×10^8	3×10^8	3×10^8	1×10^8	6×10^8	0
39.3	1×10^8	0	1×10^8	0	1×10^8	1×10^8	0	0	1×10^7	1×10	2×10^9	4×10^9	2×10^9	8×10^8	7×10^8	9×10^7
41.15	2×10^8	2×10^7	9×10^7	5×10^8	2×10^9	8×10^8	0	0	0	6×10^9	3×10^8	2×10^9	9×10^8	2×10^9	1×10^9	0

42.35	8×10^8	5×10^7	1×10^8	3×10^9	4×10^9	9 × 108	2×10^8	0	0	1 × 10	0	2 × 109	0	8 × 108	1 × 10	5×10^8
50	5×10^9	3×10^8	2×10^8	0	1×10^9	0	0	0	2 × 108	2 × 10	0	1 × 109	0	2 × 109	2 × 10	0
54	6×10^9	0	0	0	0	0	0	0	0	2 × 10	0	2 × 109	0	6 × 109	2 × 10	0

Note. [a]a tentative placement of a methyl on the C-31 position (Talbot, Bischoff, *et al*., 2016).

Appendix XIII

Figure 8 Cross-plot of BHT and BHT-CE, in response unit (RU) per g of OC.

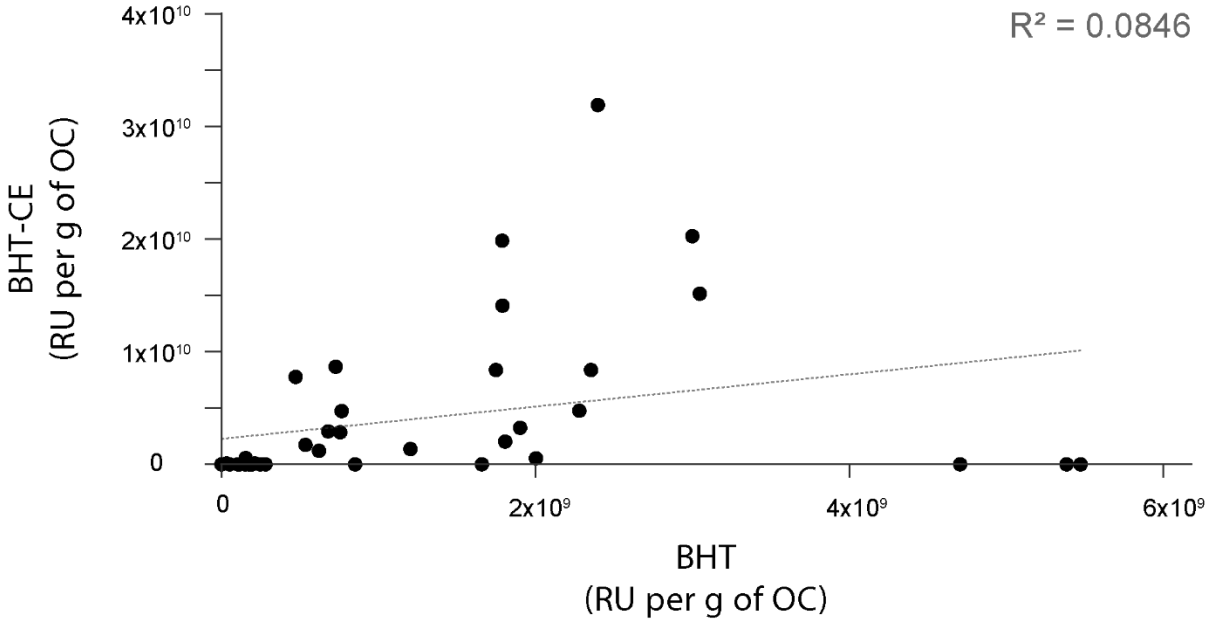

Figure 9 Cross-plot showing the linear relationship between BHT and anhydro-BHT, in response unit (RU) per g of OC.

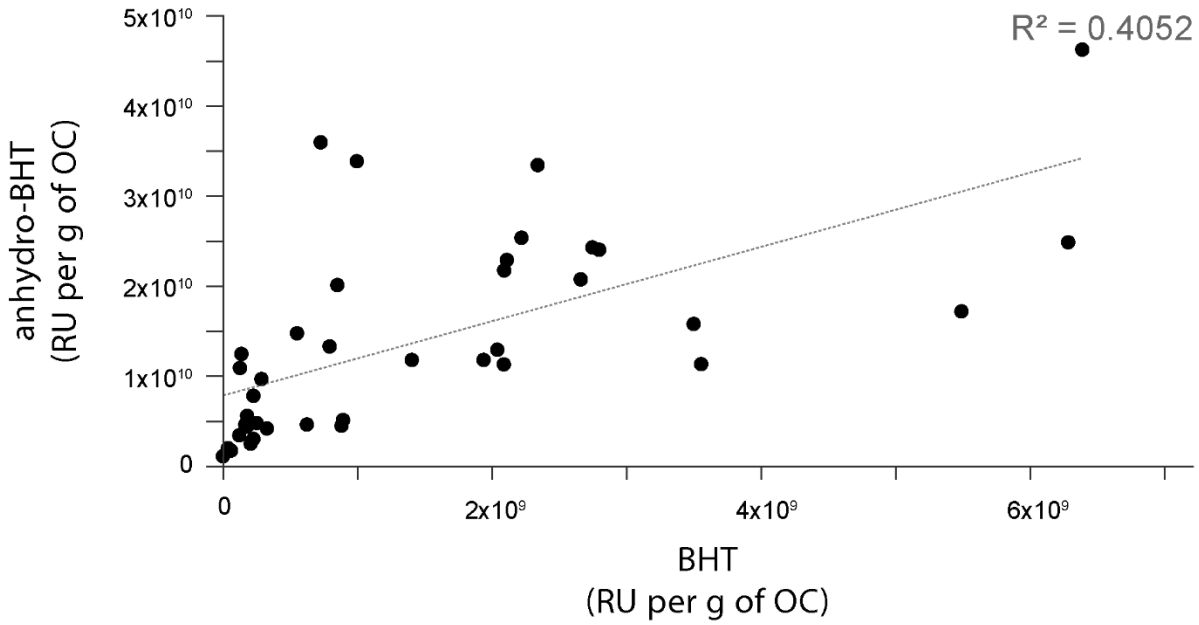

Figure 10 Cross-plot of BHT-CE and anhydro-BHT, in response unit (RU) per g of OC.

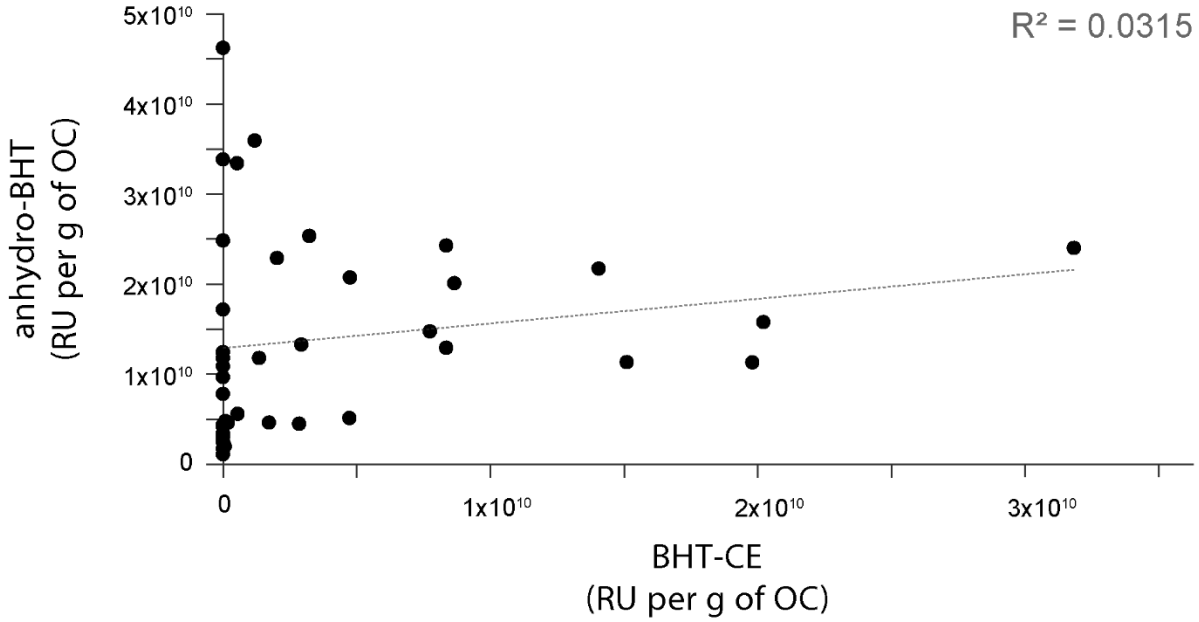

Figure 11 Cross-plot showing the linear relationship between aminotriol and anhydro-aminotriol, in response unit (RU) per g of OC.

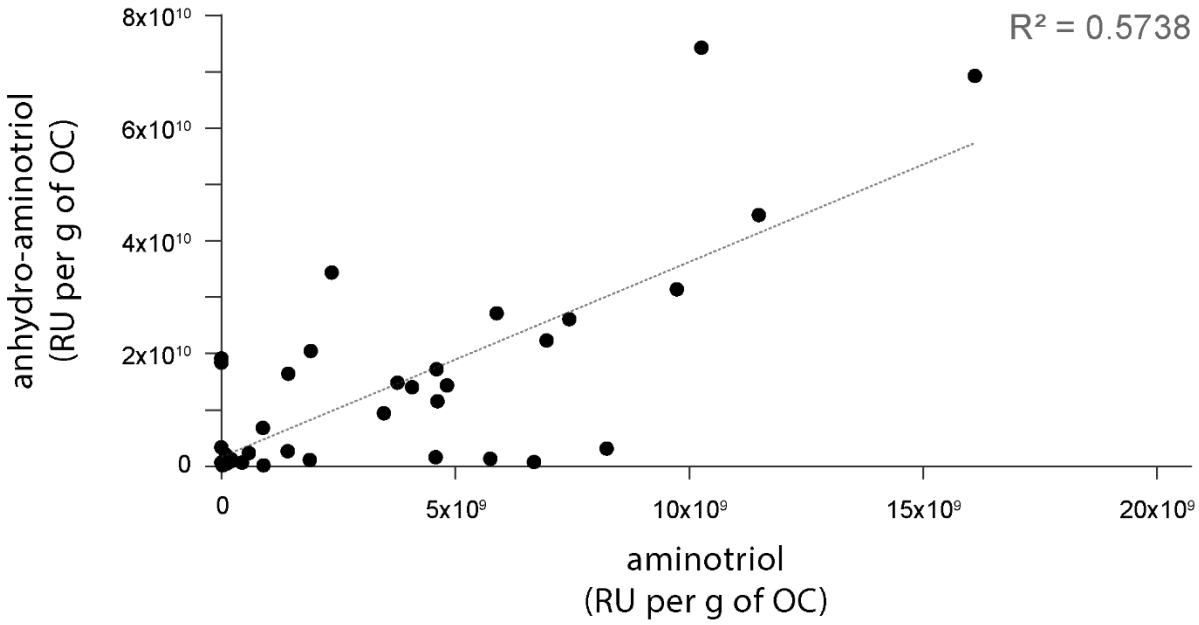

Figure 12 Cross-plot showing the linear relationship between 3Me-aminotriol and anhydro-3Me-aminotriol, in response unit (RU) per g of OC.

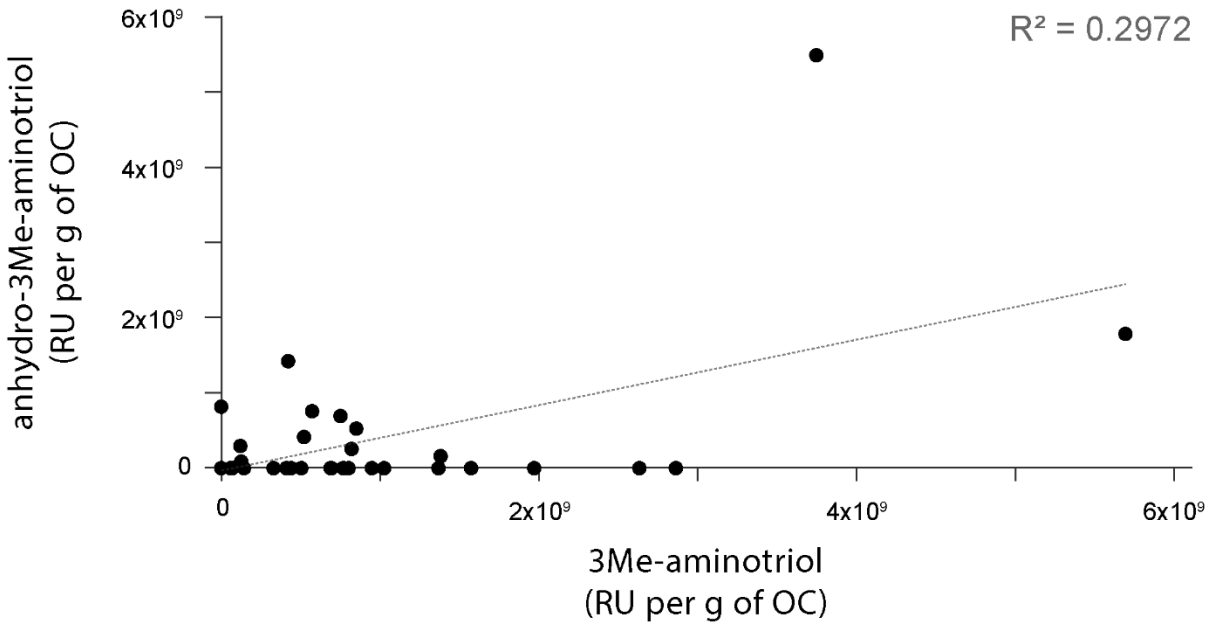

Figure 14 Cross-plot showing the linear relationship between TOC (%) and Total BHP in response unit (RU) per g of OC.

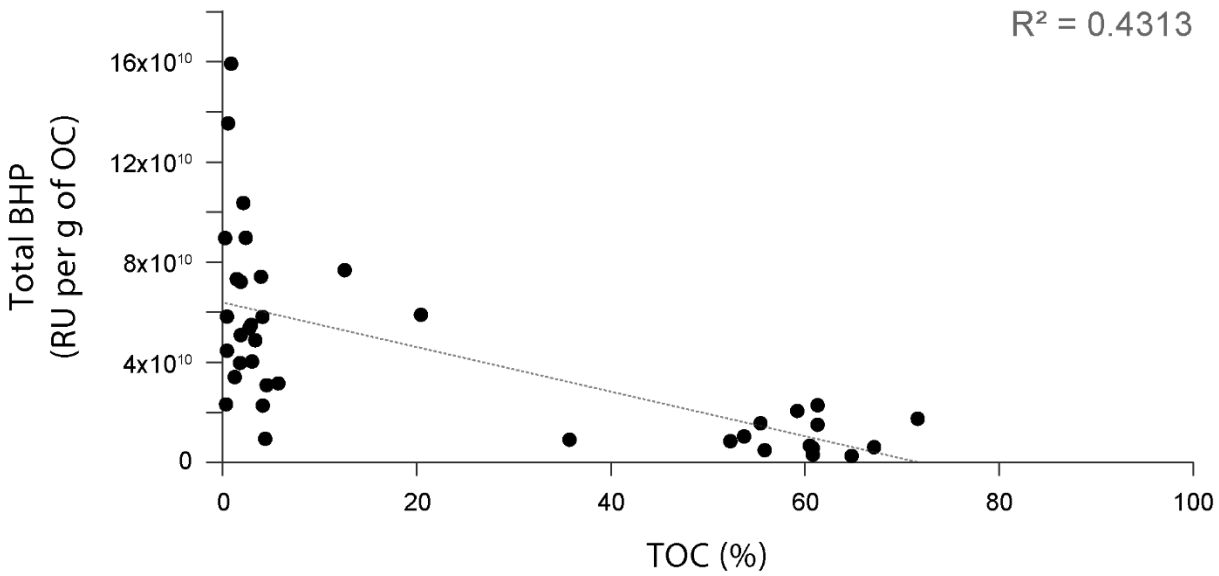

References

Abernethy, S. *et al.* (2021) ‘Methane removal and the proportional reductions in surface temperature and ozone’, *Philosophical Transactions of the Royal Society A: Mathematical, Physical and Engineering Sciences*, 379(2210). doi: 10.1098/rsta.2021.0104.

Acosta, R. P. *et al.* (2022) ‘Evolution of the Atlantic Intertropical Convergence Zone, and the South American and African Monsoons Over the Past 95-Myr and Their Impact on the Tropical Rainforests’, *Paleoceanography and Paleoclimatology*, 37(7). doi: 10.1029/2021PA004383.

Anagnostou, E. *et al.* (2020) ‘Proxy evidence for state-dependence of climate sensitivity in the Eocene greenhouse’, *Nature Communications*, 11. doi: 10.1038/s41467-020-17887-x.

Anderson, B. *et al.* (2010) *Methane and Nitrous Oxide Emissions From Natural Sources*. Washington DC.

Armstrong Mckay, D. I. and Lenton, T. M. (2018) ‘Reduced carbon cycle resilience across the Palaeocene – Eocene Thermal Maximum’, *climate of*, 14, pp. 1515–1527. doi: 10.5194/cp-14-1515-2018.

Aze, T. *et al.* (2014) ‘Extreme warming of tropical waters during the Paleocene – Eocene Thermal Maximum’, *Geology*, 42(9), pp. 739–742. doi: 10.1130/G35637.1.

Babila, T. L. *et al.* (2018) ‘Capturing the global signature of surface ocean acidification during the Palaeocene-Eocene Thermal Maximum’, *Philosophical Transactions of the Royal Society A: Mathematical, Physical and Engineering Sciences*, 376(2130). doi: 10.1098/rsta.2017.0072.

Babila, T. L. *et al.* (2022) ‘Surface ocean warming and acidification driven by rapid carbon release precedes Paleocene-Eocene Thermal Maximum’, *Science Advances*, 8. doi: 10.1126/sciadv.abg1025.

Backman, J. *et al.* (2006) *Artic Coring Expedition (ACEX), Proc. Integr. Ocean Drill. Program, 302*. Available at: http://publications.iodp.org/proceedings/302/302toc.htm.

Bakkelund, A. *et al.* (2018) ‘Net fractionation of hydrogen isotopes in *n*-alkanoic acids from soils in the northern boreal forest’, *Organic Geochemistry*, 125. doi: 10.1016/j.orggeochem.2018.08.005.

Banta, A. B., Wei, J. H. and Welander, P. V. (2015) ‘A distinct pathway for tetrahymanol synthesis in bacteria’, *Proceedings of the National Academy of Sciences of the United States of America*, 112(44), pp. 13478–13483. doi: 10.1073/pnas.1511482112.

Barnet, J. S. K. *et al.* (2019) 'A High-Fidelity Benthic Stable Isotope Record of Late Cretaceous–Early Eocene Climate Change and Carbon-Cycling', *Paleoceanography and Paleoclimatology*, 34(4), pp. 672–691. doi: 10.1029/2019PA003556.

Barnet, J. S. K. *et al.* (2020) 'Coupled evolution of temperature and carbonate chemistry during the Paleocene–Eocene; new trace element records from the low latitude Indian Ocean', *Earth and Planetary Science Letters*, 545. doi: 10.1016/j.epsl.2020.116414.

Bauersachs, T. *et al.* (2015) 'Distribution of glycerol ether lipids in halophilic, methanogenic and hyperthermophilic archaea', *Organic Geochemistry*, 83–84, pp. 101–108. doi: 10.1016/j.orggeochem.2015.03.009.

Becker, K. W. *et al.* (2016) 'Unusual butane- and pentanetriol-based tetraether lipids in Methanomassiliicoccus Luminyensis, a representative of the seventh order of methanogens', *Applied and Environmental Microbiology*, 82, pp. 4505–4516. doi: 10.1128/AEM.00772-16.

Bednarczyk, A. *et al.* (2005) '32,35-Anhydrobacteriohopanetetrol: An unusual bacteriohopanepolyol widespread in recent and past environments', *Organic Geochemistry*, 36(4), pp. 673–677. doi: 10.1016/j.orggeochem.2004.10.014.

Beerling, D. *et al.* (2009) 'Methane and the CH_4 related greenhouse effect over the past 400 million years', *American Journal of Science*, 309, pp. 97–113. doi: 10.2475/02.2009.01.

Beerling, D. J. *et al.* (2011) 'Enhanced chemistry-climate feedbacks in past greenhouse worlds', *Proceedings of the National Academy of Sciences of the United States of America*, 108(24), pp. 9770–9775. doi: 10.1073/pnas.1102409108.

Belin, B. J. *et al.* (2018) 'Hopanoid lipids: From membranes to plant-bacteria interactions', *Nature Reviews Microbiology*, 16(5), pp. 304–315. doi: 10.1038/nrmicro.2017.173.

Berhe, A. A. *et al.* (2007) 'The Significance of the Erosion-induced Terrestrial Carbon Sink', *BioScience*, 57(4), pp. 337–346. doi: 10.1641/B570408.

Berner, R. A. and Caldeira, K. (1997) 'The need for mass balance and feedback in the geochemical carbon', *Geology*, 25(10), pp. 955–953. doi: 10.1130/0091-7613(1997)025<0955.

Berner, R. A., Lasaga, A. C. and Garrels, R. M. (1983) 'The carbonate-silicate geochemical cycle and its effect on atmospheric carbon dioxide over the past 100 million years', *American Journal of Science*, 283(7), pp. 641–683. doi: 10.2475/ajs.283.7.641.

Beyssac, O. *et al.* (2002) 'Raman spectra of carbonaceous material in metasediments: A new geothermometer', *Journal of Metamorphic Geology*, 20, pp. 859–871. doi: 10.1046/j.1525-1314.2002.00408.x.

Beyssac, O. *et al.* (2004) 'Thermal metamorphism in the lesser Himalaya of Nepal determined from Raman spectroscopy of carbonaceous material', *Earth and Planetary Science Letters*, 225, pp. 233–241. doi: 10.1016/j.epsl.2004.05.023.

Bhattacharya, T. *et al.* (2018) 'Ice-sheet modulation of deglacial North American monsoon intensification', *Nature Geoscience*, 11(11), pp. 848–852. doi: 10.1038/s41561-018-0220-7.

Bianchi, T. S. *et al.* (2018) 'Centers of organic carbon burial and oxidation at the land-ocean interface', *Organic Geochemistry*, 115, pp. 138–155. doi: 10.1016/j.orggeochem.2017.09.008.

Blair, N. E. *et al.* (2003) 'The persistence of memory: The fate of ancient sedimentary organic carbon in a modern sedimentary system', *Geochimica et Cosmochimica Acta*, 67(1), pp. 63–73. doi: 10.1016/S0016-7037(02)01043-8.

Blanc-Betes, E. *et al.* (2016) 'Winter precipitation and snow accumulation drive the methane sink or source strength of Arctic tussock tundra', *Global Change Biology*, 22(8), pp. 2818–2833. doi: 10.1111/gcb.13242.

Blewett, J. *et al.* (2020) 'Effects of temperature and pH on archaeal membrane lipid distributions in freshwater wetlands', *Organic Geochemistry*, 148. doi: 10.1016/j.orggeochem.2020.104080.

Bligh, E. G. and Dyer, W. J. (1959) 'Canadian Journal of Biochemistry and Physiology', *Canadian Journal of Biochemistry and Physiology*, 37(8).

Blumenberg, M. *et al.* (2012) 'Novel findings on hopanoid occurrences among sulfate reducing bacteria: Is there a direct link to nitrogen fixation?', *Organic Geochemistry*, 49. doi: 10.1016/j.orggeochem.2012.05.003.

Blumenberg, M. *et al.* (2013) 'Bacteriohopanepolyols record stratification, nitrogen fixation and other biogeochemical perturbations in Holocene sediments of the central Baltic Sea', *Biogeosciences*, 10(4), pp. 2725–2735. doi: 10.5194/bg-10-2725-2013.

Blumenberg, M. *et al.* (2024) 'Biomarker Reconstruction of a High-Latitude Late Paleocene to Early Eocene Coal Swamp Environment Across the PETM and ETM-2 (Ellesmere Island, Arctic Canada)', *Paleoceanography and Paleoclimatology*, 39(2). doi: 10.1029/2023PA004712.

Blunier, T. *et al.* (1995) 'Variations in atmospheric methane concentration during the Holocene epoch', *Letters to Nature*, 374. doi: 10.1038/scientificamerican02071914-131.

Bock, M. *et al.* (2017) 'Glacial/interglacial wetland, biomass burning, and geologic methane emissions constrained by dual stable isotopic CH4 ice core records', *Proceedings of the*

National Academy of Sciences of the United States of America, 114(29). doi: 10.1073/pnas.1613883114.

Bolle, M. P. *et al.* (2000) 'The Paleocene-Eocene transition in the marginal northeastern Tethys (Kazakhstan and Uzbekistan)', *International Journal of Earth Sciences*, 89(2), pp. 390–414. doi: 10.1007/s005310000092.

Bornemann, A. *et al.* (2014) 'Persistent environmental change after the Paleocene-Eocene Thermal Maximum in the eastern North Atlantic', *Earth and Planetary Science Letters*, 394, pp. 70–81. doi: 10.1016/j.epsl.2014.03.017.

Bosmans, J. H. C. *et al.* (2015) 'Obliquity forcing of low-latitude climate', *Climate of the Past*, 11(10), pp. 1335–1346. doi: 10.5194/cp-11-1335-2015.

Bouchez, J. *et al.* (2010) 'Oxidation of petrogenic organic carbon in the Amazon floodplain as a source of atmospheric CO2', *Geology*, 38(3), pp. 255–258. doi: 10.1130/G30608.1.

Bouchez, J. *et al.* (2014) 'Source, transport and fluxes of Amazon River particulate organic carbon: Insights from river sediment depth-profiles', *Geochimica et Cosmochimica Acta*, 133, pp. 280–298. doi: 10.1016/j.gca.2014.02.032.

Bourbonniere, R. A. and Meyers, P. A. (1996) 'Sedimentary geolipid records of historical changes in the watersheds and productivities of Lakes Ontario and Erie', *Limnology and Oceanography*, 41(2), pp. 352–359. doi: 10.4319/lo.1996.41.2.0352.

Bowen, G. J. *et al.* (2004) 'A humid climate state during the Palaeocene/Eocene thermal maximum', *Nature*, 432(7016), pp. 495–499. doi: 10.1038/nature03115.

Bowen, G. J. *et al.* (2006) 'Eocene hyperthermal event offers insight into greenhouse warming', *Eos*, 87(17), pp. 165–169. doi: 10.1029/2006eo170002.

Bowen, G. J. (2008) 'Spatial analysis of the intra-annual variation of precipitation isotope ratios and its climatological corollaries', *Journal of Geophysical Research Atmospheres*, 113(5), pp. 1–10. doi: 10.1029/2007JD009295.

Bowen, G. J. (2013) 'Up in smoke: A role for organic carbon feedbacks in Paleogene hyperthermals', *Global and Planetary Change*, 109, pp. 18–29. doi: 10.1016/j.gloplacha.2013.07.001.

Bowen, G. J. *et al.* (2014) 'Two massive, rapid releases of carbon during the onset of the Palaeocene-Eocene thermal maximum', *Nature Geoscience*, 8(1), pp. 44–47. doi: 10.1038/ngeo2316.

Bowen, G. J. (2024) *The Online Isotopes in Precipitation Calculator, version 3.2.* Available at: http://www.waterisotopes.org.

Bowen, G. J. and Revenaugh, J. (2003) 'Interpolating the isotopic composition of modern meteoric precipitation', *Water Resources Research*, 39(10). doi: 10.1029/2003WR002086.

Bowen, G. J. and Zachos, J. C. (2010) 'Rapid carbon sequestration at the termination of the Palaeocene-Eocene Thermal Maximum', *Nature Geoscience*, 3, pp. 866–869. doi: 10.1038/ngeo1014.

Bradley, A. S. *et al.* (2010) 'Adenosylhopane: The first intermediate in hopanoid side chain biosynthesis', *Organic Geochemistry*, 41(10), pp. 1075–1081. doi: 10.1016/j.orggeochem.2010.07.003.

Bralower, T. J. *et al.* (2018) 'Evidence for Shelf Acidification During the Onset of the Paleocene-Eocene Thermal Maximum', *Paleoceanography and Paleoclimatology*, 33, pp. 1408–1426. doi: 10.1029/2018PA003382.

Bray, E. E. and Evans, E. D. (1961) 'Distribution of *n*-paraffins as a clue to recognition of source beds', *Geochimica et Cosmochimica Acta*, 22(1), pp. 2–15. doi: 10.1016/0016-7037(61)90069-2.

Buan, N. R. (2018) 'Methanogens: Pushing the boundaries of biology', *Emerging Topics in Life Sciences*, 2(4), pp. 629–646. doi: 10.1042/ETLS20180031.

Bubier, J. *et al.* (2005) 'A comparison of methane flux in a boreal landscape between a dry and a wet year', *Global Biogeochemical Cycles*, 19(1). doi: 10.1029/2004GB002351.

Buffett, B. and Archer, D. (2004) 'Global inventory of methane clathrate: Sensitivity to changes in the deep ocean', *Earth and Planetary Science Letters*, 227(3–4), pp. 185–199. doi: 10.1016/j.epsl.2004.09.005.

Burdige, D. J. (2007) 'Preservation of organic matter in marine sediments: Controls, mechanisms, and an imbalance in sediment organic carbon budgets?', *Chemical Reviews*, 107(2), pp. 467–485. doi: 10.1021/cr050347q.

Bush, R. T. and McInerney, F. A. (2013) 'Leaf wax *n*-alkane distributions in and across modern plants: Implications for paleoecology and chemotaxonomy', *Geochimica et Cosmochimica Acta*, 117, pp. 161–179. doi: 10.1016/j.gca.2013.04.016.

Byrne, M. P. and O'Gorman, P. A. (2015) 'The response of precipitation minus evapotranspiration to climate warming: Why the "Wet-get-wetter, dry-get-drier" scaling does not hold over land', *Journal of Climate*, 28(20), pp. 8078–8092. doi: 10.1175/JCLI-D-15-0369.1.

Campbell, J. *et al.* (2024) 'CO_2-driven and orbitally driven oxygen isotope variability in the Early Eocene', *Climate of the Past*, 20(3), pp. 495–522. doi: 10.5194/cp-20-495-2024.

Canadell, J. G. *et al.* (2021) 'Global Carbon and Other Biogeochemical Cycles and Feedbacks', in Masson-Delmotte, V., P. Zhai, A. Pirani, S.L. Connors, C. Péan, S. Berger, N. Caud, Y. Chen, L. Goldfarb, M.I. Gomis, M. Huang, K. Leitzell, E. Lonnoy, J.B.R. Matthews, T.K. Maycock, T. Waterfield, O. Yelekçi, R. Yu, and B. Z. (ed.) *Climate Change 2021: The Physical Science Basis. Contribution of Working Group I to the Sixth Assessment Report of the Intergovernmental Panel on Climate Change*. Cambridge University Press, pp. 673–816. doi: 10.1017/9781009157896.007.674.

Canfield, D. E. *et al.* (2021) 'Petrographic carbon in ancient sediments constrains Proterozoic Era atmospheric oxygen levels', *Proceedings of the National Academy of Sciences of the United States of America*, 118(23), pp. 1–8. doi: 10.1073/pnas.2101544118.

Carmichael, M. J. *et al.* (2016) 'A model-model and data-model comparison for the early Eocene hydrological cycle', *Climate of the Past*, 12(2), pp. 455–481. doi: 10.5194/cp-12-455-2016.

Carmichael, M. J. *et al.* (2017) 'Hydrological and associated biogeochemical consequences of rapid global warming during the Paleocene-Eocene Thermal Maximum', *Global and Planetary Change*, 157, pp. 114–138. doi: 10.1016/j.gloplacha.2017.07.014.

Carmichael, M. J., Pancost, R. D. and Lunt, D. J. (2018) 'Changes in the occurrence of extreme precipitation events at the Paleocene – Eocene thermal maximum', *Earth and Planetary Science Letters*, 501, pp. 24–36. doi: 10.1016/j.epsl.2018.08.005.

Chen, C. *et al.* (2018) 'Estimating regional flood discharge during Palaeocene-Eocene global warming', *Scientific Reports*, 8(1), pp. 1–8. doi: 10.1038/s41598-018-31076-3.

Chikaraishi, Y. and Naraoka, H. (2003) 'Compound-specific δD-δ13C analyses of *n*-alkanes extracted from terrestrial and aquatic plants', *Phytochemistry*, 63, pp. 361–371. doi: 10.1016/S0031-9422(02)00749-5.

Chou, C. *et al.* (2013) 'Increase in the range between wet and dry season precipitation', *Nature Geoscience*, 6(4), pp. 263–267. doi: 10.1038/ngeo1744.

Chou, C. and Neelin, J. D. (2004) 'Mechanisms of global warming impacts on regional tropical precipitation*', *Journal of Climate*, 17(13), pp. 2688–2701. doi: 10.1175/2008JCLI2154.1.

Chu, H. *et al.* (2014) 'Net ecosystem methane and carbon dioxide exchanges in a Lake Erie coastal marsh and a nearby cropland', *Journal of Geophysical Research: Biogeosciences*, 119(5), pp. 722–740. doi: 10.1002/2013JG002520.

Clark, K. E. *et al.* (2013) 'New views on " old " carbon in the Amazon River: Insight from the source of organic carbon eroded from the Peruvian Andes', *Geochemistry, Geophysics,*

Geosystems, 14(5), pp. 1644–1659. doi: 10.1002/ggge.20122.

Clark, K. E. *et al.* (2016) 'Storm-triggered landslides in the Peruvian Andes and implications for topography, carbon cycles, and biodiversity', *Earth Surface Dynamics*, pp. 47–70. doi: 10.5194/esurf-4-47-2016.

Clark, K. E. *et al.* (2017) 'Erosion of organic carbon from the Andes and its effects on ecosystem carbon dioxide balance', *Journal of Geophysical Research: Biogeosciences*, 122(3), pp. 449–469. doi: 10.1002/2016JG003615.

Clark, K. E. *et al.* (2022) 'Extreme rainstorms drive exceptional organic carbon export from forested humid-tropical rivers in Puerto Rico', *Nature Communications*, 13(1), pp. 1–8. doi: 10.1038/s41467-022-29618-5.

Clarkson, M. O. *et al.* (2021) 'Upper limits on the extent of seafloor anoxia during the PETM from uranium isotopes', *Nature Communications*, (2021). doi: 10.1038/s41467-020-20486-5.

Collinson, M. E. *et al.* (2007) 'Episodic fire, runoff and deposition at the Palaeocene-Eocene boundary', *Journal of the Geological Society*, 164(1), pp. 87–97. doi: 10.1144/0016-76492005-185.

Collister, J. W. *et al.* (1992) 'An isotopic biogeochemical study of the Green River oil shale', *Organic Geochemistry*, 19(1–3), pp. 265–276. doi: 10.1016/0146-6380(92)90042-V.

Contreras, L. *et al.* (2014) 'Southern high-latitude terrestrial climate change during the Palaeocene-Eocene derived from a marine pollen record (ODP Site 1172, East Tasman Plateau)', *Climate of the Past*, 10(4), pp. 1401–1420. doi: 10.5194/cp-10-1401-2014.

Cooke, M. P., Talbot, H. M. and Wagner, T. (2008) 'Tracking soil organic carbon transport to continental margin sediments using soil-specific hopanoid biomarkers: A case study from the Congo fan (ODP site 1075)', *Organic Geochemistry*, 39(8), pp. 965–971. doi: 10.1016/j.orggeochem.2008.03.009.

Cramwinckel, M. J. *et al.* (2018) 'Synchronous tropical and polar temperature evolution in the Eocene', *Nature*, 559(7714), pp. 382–386. doi: 10.1038/s41586-018-0272-2.

Cramwinckel, M. J. *et al.* (2023) 'Global and Zonal-Mean Hydrological Response to Early Eocene Warmth', *Paleoceanography and Paleoclimatology*, 38(6), pp. 1–21. doi: 10.1029/2022PA004542.

Crouch, E. M. *et al.* (2003) 'The Apectodinium acme and terrestrial discharge during the Paleocene-Eocene thermal maximum: New palynological, geochemical and calcareous nannoplankton observations at Tawanui, New Zealand', *Palaeogeography, Palaeoclimatology, Palaeoecology*, 194(4), pp. 387–403. doi: 10.1016/S0031-

0182(03)00334-1.

Crutzen, P. (1973) ‘A discussion of the chemistry of some minor constituents in the stratosphere and troposphere’, *Pure and Applied Geophysics PAGEOPH*, 106–108(1), pp. 1385–1399. doi: 10.1007/BF00881092.

Cui, Y. *et al.* (2011) ‘Slow release of fossil carbon during the palaeocene-eocene thermal maximum’, *Nature Geoscience*, 4, pp. 481–485. doi: 10.1038/ngeo1179.

Cui, Y. *et al.* (2021) ‘Synchronous Marine and Terrestrial Carbon Cycle Perturbation in the High Arctic During the PETM’, *Paleoceanography and Paleoclimatology*, 36(4), pp. 1–21. doi: 10.1029/2020PA003942.

Cvejic, J. H. *et al.* (2000) ‘Bacterial triterpenoids of the hopane series from the methanotrophic bacteria Methylocaldum spp.: Phylogenetic implications and first evidence for an unsaturated aminobacteriohopanepolyol’, *FEMS Microbiology Letters*, 182(2), pp. 361–365. doi: 10.1016/S0378-1097(99)00610-2.

Daniels, W. C. *et al.* (2017) ‘Hydrogen isotope fractionation in leaf waxes in the Alaskan Arctic tundra’, *Geochimica et Cosmochimica Acta*, 213, pp. 216–236. doi: 10.1016/j.gca.2017.06.028.

Dansgaard, W. (1964) ‘Stable isotopes in precipitation’, *Tellus A: Dynamic Meteorology and Oceanography*, 16(4), p. 436. doi: 10.3402/tellusa.v16i4.8993.

Dean, J. F. *et al.* (2018) ‘Methane Feedbacks to the Global Climate System in a Warmer World’, *Reviews of Geophysics*, 56(1), pp. 207–250. doi: 10.1002/2017RG000559.

Deconto, R. M. *et al.* (2012) ‘Past extreme warming events linked to massive carbon release from thawing permafrost’, *Nature*, 484(7392), pp. 87–91. doi: 10.1038/nature10929.

DeConto, R. M. *et al.* (2008) ‘Thresholds for Cenozoic bipolar glaciation’, *Nature*, 455(7213), pp. 652–656. doi: 10.1038/nature07337.

DeConto, R. and Pollard, D. (2003) ‘Rapid Cenozoic glaciation of Antarctica induced by declining atmosheric CO_2’, *Nature*, 421(2001), pp. 245–249. doi: https://doi.org/10.1038/nature01290.

Dellinger, M. *et al.* (2023) ‘High rates of rock organic carbon oxidation sustained as Andean sediment transits the Amazon foreland-floodplain’, *Proceedings of the National Academy of Sciences*, 120(39). doi: 10.1073/pnas.2306343120.

Delmotte, M. *et al.* (2004) ‘Atmospheric methane during the last four glacial-interglacial cycles: Rapid changes and their link with Antarctic temperature’, *Journal of Geophysical Research D: Atmospheres*, 109(12). doi: 10.1029/2003JD004417.

Dickens, G. R. *et al.* (1995) 'Dissociation of oceanic methane hydrate as a cause of the carbon isotope excursion at the end of the Paleocene', *Paleoceanography*, 10(6), pp. 965–971. doi: 10.1029/95PA02087.

Dickens, G. R. (2011) 'Down the Rabbit Hole: Toward appropriate discussion of methane release from gas hydrate systems during the Paleocene-Eocene thermal maximum and other past hyperthermal events', *Climate of the Past*, 7(3), pp. 831–846. doi: 10.5194/cp-7-831-2011.

Dickens, G. R., Castillo, M. M. and Walker, J. C. G. (1997) 'A blast of gas in the latest Paleocene: Simulating first-order effects of massive dissociation of oceanic methane hydrate', *Geology*, 25(3), pp. 259–262. doi: 10.1130/0091-7613(1997)025<0259:ABOGIT>2.3.CO;2.

Dickson, A. J. *et al.* (2014) 'The spread of marine anoxia on the northern Tethys margin during the Paleocene-Eocene Thermal Maximum', *Paleoceanography*, 29(6), pp. 471–488. doi: 10.1002/2014PA002629.Received.

Dickson, A. J. *et al.* (2015) 'Evidence for weathering and volcanism during the PETM from Arctic Ocean and Peri-Tethys osmium isotope records', *Palaeogeography, Palaeoclimatology, Palaeoecology*, 438, pp. 300–307. doi: 10.1016/j.palaeo.2015.08.019.

Diefendorf, A. F. *et al.* (2010) 'Global patterns in leaf ^{13}C discrimination and implications for studies of past and future climate', *Proceedings of the National Academy of Sciences of the United States of America*, 107(13), pp. 5738–5743. doi: 10.1073/pnas.0910513107.

Diefendorf, A. F. *et al.* (2011) 'Production of *n*-alkyl lipids in living plants and implications for the geologic past', *Geochimica et Cosmochimica Acta*, 75(23), pp. 7472–7485. doi: 10.1016/j.gca.2011.09.028.

Diefendorf, A. F., Freeman, K. H. and Wing, S. L. (2014) 'A comparison of terpenoid and leaf fossil vegetation proxies in Paleocene and Eocene Bighorn Basin sediments', *Organic Geochemistry*, 71, pp. 30–42. doi: 10.1016/j.orggeochem.2014.04.004.

Diefendorf, A. F. and Freimuth, E. J. (2017) 'Extracting the most from terrestrial plant-derived *n*-alkyl lipids and their carbon isotopes from the sedimentary record: A review', *Organic Geochemistry*, 103. doi: 10.1016/j.orggeochem.2016.10.016.

van Dongen, B. E. *et al.* (2006) 'Well preserved Palaeogene and Cretaceous biomarkers from the Kilwa area, Tanzania', *Organic Geochemistry*, 37(5), pp. 539–557. doi: 10.1016/j.orggeochem.2006.01.003.

Doubrawa, M. *et al.* (2022) 'Shelf Ecosystems Along the U.S. Atlantic Coastal Plain Prior to and During the Paleocene-Eocene Thermal Maximum: Insights Into the Stratigraphic

Architecture', *Paleoceanography and Paleoclimatology*, 37(10), pp. 1–21. doi: 10.1029/2022PA004475.

Douville, H. *et al.* (2021) 'Water Cycle Changes', in Masson-Delmotte, V. et al. (eds) *Climate Change 2021: The Physical Science Basis. Contribution of Working Group I to the Sixth Assessment Report of the Intergovernmental Panel on Climate Change*. Cambridge, United Kingdom and New York, NY, USA: Cambridge University Press, pp. 1055–1210.

Drozd, J. K., Evans, T. W. and Summons, R. E. (2023) 'Lipid biomarker comparison of relict and active microbial mats from the McMurdo Ice Shelf, Antarctica', *Organic Geochemistry*, 179(January), p. 104591. doi: 10.1016/j.orggeochem.2023.104591.

Dunkley Jones, T. *et al.* (2018) 'Dynamics of sediment flux to a bathyal continental margin section through the Paleocene-Eocene Thermal Maximum', *Climate of the Past*, 14(7), pp. 1035–1049. doi: 10.5194/cp-14-1035-2018.

Dyonisius, M. N. *et al.* (2020) 'Old carbon reservoirs were not important in the deglacial methane budget', *Science*, 367(6480), pp. 907–910. doi: 10.1126/science.aax0504.

Dypvik, H. *et al.* (2011) 'The Paleocene-Eocene thermal maximum (PETM) in Svalbard — clay mineral and geochemical signals', *Palaeogeography, Palaeoclimatology, Palaeoecology*, 302(3–4), pp. 156–169. doi: 10.1016/j.palaeo.2010.12.025.

Edwards, E. J. *et al.* (2010) 'The origins of C4 grasslands: integrating evolutionary and ecosystem science.', *Science*, 328(April), pp. 587–59.

Egger, H. *et al.* (2005) 'Early Eocene climatic, volcanic, and biotic events in the northwestern Tethyan Untersberg section, Austria', *Palaeogeography, Palaeoclimatology, Palaeoecology*, 217(3–4), pp. 243–264. doi: 10.1016/j.palaeo.2004.12.006.

Eglinton, G. and Hamilton, R. J. (1967) 'Leaf epicuticular waxes', *Science*, 156(3780), pp. 1322–1335. doi: 10.1126/science.156.3780.1322.

Eglinton, T. I. *et al.* (2021) 'Climate control on terrestrial biospheric carbon turnover', *Proceedings of the National Academy of Sciences of the United States of America*, 118(8). doi: 10.1073/pnas.2011585118.

Eickhoff, M. *et al.* (2013) 'Bacteriohopanoid inventory of Geobacter sulfurreducens and Geobacter metallireducens', *Organic Geochemistry*, 58, pp. 107–114. doi: 10.1016/j.orggeochem.2013.02.013.

Eickhoff, M. *et al.* (2014) 'Diagenetic degradation products of bacteriohopanepolyols produced by Rhodopseudomonas palustris strain TIE-1', *Organic Geochemistry*, 68, pp. 31–38. doi: 10.1016/j.orggeochem.2014.01.002.

Eldholm, O. and Thomas, E. (1993) 'Environmental impact of volcanic margin formation', *Earth and Planetary Science Letters*, 117(3–4), pp. 319–329. doi: 10.1016/0012-821X(93)90087-P.

Elling, F. J. *et al.* (2019) 'Archaeal lipid biomarker constraints on the Paleocene-Eocene carbon isotope excursion', *Nature Communications*, 10(1). doi: 10.1038/s41467-019-12553-3.

Elling, F. J. *et al.* (2021) 'Linking diatom-diazotroph symbioses to nitrogen cycle perturbations and deep-water anoxia: Insights from Mediterranean sapropel events', *Earth and Planetary Science Letters*, 571, p. 117110. doi: 10.1016/j.epsl.2021.117110.

Elling, F. J. *et al.* (2022) 'Marine and terrestrial nitrifying bacteria are sources of diverse bacteriohopanepolyols', *Geobiology*, 20(3), pp. 399–420. doi: 10.1111/gbi.12484.

Elson, A. L. *et al.* (2022) 'Hydroclimate variability in the United States continental interior during the early Eocene Climatic Optimum', *Palaeogeography, Palaeoclimatology, Palaeoecology*, 595(March). doi: 10.1016/j.palaeo.2022.110959.

Elvert, M. *et al.* (2016) 'Methane turnover and environmental change from Holocene lipid biomarker records in a thermokarst lake in Arctic Alaska', *Holocene*, 26(11), pp. 1766–1777. doi: 10.1177/0959683616645942.

Evans, D. *et al.* (2024) 'The Temperature of the Deep Ocean Is a Robust Proxy for Global Mean Surface Temperature During the Cenozoic', *Paleoceanography and Paleoclimatology*, 39(5). doi: 10.1029/2023PA004788.

Farnsworth, A. *et al.* (2019) 'Climate Sensitivity on Geological Timescales Controlled by Nonlinear Feedbacks and Ocean Circulation', *Geophysical Research Letters*, 46(16), pp. 9880–9889. doi: 10.1029/2019GL083574.

Farrimond, P., Taylor, A. and Telnás, N. (1998) 'Biomarker maturity parameters : the role of generation and thermal degradation', *Organic Geochemistry*, 29(5–7), pp. 1181–1197. doi: 10.1016/S0146-6380(98)00079-5.

Feakins, S. J. (2013) 'Pollen-corrected leaf wax D/H reconstructions of northeast African hydrological changes during the late Miocene', *Palaeogeography, Palaeoclimatology, Palaeoecology*, 374, pp. 62–71. doi: 10.1016/j.palaeo.2013.01.004.

Feakins, S. J. *et al.* (2016) 'Plant leaf wax biomarkers capture gradients in hydrogen isotopes of precipitation from the Andes and Amazon', *Geochimica et Cosmochimica Acta*, 182, pp. 155–172. doi: 10.1016/j.gca.2016.03.018.

Ficken, K. J. *et al.* (2000) 'An *n*-alkane proxy for the sedimentary input of submerged/floating

freshwater aquatic macrophytes', *Organic Geochemistry*, 31(7–8), pp. 745–749. doi: 10.1016/S0146-6380(00)00081-4.

Fiedler, S. *et al.* (2020) 'Simulated tropical precipitation assessed across three major phases of the coupled model intercomparison project (CMIP)', *Monthly Weather Review*, 148(9), pp. 3653–3680. doi: 10.1175/MWR-D-19-0404.1.

Foote, E. (1856) 'Circumstances Affecting the Heat of the Sun's Rays', *The American Journal of Science and Arts*, 22(66), pp. 382–383.

Foreman, B. Z., Heller, P. L. and Clementz, M. T. (2012) 'Fluvial response to abrupt global warming at the Palaeocene/Eocene boundary', *Nature*, 491(7422), pp. 92–95. doi: 10.1038/nature11513.

Fornace, K. L. *et al.* (2014) 'A 60,000-year record of hydrologic variability in the Central Andes from the hydrogen isotopic composition of leaf waxes in Lake Titicaca sediments', *Earth and Planetary Science Letters*, 408, pp. 263–271. doi: 10.1016/j.epsl.2014.10.024.

Forster, P. *et al.* (2021) 'The Earth's Energy Budget, Climate Feedbacks, and Climate Sensitivity', in Masson-Delmotte, V. et al. (eds) *Climate Change ResearchClimate Change 2021: The Physical Science Basis. Contribution of Working Group I to the Sixth Assessment Report of the Intergovernmental Panel on Climate Change*. Cambridge, United Kingdom and New York, NY, USA: Cambridge University Press, pp. 923–1054. doi: 10.12006/j.issn.1673-1719.2021.191.

Forsythe, P. J. (2001) *Institute of Geological and Nuclear Sciences Geological Map, sheet 19, scale 1:250,000*. Lower Hutt, New Zealand.

Foster, G. L., Royer, D. L. and Lunt, D. J. (2017) 'Future climate forcing potentially without precedent in the last 420 million years', *Nature Communications*, 8. doi: 10.1038/ncomms14845.

Freeman, K. H. *et al.* (1990) 'Evidence from carbon isotope measurements for diverse origins', *Nature*, 343(January).

French, K. L. *et al.* (2012) 'Diagenetic and detrital origin of moretane anomalies through the Permian-Triassic boundary', *Geochimica et Cosmochimica Acta*, 84, pp. 104–125. doi: 10.1016/j.gca.2012.01.004.

Frieling, J. *et al.* (2016) 'Thermogenic methane release as a cause for the long duration of the PETM', *Proceedings of the National Academy of Sciences of the United States of America*, 113(43), pp. 12059–12064. doi: 10.1073/pnas.1603348113.

Frieling, J. *et al.* (2017) 'Extreme warmth and heat-stressed plankton in the tropics during the

Paleocene-Eocene Thermal Maximum', *Science Advances*, 3(3). doi: 10.1126/sciadv.1600891.

Galy, V. *et al.* (2007) 'Efficient organic carbon burial in the Bengal fan sustained by the Himalayan erosional system', *Nature*, 450(7168), pp. 407–410. doi: 10.1038/nature06273.

Galy, V. *et al.* (2008) 'Recycling of Graphite During Himalayan Erosion: A Geological Stabilization of Carbon in the Crust', *Science*, 322(5903), pp. 943–945. doi: 10.1126/science.1161408.

Galy, V., Peucker-Ehrenbrink, B. and Eglinton, T. (2015) 'Global carbon export from the terrestrial biosphere controlled by erosion', *Nature*, 521, pp. 204–207. doi: 10.1038/nature14400.

Gamarra, B., Sachse, D. and Kahmen, A. (2016) 'Effects of leaf water evaporative 2H-enrichment and biosynthetic fractionation on leaf wax *n*-alkane δ2H values in C3 and C4 grasses', *Plant Cell and Environment*, 39(11), pp. 2390–2403. doi: 10.1111/pce.12789.

Gao, L. *et al.* (2014) 'Major evolutionary trends in hydrogen isotope fractionation of vascular plant leaf waxes', *PLoS ONE*, 9(11). doi: 10.1371/journal.pone.0112610.

Garcin, Y. *et al.* (2014) 'Reconstructing C3 and C4 vegetation cover using *n*-alkane carbon isotope ratios in recent lake sediments from Cameroon, Western Central Africa', *Geochimica et Cosmochimica Acta*, 142, pp. 482–500. doi: 10.1016/j.gca.2014.07.004.

Garel, S. *et al.* (2013) 'Paleohydrological and paleoenvironmental changes recorded in terrestrial sediments of the Paleocene-Eocene boundary (Normandy, France)', *Palaeogeography, Palaeoclimatology, Palaeoecology*, 376, pp. 184–199. doi: 10.1016/j.palaeo.2013.02.035.

Gaskell, D. E. *et al.* (2022) 'The latitudinal temperature gradient and its climate dependence as inferred from foraminiferal $\delta^{18}O$ over the past 95 million years', *Proceedings of the National Academy of Sciences of the United States of America*, 119(11). doi: 10.1073/pnas.2111332119.

Gavrilov, Y. O., Shcherbinina, E. A. and Oberhänsli, H. (2003) 'Paleocene-Eocene boundary events in the northeastern Peri-Tethys', *Special Paper of the Geological Society of America*, 369, pp. 147–168. doi: 10.1130/0-8137-2369-8.147.

Gernon, T. M. *et al.* (2022) 'Transient mobilization of subcrustal carbon coincident with Palaeocene–Eocene Thermal Maximum', *Nature Geoscience*, 15(7), pp. 573–579. doi: 10.1038/s41561-022-00967-6.

Gibson, T. G., Bybell, L. M. and Mason, D. B. (2000) 'Stratigraphic and climatic implications

of clay mineral changes around the Paleocene/Eocene boundary of the northeastern US margin', *Sedimentary Geology*, 134(1–2), pp. 65–92. doi: 10.1016/S0037-0738(00)00014-2.

Goñi, M. A. *et al.* (2013) 'Particulate organic matter export by two contrasting small mountainous rivers from the Pacific Northwest, U.S.A.', *Journal of Geophysical Research: Biogeosciences*, 118(1), pp. 112–134. doi: 10.1002/jgrg.20024.

Goodrich, J. P. *et al.* (2015) 'Overriding control ofmethane flux temporal variability by water table dynamics in a Southern Hemisphere, raised bog', *Journal of Geophysical Research: Biogeosciences*, 120, pp. 965–978. doi: 10.1002/2014JG002844.Received.

Graham, H. V. *et al.* (2014) 'Isotopic characteristics of canopies in simulated leaf assemblages', *Geochimica et Cosmochimica Acta*, 144, pp. 82–95. doi: 10.1016/j.gca.2014.08.032.

Greve, P. *et al.* (2014) 'Global assessment of trends in wetting and drying over land', *Nature Geoscience*, 7(10), pp. 716–721. doi: 10.1038/NGEO2247.

Gu, X. and Brantley, S. L. (2022) 'How Particle Size Influences Oxidation of Ancient Organic Matter during Weathering of Black Shale', *ACS Earth Space Chem.*, 6, pp. 1443–1459. doi: 10.1021/acsearthspacechem.1c00442.

Gutjahr, M. *et al.* (2017) 'Very large release of mostly volcanic carbon during the Palaeocene – Eocene Thermal Maximum', *Nature*, 548, pp. 573–577. doi: 10.1038/nature23646.

Handley, L. *et al.* (2008) 'Large terrestrial and marine carbon and hydrogen isotope excursions in a new Paleocene/Eocene boundary section from Tanzania', *Earth and Planetary Science Letters*, 275(1), pp. 17–25. doi: 10.1016/j.epsl.2008.07.030.

Handley, L. *et al.* (2010) 'Bacteriohopanepolyols as tracers for continental and marine organic matter supply and phases of enhanced nitrogen cycling on the late Quaternary Congo deep sea fan', *Organic Geochemistry*, 41(9), pp. 910–914. doi: 10.1016/j.orggeochem.2010.04.016.

Handley, L. *et al.* (2012) 'Changes in the hydrological cycle in tropical East Africa during the Paleocene-Eocene Thermal Maximum', *Palaeogeography, Palaeoclimatology, Palaeoecology*, 329–330, pp. 10–21. doi: 10.1016/j.palaeo.2012.02.002.

Handley, L., Crouch, E. M. and Pancost, R. D. (2011) 'A New Zealand record of sea level rise and environmental change during the Paleocene-Eocene Thermal Maximum', *Palaeogeography, Palaeoclimatology, Palaeoecology*, 305, pp. 185–200. doi: 10.1016/j.palaeo.2011.03.001.

Hansen, J. *et al.* (2013) 'Climate sensitivity, sea level and atmospheric carbon dioxide',

Philosophical Transactions of the Royal Society A: Mathematical, Physical and Engineering Sciences, 371. doi: 10.1098/rsta.2012.0294.

Hanson, R. S. and Hanson, T. E. (1996) 'Methanotrophic bacteria', *Microbiological Reviews*, 60(2), pp. 439–471. doi: 10.1128/mmbr.60.2.439-471.1996.

Harding, I. C. *et al.* (2011) 'Sea-level and salinity fluctuations during the Paleocene-Eocene thermal maximum in Arctic Spitsbergen', *Earth and Planetary Science Letters*, 303(1–2), pp. 97–107. doi: 10.1016/j.epsl.2010.12.043.

Hare, V. J. and Lavergne, A. (2021) 'Differences in carbon isotope discrimination between angiosperm and gymnosperm woody plants, and their geological significance', *Geochimica et Cosmochimica Acta*, 300, pp. 215–230. doi: 10.1016/j.gca.2021.02.029.

Harper, D. T. *et al.* (2020) 'The Magnitude of Surface Ocean Acidification and Carbon Release During Eocene Thermal Maximum 2 (ETM-2) and the Paleocene-Eocene Thermal Maximum (PETM)', *Paleoceanography and Paleoclimatology*, 35. doi: 10.1029/2019PA003699.

Harris, A. D. *et al.* (2010) 'Integrated stratigraphic studies of Paleocene-lowermost Eocene sequences, New Jersey Coastal Plain: Evidence for glacioeustatic control', *Paleoceanography*, 25(3), pp. 1–18. doi: 10.1029/2009PA001800.

Hatten, J. A., Goñi, M. A. and Wheatcroft, R. A. (2012) 'Chemical characteristics of particulate organic matter from a small, mountainous river system in the Oregon Coast Range, USA', *Biogeochemistry*, 107(1–3), pp. 43–66. doi: 10.1007/s10533-010-9529-z.

Hayes, J. M. (1993) 'Factors controlling ^{13}C contents of sedimentary organic compounds: Principles and evidence', *Marine Geology*, 113(1–2), pp. 111–125. doi: 10.1016/0025-3227(93)90153-M.

Hefter, J., Naafs, B. D. A. and Zhang, S. (2017) 'Tracing the source of ancient reworked organic matter delivered to the North Atlantic Ocean during Heinrich Events', *Geochimica et Cosmochimica Acta*, 205, pp. 211–225. doi: 10.1016/j.gca.2017.02.008.

Held, I. M. and Soden, B. J. (2006) 'Robust Responses of the Hydrological Cycle to Global Warming', *Journal of Climate*, 19(21), pp. 5685–5699. doi: 10.1175/JCLI3990.1.

Hemingway, J. D., Kusch, S., *et al.* (2018) 'A novel method to measure the ^{13}C composition of intact bacteriohopanepolyols', *Organic Geochemistry*, 123, pp. 144–147. doi: 10.1016/j.orggeochem.2018.07.002.

Hemingway, J. D., Hilton, R. G., *et al.* (2018) 'Microbial oxidation of lithospheric organic carbon in rapidly eroding tropical mountain soils', *Science*, 360, pp. 209–212. Available at:

https://www.science.org/doi/10.1126/science.aao6463.

Henry, D. G. *et al.* (2019) 'Raman spectroscopy as a tool to determine the thermal maturity of organic matter: Application to sedimentary, metamorphic and structural geology', *Earth-Science Reviews*, 198. doi: 10.1016/j.earscirev.2019.102936.

Herold, N. *et al.* (2014) 'A suite of early Eocene (~55 Ma) climate model boundary conditions', *Geoscientific Model Development*, 7, pp. 2077–2090. doi: 10.5194/gmd-7-2077-2014.

Higgins, J. A. and Schrag, D. P. (2006) 'Beyond methane: Towards a theory for the Paleocene-Eocene Thermal Maximum', *Earth and Planetary Science Letters*, 245, pp. 523–537. doi: 10.1016/j.epsl.2006.03.009.

Hilton, R. G. *et al.* (2008) 'Tropical-cyclone-driven erosion of the terrestrial biosphere from mountains', *Nature Geoscience*, 1, pp. 759–762. doi: 10.1038/ngeo333.

Hilton, R. G. *et al.* (2010) 'The isotopic composition of particulate organic carbon in mountain rivers of Taiwan', *Geochimica et Cosmochimica Acta*, 74(11), pp. 3164–3181. doi: 10.1016/j.gca.2010.03.004.

Hilton, R. G., Galy, A., *et al.* (2011) 'Efficient transport of fossil organic carbon to the ocean by steep mountain rivers: An orogenic carbon sequestration mechanism', *Geology*, 39(1), pp. 71–74. doi: 10.1130/G31352.1.

Hilton, R. G., Meunier, P., *et al.* (2011) 'Landslide impact on organic carbon cycling in a temperate montane forest', *Earth Surface Processes and Landforms*, 36(12), pp. 1670–1679. doi: 10.1002/esp.2191.

Hilton, R. G. *et al.* (2012) 'Climatic and geomorphic controls on the erosion of terrestrial biomass from subtropical mountain forest', *Global Biogeochemical Cycles*, 26(3). doi: 10.1029/2012GB004314.

Hilton, R. G. *et al.* (2014) 'Geological respiration of a mountain belt revealed by the trace element rhenium', *Earth and Planetary Science Letters*, 403, pp. 27–36. doi: 10.1016/j.epsl.2014.06.021.

Hilton, R. G. *et al.* (2015) 'Erosion of organic carbon in the Arctic as a geological carbon dioxide sink', *Nature*, 524, pp. 84–87. doi: 10.1038/nature14653.

Hilton, R. G. (2017) 'Climate regulates the erosional carbon export from the terrestrial biosphere', *Geomorphology*, 277, pp. 118–132. doi: 10.1016/j.geomorph.2016.03.028.

Hilton, R. G., Galy, A. and Hovius, N. (2008) 'Riverine particulate organic carbon from an active mountain belt: Importance of landslides', *Global Biogeochemical Cycles*, 22(1), pp. 1–

12. doi: 10.1029/2006GB002905.

Hilton, R. G. and West, A. J. (2020) ‘Mountains, erosion and the carbon cycle’, *Nature Reviews Earth & Environment*, 1, pp. 284–299. doi: 10.1038/s43017-020-0058-6.

Hinrichs, K.-U. *et al.* (1999) ‘Methane-consuming archaebacteria in marine sediments’, *Letters to Nature*, 398(April), pp. 802–805.

Hinrichs, K. *et al.* (2000) ‘Mass spectra of *sn* -2-hydroxyarchaeol, a polar lipid biomarker for anaerobic methanotrophy’, *Geochemistry, Geophysics, Geosystems*, 1(5), pp. 11–13. doi: 10.1029/2000gc000042.

Hoegh-Guldberg, O. *et al.* (2019) ‘The human imperative of stabilizing global climate change at 1.5°C’, *Science*, 365(1263). doi: 10.1126/science.aaw6974.

Hofmann, K. *et al.* (2016) ‘Methane-cycling microorganisms in soils of a high-alpine altitudinal gradient’, *FEMS Microbiology Ecology*, 92(3). doi: 10.1093/femsec/fiw009.

Hollis, C. J. *et al.* (2012) ‘Early Paleogene temperature history of the Southwest Pacific Ocean: Reconciling proxies and models’, *Earth and Planetary Science Letters*, 349–350, pp. 53–66. doi: 10.1016/j.epsl.2012.06.024.

Hollis, C. J. *et al.* (2019) ‘The DeepMIP contribution to PMIP4: Methodologies for selection, compilation and analysis of latest Paleocene and early Eocene climate proxy data, incorporating version 0.1 of the DeepMIP database’, *Geoscientific Model Development*, 12(7), pp. 3149–3206. doi: 10.5194/gmd-12-3149-2019.

Hönisch, B. *et al.* (2023) ‘Toward a Cenozoic history of atmospheric CO_2’, *Science*, 382(6675). doi: 10.1126/science.adi5177.

Hopmans, E. C. *et al.* (2021) ‘Analysis of non-derivatized bacteriohopanepolyols using UHPLC-HRMS reveals great structural diversity in environmental lipid assemblages’, *Organic Geochemistry*, 160. doi: 10.1016/j.orggeochem.2021.104285.

Horan, K. *et al.* (2017) ‘Mountain glaciation drives rapid oxidation of rock-bound organic carbon’, *Science Advances*, 3(10). doi: 10.1126/sciadv.1701107.

Huang, X. *et al.* (2018) ‘Response of carbon cycle to drier conditions in the mid-Holocene in central China’, *Nature Communications*, 9(1), pp. 1–9. doi: 10.1038/s41467-018-03804-w.

Huang, Y. *et al.* (2001) ‘Climate change as the dominant control on glacial-interglacial variations in C3 and C4 plant abundance’, *Science*, 293(5535), pp. 1647–1651. doi: 10.1126/science.1060143.

Huber, M. and Caballero, R. (2011) ‘The early Eocene equable climate problem revisited’,

Climate of the Past, 7, pp. 603–633. doi: 10.5194/cp-7-603-2011.

Inagaki, F. *et al.* (2015) 'Exploring deep microbial life in coal-bearing sediment down to ~2.5 km below the ocean floor', *Science*, 349(6246), pp. 420–424. doi: 10.1126/science.aaa6882.

Inglis, G. N. *et al.* (2015) 'Ecological and biogeochemical change in an early Paleogene peat-forming environment: Linking biomarkers and palynology', *Palaeogeography, Palaeoclimatology, Palaeoecology*, 438, pp. 245–255. doi: 10.1016/j.palaeo.2015.08.001.

Inglis, G. N. *et al.* (2018) 'Distributions of geohopanoids in peat: Implications for the use of hopanoid-based proxies in natural archives', *Geochimica et Cosmochimica Acta*, 224, pp. 249–261. doi: 10.1016/j.gca.2017.12.029.

Inglis, G. N., Farnsworth, A., *et al.* (2019) 'Terrestrial environmental change across the onset of the PETM and the associated impact on biomarker proxies: A cautionary tale', *Global and Planetary Change*, 181, p. 102991. doi: 10.1016/j.gloplacha.2019.102991.

Inglis, G. N., Naafs, B. D. A., *et al.* (2019) '$\delta^{13}C$ values of bacterial hopanoids and leaf waxes as tracers for methanotrophy in peatlands', *Geochimica et Cosmochimica Acta*, 260, pp. 244–256. doi: 10.1016/j.gca.2019.06.030.

Inglis, G. N., Carmichael, M. J., *et al.* (2020) 'A long-term, high-latitude record of Eocene hydrological change in the Greenland region', *Palaeogeography, Palaeoclimatology, Palaeoecology*, 537. doi: 10.1016/j.palaeo.2019.109378.

Inglis, G. N., Bragg, F., *et al.* (2020) 'Global mean surface temperature and climate sensitivity of the early Eocene Climatic Optimum (EECO), Paleocene-Eocene Thermal Maximum (PETM), and latest Paleocene', *Climate of the Past*, 16(5), pp. 1953–1968. doi: 10.5194/cp-16-1953-2020.

Inglis, G. N. *et al.* (2021) 'Terrestrial methane cycle perturbations during the onset of the Paleocene-Eocene Thermal Maximum', *Geology*, 49(5), pp. 520–524. doi: 10.1130/G48110.1.

Inglis, G. N., Bhattacharya, T., *et al.* (2022) 'Biomarker Approaches for Reconstructing Terrestrial Environmental Change', *Annual Review of Earth and Planetary Sciences*, 50, pp. 369–394. doi: 10.1146/annurev-earth-032320- 095943 Copyright.

Inglis, G. N., Toney, J. L., *et al.* (2022) 'Enhanced Terrestrial Carbon Export From East Antarctica During the Early Eocene', *Paleoceanography and Paleoclimatology*, 37(2), pp. 1–14. doi: 10.1029/2021PA004348.

Inglis, G. N. *et al.* (2023) 'Impact of organic carbon reworking upon GDGT temperature proxies during the Paleocene-Eocene Thermal Maximum', *Organic Geochemistry*, 183. doi:

10.1016/j.orggeochem.2023.104644.

IPCC (2013) *Climate Change 2013: The Physical Science Basis. Contribution of Working Group I to the Fifth Assessment Report of the Intergovernmental Panel on Climate Change*. Edited by T. F. Stocker et al. Cambridge, United Kingdom and New York, NY, USA: Cambridge University Press.

IPCC (2021) *Climate Change 2021: The Physical Science Basis. Contribution of Working Group I to the Sixth Assessment Report of the Intergovernmental Panel on Climate Change*. Edited by V. Masson-Delmotte et al. Cambridge, United Kingdom and New York, NY, USA: Cambridge University Press. doi: 10.1017/9781009157896.

Jaramillo, C. *et al.* (2010) 'Effects of rapid global warming at the paleocene-eocene boundary on neotropical vegetation', *Science*, 330(6006), pp. 957–961. doi: 10.1126/science.1193833.

Jaramillo, C. A. *et al.* (2007) 'The Palynology of the Cerrajon Formation (Upper Paleocene) of Northern Colombia', *Palynology*, 31, pp. 153–189.

Jaramillo, C. A., Rueda, M. and Torres, V. (2011) 'A palynological zonation for the Cenozoic of the Llanos and Llanos Foothills of Colombia', *Palynology*, 35(1), pp. 46–84. doi: 10.1080/01916122.2010.515069.

Jehlicka, J. and Rouzaud, J.-N. (1990) 'Organic geochemistry of precambrian shales and schists (Bohemian massif, Central Europe)', *Organic Geochemistry*, 16(4–6), pp. 865–872. doi: 10.1016/0146-6380(90)90123-H.

Jiang, J. *et al.* (2023) 'Eustatic change across the Paleocene-Eocene Thermal Maximum in the epicontinental Tarim seaway', *Global and Planetary Change*, 229(February), p. 104241. doi: 10.1016/j.gloplacha.2023.104241.

Jin, S. *et al.* (2024) 'Spatiotemporal distribution of global mercury enrichments through the Paleocene-Eocene Thermal Maximum and links to volcanism', *Earth-Science Reviews*, 248. doi: 10.1016/j.earscirev.2023.104647.

Joabsson, A. and Christensen, T. R. (2001) 'Methane emissions from wetlands and their relationship with vascular plants: an Arctic example', *Global Change Biology*, 7(8), pp. 919–932. doi: 10.1046/j.1354-1013.2001.00044.x.

John, C. M. *et al.* (2008) 'North American continental margin records of the Paleocene-Eocene thermal maximum: Implications for global carbon and hydrological cycling', *Paleoceanography*, 23(2). doi: 10.1029/2007PA001465.

John, C. M. *et al.* (2012) 'Clay assemblage and oxygen isotopic constraints on the weathering response to the Paleocene-Eocene thermal maximum, East Coast of North

America', *Geology*, 40(7), pp. 591–594. doi: 10.1130/G32785.1.

Jones, M. T. *et al.* (2019) 'Mercury anomalies across the Palaeocene-Eocene Thermal Maximum', *Climate of the Past*, 15(1), pp. 217–236. doi: 10.5194/cp-15-217-2019.

Jones, S. M. *et al.* (2019) 'Large Igneous Province thermogenic greenhouse gas flux could have initiated Paleocene-Eocene Thermal Maximum climate change', *Nature Communications*, 10(5547), pp. 1–16. doi: 10.1038/s41467-019-12957-1.

De Jonge, C. *et al.* (2016) 'Bacteriohopanepolyol distribution in Yenisei River and Kara Sea suspended particulate matter and sediments traces terrigenous organic matter input', *Geochimica et Cosmochimica Acta*, 174, pp. 85–101. doi: 10.1016/j.gca.2015.11.008.

Junium, C. K., Dickson, A. J. and Uveges, B. T. (2018) 'Perturbation to the nitrogen cycle during rapid Early Eocene global warming', *Nature Communications*, 9(1). doi: 10.1038/s41467-018-05486-w.

Kaiho, K. *et al.* (1996) 'Latest Paleocene benthic foraminferal extinction and environmental changes at Tawanui , New Zealand', *Paleoceanography*, 11(4), pp. 447–465. doi: 10.1029/96PA01021.

Kao, S. J. *et al.* (2008) 'Enhanced supply of fossil organic carbon to the Okinawa trough since the last deglaciation', *Paleoceanography*, 23(2), pp. 1–10. doi: 10.1029/2007PA001440.

Kao, S. J. *et al.* (2014) 'Preservation of terrestrial organic carbon in marine sediments offshore Taiwan: Mountain building and atmospheric carbon dioxide sequestration', *Earth Surface Dynamics*, 2(1), pp. 127–139. doi: 10.5194/esurf-2-127-2014.

Katz, M. E. *et al.* (1999) 'The Source and Fate of Massive Carbon Input During the Latest Paleocene Thermal Maximum', *Science*, 286(5444), pp. 1531–1533. doi: 10.1126/science.286.5444.1531.

Kawamura, K. and Ishimura, Y. (2003) 'Four years' observations of terrestrial lipid class compounds in marine aerosols from the western North Pacific', *Global Biogeochemical Cycles*, 17(1), pp. 3–19. doi: 10.1029/2001gb001810.

Kaya, M. Y. *et al.* (2022) 'The Eurasian epicontinental sea was an important carbon sink during the Palaeocene-Eocene thermal maximum', *Communications Earth and Environment*, 3(1), pp. 1–10. doi: 10.1038/s43247-022-00451-4.

Keeling, C. D. *et al.* (2001) *Exchanges of atmospheric CO_2 and $^{13}CO_2$ with the terrestrial biosphere and oceans from 1978 to 2000. I Global Aspects*, *UC San Diego: Scripps Institution of Oceanography*. Available at: http://escholarship.org/uc/item/09v319r9.

van Kemenade, Z. R. *et al.* (2022) 'Bacteriohopanetetrol-x: Constraining its application as a lipid biomarker for marine anammox using the water column oxygen gradient of the Benguela upwelling system', *Biogeosciences*, 19(1), pp. 201–221. doi: 10.5194/bg-19-201-2022.

van Kemenade, Z. R. *et al.* (2023) 'Marine nitrogen cycling dynamics under altering redox conditions: Insights from deposition of sapropels S1 and the ambiguous S2 in the Eastern Mediterranean Sea', *Geochimica et Cosmochimica Acta*, 354(October 2022), pp. 197–210. doi: 10.1016/j.gca.2023.06.018.

Kender, S. *et al.* (2012) 'Marine and terrestrial environmental changes in NW Europe preceding carbon release at the Paleocene-Eocene transition', *Earth and Planetary Science Letters*, 353–354, pp. 108–120. doi: 10.1016/j.epsl.2012.08.011.

Kennett, J. P. and Stott, L. D. (1991) 'Abrupt deep-sea warming, palaeoceanographic changes and benthic extinctions at the end of the Palaeocene', *Nature*, 353, pp. 225–229.

Kiehl, J. T. *et al.* (2018) 'Greenhouse- and orbital-forced climate extremes during the early Eocene', *Philosophical Transactions of the Royal Society A: Mathematical, Physical and Engineering Sciences*, 376(2130). doi: 10.1098/rsta.2017.0085.

Kiehl, J. T. *et al.* (2021) 'Simulated changes to tropical cyclones across the Paleocene-Eocene Thermal Maximum (PETM) boundary', *Palaeogeography, Palaeoclimatology, Palaeoecology*, 572, p. 110421. doi: 10.1016/j.palaeo.2021.110421.

Kim, J. H. *et al.* (2011) 'Occurrence and abundance of soil-specific bacterial membrane lipid markers in the Têt watershed (southern France): Soil-specific BHPs and branched GDGTs', *Geochemistry, Geophysics, Geosystems*, 12(2). doi: 10.1029/2010GC003364.

Kip, N. *et al.* (2010) 'Global prevalence of methane oxidation by symbiotic bacteria in peat-moss ecosystems', *Nature Geoscience*, 3(9), pp. 617–621. doi: 10.1038/ngeo939.

Kirtland Turner, S. *et al.* (2014) 'Persistence of carbon release events through the peak of early Eocene global warmth', *Nature Geoscience*, 7(10), pp. 748–751. doi: 10.1038/NGEO2240.

Kirtland Turner, S. (2018) 'Constraints on the onset duration of the Paleocene-Eocene Thermal Maximum', *Philosophical Transactions of the Royal Society A*, 376(2130), pp. 1–16. doi: 10.1098/rsta.2017.0082.

Koga, Y. *et al.* (1993) 'Ether polar lipids of methanogenic bacteria: Structures, comparative aspects, and biosyntheses', *Microbiological Reviews*, 57(1), pp. 164–182. doi: 10.1128/mr.57.1.164-182.1993.

Koga, Y. and Morii, H. (2007) 'Biosynthesis of Ether-Type Polar Lipids in Archaea and

Evolutionary Considerations', *Microbiology and Molecular Biology Reviews*, 71(1), pp. 97–120. doi: 10.1128/mmbr.00033-06.

Kolouchová, I. *et al.* (2021) 'Analysis of bacteriohopanoids from thermophilic bacteria by liquid chromatography–mass spectrometry', *Microorganisms*, 9(10). doi: 10.3390/microorganisms9102062.

Komada, T., Druffel, E. R. M. and Trumbore, S. E. (2004) 'Oceanic export of relict carbon by small mountainous rivers', *Geophysical Research Letters*, 31(7). doi: 10.1029/2004GL019512.

Kopp, R. E. *et al.* (2009) 'An Appalachian Amazon? Magnetofossil evidence for the development of a tropical river-like system in the mid-Atlantic United States during the Paleocene-Eocene thermal maximum', *Paleoceanography*, 24(4), pp. 1–17. doi: 10.1029/2009PA001783.

Korasidis, V. A. *et al.* (2022) 'Global Changes in Terrestrial Vegetation and Continental Climate During the Paleocene-Eocene Thermal Maximum', *Paleoceanography and Paleoclimatology*, 37(4), pp. 1–21. doi: 10.1029/2021PA004325.

Kraus, M. J. *et al.* (2013) 'Paleohydrologic response to continental warming during the Paleocene-Eocene Thermal Maximum, Bighorn Basin, Wyoming', *Palaeogeography, Palaeoclimatology, Palaeoecology*, 370, pp. 196–208. doi: 10.1016/j.palaeo.2012.12.008.

Kraus, M. J. and Riggins, S. (2007) 'Transient drying during the Paleocene-Eocene Thermal Maximum (PETM): Analysis of paleosols in the bighorn basin, Wyoming', *Palaeogeography, Palaeoclimatology, Palaeoecology*, 245(3–4), pp. 444–461. doi: 10.1016/j.palaeo.2006.09.011.

Kurtz, A. C. *et al.* (2003) 'Early Cenozoic decoupling of the global carbon and sulfur cycles', *Paleoceanography*, 18(4), pp. 1–14. doi: 10.1029/2003PA000908.

Kusch, S. *et al.* (2018) 'Improved chromatography reveals multiple new bacteriohopanepolyol isomers in marine sediments', *Organic Geochemistry*, 124, pp. 12–21. doi: 10.1016/j.orggeochem.2018.07.010.

Kusch, S. *et al.* (2021) 'Bacterial and archaeal lipids trace chemo(auto)trophy along the redoxcline in Vancouver Island fjords', *Geobiology*, 19(5), pp. 521–541. doi: 10.1111/gbi.12446.

Kusch, S. and Rush, D. (2022) 'Revisiting the precursors of the most abundant natural products on Earth: A look back at 30+ years of bacteriohopanepolyol (BHP) research and ahead to new frontiers', *Organic Geochemistry*, 172. doi: 10.1016/j.orggeochem.2022.104469.

Kvenvolden, K. A. (1993) 'Gas hydrates—geological perspective and global change', *Reviews of Geophysics*, 31(2), pp. 173–187. doi: 10.1029/93RG00268.

Ladd, S. N. *et al.* (2021) 'Leaf Wax Hydrogen Isotopes as a Hydroclimate Proxy in the Tropical Pacific', *Journal of Geophysical Research: Biogeosciences*, 126(3), pp. 1–21. doi: 10.1029/2020JG005891.

Lamarche-Gagnon, G. *et al.* (2019) 'Greenland melt drives continuous export of methane from the ice-sheet bed', *Nature*, 565(7737), pp. 73–77. doi: 10.1038/s41586-018-0800-0.

Lan, X., Thoning, K. W. and Dlugokencky, E. J. (2024) *Trends in globally-averaged CH_4, N_2O, and SF_6 determined from NOAA Global Monitoring Laboratory measurements. Version 2024-12*. Available at: https://doi.org/10.15138/P8XG-AA10.

Larrasoaña, J. C. *et al.* (2012) 'Magnetotactic bacterial response to Antarctic dust supply during the Palaeocene-Eocene thermal maximum', *Earth and Planetary Science Letters*, 333–334, pp. 122–133. doi: 10.1016/j.epsl.2012.04.003.

Lauretano, V., Zachos, J. C. and Lourens, L. J. (2018) 'Orbitally Paced Carbon and Deep-Sea Temperature Changes at the Peak of the Early Eocene Climatic Optimum Paleoceanography and Paleoclimatology', *Paleoceanography and Paleoclimatology*, 33(10), pp. 1050–1065. doi: 10.1029/2018PA003422.

Lee, J.-Y. *et al.* (2021) 'Future Global Climate: Scenario-based Projections and Near-term Information', in Masson-Delmotte, V. et al. (eds) *Climate Change 2021: The Physical Science Basis. Contribution of Working Group I to the Sixth Assessment Report of the Intergovernmental Panel on Climate Change*. Cambridge, United Kingdom and New York, NY, USA: Cambridge University Press, pp. 553–672.

Lee, J. E. *et al.* (2007) 'Analysis of the global distribution of water isotopes using the NCAR atmospheric general circulation model', *Journal of Geophysical Research Atmospheres*, 112(16). doi: 10.1029/2006JD007657.

Leithold, E. L., Blair, N. E. and Perkey, D. W. (2006) 'Geomorphologic controls on the age of particulate organic carbon from small mountainous and upland rivers', *Global Biogeochemical Cycles*, 20(3), pp. 1–11. doi: 10.1029/2005GB002677.

Lengger, S. K. *et al.* (2019) 'Dark carbon fixation in the Arabian Sea oxygen minimum zone contributes to sedimentary organic carbon (SOM)', *Global Biogeochemical Cycles*, 33(12), pp. 1715–1732. doi: 10.1029/2019GB006282.

Li, J. *et al.* (2020) 'Sea level , biotic and carbon-isotope response to the Paleocene – Eocene thermal maximum in Tibetan Himalayan platform carbonates', *Global and Planetary Change*, 194, p. 103316. doi: 10.1016/j.gloplacha.2020.103316.

Littler, K. *et al.* (2014) 'A high-resolution benthic stable-isotope record for the South Atlantic: Implications for orbital-scale changes in Late Paleocene-Early Eocene climate and carbon cycling', *Earth and Planetary Science Letters*, 401, pp. 18–30. doi: 10.1016/j.epsl.2014.05.054.

Liu, J. and An, Z. (2019) 'Variations in hydrogen isotopic fractionation in higher plants and sediments across different latitudes: Implications for paleohydrological reconstruction', *Science of the Total Environment*, 650, pp. 470–478. doi: 10.1016/j.scitotenv.2018.09.047.

Liu, Z., Bowen, G. J. and Welker, J. M. (2010) 'Atmospheric circulation is reflected in precipitation isotope gradients over the conterminous United States', *Journal of Geophysical Research Atmospheres*, 115(22). doi: 10.1029/2010JD014175.

Loulergue, L. *et al.* (2008) 'Orbital and millennial-scale features of atmospheric CH_4 over the past 800,000 years', *Nature*, 453(May), pp. 383–386. doi: 10.1038/nature06950.

Lourens, L. J. *et al.* (2005) 'Astronomical pacing of late Palaeocene to early Eocene global warming events', *Nature*, 435, pp. 1083–1087. doi: 10.1038/nature03814.

Lunt, D. J. *et al.* (2017) 'The DeepMIP contribution to PMIP4 : experimental design for model simulations of the EECO , PETM , and pre-PETM (version 1.0)', *Geoscientific Model Development*, 10, pp. 889–901. doi: 10.5194/gmd-10-889-2017.

Lunt, D. J. *et al.* (2021) 'DeepMIP : model intercomparison of early Eocene climatic optimum (EECO) large-scale climate features and comparison with proxy data', *Climate of the Past*, 17, pp. 203–227. doi: 10.5194/cp-17-203-2021.

Lunt, D. J. *et al.* (2024) 'Paleoclimate data provide constraints on climate models' large-scale response to past CO_2 changes', *Communications Earth and Environment*, 5(1), pp. 1–9. doi: 10.1038/s43247-024-01531-3.

Lyons, S. L. *et al.* (2019) 'Palaeocene–Eocene Thermal Maximum prolonged by fossil carbon oxidation', *Nature Geoscience*, 12, pp. 54–60. doi: 10.1038/s41561-018-0277-3.

Lyster, S. J. *et al.* (2020) 'Predicting sediment discharges and erosion rates in deep time—examples from the late Cretaceous North American continent', *Basin Research*, 32(6), pp. 1547–1573. doi: 10.1111/bre.12442.

Ma, Z. *et al.* (2014) 'Carbon sequestration during the Palaeocene-Eocene Thermal Maximum by an efficient biological pump', *Nature Geoscience*, 7, pp. 382–388. doi: 10.1038/ngeo2139.

Mackenzie, A. S. *et al.* (1980) 'Molecular parameters of maturation in the Toarcian shales, Paris Basin, France—I. Changes in the configurations of acyclic isoprenoid alkanes, steranes and triterpanes', *Geochimica et Cosmochimica Acta*, 44(11), pp. 1709–1721. doi:

10.1016/0016-7037(80)90222-7.

Magill, C. R., Ashley, G. M. and Freeman, K. H. (2013) 'Water, plants, and early human habitats in eastern Africa', *Proceedings of the National Academy of Sciences*, 110(4), pp. 1175–1180. doi: 10.1073/pnas.1209405109.

Marwick, J. (1960) *Tertiary Mollusca from Otaio Gorge South Canterbury*. Lower Hutt, New Zealand.

Marzi, P., Torkelson, B. E. and Olson, R. K. (1993) 'A revised carbon preference index', *Organic*, 20(8), pp. 1303–1306.

Mayer, M. H. *et al.* (2021) 'Anaerobic 3-methylhopanoid production by an acidophilic photosynthetic purple bacterium', *Archives of Microbiology*, 203(10). doi: 10.1007/s00203-021-02561-7.

McCartney, C. A. *et al.* (2013) 'Technical note: Comparison of biomarker and molecular biological methods for estimating methanogen abundance', *Journal of Animal Science*, 91, pp. 5724–5728. doi: 10.2527/jas.2013-6513.

McFarlin, J. M. *et al.* (2019) 'Calibration of modern sedimentary δ^2H plant wax-water relationships in Greenland lakes', *Quaternary Science Reviews*, 225, p. 105978. doi: 10.1016/j.quascirev.2019.105978.

McInerney, F. A. and Wing, S. L. (2011) 'The Paleocene-Eocene Thermal Maximum: A perturbation of carbon cycle, climate, and biosphere with implications for the future', *Annual Review of Earth and Planetary Sciences*, 39, pp. 489–516. doi: 10.1146/annurev-earth-040610-133431.

Mead, R. *et al.* (2005) 'Sediment and soil organic matter source assessment as revealed by the molecular distribution and carbon isotopic composition of *n*-alkanes', *Organic Geochemistry*, 36(3), pp. 363–370. doi: 10.1016/j.orggeochem.2004.10.003.

Meckler, A. N. *et al.* (2022) 'Cenozoic evolution of deep ocean temperature from clumped isotope thermometry', *Science*, 377(6601), pp. 86–90. doi: 10.1126/science.abk0604.

Meissner, K. J. *et al.* (2014) 'The Paleocene-Eocene Thermal Maximum: How much carbon is enough?', *Paleoceanography*, 29(10), pp. 946–963. doi: 10.1002/2014PA002650.

Meyers, P. A. and Ishiwatari, R. (1993) 'Lacustrine organic geochemistry—an overview of indicators of organic matter sources and diagenesis in lake sediments', *Organic Geochemistry*, 20(7), pp. 867–900. doi: 10.1016/0146-6380(93)90100-P.

Meyers, S. R. (2014) 'Astrochron: An R Package for Astrochronology'. Available at: https://cran.r-project.org/package=astrochron.

Minshull, T. A. *et al.* (2016) 'Mechanistic insights into a hydrate contribution to the Paleocene-Eocene carbon cycle perturbation from coupled thermohydraulic simulations', *Geophysical Research Letters*, 43(16), pp. 8637–8644. doi: 10.1002/2016GL069676.

Moore, E. A. and Kurtz, A. C. (2008) 'Black carbon in Paleocene-Eocene boundary sediments: A test of biomass combustion as the PETM trigger', *Palaeogeography, Palaeoclimatology, Palaeoecology*, 267, pp. 147–152. doi: 10.1016/j.palaeo.2008.06.010.

Morón, S. *et al.* (2007) 'Ciclicidad en la Formación Cerrejón', *Boletín de Geología*, 29(1), pp. 21–30.

Murphy, B. H., Farley, K. A. and Zachos, J. C. (2010) 'An extraterrestrial ^{3}He-based timescale for the Paleocene-Eocene thermal maximum (PETM) from Walvis Ridge, IODP Site 1266', *Geochimica et Cosmochimica Acta*, 74(17), pp. 5098–5108. doi: 10.1016/j.gca.2010.03.039.

Murray-Tortarolo, G. *et al.* (2017) 'The decreasing range between dry- and wet-season precipitation over land and its effect on vegetation primary productivity', *PLoS ONE*, 12(12). doi: 10.1371/journal.pone.0190304.

Naafs, B. D. A., McCormick, D., *et al.* (2018) 'Archaeal and bacterial H-GDGTs are abundant in peat and their relative abundance is positively correlated with temperature', *Geochimica et Cosmochimica Acta*, 227, pp. 156–170. doi: 10.1016/j.gca.2018.02.025.

Naafs, B. D. A., Rohrssen, M., *et al.* (2018) 'High temperatures in the terrestrial mid-latitudes during the early Palaeogene', *Nature Geoscience*, 11(10), pp. 766–771. doi: 10.1038/s41561-018-0199-0.

Naafs, B. D. A. *et al.* (2019) 'The potential of biomarker proxies to trace climate, vegetation, and biogeochemical processes in peat: A review', *Global and Planetary Change*, 179, pp. 57–79. doi: 10.1016/j.gloplacha.2019.05.006.

Naeher, S. *et al.* (2014) 'Tracing the methane cycle with lipid biomarkers in Lake Rotsee (Switzerland)', *Organic Geochemistry*, 66, pp. 174–181. doi: 10.1016/j.orggeochem.2013.11.002.

Neunlist, S. and Rohmer, M. (1985) 'Novel hopanoids from the methylotrophic bacteria Methylococcus capsulatus and Methylomonas methanica. (22S)-35-aminobacteriophane-30,31, 32,33,34-pentol and (22S)-35-amino-3β-methylbacteriophane-30,31,32,33,34-pentol', *Biochemical Journal*, 231(3), pp. 635–639. doi: 10.1042/bj2310635.

Nicholas, C. J. *et al.* (2006) 'Stratigraphy and sedimentology of the Upper Cretaceous to Paleogene Kilwa Group, southern coastal Tanzania', *Journal of African Earth Sciences*, 45, pp. 431–466. doi: 10.1016/j.jafrearsci.2006.04.003.

Nisbet, E. G. *et al.* (2019) 'Very Strong Atmospheric Methane Growth in the 4 Years 2014 – 2017: Implications for the Paris Agreement Global Biogeochemical Cycles', *Global Biogeochemical Cycles*, 33, pp. 318–342. doi: 10.1029/2018GB006009.

Nishimura, M. and Baker, E. W. (1986) 'Possible origin of *n*-alkanes with a remarkable even-to-odd predominance in recent marine sediments', *Geochimica et Cosmochimica Acta*, 50(2), pp. 299–305. doi: 10.1016/0016-7037(86)90178-X.

Nusbaumer, J. *et al.* (2017) 'Evaluating hydrological processes in the Community Atmosphere Model Version 5 (CAM5) using stable isotope ratios of water', *Journal of Advances in Modeling Earth Systems*, 9(2), pp. 949–977. doi: 10.1002/2016MS000839.

Ocko, I. B. *et al.* (2021) 'Acting rapidly to deploy readily available methane mitigation measures by sector can immediately slow global warming', *Environmental Research Letters*, 16(5). doi: 10.1088/1748-9326/abf9c8.

Okabe, S. *et al.* (2024) 'Salinity Tolerance and Osmoadaptation Strategies in Four Genera of Anammox Bacteria: Brocadia, Jettenia, Kuenenia, and Scalindua', *Environmental Science and Technology*, 58(12), pp. 5357–5371. doi: 10.1021/acs.est.3c07324.

Olefeldt, D. *et al.* (2013) 'Environmental and physical controls on northern terrestrial methane emissions across permafrost zones', *Global Change Biology*, 19(2), pp. 589–603. doi: 10.1111/gcb.12071.

Osborne, K. A. (2016) *Environmental controls on bacteriohopanepolyol signatures in estuarine sediments*. Newcastle University.

Osborne, K. A. *et al.* (2017) 'Methanotroph-derived bacteriohopanepolyol signatures as a function of temperature related growth, survival, cell death and preservation in the geological record', *Environmental Microbiology Reports*, 9(5), pp. 492–500. doi: 10.1111/1758-2229.12570.

Otto, A. and Simoneit, B. R. T. (2001) 'Chemosystematics and diagenesis of terpenoids in fossil conifer species and sediment from the Eocene Zeitz formation, Saxony, Germany', *Geochimica et Cosmochimica Acta*, 65(20), pp. 3505–3527. doi: 10.1016/S0016-7037(01)00693-7.

Ourisson, G. and Albrecht, P. (1992) 'Hopanoids. 1. Geohopanoids: the most abundant natural products on Earth?', *Accounts on Chemical Research*, 25(9), pp. 398–402.

Pagani, M., Caldeira, K., *et al.* (2006) 'An ancient carbon mystery', *Science*, 314(5805), pp. 1556–1557. doi: 10.1126/science.1136110.

Pagani, M., Pedentchouk, N., *et al.* (2006) 'Arctic hydrology during global warming at the

Palaeocene/Eocene thermal maximum', *Nature*, 442(7103), pp. 671–675. doi: 10.1038/nature05043.

Pagani, M. *et al.* (2011) 'The role of carbon dioxide during the onset of antarctic glaciation', *Science*, 334(6060), pp. 1261–1264. doi: 10.1126/science.1203909.

Panchuk, K., Ridgwell, A. and Kump, L. R. (2008) 'Sedimentary response to Paleocene-Eocene thermal maximum carbon release: A model-data comparison', *Geology*, 36(4), pp. 315–318. doi: 10.1130/G24474A.1.

Pancost, R. D. *et al.* (2000) '$\delta^{13}C$ values and radiocarbon dates of microbial biomarkers as tracers for carbon recycling in peat deposits', *Geology*, 28(7), pp. 663–666. doi: 10.1130/0091-7613(2000)028<0663:CVARDO>2.3.CO;2.

Pancost, R. D. *et al.* (2007) 'Increased terrestrial methane cycling at the Palaeocene-Eocene thermal maximum', *Nature*, 449, pp. 332–335. doi: 10.1038/nature06012.

Pancost, R. D. *et al.* (2008) 'Kerogen-bound glycerol dialkyl tetraether lipids released by hydropyrolysis of marine sediments: A bias against incorporation of sedimentary organisms?', *Organic Geochemistry*, 39(9), pp. 1359–1371. doi: 10.1016/j.orggeochem.2008.05.002.

Pancost, R. D. *et al.* (2011) 'Archaeol as a methanogen biomarker in ombrotrophic bogs', *Organic Geochemistry*, 42, pp. 1279–1287. doi: 10.1016/j.orggeochem.2011.07.003.

Pancost, R. D. *et al.* (2013) 'Early Paleogene evolution of terrestrial climate in the SW Pacific , Southern New Zealand', 14(12), pp. 5413–5429. doi: 10.1002/2013GC004935.

Pancost, R. D. (2024) 'Biomarker carbon and hydrogen isotopes reveal changing peatland vegetation, hydroclimate and biogeochemical tipping points', *Quaternary Science Reviews*, 339. doi: 10.1016/j.quascirev.2024.108828.

Pancost, R. D. and Boot, C. S. (2004) 'The palaeoclimatic utility of terrestrial biomarkers in marine sediments', *Marine Chemistry*, 92(1–4), pp. 239–261. doi: 10.1016/j.marchem.2004.06.029.

Pancost, R. D. and Sinninghe Damsté, J. S. (2003) 'Carbon isotopic compositions of prokaryotic lipids as tracers of carbon cycling in diverse settings', *Chemical Geology*, 195(1–4), pp. 29–58. doi: 10.1016/S0009-2541(02)00387-X.

Papadomanolaki, N. M., Sluijs, A. and Slomp, C. P. (2022) 'Eutrophication and Deoxygenation Forcing of Marginal Marine Organic Carbon Burial During the PETM', *Paleoceanography and Paleoclimatology*, 37(3), pp. 1–23. doi: 10.1029/2021PA004232.

Pearson, P. N., Foster, G. L. and Wade, B. S. (2009) 'Atmospheric carbon dioxide through

the Eocene-Oligocene climate transition', *Nature*, 461(7267), pp. 1110–1113. doi: 10.1038/nature08447.

Pedentchouk, N. *et al.* (2008) 'δ^{13}C and δD compositions of *n*-alkanes from modern angiosperms and conifers: An experimental set up in central Washington State, USA', *Organic Geochemistry*, 39(8), pp. 1066–1071. doi: 10.1016/j.orggeochem.2008.02.005.

Peiseler, B. and Rohmer, M. (1992) 'Prokaryotic triterpenoids of the hopane series. Bacteriohopanetetrols of new side-chain configuration from Acetobacter species', *Journal of Chemical Research*, pp. 298–299.

Penman, D. E. *et al.* (2014) 'Rapid and sustained surface ocean acidification during the Paleocene-Eocene Thermal Maximum', *Paleoceanography*, 29(5), pp. 357–369. doi: 10.1002/2014PA002621.

Peters, K. E., Walters, C. C. and Moldowan, J. M. (2005) *The Biomarker Guide Vols 1*. Cambridge: Cambridge University Press.

Petsch, S. T., Berner, R. A. and Eglinton, T. I. (2000) 'A field study of the chemical weathering of ancient sedimentary organic matter', *Organic Geochemistry*, 31(5), pp. 475–487. doi: 10.1016/S0146-6380(00)00014-0.

Piedrahita, V. A. *et al.* (2022) 'Orbital phasing of the Paleocene-Eocene Thermal Maximum', *Earth and Planetary Science Letters*, 598, p. 117839. doi: 10.1016/j.epsl.2022.117839.

Poag, C. W. and Sevon, W. D. (1989) 'A record of Appalachian denudation in postrift Mesozoic and Cenozoic sedimentary deposits of the U.S. Middle Atlantic continental margin', *Geomorphology*, 2(1–3), pp. 119–157. doi: 10.1016/0169-555X(89)90009-3.

Pogge von Strandmann, P. A. E. *et al.* (2021) 'Lithium isotope evidence for enhanced weathering and erosion during the Paleocene-Eocene Thermal Maximum', *Science Advances*, 7(42), pp. 1–12. doi: 10.1126/sciadv.abh4224.

Polik, C. A., Elling, F. J. and Pearson, A. (2018) 'Impacts of Paleoecology on the TEX_{86} Sea Surface Temperature Proxy in the Pliocene-Pleistocene Mediterranean Sea', *Paleoceanography and Paleoclimatology*, 33(12), pp. 1472–1489. doi: 10.1029/2018PA003494.

Polissar, P. J. *et al.* (2021) 'Hydrologic Changes Drove the Late Miocene Expansion of C4 Grasslands on the Northern Indian Subcontinent', *Paleoceanography and Paleoclimatology*, 36(4), pp. 1–22. doi: 10.1029/2020PA004108.

Polissar, P. J. and D'Andrea, W. J. (2014) 'Uncertainty in paleohydrologic reconstructions from molecular δD values', *Geochimica et Cosmochimica Acta*, 129, pp. 146–156. doi:

10.1016/j.gca.2013.12.021.

Prather, M. J., Holmes, C. D. and Hsu, J. (2012) 'Reactive greenhouse gas scenarios: Systematic exploration of uncertainties and the role of atmospheric chemistry', *Geophysical Research Letters*, 39(9), pp. 6–10. doi: 10.1029/2012GL051440.

R Core Team (2021) 'R: A language and environment for statistical computing. R Foundation for Statistical Computing, Vienna, Austria.' Available at: https://www.r-project.org/.

Rae, J. W. B. *et al.* (2021) 'Atmospheric CO_2 over the Past 66 Million Years from Marine Archives', *Annual Review of Earth and Planetary Sciences*, 49, pp. 609–641. doi: 10.1146/annurev-earth-082420- 063026 Copyright.

Ramos Scharrón, C. E., Castellanos, E. J. and Restrepo, C. (2012) 'The transfer of modern organic carbon by landslide activity in tropical montane ecosystems', *Journal of Geophysical Research*, 117. doi: 10.1029/2011JG001838.

Ribeiro, I. O. *et al.* (2018) 'Impact of the biomass burning on methane variability during dry years in the Amazon measured from an aircraft and the AIRS sensor', *Science of the Total Environment*, 624, pp. 509–516. doi: 10.1016/j.scitotenv.2017.12.147.

Richter, N. *et al.* (2023) 'Distributions of bacteriohopanepolyols in lakes and coastal lagoons of the Azores Archipelago', *Biogeosciences*, 20(11), pp. 2065–2098. doi: 10.5194/bg-20-2065-2023.

Robert, C. and Kennett, J. P. (1994) 'Antarctic subtropical humid episode at the Paleocene-Eocene boundary: clay-mineral evidence', *Geology*, 22(3), pp. 211–214. doi: 10.1130/0091-7613(1994)022<0211:ASHEAT>2.3.CO;2.

Röhl, U. *et al.* (2007) 'On the duration of the Paleocene-Eocene thermal maximum (PETM)', *Geochemistry, Geophysics, Geosystems*, 8(12). doi: 10.1029/2007GC001784.

Rohmer, M., Bouvier-Nave, P. and Ourisson, G. (1984) 'Distribution of hopanoid triterpenes in prokaryotes', *Journal of General Microbiology*, 130(5), pp. 1137–1150. doi: 10.1099/00221287-130-5-1137.

Rommerskirchen, F. *et al.* (2003) 'A north to south transect of Holocene southeast Atlantic continental margin sediments: Relationship between aerosol transport and compound-specific $\delta^{13}C$ land plant biomarker and pollen records', *Geochemistry, Geophysics, Geosystems*, 4(12), pp. 1–29. doi: 10.1029/2003GC000541.

Rosa-Putra, S. *et al.* (2001) 'Novel hopanoids from *Frankia* spp. and related soil bacteria: Squalene cyclization and significance of geological biomarkers revisited', *European Journal of Biochemistry*, 268(15), pp. 4300–4306. doi: 10.1046/j.1432-1327.2001.02348.x.

Rush, D. *et al.* (2014) 'Anaerobic ammonium-oxidising bacteria : A biological source of the bacteriohopanetetrol stereoisomer in marine sediments', *Geochimica et Cosmochimica Acta*, 140, pp. 50–64. doi: 10.1016/j.gca.2014.05.014.

Rush, D. *et al.* (2016) 'The bacteriohopanepolyol inventory of novel aerobic methane oxidising bacteria reveals new biomarker signatures of aerobic methanotrophy in marine systems', *PLoS ONE*, 11(11), pp. 1–27. doi: 10.1371/journal.pone.0165635.

Rush, D. *et al.* (2019) 'Biomarker evidence for the occurrence of anaerobic ammonium oxidation in the eastern Mediterranean Sea during Quaternary and Pliocene sapropel formation', *Biogeosciences*, 16, pp. 2467–2479. doi: 10.5194/bg-16-2467-2019.

Rush, W. D. *et al.* (2021) 'Increased frequency of extreme precipitation events in the North Atlantic during the PETM: Observations and theory', *Palaeogeography, Palaeoclimatology, Palaeoecology*, 568, p. 110289. doi: 10.1016/j.palaeo.2021.110289.

Sachse, D. *et al.* (2012) 'Molecular Paleohydrology : Interpreting the Hydrogen-Isotopic Composition of Lipid Biomarkers from Photosynthesizing Organisms', *Annual Review of Earth and Planetary Sciences*, 40, pp. 221–249. doi: 10.1146/annurev-earth-042711-105535.

Sachse, D., Radke, J. and Gleixner, G. (2006) 'δD values of individual n-alkanes from terrestrial plants along a climatic gradient — Implications for the sedimentary biomarker record', *Organic Geochemistry*, 37(4), pp. 469–483. doi: 10.1016/j.orggeochem.2005.12.003.

Saito, H. and Suzuki, N. (2007) 'Distributions and sources of hopanes, hopanoic acids and hopanols in Miocene to recent sediments from ODP Leg 190, Nankai Trough', *Organic Geochemistry*, 38(10), pp. 1715–1728. doi: 10.1016/j.orggeochem.2007.05.012.

Saito, M. *et al.* (2016) 'Enhanced methane emissions during Amazonian drought by biomass burning', *PLoS ONE*, 11(11). doi: 10.1371/journal.pone.0166039.

Sauer, P. E. *et al.* (2001) 'Compound-specific D/H ratios of lipid biomarkers from sediments as a proxy for environmental and climatic conditions', *Geochimica et Cosmochimica Acta*, 65(2), pp. 213–222. doi: 10.1016/S0016-7037(00)00520-2.

Saunois, M. *et al.* (2020) 'The Global Methane Budget 2000–2017', *Microbial production and consumption of greenhouse gases*.

Scalan, E. S. and Smith, J. E. (1970) 'An improved measure of the odd-even predominance in the normal alkanes of sediment extracts and petroleum', *Geochimica et Cosmochimica Acta*, 34(5), pp. 611–620. doi: 10.1016/0016-7037(70)90019-0.

Schaeffer, P. *et al.* (2008) 'Acid-catalyzed formation of 32,35-anhydrobacteriohopanetetrol from bacteriohopanetetrol', *Organic Geochemistry*, 39(10), pp. 1479–1482. doi:

10.1016/j.orggeochem.2008.07.007.

Schefuß, E. *et al.* (2003) 'Carbon isotope analyses of *n*-alkanes in dust from the lower atmosphere over the central eastern Atlantic', *Geochimica et Cosmochimica Acta*, 67(10), pp. 1757–1767. doi: 10.1016/S0016-7037(02)01414-X.

Schefuß, E. *et al.* (2016) 'Hydrologic control of carbon cycling and aged carbon discharge in the Congo River basin', *Nature Geoscience*, 9(9), pp. 687–690. doi: 10.1038/ngeo2778.

Schefuß, E., Schouten, S. and Schneider, R. R. (2005) 'Climatic controls on central African hydrology during the past 20,000 years', *Nature*, 437, pp. 1003–1006. doi: 10.1038/nature03945.

Scheingross, J. S. *et al.* (2021) 'The fate of fluvially-deposited organic carbon during transient floodplain storage', *Earth and Planetary Science Letters*, 561(116822), pp. 1–13. doi: 10.1016/j.epsl.2021.116822.

Schmidt, G. A., Shindell, D. T. and Harder, S. (2004) 'A note on the relationship between ice core methane concentrations and insolation', *Geophysical Research Letters*, 31(23). doi: 10.1029/2004GL021083.

Schmitz, B. and Pujalte, V. (2003) 'Sea-level, humidity, and land-erosion records across the initial Eocene thermal maximum from a continental-marine transect in northern Spain', *Geology*, 31(8), pp. 689–692. doi: 10.1130/G19527.1.

Schmitz, B. and Pujalte, V. (2007) 'Abrupt increase in seasonal extreme precipitation at the Paleocene-Eocene boundary', *Geology*, 35(3), pp. 215–218. doi: 10.1130/G23261A.1.

Schneider-Mor, A. and Bowen, G. J. (2013) 'Coupled and decoupled responses of continental and marine organic-sedimentary systems through the Paleocene-Eocene thermal maximum, New Jersey margin, USA', *Paleoceanography*, 28(1), pp. 105–115. doi: 10.1002/palo.20016.

Schouten, S., Hopmans, E. C. and Sinninghe Damsté, J. S. (2013) 'The organic geochemistry of glycerol dialkyl glycerol tetraether lipids: A review', *Organic Geochemistry*, 54, pp. 19–61. doi: 10.1016/j.orggeochem.2012.09.006.

Schuur, E. A. G. *et al.* (2015) 'Climate change and the permafrost carbon feedback', *Nature*, 520, pp. 171–179. doi: 10.1038/nature14338.

Schwartz-Narbonne, R. *et al.* (2020) 'A unique bacteriohopanetetrol stereoisomer of marine anammox', *Organic Geochemistry*, 143, p. 103994. doi: 10.1016/j.orggeochem.2020.103994.

Schwartz-Narbonne, R. *et al.* (2023) 'Bacterial physiology highlighted by the $\delta^{13}C$ fractionation of bacteriohopanetetrol isomers', *Organic Geochemistry*, 181(May). doi:

10.1016/j.orggeochem.2023.104617.

Secord, R. *et al.* (2012) ‘Evolution of the Earliest Horses Driven by Climate Change in the Paleocene-Eocene Thermal Maximum’, *Science Reports*, 335, pp. 478–489. doi: 10.1007/978-1-4020-4411-3_168.

Self-Trail, J. (2011) ‘Paleogene Calcareous Nannofossils of the South Dover Bridge core, Southern Maryland (USA).’, *Journal of Nannoplankton Research*, 32(1). doi: 10.58998/jnr2219.

Self-Trail, J. M. *et al.* (2012) ‘Calcareous nannofossil assemblage changes across the Paleocene-Eocene Thermal Maximum: Evidence from a shelf setting’, *Marine Micropaleontology*, 92–93, pp. 61–80. doi: 10.1016/j.marmicro.2012.05.003.

Self-Trail, J. M. *et al.* (2017) ‘Shallow marine response to global climate change during the Paleocene-Eocene Thermal Maximum, Salisbury Embayment, USA’, *Paleoceanography*, 32, pp. 710–728. doi: 10.1002/2017PA003096.

Sessions, A. L. *et al.* (1999) ‘Fractionation of hydrogen isotopes in lipid biosynthesis’, *Organic Geochemistry*, 30(9), pp. 1193–1200. doi: 10.1016/S0146-6380(99)00094-7.

Sessions, A. L. *et al.* (2004) ‘Isotopic exchange of carbon-bound hydrogen over geologic timescales’, *Geochimica et Cosmochimica Acta*, 68(7), pp. 1545–1559. doi: 10.1016/j.gca.2003.06.004.

Sessions, A. L. (2016) ‘Factors controlling the deuterium contents of sedimentary hydrocarbons’, *Organic Geochemistry*, 96, pp. 43–64. doi: 10.1016/j.orggeochem.2016.02.012.

Shaffer, G. *et al.* (2016) ‘Deep time evidence for climate sensitivity increase with warming’, *Geophysical Research Letters*, 43(12), pp. 6538–6545. doi: 10.1002/2016GL069243.

Shcherbinina, E. *et al.* (2016) ‘Environmental dynamics during the Paleocene-Eocene thermal maximum (PETM) in the northeastern Peri-Tethys revealed by high-resolution micropalaeontological and geochemical studies of a Caucasian key section’, *Palaeogeography, Palaeoclimatology, Palaeoecology*, 456, pp. 60–81. doi: 10.1016/j.palaeo.2016.05.006.

Shields, C. A. *et al.* (2021) ‘Atmospheric rivers in high-resolution simulations of the Paleocene Eocene Thermal Maximum (PETM)’, *Palaeogeography, Palaeoclimatology, Palaeoecology*, 567, p. 110293. doi: 10.1016/j.palaeo.2021.110293.

da Silveira Lobo Sternberg, L. (1988) ‘D/H ratios of environmental water recorded by D/H ratios of plant lipids’, *Nature*, 333, pp. 59–61.

Slingo, J. *et al.* (2022) 'Ambitious partnership needed for reliable climate prediction', *Nature Climate Change*, 12, pp. 494–496. doi: 10.1038/s41558-022-01383-9.

Sloan, L. C. *et al.* (1992) 'Possible methane-induced polar warming in the early Eocene', *Nature*, 357, pp. 320–322. doi: 10.1038/357320a0.

Sluijs, A. *et al.* (2006) 'Subtropical Arctic Ocean temperatures during the Palaeocene/Eocene thermal maximum', *Nature*, 441(1), pp. 610–613. doi: 10.1038/nature04668.

Sluijs, A. *et al.* (2007) 'Environmental precursors to rapid light carbon injection at the Palaeocene/Eocene boundary', *Nature*, 450(7173), pp. 1218–1221. doi: 10.1038/nature06400.

Sluijs, A., Röhl, U., *et al.* (2008) 'Arctic late Paleocene–early Eocene paleoenvironments with special emphasis on the Paleocene-Eocene thermal maximum (Lomonosov Ridge , Integrated Ocean Drilling Program Expedition 302)', *Paleoceanography*, 23(1), pp. 1–17. doi: 10.1029/2007PA001495.

Sluijs, A., Brinkhuis, H., *et al.* (2008) 'Eustatic variations during the Paleocene-Eocene greenhouse world', *Paleoceanography*, 23(4), pp. 1–18. doi: 10.1029/2008PA001615.

Sluijs, A. *et al.* (2011) 'Southern ocean warming, sea level and hydrological change during the Paleocene-Eocene thermal maximum', *Climate of the Past*, 7(1), pp. 47–61. doi: 10.5194/cp-7-47-2011.

Sluijs, A. *et al.* (2014) 'Warming, euxinia and sea level rise during the Paleocene-Eocene Thermal Maximum on the Gulf Coastal Plain: implications for ocean oxygenation and nutrient cycling', *Climate of the Past*, 10(4), pp. 1421–1439. doi: 10.5194/cp-10-1421-2014.

Sluijs, A. *et al.* (2020) 'Late Paleocene–early Eocene Arctic Ocean sea surface temperatures: reassessing biomarker paleothermometry at Lomonosov Ridge', *Climate of the Past*, 16(6), pp. 2381–2400. doi: 10.5194/cp-16-2381-2020.

Sluijs, A. and Brinkhuis, H. (2009) 'A dynamic climate and ecosystem state during the Paleocene-Eocene Thermal Maximum: Inferences from dinoflagellate cyst assemblages on the New Jersey Shelf', *Biogeosciences*, 6(8), pp. 1755–1781. doi: 10.5194/bg-6-1755-2009.

Smit, N. T. (2021) *Novel lipid biomarkers for detecting microbial oxidation of methane in the environment*. Utrecht University.

Smith, F. A., Wing, S. L. and Freeman, K. H. (2007) 'Magnitude of the carbon isotope excursion at the Paleocene-Eocene thermal maximum: The role of plant community change', *Earth and Planetary Science Letters*, 262(1–2), pp. 50–65. doi: 10.1016/j.epsl.2007.07.021.

Smith, J. C. *et al.* (2013) 'Runoff-driven export of particulate organic carbon from soil in

temperate forested uplands', *Earth and Planetary Science Letters*, 365, pp. 198–208. doi: 10.1016/j.epsl.2013.01.027.

Smith, L. C. *et al.* (2004) 'Siberian Peatlands a Net Carbon Sink and Global Methane Source since the Early Holocene', *Science*, 303(5656), pp. 353–356. doi: 10.1126/science.1090553.

Song, Haijun *et al.* (2019) 'Seawater Temperature and Dissolved Oxygen over the Past 500 Million Years', *Journal of Earth Science*, 30(2), pp. 236–243. doi: 10.1007/s12583-018-1002-2.

Soulet, G. *et al.* (2021) 'Temperature control on CO_2 emissions from the weathering of sedimentary rocks', *Nature Geoscience*, 14(9), pp. 665–671. doi: 10.1038/s41561-021-00805-1.

Sparkes, R. B. *et al.* (2013) 'Automated analysis of carbon in powdered geological and environmental samples by Raman spectroscopy', *Applied Spectroscopy*, 67(7), pp. 779–788. doi: 10.1366/12-06826.

Sparkes, R. B. *et al.* (2018) 'Carbonaceous material export from Siberian permafrost tracked across the Arctic Shelf using Raman spectroscopy', *Cryosphere*, 12, pp. 3293–3309. doi: 10.5194/tc-12-3293-2018.

Sparkes, R. B. *et al.* (2020) 'Survival of graphitized petrogenic organic carbon through multiple erosional cycles', *Earth and Planetary Science Letters*, 531. doi: 10.1016/j.epsl.2019.115992.

Spencer-Jones, C. L. *et al.* (2015) 'Bacteriohopanepolyols in tropical soils and sediments from the Congo River catchment area', *Organic Geochemistry*, 89–90. doi: 10.1016/j.orggeochem.2015.09.003.

Spencer-Jones, C. L., Wagner, T. and Talbot, H. M. (2017) 'A record of aerobic methane oxidation in tropical Africa over the last 2.5 Ma', *Geochimica et Cosmochimica Acta*, 218, pp. 27–39. doi: 10.1016/j.gca.2017.08.042.

Stallard, R. F. (1998) 'Terrestrial sedimentation and the carbon cycle: Coupling weathering and erosion to carbon burial', *Global Biogeochemical Cycles*, 12(2), pp. 231–257. doi: 10.1029/98GB00741.

Stassen, P., Thomas, E. and Speijer, R. P. (2012) 'Integrated stratigraphy of the Paleocene-Eocene thermal maximum in the New Jersey Coastal Plain: Toward understanding the effects of global warming in a shelf environment', *Paleoceanography*, 27(4), pp. 1–17. doi: 10.1029/2012PA002323.

Storey, M., Duncan, R. A. and Swisher, C. C. (2007) 'Paleocene-Eocene thermal maximum

and the opening of the northeast Atlantic', *Science*, 316(5824), pp. 587–589. doi: 10.1126/science.1135274.

Sun, X. *et al.* (2022) 'Oxidation of petrogenic organic carbon in a large river-dominated estuary', *Geochimica et Cosmochimica Acta*, 338, pp. 136–153. doi: 10.1016/j.gca.2022.10.028.

Svensen, H. *et al.* (2004) 'Release of methane from a volcanic basin as a mechanism for initial Eocene global warming', *Nature*, 429, pp. 542–545. doi: 10.1038/nature02566.

Svensen, H., Planke, S. and Corfu, F. (2010) 'Zircon dating ties NE Atlantic sill emplacement to initial Eocene global warming', *Journal of the Geological Society*, 167(3), pp. 433–436. doi: 10.1144/0016-76492009-125.

Talbot, H. M. *et al.* (2001) 'Analysis of intact bacteriohopanepolyols from methanotrophic bacteria by reversed-phase high-performance liquid chromatography-atmospheric pressure chemical ionisation mass spectrometry', *Journal of Chromatography A*, 921(2), pp. 175–185. doi: 10.1016/S0021-9673(01)00871-8.

Talbot, H. M. *et al.* (2003) 'Diverse biohopanoid compositions of non-marine sediments', *Organic Geochemistry*, 34(10), pp. 1353–1371. doi: 10.1016/S0146-6380(03)00159-1.

Talbot, H. M. *et al.* (2005) 'Bacteriohopanepolyols in hydrothermal vent biogenic silicates', *Organic Geochemistry*, 36, pp. 663–672. doi: 10.1016/j.orggeochem.2004.10.015.

Talbot, H. M. *et al.* (2008) 'Cyanobacterial bacteriohopanepolyol signatures from cultures and natural environmental settings', *Organic Geochemistry*, 39(2), pp. 232–263. doi: 10.1016/j.orggeochem.2007.08.006.

Talbot, H. M. *et al.* (2014) 'Variability in aerobic methane oxidation over the past 1.2 Myrs recorded in microbial biomarker signatures from Congo fan sediments', *Geochimica et Cosmochimica Acta*, 133, pp. 387–401. doi: 10.1016/j.gca.2014.02.035.

Talbot, H. M., Mcclymont, E. L., *et al.* (2016) 'Organic Geochemistry Origin and preservation of bacteriohopanepolyol signatures in Sphagnum peat from Bissendorfer Moor (Germany)', *Organic Geochemistry*, 97, pp. 95–110. doi: 10.1016/j.orggeochem.2016.04.011.

Talbot, H. M., Bischoff, J., *et al.* (2016) 'Polyfunctionalised bio- and geohopanoids in the Eocene Cobham Lignite', *Organic Geochemistry*, 96, pp. 77–92. doi: 10.1016/j.orggeochem.2016.03.006.

Talbot, H. M. and Farrimond, P. (2007) 'Bacterial populations recorded in diverse sedimentary biohopanoid distributions', *Organic Geochemistry*, 38(8), pp. 1212–1225. doi: 10.1016/j.orggeochem.2007.04.006.

Thauer, R. K. (1998) ‘Biochemistry of methanogenesis: a tribute to Marjory Stephenson’, *Microbiology*, 144, pp. 2377–2406.

Thauer, R. K. *et al.* (2008) ‘Methanogenic archaea: Ecologically relevant differences in energy conservation’, *Nature Reviews Microbiology*, 6(8), pp. 579–591. doi: 10.1038/nrmicro1931.

Thomas, D. J. *et al.* (2002) ‘Warming the fuel for the fire: Evidence for the thermal dissociation of methane hydrate during the Paleocene-Eocene thermal maximum’, *Geology*, 30(12), pp. 1067–1070.

Tian, W. *et al.* (2023) ‘Water table level controls methanogenic and methanotrophic communities and methane emissions in a Sphagnum-dominated peatland’, *Microbiology Spectrum*, 11(5). doi: 10.1128/spectrum.01992-23.

Tierney, J. E. *et al.* (2008) ‘Northern hemisphere controls on tropical southeast African climate during the past 60,000 years’, *Science*, 322(5899), pp. 252–255. doi: 10.1126/science.1160485.

Tierney, J. E. *et al.* (2020) ‘Past climates inform our future’, *Science*, 370(6517). doi: 10.1126/science.aay3701.

Tierney, J. E. *et al.* (2022) ‘Spatial patterns of climate change across the Paleocene–Eocene Thermal Maximum’, *Proceedings of the National Academy of Sciences of the United States of America*, 119(42), pp. 1–7. doi: 10.1073/pnas.2205326119.

Tierney, J. E., Pausata, F. S. R. and De Menocal, P. B. (2017) ‘Rainfall regimes of the Green Sahara’, *Science Advances*, 3(1). doi: 10.1126/sciadv.1601503.

Tierney, J. E., Ummenhofer, C. C. and DeMenocal, P. B. (2015) ‘Past and future rainfall in the Horn of Africa’, *Science Advances*, 1(9). doi: 10.1126/sciadv.1500682.

Tipple, B. J. and Pagani, M. (2010) ‘A 35 Myr North American leaf-wax compound-specific carbon and hydrogen isotope record: Implications for C4 grasslands and hydrologic cycle dynamics’, *Earth and Planetary Science Letters*, 299(1–2), pp. 250–262. doi: 10.1016/j.epsl.2010.09.006.

Tipple, B. J. and Pagani, M. (2013) ‘Environmental control on eastern broadleaf forest species’ leaf wax distributions and D/H ratios’, *Geochimica et Cosmochimica Acta*, 111, pp. 64–77. doi: 10.1016/j.gca.2012.10.042.

Trenberth, K. E. (1998) ‘Atmospheric moisture residence times and cycling: Implications for rainfall rates and climate change’, *Climatic Change*, 39(4), pp. 667–694. doi: 10.1023/A:1005319109110.

Tripati, A. and Elderfield, H. (2005) 'Deep-Sea Temperature and Circulation Changes at the Paleocene-Eocene Thermal Maximum', *Science*, 308(5730), pp. 29–31. doi: 10.1126/science.1109202.

Turetsky, M. R. *et al.* (2014) 'A synthesis of methane emissions from 71 northern, temperate, and subtropical wetlands', *Global Change Biology*, 20, pp. 2183–2197. doi: 10.1111/gcb.12580.

Tveit, A. T. *et al.* (2015) 'Metabolic and trophic interactions modulate methane production by Arctic peat microbiota in response to warming', *Proceedings of the National Academy of Sciences of the United States of America*, 112(19). doi: 10.1073/pnas.1420797112.

Valdes, P. J., Scotese, C. R. and Lunt, D. J. (2021) 'Deep ocean temperatures through time', *Climate of the Past*, 17(4), pp. 1483–1506. doi: 10.5194/cp-17-1483-2021.

Valentine, D. W., Holland, E. A. and Schimel, D. S. (1994) 'Ecosystem and physiological controls over methane production in northern wetlands', *Journal of Geophysical Research: Atmospheres*, 99(D1), pp. 1563–1571. doi: 10.1029/93jd00391.

Villasante-Marcos, V. *et al.* (2009) 'Rock magnetic properties across the Paleocene-Eocene Thermal Maximum in Marlborough, New Zealand', *Geologica Acta*, 7(1–2), pp. 229–242. doi: 10.1344/105.000000280.

Waddell, L. M. and Moore, T. C. (2008) 'Salinity of the Eocene Arctic Ocean from oxygen isotope analysis of fish bone carbonate', *Paleoceanography*, 23(1). doi: 10.1029/2007PA001451.

Wagner, T. *et al.* (2014) 'Microbial biomarkers support organic carbon transport from methane-rich Amazon wetlands to the shelf and deep sea fan during recent and glacial climate conditions', *Organic Geochemistry*, 67, pp. 85–98. doi: 10.1016/j.orggeochem.2013.12.003.

Walker, J. C. G., Hays, P. B. and Kasting, J. F. (1981) 'A Negative Feedback Mechanism for the Long-term Stabilization of Earth's Surface Temperature', *Journal of Geophysical Research*, 86(10), pp. 9776–9782. doi: 10.1029/JC086iC10p09776.

Walters, A. P. *et al.* (2023) 'Climate system asymmetries drive eccentricity pacing of hydroclimate during the early Eocene greenhouse', *Science Advances*, 9(31). doi: 10.1126/sciadv.adg8022.

Wan, N. *et al.* (2024) 'Global total precipitable water variations and trends over the period 1958-2021', *Hydrology and Earth System Sciences*, 28(9), pp. 2123–2137. doi: 10.5194/hess-28-2123-2024.

Wang, J. *et al.* (2019) 'The isotopic composition and fluxes of particulate organic carbon exported from the eastern margin of the Tibetan Plateau', *Geochimica et Cosmochimica Acta*, 252, pp. 1–15. doi: 10.1016/j.gca.2019.02.031.

Wang, J. *et al.* (2020) 'Long-term patterns of hillslope erosion by earthquake-induced landslides shape mountain landscapes', *Science Advances*, 6(23). doi: 10.1126/sciadv.aaz6446.

Welander, P. V. and Summons, R. E. (2012) 'Discovery, taxonomic distribution, and phenotypic characterization of a gene required for 3-methylhopanoid production', *Proceedings of the National Academy of Sciences of the United States of America*, 109(32). doi: 10.1073/pnas.1208255109.

Westerhold, T. *et al.* (2009) 'Latest on the absolute age of the Paleocene-Eocene Thermal Maximum (PETM): New insights from exact stratigraphic position of key ash layers + 19 and - 17', *Earth and Planetary Science Letters*, 287(3–4), pp. 412–419. doi: 10.1016/j.epsl.2009.08.027.

Westerhold, T. *et al.* (2018) 'Global Extent of Early Eocene Hyperthermal Events: A New Paci fi c Benthic Foraminiferal Isotope Record From Shatsky Rise (ODP Site 1209)', *Paleoceanography and Paleoclimatology*, 33, pp. 626–642. doi: 10.1029/2017PA003306.

Westerhold, T. *et al.* (2020) 'An astronomically dated record of Earth's climate and its predictability over the last 66 million years', *Science*, 369(6509), pp. 1383–1387. doi: 10.1126/science.aba6853.

Wilkes, H. (ed.) (2020) *Hydrocarbons, Oils and Lipids: Diversity, Origin, Chemistry and Fate*. Cham, Switzerland: Springer International Publishing. doi: 10.1007/978-3-319-90569-3.

Willard, D. A. *et al.* (2019) 'Arctic vegetation, temperature, and hydrology during Early Eocene transient global warming events', *Global and Planetary Change*, 178, pp. 139–152. doi: 10.1016/j.gloplacha.2019.04.012.

Wilson, C. *et al.* (2016) 'Contribution of regional sources to atmospheric methane over the Amazon Basin in 2010 and 2011', *Global biogeochemical cycles*, 30, pp. 400–420. doi: 10.1111/1462-2920.13280.

Wilton, D. J. *et al.* (2019) 'A predictive algorithm for wetlands in deep time paleoclimate models', *Geoscientific Model Development*, 12, pp. 1351–1364.

van Winden, J. F. *et al.* (2010) 'Lipids of symbiotic methane-oxidizing bacteria in peat moss studied using stable carbon isotopic labelling', *Organic Geochemistry*, 41(9), pp. 1040–1044. doi: 10.1016/j.orggeochem.2010.04.015.

van Winden, J. F., Talbot, H. M., *et al.* (2012) 'Bacteriohopanepolyol signatures as markers for methanotrophic bacteria in peat moss', *Geochimica et Cosmochimica Acta*, 77, pp. 52–61. doi: 10.1016/j.gca.2011.10.026.

van Winden, J. F., Reichart, G. J., *et al.* (2012) 'Temperature-induced increase in methane release from peat bogs: A mesocosm experiment', *PLoS ONE*, 7(6). doi: 10.1371/journal.pone.0039614.

van Winden, J. F. *et al.* (2020) 'Influence of temperature on the $\delta^{13}C$ values and distribution of methanotroph-related hopanoids in *Sphagnum*-dominated peat bogs', *Geobiology*, 18(4), pp. 497–507. doi: 10.1111/gbi.12389.

Windler, G. *et al.* (2020) 'Unraveling Glacial Hydroclimate in the Indo-Pacific Warm Pool: Perspectives From Water Isotopes', *Paleoceanography and Paleoclimatology*, 35(12), pp. 1–17. doi: 10.1029/2020PA003985.

Windler, G., Tierney, J. E. and Anchukaitis, K. J. (2021) 'Glacial-Interglacial Shifts Dominate Tropical Indo-Pacific Hydroclimate During the Late Pleistocene', *Geophysical Research Letters*, 48(15), pp. 1–10. doi: 10.1029/2021GL093339.

Wing, S. L. *et al.* (2005) 'Transient Floral Change and Rapid Global Warming at the Paleocene-Eocene Boundary', *Science*, 310, pp. 993–996.

Wing, S. L. *et al.* (2009) 'Late Paleocene fossils from the Cerrejón Formation, Colombia, are the earliest record of Neotropical rainforest', *Proceedings of the National Academy of Sciences of the United States of America*, 106(44), pp. 18627–18632. doi: 10.1073/pnas.0905130106.

Wing, S. L. and Currano, E. D. (2013) 'Plant response to a global greenhouse event 56 million years ago', *American Journal of Botany*, 100(7), pp. 1234–1254. doi: 10.3732/ajb.1200554.

Winguth, A. *et al.* (2010) 'Climate response at the paleocene-eocene thermal maximum to greenhouse gas forcing-a model study with CCSM3', *Journal of Climate*, 23(10), pp. 2562–2584. doi: 10.1175/2009JCLI3113.1.

Yang, H. *et al.* (2019) 'Depth-dependent variation of archaeal ether lipids along soil and peat profiles from southern China: Implications for the use of isoprenoidal GDGTs as environmental tracers', *Organic Geochemistry*, 128, pp. 42–56. doi: 10.1016/j.orggeochem.2018.12.009.

Yu, M. *et al.* (2021) 'Contrasting fates of terrestrial organic carbon pools in marginal sea sediments', *Geochimica et Cosmochimica Acta*, 309(238), pp. 16–30. doi: 10.1016/j.gca.2021.06.018.

Yvon-Durocher, G. *et al.* (2012) 'Reconciling the temperature dependence of respiration across timescales and ecosystem types', *Nature*, 487(7408), pp. 472–476. doi: 10.1038/nature11205.

Zachos, J. *et al.* (2001) 'Trends, rhythms, and aberrations in global climate 65 Ma to present', *Science*, 292, pp. 686–693. doi: 10.1126/science.1059412.

Zachos, J. C. *et al.* (2005) 'Rapid acidification of the ocean during the paleocene-eocene thermal maximum', *Science*, 308(5728), pp. 1611–1615. doi: 10.1126/science.1109004.

Zachos, J. C., Dickens, G. R. and Zeebe, R. E. (2008) 'An early Cenozoic perspective on greenhouse warming and carbon-cycle dynamics', *Nature*, 451, pp. 279–283. doi: 10.1038/nature06588.

Zeebe, R. E. (2013) 'What caused the long duration of the Paleocene-Eocene Thermal Maximum?', *Paleoceanography*, 28, pp. 440–452. doi: 10.1002/palo.20039.

Zeebe, R. E. *et al.* (2014) 'Onset of carbon isotope excursion at the Paleocene-Eocene thermal maximum took millennia, not 13 years', *Proceedings of the National Academy of Sciences of the United States of America*, 111(12), pp. 1062–1063. doi: 10.1073/pnas.1321177111.

Zeebe, R. E. *et al.* (2017) 'Orbital forcing of the Paleocene and Eocene carbon cycle', *Paleoceanography*, 32, pp. 440–465. doi: 10.1002/2016PA003054.

Zeebe, R. E. and Lourens, L. J. (2019) 'Solar System chaos and the Paleocene–Eocene boundary age constrained by geology and astronomy', *Science*, 929(6456), pp. 926–929. doi: 10.1126/science.aax0612.

Zeebe, R. E., Zachos, J. C. and Dickens, G. R. (2009) 'Carbon dioxide forcing alone insufficient to explain Palaeocene-Eocene Thermal Maximum warming', *Nature Geoscience*, 2, pp. 576–580. doi: 10.1038/ngeo578.

Zhang, Y. G. *et al.* (2011) 'Methane Index: A tetraether archaeal lipid biomarker indicator for detecting the instability of marine gas hydrates', *Earth and Planetary Science Letters*, 307(3–4), pp. 525–534. doi: 10.1016/j.epsl.2011.05.031.

Zheng, Y. *et al.* (2014) 'Holocene variations in peatland methane cycling associated with the Asian summer monsoon system', *Nature Communications*, 5, pp. 1–7. doi: 10.1038/ncomms5631.

Zhu, C. *et al.* (2010) 'Intense aerobic methane oxidation in the Yangtze Estuary: A record from 35-aminobacteriohopanepolyols in surface sediments', *Organic Geochemistry*, 41(9), pp. 1056–1059. doi: 10.1016/j.orggeochem.2010.03.015.

Zhu, C. *et al.* (2014) 'Identification of unusual butanetriol dialkyl glycerol tetraether and pentanetriol dialkyl glycerol tetraether lipids in marine sediments', *Rapid Communications in Mass Spectrometry*, 28(4), pp. 332–338. doi: 10.1002/rcm.6792.

Zhu, J. *et al.* (2020) 'Simulation of early Eocene water isotopes using an Earth system model and its implication for past climate reconstruction', *Earth and Planetary Science Letters*, 537(116164), pp. 1–11. doi: 10.1016/j.epsl.2020.116164.

Zhu, J., Poulsen, C. J. and Tierney, J. E. (2019) 'Simulation of Eocene extreme warmth and high climate sensitivity through cloud feedbacks', *Science Advances*, 5(9), pp. 1–11. doi: 10.1126/sciadv.aax1874.

Zindorf, M. *et al.* (2020) 'Reconstructing oxygen deficiency in the glacial Gulf of Alaska: Combining biomarkers and trace metals as paleo-redox proxies', *Chemical Geology*, 558(August). doi: 10.1016/j.chemgeo.2020.119864.

Zondervan, J. R. *et al.* (2023) 'Rock organic carbon oxidation CO_2 release offsets silicate weathering sink', *Nature*, 623(7986), pp. 329–333. doi: 10.1038/s41586-023-06581-9.

Zundel, M. and Rohmer, M. (1985) 'The biosynthesis of 2β-methylhopanoids and 3β-methylhopanoids of *Methylobactevium organophilum* and *Acetobactev pasteuvianus* ssp. *pasteurianus*', *European Journal of Biochemistry*, 151(2), pp. 405–410. doi: 10.1111/j.1432-1033.1985.tb09116.x.